

Exploring connections between seagrass ecosystem services and meadow hydrodynamics

By

Rachel Schaefer

Honors Bachelor's Degree in Civil Engineering with Distinction, University of Delaware (2019)

Submitted to the Department of Civil and Environmental Engineering in partial fulfillment of the requirements for the degree of

Doctor of Philosophy

at the

Massachusetts Institute of Technology

May 2024

© 2024 Rachel Schaefer. All rights reserved

The author hereby grants to MIT a nonexclusive, worldwide, irrevocable, royalty-free license to exercise any and all rights under copyright, including to reproduce, preserve, distribute and publicly display copies of the thesis, or release the thesis under an open-access license.

Authored by: Rachel Schaefer

Department of Civil and Environmental Engineering

May 3, 2024

Certified by: Heidi Nepf

Department of Civil and Environmental Engineering

Thesis supervisor

Accepted by: Heidi Nepf

Donald and Martha Harleman Professor of Civil and Environmental Engineering
Chair, Graduate Program Committee

Exploring connections between seagrass ecosystem services and meadow hydrodynamics

By

Rachel Schaefer

Submitted to the Department of Civil and Environmental Engineering in partial fulfillment of the requirements for the degree of
Doctor of Philosophy

Abstract

Meadows of aquatic vegetation, such as seagrass, modify the flow of water and transport of sediment in the environment. The hydrodynamic drag generated by a seagrass meadow contributes to the numerous ecosystem services it provides, which includes quiescent habitat for other species, wave damping, water quality enhancement, and carbon sequestration. This thesis reports on a series of studies using physical experiments, simulations, and field measurements to relate the interactions between seagrass, waves, currents, and sediment to two ecosystem services, wave dissipation and carbon sequestration.

First, laboratory studies and simulations were used to explore how plants interact with waves and currents with the goal of predicting wave dissipation and turbulence generation. The flexibility of a plant is critical in defining its interactions with the environment. Seagrass plants deflect under currents, which streamlines the plants and reduces the parts of the plants directly experiencing the flow, and sway under waves, which reduces the relative motion between the plants and the flow. These responses, known as reconfiguration, reduce the drag seagrass plants experience compared to rigid plant of the same length. Laboratory flume and numerical experiments showed that the relative magnitudes of current and wave velocities determine the influence of reconfiguration on drag, and therefore on seagrass-induced wave attenuation and turbulence. For more flexible leaves, defined as having a ratio of drag force to restoring force due to stiffness greater than 100, drag reduction due to current-induced deflection competes against drag augmentation due to lower relative motion, such that enhancing current speeds reduces wave energy dissipation only when the current velocity is less than one-third of the maximum wave velocity. For stiffer leaves, drag augmentation dominates drag reduction so that adding a current enhances wave energy dissipation. Meanwhile, the measured effects of reconfiguration on plant-generated turbulence were used to propose a hybrid analytical model for predicting the turbulence to account for the relative contributions of waves and currents.

Second, field experiments were performed in three Massachusetts, USA seagrass meadows to relate spatial patterns in hydrodynamics with spatial patterns in sediment organic carbon. Lower velocities were expected to reduce sediment mobility and thus enhance the deposition and retention of sediment carbon. At a wave-dominated continuous meadow, results showed decreasing sediment carbon accretion rates with increasing wave velocities, which could be predicted by accounting for seagrass-induced wave damping and wave shoaling. However, at a current-dominated lagoonal continuous meadow, sediment carbon increased with increasing tidal velocities. The spatial reduction in sediment carbon at the latter site was attributed to spatial diminishment of sediment supply with increasing distance into the meadow, away from the lagoon inlet. Lastly, in a patchy current-dominated meadow the spatial variability in sediment carbon stocks did not correlate with the spatial distribution of patches. One vegetated patch

showed substantially higher sediment carbon than the rest of the meadow, which was attributed to the recent persistence of the specific patch. In addition, preliminary results for a field study comparing different methods of estimating net ecosystem carbon exchange in a seagrass meadow are also presented.

Thesis Supervisor: Dr. Heidi M. Nepf

Title: Donald and Martha Harleman Professor of Civil and Environmental Engineering

Acknowledgments

I want to first thank my thesis advisor, Dr. Heidi Nepf. I appreciate her combination of breadth and depth of knowledge with creativity and an uncanny ability to ask interesting questions. She has been patient, kind, and thoughtful, and never needed to be asked twice to get into the water to help with collecting data for field experiments. I also thank my thesis committee members, Dr. Julie Simpson and Dr. Michael Howland, for their insightful comments and advice.

Thank you to current and past members of the Nepf Lab and Environmental Fluid Mechanics group at MIT. I enjoy our conversations inside and outside of the lab, and I always appreciate your feedback and advice. I'm grateful to Dr. Julie Simpson, Dr. Gary Lei, Dr. Alyssa Novak, Ernie Lee, Ian Koe, Dr. Chuyan Zhao, Alley McConnell, Dr. Yuan Xu, and Kimberly Candelario for assisting with field data collection and sample processing. Thanks to Environmental Protection Agency scientific divers Dr. Phil Colarusso, Eric Nelson, Jean Brochi, Danielle Gaito, Chuck Protzmann, and Brent England. Thanks to Mike Sacarny, Andrew Jacobs, and Isaiah Schaeffer for assisting with field data collection and boat support. I thank Stephen Rudolph and Andy Ryan for assistance with discussing, fabricating, and fixing various elements for laboratory and field experiments. Thanks to Dr. Xiaoxia Zhang and Tian Zhao for assisting in constructing artificial seagrass models. Thanks to Dr. Pere Masqué for his advice.

Thanks to the International Atomic Energy Agency (IAEA), Ocean Acidification International Coordination Centre (OA-ICC), and the Prince Albert II of Monaco Foundation in Monaco for inviting me to join and supporting my participation in the Ocean Change and Blue

Carbon Workshop in Monaco in 2023. Thanks to the University of New Orleans, the Water Institute of the Gulf, the Delft University of Technology, Utrecht University, and Deltares for hosting and inviting me to join a National Science Foundation International Research Experiences for Students program in The Netherlands in 2022.

Special extra thanks to Dr. Phil Colarusso, Dr. Julie Simpson, and Dr. Alyssa Novak for their continued support during field experiments, for giving helpful advice and feedback, for giving me the chance to help out with seagrass restoration efforts, and of course for their friendly banter. I'm inspired by their unwavering dedication and enthusiasm.

I'm very thankful to my parents and twin sister Serena for supporting and encouraging me. Last but not least, and most importantly, thanks to my amazing partner Adam Atanas, who has given me unconditional support and love over the past few years.

Funding for this work came from the National Science Foundation (NSF) Graduate Research Fellowship under Grant #1745302 and #2141064, NSF Grant #1659923, Shell International Exploration and Production through the MIT Energy Initiative, the Louis Berger Fellowship Fund, and the MIT Department of Civil and Environmental Engineering.

Table of Contents

1. Introduction.....	24
1.1 Thesis outline	27
1.2 References	30
2. Wave damping by seagrass meadows in combined wave-current conditions.....	36
2.1 Introduction.....	37
2.2 Theoretical Background.....	40
2.2.1 Reconfiguration of and drag on flexible blades.....	40
2.2.2 Wave dissipation	44
2.3 Materials and Methods.....	48
2.3.1 Seagrass shoot model and meadow construction	49
2.3.2 Velocity measurements.....	51
2.3.3 Meadow imaging	52
2.3.4 Wave amplitude measurements	53
2.3.5 Parameter estimation	55
2.4 Results and Discussion.....	56
2.4.1 Influence of current on measured wave decay coefficient	56

2.4.2 KD prediction.....	58
2.4.3 Extension to field application.....	61
2.5 Conclusions.....	64
2.6 Acknowledgments.....	65
2.7 References.....	65
2.8 Supplementary Information.....	69
2.8.1 Compiled <i>Zostera marina</i> characteristics.....	69
2.8.2 Experimental parameters and measurements.....	71
2.8.3 Accounting for current-induced modification of waves.....	74
2.8.4 Measured KD, wc as a function of $Cawc$	76
2.8.5 Predicting the in-canopy time-averaged velocity.....	79
3. Movement of and drag force on slender flat plates in an array exposed to combinations of unidirectional and oscillatory flow.....	82
3.1 Introduction.....	83
3.2. Reconfiguration of individual blades.....	86
3.3 Modeling Framework.....	90
3.3.1 Blades within a canopy.....	90
3.3.2 Blade model setup.....	94
3.3.3 Model limitations.....	99
3.4 Results and Discussion.....	100

3.4.1 Blade reconfiguration and relative velocities	100
3.4.2 Impact of current on wave energy dissipation rate.....	106
3.4.3 Wave damping by seagrass meadow	111
3.4.4 Using effective blade length to predict wave dissipation.....	116
3.5 Conclusions	119
3.6 Acknowledgments.....	120
3.7 References	120
4. Flow structure in an artificial seagrass meadow in combined wave-current conditions	126
4.1 Introduction	127
4.2 Theoretical background for predicting velocity and turbulence in meadow.....	130
4.3 Materials and methods	134
4.3.1 Construction of artificial seagrass shoot and meadow	135
4.3.2 Velocity measurements, wave gauge measurements, and meadow imaging	135
4.3.3 Drag coefficient	137
4.4 Results	138
4.4.1 Time-averaged velocity profiles.....	138
4.4.2 Reynolds stress and turbulence kinetic energy profiles.....	141
4.4.3 Predictions of magnitude of peak Reynolds stress	142
4.4.4 Canopy turbulent kinetic energy measurements and predictions	144

4.5 Discussion	149
4.5.1 Impact of waves on mean deflected height	149
4.5.2 Reynolds stress at the top of the canopy.....	150
4.5.3 Blade reconfiguration and wake production.....	151
4.5.4 Relative strengths of wave and current velocities	152
4.6 Acknowledgments.....	152
4.7 References	153
4.8 Supplementary Information.....	158
4.8.1 Dictionary of symbols	158
4.8.2 Experimental parameters	160
4.8.3 Time-averaged velocity, Reynolds stress, and turbulent kinetic energy profiles for all cases.....	163
4.8.4 Additional figures	166
5. Spatial heterogeneity in sediment and carbon accretion rates within a seagrass meadow correlated with the hydrodynamic intensity.....	168
5.1 Introduction.....	169
5.2 Methods.....	172
5.2.1 Meadow and sediment characteristics	172
5.2.2 Velocity and turbulence.....	175
5.3 Results and Discussion.....	178

3.1 Meadow structure and sediment characteristics	178
5.3.2 Velocity, turbulent kinetic energy, and sediment accumulation rate	181
5.3.3 Sediment organic carbon content and carbon accretion rates.....	185
5.3.4 Using hydrodynamic gradients to constrain meadow-scale estimates of carbon	189
5.4 Conclusions	196
5.5 Acknowledgements	196
5.6 References	197
5.7 Supplementary Information.....	201
5.7.1 Tilt current meter measurements in the presence of waves.....	201
5.7.2 Additional data analysis.....	202
6. Proximity to inlet channel drives spatial variation in sediment organic carbon across a lagoonal seagrass meadow.....	205
6.1 Introduction	206
6.2. Materials and Methods.....	209
6.2.1 Field site	209
6.2.2 Sediment sample collection	210
6.2.3 Seagrass parameters and sample collection.....	212
6.2.4 Laboratory sample analyses	212
6.2.5 Velocity data collection and processing	215
6.3 Results	216

6.3.1 Seagrass and sediment characteristics	216
6.3.2 Mass and carbon accumulation rates	221
6.3.3 Exposure to waves and currents	222
6.4. Discussion	225
6.4.1 Drivers of spatial gradients in sediment carbon	225
6.5 Conclusions	231
6.6 Acknowledgments	232
6.7 References	232
6.8 Supplementary Information.....	238
6.8.1 Sediment grain size distributions.....	238
6.8.2 Carbon and nitrogen content and stable isotope ratio profiles	239
6.8.3 ²¹⁰ Pb sediment core profiles	243
7. Stability of a patchy seagrass meadow and implications for carbon retention.....	244
7.1. Introduction	245
7.2. Methods and Materials	249
7.2.1 Study site	249
7.2.2 Sediment and seagrass sample collection.....	250
7.2.3 Laboratory sample analysis	252
7.2.4 Velocity data collection and processing.....	254
7.2.5 Image analysis	255

7.2.6 Statistical analyses	256
7.3. Results	256
7.3.1 Stable isotope measurements.....	257
7.3.2 Seagrass meadow parameters	258
7.3.3 Hydrodynamic conditions.....	259
7.3.4 Sediment sample analyses	260
7.3.5 Landscape configuration analysis.....	264
7.4. Discussion	266
7.4.1 Sediment transport and resuspension	267
7.4.2 Mechanisms sustaining a patchy landscape configurations	270
7.4.3 Persistence of sediment organic carbon pools.....	274
7.5. Conclusions	276
7.6 Acknowledgments.....	276
7.7 References	277
7.8 Supplementary Information.....	284
7.8.1 Details of ^{210}Pb and ^{137}Cs methodology	284
7.8.2 Velocity measurement processing details.....	287
7.8.3 Historical imagery sources	291
7.8.4 Differences in delineated vegetated pixels over time.....	292
7.8.5 Total meadow area delineation example	293

7.8.6 Seagrass meadow density and morphology measurements	294
7.8.7 Sediment core profiles of carbon isotope ratios and organic carbon stocks.....	295
7.8.8 Near-surface grain size distributions	297
8. Preliminary results for comparing different methods of estimating the net ecosystem carbon exchange in a seagrass meadow	298
8.1. Introduction	298
8.2 Methods.....	301
8.2.1 Field site stations	301
8.2.2 Sediment sample collection and laboratory processing.....	302
8.2.3 Seagrass sample collection	303
8.2.4 Hydrodynamic intensity measurements	305
8.2.5 Elemental analyses and stable isotope ratios	306
8.2.6 Sediment accumulation rates	306
8.3 Preliminary Results and Discussion.....	307
8.3.1 Seagrass characteristics and growth	307
8.3.2 Sediment sample properties.....	310
8.3.3 Hydrodynamics across the meadow	314
8.3.4 Net ecosystem carbon budget.....	316
8.4 Conclusions and Next Steps.....	318
8.5 References	319

8.6. Supplementary Figures.....	322
9. Summary and ideas for future work.....	325

List of Figures

2.1 Sketch of wave damping laboratory flume setup.....	49
2.2 Images of artificial meadow.....	50
2.3 Example of measured wave amplitudes across meadow	54
2.4 Measured wave damping coefficients.....	58
2.5 Predicted vs. measured wave damping coefficients	59
2.6 Predicted vs. measured mean canopy deflected height, in-canopy time-averaged velocity, and wave damping coefficients.....	62
2.S.1 Measured wave damping coefficient vs. wave-current Cauchy number	77
2.S.2 Product of measured wave damping coefficient and initial wave amplitude vs. initial wave amplitude	78
2.S.3 Measured mean canopy deflected height vs. depth-averaged, time-averaged velocity and vs. canopy-averaged, time-averaged velocity	80
2.S.4 Measured vs. predicted maximum wave-induced current and canopy-averaged wave- induced current for pure wave cases	81

3.1 Sketch of blade reconfiguration under pure current, pure wave, and combined wave-current conditions.....	90
3.2 Sketch of impact of flexible seagrass meadow on pure current and pure wave flow conditions.....	91
3.3 Schematic of numerical blade model.....	95
3.4 Heat maps of relative velocity magnitudes normalized by wave velocities along flexible blades over wave periods for more flexible blade case	102
3.5 Heat maps of relative velocity magnitudes normalized by wave velocities along flexible blades over wave periods for stiffer blade case	103
3.6 Ratio of mean deflected blade height to blade length vs. current Cauchy number	105
3.7 Impact of imposed currents on horizontal blade excursion over a wave period.....	106
3.8 Temporal rate of wave energy dissipation in combined wave-current conditions normalized by that of the corresponding pure wave conditions with increasing current-to-wave velocity ratios	109
3.9 Flow condition corresponding to minimum temporal rate of wave energy dissipation vs. wave Cauchy number.....	110
3.10 Influence of simulated <i>Posidonia oceanica</i> L. on spatial wave amplitude evolution in following and opposing currents.....	114
3.11 Assessing accuracy of effective blade lengths inferred from temporal wave energy dissipation rates in combined wave-current conditions	118
4.1 Sketch of velocity and Reynolds stress profiles in submerged canopy	131

4.2 Sketch of velocity and turbulence measurements laboratory flume setup.....	134
4.3 Velocity, Reynolds stress, and turbulent kinetic energy profiles for the pure wave conditions and combined wave-current conditions with the largest imposed current	139
4.4 Wave-to-current velocity ratio vs. current Reynolds number.....	140
4.5 Maximum Reynolds stress in combined wave-current conditions versus that of the corresponding pure wave conditions, and predicted vs. measured maximum Reynolds stress for pure current, pure wave, and combined wave-current conditions.....	143
4.6 Measured canopy-averaged turbulent kinetic energy vs. squared sum of wave velocity and in-canopy depth-averaged, time-averaged velocity	145
4.7 Measured canopy-averaged turbulent kinetic energy vs. proposed hybrid model.....	147
4.8 Measured canopy-averaged turbulent kinetic energy compared to that of pure current and pure wave conditions	148
4.9 Sketch of blade model under wave crest and wave trough for the largest wave condition, depicting how blades might sweep the bed.....	151
4.S.1 Time-averaged velocity profiles	163
4.S.2 Reynolds stress and turbulent kinetic energy profiles for 27 cm water depth.....	164
4.S.3 Reynolds stress and turbulent kinetic energy profiles for 45 cm water depth.....	165
4.S.4 Ratio of lower-bound canopy-averaged wake production to canopy-averaged measured shear production vs. wave-to-current velocity ratio	166
4.S.5 Measured mean canopy deflected height vs. sum of wave and current velocities ..	167

5.1 Map and experimental schematic of Nahant seagrass meadow field site	173
5.2 ²¹⁰ Pb and ²²⁶ Ra profiles from which sediment mass and carbon accumulation rates were able to be determined at Nahant.....	181
5.3 Approximate high tide and low tide water depths and root-mean-squared velocities measured over two-week deployment at Nahant	183
5.4 Predicted turbulent kinetic energy during recorded storm events and comparison of sediment accumulation rate to turbulent kinetic energy at Nahant.....	185
5.5 Sediment organic carbon and carbon accretion rate vs. distance from nearest meadow edge and distance from offshore meadow edge at Nahant	188
5.6 Nahant carbon accretion rate vs. predicted turbulent kinetic energy.....	189
5.7 Spatial evolution of wave velocities, turbulent kinetic energy, and carbon accretion rates at Nahant based on measurements and predictive models.....	194
5.S.1 Laboratory flume comparisons of tilt current meter and acoustic Doppler velocimeter measurements.....	202
5.S.2 Mean meadow sediment organic carbon content by depth zone at Nahant.....	203
5.S.3 Mean meadow carbon accretion rates by depth zone at Nahant.....	204
5.S.4 Meadow mean sediment organic carbon and meadow mean carbon accretion rates vs. mean seagrass shoot density at Nahant.....	204
6.1 Map of Menemsha Pond seagrass meadow field site	210
6.2 Sediment organic carbon content, stable isotope, and sediment trap measurements across Menemsha Pond transect	219

6.3 Menemsha Pond surface sediment vial sample organic carbon measurements.....	220
6.4 Average sediment mass accumulation rate and sediment organic carbon accumulation rates across Menemsha Pond transect.....	221
6.5 Menemsha Pond tidal velocity and wave velocity record	222
6.6 Menemsha Pond polar compass plots of magnitudes and directions of peak tidal velocity from the flood and ebb phases of each tidal cycle during spring tides and neap tides, overlaid on a map of the measurement transect.....	223
6.7 Average sediment core organic carbon content, average sediment trap mass, and average sediment organic carbon accumulation rate vs. average peak in-canopy tidal velocities across Menemsha Pond transect.	224
6.8 Sketches of flow circulation patterns near the inlet to Menemsha Pond during the flood and ebb tidal phases	227
6.9 Record of tidal velocity components perpendicular to inlet channel to Menemsha Pond	228
6.10 Average tidal velocity components perpendicular to inlet channel to Menemsha Pond and particle advection and settling time-scale ratios across Menemsha Pond transect	229
6.S.1 Near-surface sediment grain size distributions at Menemsha Pond	238
6.S.2 Sediment core organic carbon content profiles at Menemsha Pond.....	239
6.S.3 Sediment core nitrogen content profiles at Menemsha Pond	240
6.S.4 Sediment core carbon stable isotope ratio profiles at Menemsha Pond	241
6.S.5 Sediment core nitrogen stable isotope ratio profiles at Menemsha Pond.....	242

6.S.6 Sediment core ^{210}Pb , ^{226}Ra profiles at Menemsha Pond.....	243
7.1 Map of Gloucester patchy seagrass meadow field site	249
7.2 Box plots of carbon isotope signatures $\delta^{13}\text{C}$ from seagrass leaf samples, sediment trap and sediment core samples.....	257
7.3 Example Gloucester carbon stable isotope ratio and organic carbon density sediment core profiles	258
7.4 Gloucester tidal velocity and wave velocity record.....	260
7.5 Average sediment trap mass cumulative organic carbon stocks vs. average peak in- canopy or unvegetated tidal velocity at Gloucester	261
7.6 Spatial pattern analysis heat maps overlaid with average sediment organic carbon content at Gloucester	265
7.7 Average sediment core organic carbon content vs. measurement station spatial pattern analysis values at Gloucester	266
7.8 Vegetation coverage for each processed image and percentage of vegetation cover in an image of interest that was consecutively vegetated in chronologically earlier images vs. time interval between image of interest and earlier image at Gloucester	273
7.S.1 Gloucester ^{210}Pb sediment core profiles	287
7.S.2 Gloucester vegetation coverage raster changes across historical imagery	293
7.S.3 Example delineation of vegetated patches in a historical image of Gloucester field site	294
7.S.4 Gloucester carbon stable isotope ratio sediment core profiles	296

7.S.5 Gloucester organic carbon density sediment core profiles	297
7.S.6 Gloucester organic carbon content sediment core profiles.....	297
7.S.7 Gloucester near-surface sediment grain size distributions	298
8.1 Map of Hadley Harbor seagrass meadow field site	303
8.2 Average shoot densities and longest leaf lengths at Hadley Harbor.....	309
8.3 Average seagrass growth rates per shoot at Hadley Harbor	309
8.4 Water temperatures near ECHOES location at Hadley Harbor	310
8.5 Average seagrass sample carbon stable isotope ratios, nitrogen stable isotope ratios, organic carbon content, and nitrogen content at Hadley Harbor	311
8.6 Average sediment trap deposition rates at Hadley Harbor	312
8.7 Average sediment trap sample carbon stable isotope ratios, nitrogen stable isotope ratios, organic carbon content, and nitrogen content at Hadley Harbor	313
8.8 Comparisons of seagrass and sediment sample carbon stable isotope ratios and nitrogen stable isotope ratios at Hadley Harbor	314
8.9 Example tidal velocities, wave velocities, and pressure records at Hadley Harbor ...	316
8.10 Tidal speed records across all stations and deployments at Hadley Harbor	316
8.S.1 Hadley Harbor organic carbon content and nitrogen content sediment core profiles	323
8.S.2 Hadley Harbor carbon stable isotope ratio and nitrogen stable isotope ratio sediment core profiles	324
8.S.3 Hadley Harbor ²¹⁰ Pb sediment core activity profiles.....	325

List of Tables

2.S.1 Compiled <i>Zostera marina</i> L. characteristics and parameters of artificial seagrass models used in flume study.....	69
2.S.2 Experimental parameters and measurements for wave damping laboratory flume experiments.....	71
3.1 Forces included in blade model simulation	96
3.2 Blade model simulation test case conditions	99
3.3 Test parameters for simulating <i>Posidonia oceanica</i> L. blades	113
4.S.1 Descriptions and units of symbols used in Chapter 4.....	158
4.S.2 Experimental parameters and measurements for velocity and turbulence laboratory flume experiments.....	160
5.1 Measured meadow structure and sediment characteristics at Nahant.....	179
6.1 Menemsha Pond measurement station parameters	217
7.1 Gloucester statistical analysis results.....	262
7.S.1 List of year, time of year, and source of historical imagery used in the study	292
7.S.2 Seagrass meadow density and morphological characteristics measured in July, 2022 at the vegetated stations at Gloucester	294

Chapter 1

Introduction

The ability of aquatic vegetation to physically modify their environment has earned them the title of “ecosystem engineers” (Bos et al., 2007; Jones et al., 1994). For example, meadows of seagrass attenuate tidal velocities within the canopy and thereby create quiescent habitat for a rich variety of fish and shellfish (e.g., Irlandi & Peterson, 1991; Pollard, 1984). Seagrass meadows also dampen the energy of waves propagating through them (e.g., Fonseca & Cahalan, 1992; Infantes et al., 2012), improve water quality through nutrient uptake (e.g., Szmant et al. 1996; Short & Short, 1984; Ward et al. 1984), and sequester organic carbon in their underlying sediments (e.g., Mateo et al., 1997; Miyajima et al., 1998). In 2014, the total value of seagrass ecosystems services has been roughly estimated to be at least \$10 trillion USD per year (Costanza et al., 2014).

However, seagrass meadows are disappearing at a rate of 7% per year globally (Waycott et al., 2009), threatening the biodiversity, coastal protection, and reservoirs of carbon that depend on the physical presence of the seagrass. Projects to restore seagrass meadows are continuing to evolve (Tan et al., 2020) but have an estimated overall long-term success rate of less than 40% (van Katwijk et al., 2016). Common restoration techniques include planting mature seagrass into

unvegetated areas (e.g., Orth et al., 1999) or dispersing large amounts of seeds (e.g., Orth et al., 1994). Incorporating knowledge of how individual plants and entire meadows modify flow and sediment can inform the choice of both the selection of potential sites for restoration and the restoration technique.

Yet most studies on seagrass meadow hydrodynamics only consider tidal currents with no waves, or waves with no currents, while seagrasses, existing along coastlines on every continent except Antarctica (Unsworth et al., 2019), experience a wide range of combined wave and current conditions. Accounting for the combined influences of both waves and currents on seagrass is important in large part because seagrass plants are flexible. Seagrass plants deflect in response to currents, which streamlines the plant and reduces the portion of the plant that is exposed to the flow, and sway in response to waves, which reduces the relative motion between the water and the plants. These postural changes, known as reconfiguration, typically lead to a reduction in hydrodynamic drag forces (Gosselin, 2019). Hydrodynamic drag is responsible for the ability of seagrass meadows to attenuate currents within the meadow (Brunet et al., 1994; Raupach et al., 1996) and dissipate wave energy in the direction of wave energy propagation (Dalrymple et al., 1984), as well as its ability to generate turbulent leaf-scale eddies that enhance nutrient uptake (Anderson & Charters, 1982). For example, van Keulen & Borowitzka (2002) measured profiles of horizontal current (time-averaged) velocities in seagrass meadows in Shoalwater Bay, Australia and observed strong velocity shear at the tops of the meadows, with velocities above the meadow greater than velocities within the meadow by an order of magnitude. Later, Bradley & Houser (2009) observed a 30% reduction in wave height across 40 m of seagrass in coastal Florida.

The reduction of current velocity within the canopy as well as meadow-induced wave damping can enhance the retention and burial of sediment organic carbon, preventing additional release of carbon dioxide to the atmosphere (e.g., Oreska et al., 2017; Fourqurean et al., 2012). The potential greenhouse gas emissions mitigation associated with the long-term immobilization of organic carbon in seagrass sediments may be assessed to produce carbon credits, which can provide financial incentives for seagrass restoration projects (e.g., Fourqurean et al., 2012; Howard et al., 2023). Carbon credit restoration projects require rigorous monitoring, reporting, and verification procedures in order to demonstrate “additionality,” or the increased effectiveness of the vegetation in retaining carbon compared to the baseline degraded or unvegetated scenario (e.g., Lafratta et al., 2020). However, substantial spatial variability in sediment organic carbon content and accumulation rates has been observed between different seagrass meadows (e.g., Lavery et al., 2013; Mazarrasa et al., 2021) as well as within the same, monospecific meadow (e.g., Lei et al., 2023; Ricart et al., 2015), which makes it difficult to easily quantify additionality. Factors such as the species of seagrass (e.g., Serrano et al., 2016), the hydrodynamic intensity (e.g., Lei et al., 2023; Samper-Villarreal et al., 2016), sediment particle sizes (e.g., Serrano et al., 2016; Kennedy et al., 2022), climate (e.g., Mazarrasa et al., 2021), proximity to carbon sources (e.g., Asplund et al., 2021), biogeochemical processes (e.g., Lavery et al., 2013), and landscape configuration (whether or not the meadow has bare patches; Asplund et al., 2021; Ricart et al., 2015, 2017) may drive spatial heterogeneity in carbon stocks and accretion rates.

The ways in which spatial variability in hydrodynamic intensity and vegetation patchiness can influence spatial variability in organic carbon storage may depend on the relative magnitudes of waves and current velocities. Therefore, a more precise understanding of seagrass

reconfiguration under a wide range of realistic flow conditions is necessary not only for more optimized restoration site selection and design, but also for a better understanding of how the restored seagrasses will engineer their environment. Through a combination of laboratory, numerical, and field experiments, this thesis builds on previous work to examine connections between seagrass hydrodynamics and the ecosystem services seagrass meadows provide.

1.1 Thesis outline

The following chapters in this thesis consist of published papers, a manuscript that has been submitted and are in the review process, a manuscript in preparation for submission, and a preliminary report of an ongoing project. Chapter 2 describes a laboratory experiment about the impacts of added currents on wave damping by a seagrass meadow (Schaefer & Nepf, 2022a). I constructed an array of physically-scaled artificial seagrass plants and measured the spatial evolution of wave amplitude across the meadow for pure waves (no currents) and conditions with combined waves and currents. I found that adding currents to smaller waves deflected the plants, reducing vegetation-induced drag relative to pure waves and therefore reducing wave damping. However, the interaction of waves with the meadow generated a time-averaged flow that scales with the wave amplitude (Luhar et al., 2010; Luhar, 2021). Larger waves induced larger mean flows, such that added current did not affect wave energy dissipation as much as for smaller waves. Furthermore, I adapted an analytical model for predicting seagrass meadow wave damping that accounted for the effects of reconfiguration (Lei & Nepf, 2019) for combined wave-current conditions.

Chapter 3 builds on Chapter 2 by numerical modeling the wave energy dissipation generated by seagrass leaves, which allowed for investigation of both a wider range of leaf stiffnesses, which can represent different seagrass or other plant species, and a wider range of combined wave and current conditions (Schaefer & Nepf, 2024). For more flexible leaves, weak current combined with a wave generally reduced wave energy dissipation due to the deflection caused by the current. However, as the current became stronger, with wave velocity held constant, the degree of deflection eventually limited the wave-induced swaying of the leaf, which increased drag relative to the corresponding pure wave condition. This finding defined an important limitation to the model developed in Chapter 2. Specifically, the previous model is valid when the current generated deflection, but did not reduce the wave-following motion of the blades, which corresponded to current to wave velocity ratios above $1/3$. Meanwhile, for stiffer leaves, the addition of any magnitude of current may enhance wave energy dissipation, even though the leaves still reconfigure in response to the flow. Importantly, the current velocity discussed here is that which is within the canopy and directly impacting the blades. Due to the ability of seagrass meadows to attenuate current velocities within the meadow, the range of current-to-wave velocity ratios experienced by the blades is lower than the velocity ratios outside of the meadow.

Chapter 4 presents a laboratory study on the mutual influences of waves and currents on the structure of flow and turbulence within the physically-scaled seagrass meadow used in Chapter 2 (Schaefer & Nepf, 2022b). In combined wave and current conditions, the wave velocity was less efficient than the current velocity in generating leaf-scale turbulence in the meadow because the wave-induced swaying reduced the relative velocity between the leaves and

the wave. A modified hybrid model is proposed to predict leaf-generated turbulence in a flexible canopy to account for the relative contributions of waves and currents.

In Chapters 5, 6, and 7, experiments were conducted in real seagrass meadows in the field. Chapter 5 describes a study on correlations between the spatial patterns in sediment organic carbon content and accumulation rates in a continuous meadow at a wave dominated site (Lei et al., 2023). Less carbon accumulated and was retained in areas of the meadow that experienced higher wave velocities, which was attributed to higher sediment resuspension (assuming the supply of sediment was not a limiting factor). By predicting the effect of the seagrass meadow and changing water depth on wave propagation across the meadow, I successfully predicted the spatial change in carbon accumulation rates.

Chapter 6 also explored the correlation between carbon content and accretion rate with hydrodynamic conditions, but this time in a continuous meadow located in a current-dominated lagoonal environment. Sediment organic carbon content decreased with distance from the inlet channel to the lagoon and decreased with peak tidal velocities. Meanwhile, outside of the edge of the meadow, sediment carbon accumulation rates also decreased with distance from the inlet channel and decreased with peak tidal velocities. To explain these trends, first consider that water entering the lagoon during the flood phase of a tidal cycle carries fresh carbon-laden sediment, but as the water travels across the meadow, much of the sediment settles to the bed, such that the farther interior of the meadow receives a lower supply of sediment compared to the edge of the meadow. On the other hand, higher velocities at the edge of the meadow reduce the effective accumulation of the sediment. In other words, even though the lower velocities farther into the meadow facilitate the deposition of sediment and carbon, a much lower volume of sediment and carbon is actually delivered to that region.

Finally, Chapter 7 describes a study in a patchy coastal seagrass meadow at a current-dominated site. I expected to observe higher sediment organic carbon stocks in vegetated patches compared to surrounding bare areas, but measured similar carbon stocks across the meadow except in one particular patch. Through analysis of historical aerial and satellite images, I found that the highest sediment organic carbon content was associated with the area that had the highest recent persistence of vegetation. In general, due to the dynamic shifting of patches over time, carbon that accumulates due to the presence of vegetation does not persist.

Complementing the previous three chapters on sediment organic carbon storage in seagrass meadows, Chapter 8 describes preliminary results for an ongoing field study in a seagrass meadow that aims to compare different methods for estimating net ecosystem carbon uptake, including aquatic eddy covariance, seagrass growth rates, and sediment core carbon accumulation rates.

Pulling it all together, Chapter 9 summarizes the main findings described in the thesis and gives possible directions for future work.

1.2 References

Anderson, S. M., & Charters, A. C. (1982). A fluid dynamics study of seawater flow through *Gelidium nudifrons*. *Limnology and Oceanography*, 27(3), 399–412.
<https://doi.org/10.4319/lo.1982.27.3.0399>

Asplund, M. E., Dahl, M., Ismail, R. O., Arias-Ortiz, A., Deyanova, D., Franco, J. N., Hammar, L., Hoamby, A. I., Linderholm, H. W., Lyimo, L. D., Perry, D., Rasmusson, L. M., Ridgway, S. N., Salgado Gispert, G., D'Agata, S., Glass, L., Mahafina, J. A., Ramahery, V., Masque, P., ... Gullström, M. (2021). Dynamics and fate of blue carbon in a

- mangrove–seagrass seascape: influence of landscape configuration and land-use change. *Landscape Ecology*, 36(5), 1489–1509. <https://doi.org/10.1007/s10980-021-01216-8>
- Bos, A. R., Bouma, T. J., de Kort, G. L. J., & van Katwijk, M. M. (2007). Ecosystem engineering by annual intertidal seagrass beds: Sediment accretion and modification. *Estuarine, Coastal and Shelf Science*, 74(1–2), 344–348. <https://doi.org/10.1016/j.ecss.2007.04.006>
- Bradley, K., & Houser, C. (2009). Relative velocity of seagrass blades: Implications for wave attenuation in low-energy environments. *Journal of Geophysical Research: Earth Surface*, 114(1). <https://doi.org/10.1029/2007JF000951>
- Brunet, Y., Finnigan, J. J., & Raupach, M. R. (1994). A wind tunnel study of air flow in waving wheat: Single-point velocity statistics. *Boundary-Layer Meteorology*, 70(1–2), 95–132. <https://doi.org/10.1007/BF00712525>
- Costanza, R., de Groot, R., Sutton, P., van der Ploeg, S., Anderson, S. J., Kubiszewski, I., Farber, S., & Turner, R. K. (2014). Changes in the global value of ecosystem services. *Global Environmental Change*, 26(1), 152–158. <https://doi.org/10.1016/j.gloenvcha.2014.04.002>
- Dahl, M., Infantes, E., Clevesjö, R., Linderholm, H. W., Björk, M., & Gullström, M. (2018). Increased current flow enhances the risk of organic carbon loss from *Zostera marina* sediments: Insights from a flume experiment. *Limnology and Oceanography*, 63(6), 2793–2805. <https://doi.org/10.1002/lno.11009>
- Dalrymple, R. A., Kirby, J. T., & Hwang, P. A. (1984). Wave diffraction due to areas of energy dissipation. *Journal of Waterway, Port, Coastal, and Ocean Engineering*, 110(1), 67–79. [https://doi.org/10.1061/\(ASCE\)0733-950X\(1984\)110:1\(67\)](https://doi.org/10.1061/(ASCE)0733-950X(1984)110:1(67))
- Fonseca, M. S., & Cahalan, J. A. (1992). A preliminary evaluation of wave attenuation by four species of seagrass. *Estuarine, Coastal and Shelf Science*, 35(6), 565–576. [https://doi.org/10.1016/S0272-7714\(05\)80039-3](https://doi.org/10.1016/S0272-7714(05)80039-3)
- Fourqurean, J. W., Duarte, C. M., Kennedy, H., Marbà, N., Holmer, M., Mateo, M. A., Apostolaki, E. T., Kendrick, G. A., Krause-Jensen, D., & Serrano, O. (2012). Seagrass ecosystems as a globally significant carbon stock. *Nature Geoscience*, 5, 505–509. <https://doi.org/10.1038/ngeo1477>
- Gosselin, F. P. (2019). Mechanics of a plant in fluid flow. *Journal of Experimental Botany*, 70(14), 3533–3548. <https://doi.org/10.1093/jxb/erz288>
- Howard, J., Sutton-Grier, A. E., Smart, L. S., Lopes, C. C., Hamilton, J., Kleypas, J., Simpson, S., McGowan, J., Pessarrodona, A., Alleway, H. K., & Landis, E. (2023). Blue carbon pathways for climate mitigation: Known, emerging and unlikely. *Marine Policy*, 156(November 2022), 105788. <https://doi.org/10.1016/j.marpol.2023.105788>

- Infantes, E., Orfila, A., Simarro, G., Terrados, J., Luhar, M., & Nepf, H. (2012). Effect of a seagrass (*Posidonia oceanica*) meadow on wave propagation. *Marine Ecology Progress Series*, 456, 63–72. <https://doi.org/10.3354/meps09754>
- Irlandi, E. A., & Peterson, C. H. (1991). Modification of animal habitat by large plants: mechanisms by which seagrasses influence clam growth. *Oecologia*, 87(3), 307–318. <https://doi.org/10.1007/BF00634584>
- Jones, C. G., Lawton, J. H., Shachak, M., & Organisms, M. (1994). Organisms as ecosystem engineers. *Oikos*, 69(3), 373–386. <https://doi.org/10.2307/3545850>
- Kennedy, H., Pagès, J. F., Lagomasino, D., Arias-Ortiz, A., Colarusso, P., Fourqurean, J. W., Githaiga, M. N., Howard, J. L., Krause-Jensen, D., Kuwae, T., Lavery, P. S., Macreadie, P. I., Marbà, N., Masqué, P., Mazarrasa, I., Miyajima, T., Serrano, O., & Duarte, C. M. (2022). Species traits and geomorphic setting as drivers of global soil carbon stocks in seagrass meadows. *Global Biogeochemical Cycles*, 36, 1–18. <https://doi.org/10.1029/2022gb007481>
- Lafratta, A., Serrano, O., Masqué, P., Mateo, M. A., Fernandes, M., Gaylard, S., & Lavery, P. S. (2020). Challenges to select suitable habitats and demonstrate ‘additionality’ in Blue Carbon projects: A seagrass case study. *Ocean and Coastal Management*, 197. <https://doi.org/10.1016/j.ocecoaman.2020.105295>
- Lavery, P. S., Mateo, M. A., Serrano, O., & Rozaimi, M. (2013). Variability in the carbon storage of seagrass habitats and its implications for global estimates of blue carbon ecosystem service. *PLoS ONE*, 8(9). <https://doi.org/10.1371/journal.pone.0073748>
- Lei, J., & Nepf, H. M. (2019). Wave damping by flexible vegetation: Connecting individual blade dynamics to the meadow scale. *Coastal Engineering*, 147(October 2018), 138–148. <https://doi.org/10.1016/j.coastaleng.2019.01.008>
- Lei, J., Schaefer, R., Colarusso, P., Novak, A., Simpson, J. C., Masqué, P., & Nepf, H. (2023). Spatial heterogeneity in sediment and carbon accretion rates within a seagrass meadow correlated with the hydrodynamic intensity. *Science of the Total Environment*, 854(April 2022). <https://doi.org/10.1016/j.scitotenv.2022.158685>
- Luhar, M. (2021). Comment on “The wave-driven current in coastal canopies” by M. Abdolahpour et al. *Journal of Geophysical Research: Oceans*, 126(8), 1–6. <https://doi.org/10.1029/2019jc015644>
- Luhar, M., Coutu, S., Infantes, E., Fox, S., & Nepf, H. (2010). Wave-induced velocities inside a model seagrass bed. *Journal of Geophysical Research: Oceans*, 115(12), 1–15. <https://doi.org/10.1029/2010JC006345>
- Mateo, M. A., Romero, J., Pérez, M., Littler, M. M., & Littler, D. S. (1997). Dynamics of millenary organic deposits resulting from the growth of the Mediterranean seagrass

- Posidonia oceanica*. *Estuarine, Coastal and Shelf Science*, 44(1), 103–110.
<https://doi.org/10.1006/ecss.1996.0116>
- Mazarrasa, I., Lavery, P., Duarte, C. M., Lafratta, A., Lovelock, C. E., Macreadie, P. I., Samper-Villarreal, J., Salinas, C., Sanders, C. J., Trevathan-Tackett, S., Young, M., Steven, A., & Serrano, O. (2021). Factors determining seagrass blue carbon across bioregions and geomorphologies. *Global Biogeochemical Cycles*, 35(6), 1–17.
<https://doi.org/10.1029/2021GB006935>
- Miyajima, T., Koike, I., Yamano, H., & Iizumi, H. (1998). Accumulation and transport of seagrass-derived organic matter in reef flat sediment of Green Island, Great Barrier Reef. *Marine Ecology Progress Series*, 175, 251–259. <https://doi.org/10.3354/meps175251>
- Orth, R. J., Harwell, M. C., & Fishman, J. R. (1999). A rapid and simple method for transplanting eelgrass using single, unanchored shoots. *Aquatic Botany*, 64(1), 77–85.
[https://doi.org/10.1016/S0304-3770\(99\)00007-8](https://doi.org/10.1016/S0304-3770(99)00007-8)
- Orth, R. J., Luckenbach, M., & Moore, K. A. (1994). Seed dispersal in a marine macrophyte: implications for colonization and restoration. *Ecology*, 75(7), 1927–1939.
<https://doi.org/10.2307/1941597>
- Pollard, D. A. (1984). A review of ecological studies on seagrass-fish communities, with particular reference to recent studies in Australia. *Aquatic Botany*, 18(1–2), 3–42.
[https://doi.org/10.1016/0304-3770\(84\)90079-2](https://doi.org/10.1016/0304-3770(84)90079-2)
- Raupach, M. R., Finnigan, J. J., & Brunet, Y. (1996). Coherent eddies and turbulence in vegetation canopies: the mixing-layer analogy. *Boundary-Layer Meteorology*, 78(3–4), 351–382. <https://doi.org/10.1007/BF00120941>
- Ricart, A. M., Pérez, M., & Romero, J. (2017). Landscape configuration modulates carbon storage in seagrass sediments. *Estuarine, Coastal and Shelf Science*, 185, 69–76.
<https://doi.org/10.1016/j.ecss.2016.12.011>
- Ricart, A. M., York, P. H., Rasheed, M. A., Pérez, M., Romero, J., Bryant, C. V., & Macreadie, P. I. (2015). Variability of sedimentary organic carbon in patchy seagrass landscapes. *Marine Pollution Bulletin*, 100(1), 476–482.
<https://doi.org/10.1016/j.marpolbul.2015.09.032>
- Samper-Villarreal, J., Lovelock, C. E., Saunders, M. I., Roelfsema, C., & Mumby, P. J. (2016). Organic carbon in seagrass sediments is influenced by seagrass canopy complexity, turbidity, wave height, and water depth. *Limnology and Oceanography*, 61(3), 938–952.
<https://doi.org/10.1002/lno.10262>
- Schaefer, R. B., & Nepf, H. M. (2022a). Wave damping by seagrass meadows in combined wave-current conditions. *Limnology and Oceanography*, 67(7), 1554–1565.
<https://doi.org/10.1002/lno.12102>

- Schaefer, R. B., & Nepf, H. M. (2022b). Flow structure in an artificial seagrass meadow in combined wave-current conditions. *Frontiers in Marine Science*, 9, 1–12. <https://doi.org/10.3389/fmars.2022.836901>
- Schaefer, R., & Nepf, H. (2024). Movement of and drag force on slender flat plates in an array exposed to combinations of unidirectional and oscillatory flow. *Journal of Fluids and Structures*, 124, 104044. <https://doi.org/10.1016/j.jfluidstructs.2023.104044>
- Serrano, O., Lavery, P. S., Duarte, C. M., Kendrick, G. A., Calafat, A., York, P. H., Steven, A., & Macreadie, P. I. (2016). Can mud (silt and clay) concentration be used to predict soil organic carbon content within seagrass ecosystems? *Biogeosciences*, 13(17), 4915–4926. <https://doi.org/10.5194/bg-13-4915-2016>
- Short, F. T., & Short, C. A. (1984). The seagrass filter: Purification of estuarine and coastal waters. In V. S. Kennedy (Ed.), *The Estuary as a Filter* (pp. 395–413). Academic Press. <https://doi.org/10.1016/B978-0-12-405070-9.50024-4>
- Szmant, A. M., & Forrester, A. (1996). Water column and sediment nitrogen and phosphorus distribution patterns in the Florida Keys, USA. *Coral Reefs*, 15(1), 21–41. <https://doi.org/10.1007/s003380050026>
- Tan, Y. M., Dalby, O., Kendrick, G. A., Statton, J., Sinclair, E. A., Fraser, M. W., Macreadie, P. I., Gillies, C. L., Coleman, R. A., Waycott, M., van Dijk, K. J., Vergés, A., Ross, J. D., Campbell, M. L., Matheson, F. E., Jackson, E. L., Irving, A. D., Govers, L. L., Connolly, R. M., ... Sherman, C. D. H. (2020). Seagrass restoration is possible: Insights and lessons from Australia and New Zealand. *Frontiers in Marine Science*, 7(August). <https://doi.org/10.3389/fmars.2020.00617>
- Unsworth, R. K. F., McKenzie, L. J., Collier, C. J., Cullen-Unsworth, L. C., Duarte, C. M., Eklöf, J. S., Jarvis, J. C., Jones, B. L., & Nordlund, L. M. (2019). Global challenges for seagrass conservation. *Ambio*, 48(8), 801–815. <https://doi.org/10.1007/s13280-018-1115-y>
- van Katwijk, M. M., Thorhaug, A., Marbà, N., Orth, R. J., Duarte, C. M., Kendrick, G. A., Althuizen, I. H. J., Balestri, E., Bernard, G., Cambridge, M. L., Cunha, A., Durance, C., Giesen, W., Han, Q., Hosokawa, S., Kiswara, W., Komatsu, T., Lardicci, C., Lee, K. S., ... Verduin, J. J. (2016). Global analysis of seagrass restoration: The importance of large-scale planting. *Journal of Applied Ecology*, 53(2), 567–578. <https://doi.org/10.1111/1365-2664.12562>
- van Keulen, M., & Borowitzka, M. A. (2002). Comparison of water velocity profiles through morphologically dissimilar seagrasses measured with a simple and inexpensive current meter. *Bulletin of Marine Science*, 71(3), 1257–1267.
- Ward, L. G., Kemp, W. M., & Boynton, W. R. (1984). The influence of waves and seagrass communities on suspended particulates in an estuarine embayment. *Marine Geology*, 59(1–4), 85–103. [https://doi.org/10.1016/0025-3227\(84\)90089-6](https://doi.org/10.1016/0025-3227(84)90089-6)

Waycott, M., Duarte, C. M., Carruthers, T. J. B., Orth, R. J., Dennison, W. C., Olyarnik, S., Calladine, A., Fourqurean, J. W., Heck, K. L., Hughes, A. R., Kendrick, G. A., Kenworthy, W. J., Short, F. T., & Williams, S. L. (2009). Accelerating loss of seagrasses across the globe threatens coastal ecosystems. *Proceedings of the National Academy of Sciences of the United States of America*, 106(30), 12377–12381.
<https://doi.org/10.1073/pnas.0905620106>

Chapter 2

Wave damping by seagrass meadows in combined wave-current conditions¹

Abstract:

Laboratory experiments using an artificial seagrass meadow modeled after *Zostera marina* measured the impact of following currents on meadow-induced wave decay as a function of the imposed current velocity U_c , wave velocity U_w , and wave Cauchy number Ca_w , which is the ratio of hydrodynamic drag force to restoring force due to blade stiffness. For small wave-induced reconfiguration of individual seagrass blades ($Ca_w < 2000$) and $U_c/U_w > 0.5$, the addition of current enhanced reconfiguration, which decreased wave decay relative to pure wave conditions. In contrast, when the wave-induced reconfiguration was large ($Ca_w > 2000$), the addition of following current did not significantly enhance blade reconfiguration or impact wave damping. Due to canopy drag, the current velocity within the submerged meadow, U_1 , was

¹ This chapter was published as Schaefer and Nepf, 2022b.

significantly smaller than the depth-averaged current U_c , and a better prediction of wave decay was achieved using U_1 as the relevant velocity. The measured wave decay validated predictions based on a modified Cauchy number, defined for combined waves and current and using the in-canopy velocity U_1 . Practical assumptions to facilitate the prediction of wave decay in the field are discussed and validated.

2.1 Introduction

Seagrasses, marine plants found along coastlines throughout the world, provide habitat and food for economically important fish and shellfish (e.g., Pollard 1984), cycle nutrients (e.g., Pedersen and Borum 1992) and reduce erosion (e.g., Ginsburg and Lowenstam 1958). In addition, seagrass meadows on average sequester twice as much organic carbon per hectare as terrestrial soils (Fourqurean et al. 2012). Each of these ecosystem services is enhanced by the attenuation of wave energy by the seagrass meadow (e.g., Ward et al. 1984), which creates low energy niches that promote deposition and retention of fine material, reduce wave-driven resuspension and erosion, and provide quiescent nursery habitat. For example, wave height was observed to decrease by as much as 40% over a 40 m distance across a *Zostera marina* meadow (Boese et al. 2005). Similarly, Infantes et al. (2012) measured a 50% reduction in wave height across 1000 m of the Mediterranean seagrass *Posidonia oceanica*.

Unfortunately, seagrass populations are in decline due primarily to anthropogenic pressures on their habitats, including increasing water temperature, increasing frequency of intense storms, coastal hardening, erosion due to land use changes, eutrophication from excess

nutrient inputs, as well as dredging and boating activities (Orth et al. 2006; Waycott et al. 2009). Seagrass restoration projects aim to repopulate nearshore environments with resilient meadows. The prediction of wave decay as a function of meadow characteristics could guide restoration design and motivate protective policy by providing more accurate evaluation of the economic benefit of meadows to coastal protection and carbon sequestration.

Previous studies have studied how meadows of rigid model vegetation reduce wave energy through work done by hydrodynamic drag, describing the fractional loss of wave energy with a wave decay coefficient K_D (e.g., Dalrymple et al. 1984). The presence of a current modifies wave attenuation. Within arrays of rigid cylinders, wave decay in the presence of current is a function of the velocity ratio U_c/U_w , in which U_c and U_w are the current and wave velocities, respectively (Hu et al. 2014; Yin et al. 2020; Zhao et al. 2021). Specifically, these studies observed that wave decay in a rigid meadow decreased when a weak current was added (small U_c/U_w), but increased when a stronger current was added. These shifts were attributed to changes in wake structure under weak currents that reduce drag and thus wave decay, and the enhancement of maximum total velocity (wave plus current), which increases drag, resulting in greater wave decay.

For meadows of flexible vegetation exposed to pure waves, the wave decay coefficient K_D has been observed to decrease with increasing wave amplitude, and this is attributed to the bending of the plants in response to the wave (known as reconfiguration), which increases with wave amplitude (e.g. Luhar et al. 2017). A few studies have considered wave damping by flexible vegetation in the presence of current. Using arrays of flexible poly ribbon, representing the seagrass *Zostera noltii*, Paul et al. (2012) observed that a following current decreased wave attenuation relative to pure wave conditions, which they attributed to current-induced pronation

of the model plants. Losada et al. (2016) grew circular patches of the semi-rigid *Spartina anglica* and flexible *Puccinellia maritima* in a laboratory basin and subjected them to waves with following and opposing currents. For the majority of cases, a following current decreased wave attenuation relative to pure wave conditions. These observations in flexible meadows suggest that reconfiguration was the dominant process impacting drag in the meadow, resulting in a decrease in drag and thus a decrease in wave attenuation. This occurred despite the fact that the addition of current enhanced the maximum total velocity, which for rigid meadows lead to larger wave decay coefficients (e.g., Hu et al. 2014). A detailed discussion of the competing roles of elevated drag associated with elevated total velocity and diminished drag associated with reconfiguration can be found in Zhang and Nepf (2021).

Because previous observations of seagrass mimics suggest that reconfiguration dominates the impact of current on wave decay (e.g., Paul, 2012), the present study focused on the role of reconfiguration to develop a prediction for wave decay by a meadow of flexible plants in the presence of a following current. The impact of blade reconfiguration on the drag was represented by scaling laws, and the modified blade drag was used to predict wave decay over the meadow. The study revealed the importance of using the in-canopy velocity in the prediction of wave energy decay, which can differ significantly from the depth-averaged velocity used in previous studies.

2.2 Theoretical Background

2.2.1 Reconfiguration of and drag on flexible blades

Flexible seagrass blades reconfigure in both current and waves. In unidirectional current, flexible blades adopt a mean streamwise deflection which reduces the frontal area and presents a more streamlined body shape, both of which reduce drag (Alben et al 2002, Luhar and Nepf 2011). Under short waves (defined here with the wave orbital excursion equal to or smaller than blade length), flexible plants can move continuously with the wave fluid motion, which reduces the relative velocity between the plant and the water, which reduces the drag (Bradley and Houser 2009; Döbken 2015; Luhar et al. 2017). Under combined wave and current conditions, the current-induced deflection may limit wave-induced motion of the blade, which could limit the drag reduction associated with reconfiguration (e.g., Paul et al. 2012).

The influence of plant reconfiguration on plant drag has often been modeled using an empirically fitted drag coefficient that decreases with increasing plant flexibility (e.g. Mendez and Losada 2004; Houser et al. 2015). Alternatively, Luhar and Nepf (2011, 2016) described the impact of reconfiguration on drag using an effective blade length l_e , which is the length of rigid blade that generates the same drag force as a flexible blade of length l_b . Several studies have shown that l_e/l_b can be predicted from three dimensionless parameters (e.g. Luhar and Nepf 2011, 2016; Gosselin 2019). The Cauchy number Ca represents the ratio of hydrodynamic drag to restoring force due to stiffness, which can be defined for current (Eqn. (2.1), subscript ‘c’) and wave (Eqn. (2.2), subscript ‘w’) velocities. The buoyancy parameter B (Eqn. (2.3)) describes the ratio of restoring forces due to buoyancy and stiffness. The blade length ratio L (Eqn. (2.4)) is the

ratio of blade length l_b to wave excursion $A_w = U_w/\sigma$, in which $\sigma = 2\pi/T$ is the wave angular frequency, with T the wave period. For blades with rectangular cross-sections,

$$Ca_c = \frac{1}{2} \frac{\rho C_{D,c} w_b U_c^2 l_b^3}{EI} \quad (2.1)$$

$$Ca_w = \frac{1}{2} \frac{\rho C_{D,w} w_b U_w^2 l_b^3}{EI} \quad (2.2)$$

$$B = \frac{\Delta \rho g w_b t_b l_b^3}{EI} \quad (2.3)$$

$$L = \frac{2\pi l_b}{U_w T} \quad (2.4)$$

C_D is the drag coefficient, w_b is the blade width, t_b is the blade thickness, g is the acceleration due to gravity, ρ is the density of water, $\Delta\rho$ is the difference in density between the fluid and plant material, E is Young's modulus of elasticity, and $I = w_b t_b^3/12$ is the bending moment of inertia for rectangular blades. In the Cauchy number the wave velocity amplitude U_w is defined at the top of the meadow, and U_c is the time- and depth-averaged current velocity.

If the current Cauchy number Ca_c is less than 1, or the product of the wave Cauchy number and the blade length ratio $Ca_w L$ is less than 1, the blade motion is negligible, and the blade will behave as a rigid blade ($l_e = l_b$). If Ca_c and $Ca_w L$ are greater than 1, the blade will reconfigure, reducing the drag ($l_e < l_b$). For $Ca_w L$ and Ca_w close to one, a flexible blade may experience higher forces compared to a rigid blade of the same length ($l_e > l_b$), which has been attributed to phase shifts between the blade and fluid motion and to structural resonance (see discussions in (Luhar and Nepf 2016; Leclercq and De Langre 2018; Lei and Nepf 2019a).

In some conditions buoyancy can also impact reconfiguration. Henderson (2019) considered a dimensionless buoyancy $\beta = \frac{1}{2} \Delta \rho g w_b T / (\rho C_D l_b U_w)$ and dimensionless stiffness $S \sim (CaL)^{-1}$, and showed that when $\beta \ll S^{1/2}$ (or equivalently $B^2 \ll CaL$), the effect of buoyancy on blade reconfiguration for highly flexible vegetation (for which $S \ll 1$ and $\beta \ll 1$) can be neglected. For the experimental conditions in this study, $S \ll 1$, $\beta \ll 1$, and $B^2 \ll CaL$, such that the effects of buoyancy on blade reconfiguration will be neglected going forward.

Using scale analysis validated by measured drag forces, the following predictions of effective blade length have been developed for individual flexible blades. In pure current conditions (e.g. Alben et al. 2002; Luhar and Nepf 2011; Gosselin 2019),

$$\frac{l_e}{l_b} = 0.9 (Ca_c)^{-1/3} \quad U_c/U_w > 2, \quad (2.5)$$

which is also valid for combined wave-current conditions when $U_c/U_w > 2$ (Lei and Nepf 2019b). Eqn. (2.5) also applies in pure long wave conditions, defined by $L \ll 1$, for which the blade length is much shorter than the wave excursion, such that the blade reaches a fully pronated posture early in the wave half-cycle and is nearly stationary for most of the wave cycle (Luhar et al. 2017; Leclercq and De Langre 2018; Lei and Nepf 2019b). In this case, Ca_w replaces Ca_c in Eqn. (2.5) and the prefactor is 1.1 (see Eqn. (10) in Lei and Nepf 2019a).

In pure waves with $L \geq 1$, the blade length is greater than the wave excursion, which allows the tip of the blade to move continuously with the wave fluid motion. In this regime, the balance between drag and blade stiffness yields (Luhar and Nepf 2016)

$$\frac{l_e}{l_b} = 1.1 (Ca_w L)^{-1/4} \quad U_c/U_w < 0.25, \quad (2.6)$$

which is also valid for waves in the presence of weak current, $U_c/U_w < 0.25$ (Eqn. (9) in Lei and Nepf 2019a). For conditions in which both the waves and current contribute significantly to drag ($0.25 < U_c/U_w < 2$), Lei and Nepf (2019a) defined a wave-current Cauchy number, using the time-mean force to define an equivalent time-mean velocity, $\left(U_c^2 + \frac{1}{2}U_w^2\right)^{1/2}$:

$$Ca_{wc} = \frac{1}{2} \frac{\rho C_{D,wc} W_b l_b^3}{EI} \left(U_c^2 + \frac{1}{2} U_w^2 \right) \quad (2.7)$$

The subscript ‘wc’ denotes combined wave-current conditions. Using Eqn. (2.7), the effective blade length is described by Eqn. (13) in Lei and Nepf (2019a):

$$\frac{l_e}{l_b} = 0.9 (Ca_{wc})^{-1/3} \quad (2.8)$$

Using force measurements for individual blades exposed to combined waves and current spanning pure waves to pure current, Lei and Nepf (2019a) validated Eqns. (2.5), (2.6), and (2.8) (see Fig. 8 in Lei and Nepf 2019a). Eqn. (2.8) smoothly captured l_e/l_b for the intermediate regime $0.25 < U_c/U_w < 2$, but also did reasonably in the wave- and current-dominated regimes.

Realistically, seagrass shoots consist of multiple flexible blades of length l_b , which emerge from the bed within a rigid sheath of length l_r . For pure wave conditions, Lei and Nepf (2019b) defined the effective meadow height as the sum of effective blade length (Eqn. (2.6)) and rigid sheath length l_r :

$$l_{e,m,w} = \underbrace{1.1 (Ca_w L)_b^{-1/4} l_b}_{\text{effective blade length}} + \underbrace{l_r}_{\text{rigid sheath length}} \quad (2.9)$$

For wave-current conditions, we propose the effective meadow height (using Eqn. (2.8))

$$l_{e,m,wc} = 0.9(Ca_{wc,b})_b^{-\frac{1}{3}}l_b + l_r \quad (2.10)$$

effective blade length rigid sheath length

For simplicity, Eqn. (2.10) neglects that shoots consist of multiple blades emerging from a sheath, and instead assumes the meadow consists of individual blades. The effective meadow height captures the reduction in meadow drag associated with reconfiguration, which will be used in the next section to predict a wave decay coefficient.

2.2.2 Wave dissipation

Assuming linear wave theory and that wave energy dissipation is due only to the vegetation, the steady wave energy balance is

$$-E_v = \frac{\partial}{\partial x} \left(\frac{1}{2} \rho g a_w^2 C_g \right), \quad (2.11)$$

in which E_v is the rate of wave energy dissipation due to the vegetation, a_w is the wave amplitude, C_g is the group velocity, and x is the distance in the direction of wave propagation, with $x = 0$ at the start of the meadow. The group velocity is

$$C_g = \frac{1}{2} \left(1 + \frac{2kD}{\sinh(2kD)} \right) \left(\frac{g}{k} \tanh(kD) \right)^{\frac{1}{2}} \quad (2.12)$$

in which k is the wave number and D is the mean water depth.

E_v can be described by the rate of work done by the vegetation drag. Based on linear wave theory, Dalrymple et al. (1984) derived the rate of wave energy dissipation due to a meadow of rigid elements with height l under pure wave conditions

$$E_v = \frac{16}{3\pi} \rho C_{D,w} a_w^3 \alpha^3 \left(\frac{kg}{2\sigma} \right)^3 a_v \left(\frac{\sinh^3 kl + 3 \sinh kl}{3k \cosh^3 kD} \right), \quad (2.13)$$

$a_v = n_b w_b$ is the frontal area per meadow volume, with n_b the number of rigid blades per bed area, each of width w_b and length l . Note that Eqn. (2.13) has been modified from the original version in Dalrymple et al. (1984) by including the reduction of in-canopy wave velocity due to canopy drag. Specifically, the wave orbital velocity within the meadow is reduced, relative to linear wave theory, by a factor α , which depends on the wave period and meadow density (see Eqn. (2.18) in Lowe et al. 2005).

Eqns. (2.11) and (2.13) together describe the change in wave amplitude with distance over the meadow

$$\frac{a_w(x)}{a_{w,0}} = \frac{1}{1 + K_D a_{w,0} x}, \quad (2.14)$$

in which $a_{w,0}$ is the wave amplitude at the leading edge of the meadow, and K_D is called the wave decay coefficient,

$$K_D = \frac{2}{9\pi} C_{D,w} \alpha^3 a_w k \frac{9 \sinh(kl) + \sinh(3kl)}{\sinh(kD) (\sinh(2kD) + 2kD)} \quad (2.15)$$

Lei and Nepf (2019b) modified Eqn. (2.15) for flexible seagrass meadows by replacing the rigid meadow height (l) with the effective meadow height, $l_{e,m,w}$ (Eqn. (2.9)):

$$K_D = \frac{2}{9\pi} C_{D,w} \alpha^3 a_w k \frac{9 \sinh(kl_{e,m,w}) + \sinh(3kl_{e,m,w})}{(\sinh(kD))(\sinh(2kD) + 2kD)} \quad (2.16)$$

As an extension of Eqn. (2.15), Eqn. (2.16) assumes the blades are not bundled in a sheath, but exist as individual structures, such that $a_v = n_b w_b$. This is reasonable when the sheath occupies a small fraction of the deflected meadow height, which here was less than 15%. Eqns. (2.9) and

(2.16) were validated in pure wave conditions with measured values of K_D for meadows of flexible mimics in the lab as well as for a meadow of *Posidonia oceanica* in the field (Lei and Nepf 2019a). The focus of this paper was to extend the prediction of K_D to conditions with current.

It is important to note that Eqn. (2.15) was derived for pure wave conditions, and it does not reflect the role of current in enhancing total velocity and thus drag. Thus, it cannot predict the increase in wave decay coefficient observed for rigid canopies. By adopting Eqn. (2.15) as the basis for predicting the wave decay coefficient for a flexible meadow, we are assuming that the impact of reconfiguration has the dominant impact on meadow drag. This is true when the in-canopy- and time-averaged velocity U_1 is less than the wave velocity, $U_1 < U_w$, such that the additional current can impact reconfiguration, but not significantly add to the total velocity (e.g. Losada et al. 2016).

Further, when current is present the group velocity is modified by the Doppler shift. Specifically, wave energy propagates at the sum of the current velocity and group velocity (Longuet-Higgins and Stewart 1960). This in turn modifies the decay coefficient, as described in Losada et al. (2016) and included in Section 2.8.3 for convenience. However, the modification is small when $C_g \gg U_c$, which was true for all wave-current cases considered in the present study, so that Eqn. (2.16) could be used without correction. For cases where U_c is comparable to C_g , Eqn. (2.13) and therefore Eqn. (2.16) should be modified (see Losada et al. 2016).

In combined wave-current conditions, Losada et al. (2016) accounted for plant reconfiguration by replacing l in Eqn. (2.15) with the observed deflected meadow height h_d . Here, we propose replacing l with the wave-current effective meadow height defined from the

scale relations validated for individual blades (Eqn. (2.10)). Because the meadow drag reduces current within the meadow, individual blades are exposed to an in-canopy time-averaged velocity $U_1 < U_c$, and we propose that U_1 may be more relevant than U_c in calculating the effective meadow height.

The vertically and time-averaged velocity within a submerged meadow, U_1 , can be predicted using a two-layer model consisting of a canopy layer and overflow layer. For pure current, the fully-developed, in-canopy velocity, $U_{1,c}$, was described for a rigid meadow by Chen et al. (2013) and extended to a flexible meadow by Lei and Nepf (2021) as

$$U_{1,c} = \frac{U_c}{1 - \frac{h_d}{D} \phi + \sqrt{\frac{C_{D,c} a_v l_e}{2C(1-\phi)} \left(\frac{D-h_d}{D}\right)^3}} \quad (2.17)$$

in which $\phi (= a_v l_b t_b / h_d)$ is the canopy solid volume fraction. The turbulent stress at the top of the canopy is characterized by the coefficient $C = K_c (\delta_e / D)^{1/3}$, in which δ_e describes the distance over which turbulent momentum flux impacts the canopy velocity. When the canopy-scale vortices are not constrained by the water depth ($D/h_d \geq 2$), $\delta_e = 0.23 / (C_{D,c} a_v)$ (Nepf et al. 2007), otherwise for $D/h < 2$, $\delta_e = 0.23(D/h_d - 1) / (C_{D,c} a_v)$ (Chen et al. 2013). The empirical factor $K_c = 0.07 \pm 0.02$ (Chen et al. 2013).

In pure wave conditions, a wave-induced mean current can be generated in a submerged meadow by wave stress, with a maximum \bar{U}_{max} at $z \approx h_d$ (Luhar et al. 2010; Abdolahpour et al. 2017; Luhar 2021). From Luhar (2021), \bar{U}_{max} can be predicted as

$$\bar{U}_{max} = 0.9 U_w \sqrt{\frac{a_v k l_{e,m,w}}{\sigma} U_w} \quad (2.18)$$

The wave stress develops over a distance on the order of the wave excursion (1 to 7 cm in present study), beyond which the current induced by the wave stress (Eqn. (2.18)) requires an additional development length $L_c \sim 2 / (C_{D,c} a_v)$ (Luhar et al. 2010). For the conditions tested in the present study, wave-induced currents were expected to develop within 6 to 12 cm of the meadow leading edge. The present study considered if the time-averaged velocity within a meadow under combined waves and current can be predicted as the sum of Eqns. (2.17) and (2.18).

2.3 Materials and Methods

Experiments were conducted in a 24 m long, 38 cm wide, and 60 cm deep flume (Fig. 2.1). Waves were generated by a piston-type paddle wavemaker controlled by a Syscomp WGM-101 signal generator (see Appendix A in Luhar 2012). The wave period was $T = 2$ s. A wave damping ramp with a 1:5 slope and covered with coconut fiber mats was located at the downstream end of the flume. The front edge of the ramp was lifted to allow the recirculation of current. Based on the analysis described in Goda and Suzuki (1977), the ramp reduced the wave reflection to below 11%. Currents were recirculated through the flume via an inlet pipe 0.8 m downstream of the wavemaker and an outlet drain downstream of the ramp.

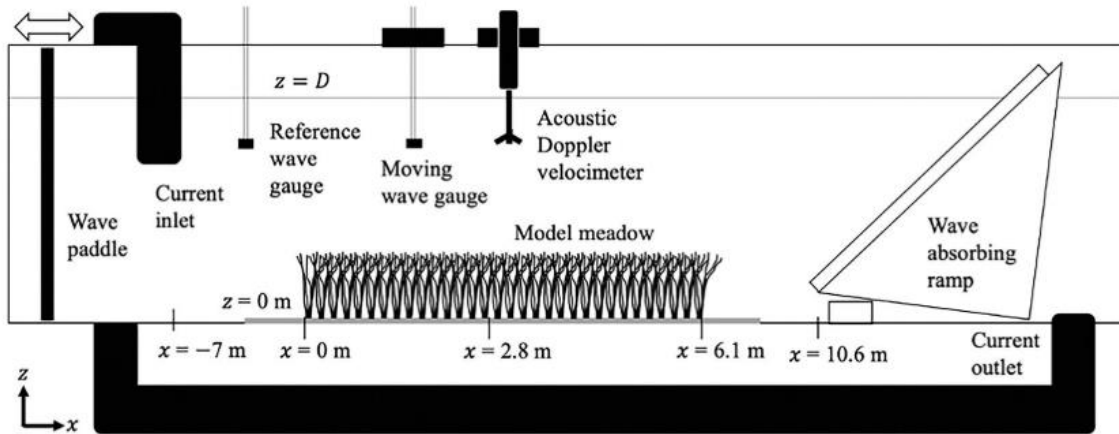


Figure 2.1: Sketch of laboratory setup in wave flume, not drawn to scale. x is positive in the direction of wave propagation, and $x = 0$ at the leading edge of the meadow. z is zero at the bed and positive upward.

2.3.1 Seagrass shoot model and meadow construction

A seagrass model was constructed to be geometrically and dynamically similar to *Zostera marina* based on field observations of morphology and wave conditions and corresponding Cauchy numbers (see Section 2.8.1). Six blades, each 13 cm long, 0.3 cm wide, and 0.1 mm thick, were laser cut from sheets of low-density polyethylene (LDPE) and wrapped symmetrically around the circumference of the top half of a 0.6 cm wide, 1.3 cm long cylindrical wooden dowel (Fig. 2.2). The rigid dowel mimics the sheath of a *Zostera marina* plant. The blades were secured with tape, increasing the diameter by 0.1 cm. The canopy height in still water was $h = 13.6$ cm. The measured Young's modulus of the blade material was 0.24 GPa, and the material density was 913 kg/m^3 .

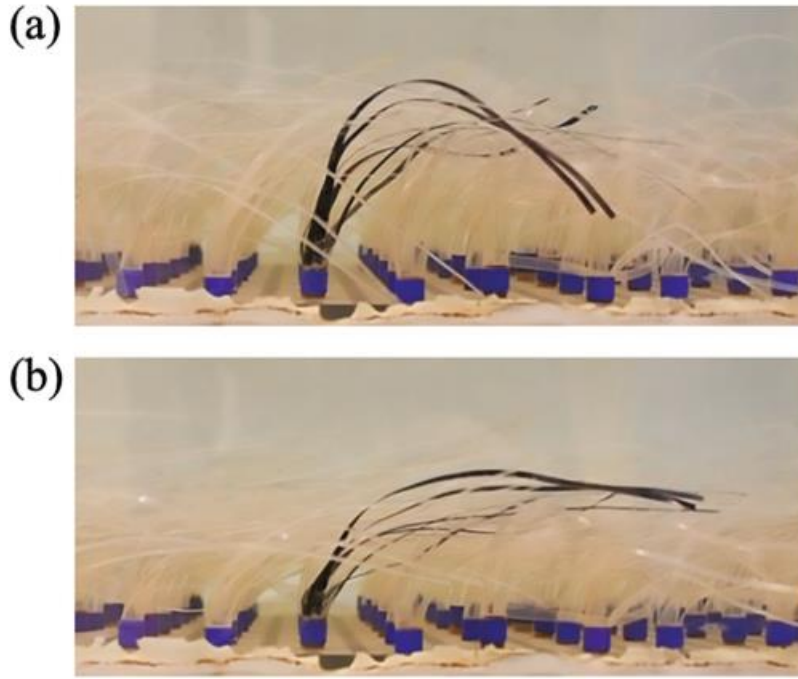


Figure 2.2: Images of experimental meadow at wave (a) crest and (b) trough. The wave amplitude at the meadow leading edge was $a_{w,0} = 1.5$ cm, wave period $T = 2$ s, imposed current $U_c = 10.4$ cm s⁻¹, and mean deflected height $h_d = 5.6$ cm. Case W3C4S in Table 2.S.2.

Individual shoots were inserted in a staggered array into pre-drilled holes in polyvinyl chloride (PVC) boards such that the sheath extended 0.6 cm above the baseboards. The shoot density was 950 shoots per square meter (5700 blades per square meter). The meadow was 6.1 m long. The x axis was aligned with the length of the flume, with $x = 0$ m at the leading edge of the meadow. The z axis was vertical with $z = 0$ m at the top of the baseboard and positive upward. One bare baseboard (1.2 m in length) was placed at each end of the meadow. Experiments were conducted in water depths D of 27 cm and 45 cm above the baseboards, corresponding to submergence ratios h/D of approximately 0.5 and 0.3 and wavelength-to-water depth ratios λ/D of 11.5 and 8.6, respectively. Wave and current magnitude and shoot density were chosen to match a range of field conditions (see Section 2.8.1), within the limitations of the

flume. For each depth, four pure wave cases, four pure current cases, and sixteen combined wave-current cases were tested (see Section 2.8.2) The blade length ratio L ranged from 2 to 10.

2.3.2 Velocity measurements

Velocity was measured with a Nortek Vectrino, which was centered longitudinally between successive shoot rows and laterally between adjacent shoots. Based on previous studies in similar staggered arrays, this position provided a good estimate of the laterally averaged velocity and turbulence in current and wave conditions (see Fig. 2 in Chen et al. 2013 and Fig. 2 in Zhang et al. 2018). To minimize interference with the measurement volume, blades were removed from model shoots within a 5-cm radius around the probe, which has been shown to have negligible impact on the velocity field, except within 1 cm of the bed (discussed in Luhar et al., 2010). The velocity was recorded for 240 s at 200 Hz. Vertical profiles were measured with a 1-cm resolution near the longitudinal center of the meadow ($x = 2.8$ m) and 1 m upstream of the meadow.

Velocity records were despiked using the acceleration thresholding methods described in Goring and Nikora (2002). The number of samples n_s in each wave period was estimated through autocorrelation. Phase (θ)-averaged velocity $\tilde{U}(\theta)$ was calculated within each of the $n_s = 403$ phase bins. The time-averaged velocity (denoted by an overbar) was calculated as

$$\bar{U} = \frac{1}{2\pi} \int_0^{2\pi} \tilde{U}(\theta) d\theta \quad (2.19)$$

The depth-averaged current, U_c was defined by vertically integrating \bar{U} upstream of the meadow. The in-canopy time-averaged velocity was defined by vertically averaging \bar{U} below the deflected meadow height. The wave velocity amplitude, $u_w(z)$, was estimated as (Zhang et al. 2018)

$$u_w = \sqrt{2 \left(\frac{1}{2\pi} \int_0^{2\pi} (\tilde{U}(\theta) - \bar{U})^2 d\theta \right)} \quad (2.20)$$

The characteristic wave velocity amplitude U_w for each case was defined from linear wave theory at the undeflected canopy height ($z = h$) using the measured wave amplitude at the leading edge of the meadow. See Schaefer and Nepf (2022) for further discussion of the velocity measurements. The estimated wave velocity factor was $\alpha = 0.99$ (calculated using Eqn. (24) in Lowe et al. 2005). Wave excursions were comparable to or smaller than the stem spacing in this experiment, making the use of Eqn. (24) in Lowe et al. (2005) reasonable. Henderson et al. (2017) described the parameter $\Lambda = C_D a_v U_w T / (4\pi)$ that determines the threshold meadow density above which canopy drag significantly reduces in-canopy wave velocities. All experimental cases fell under the threshold ($\Lambda = 1.4$), such that the reduction in in-canopy wave velocity was expected to have no impact on wave energy dissipation.

2.3.3 Meadow imaging

The mean deflected canopy height h_d was estimated using digital videos taken at 60 frames per second with a Nikon D7500 camera positioned on a tripod outside of the clear flume wall. To enhance digital tracking, all six blades on one model plant were painted black. The painted model was placed in the second row away from the wall to eliminate wall effects. Videos were taken near $x=280$ cm, beyond the mean-flow development region (Chen et al. 2013). The videos were processed and analyzed using MATLAB VideoReader, readFrame, and Sobel edge

detection functions and an algorithm to identify the painted blades based on the red-green-blue (RGB) pixel values. The vertical position of the highest part of each blade was recorded under the crest and trough and the mean deflected canopy height h_d was defined as the average across crest and trough measurements for all six blades.

2.3.4 Wave amplitude measurements

A twin-wire resistance-type wave gauge was mounted on a trolley at mid-channel width. The trolley was moved in 20-cm increments along the meadow to collect 90-s (45 waves) records of surface displacement η at 1000 Hz. A reference wave gauge simultaneously recorded surface displacement at 1 m upstream of the meadow leading edge. Each record was divided into wave periods of length $n_s = 2013$ samples. The phase-averaged surface displacement, η , in each of the n_s phase bins (phase $\theta = 2\pi n_i/n_s$, for bin number n_i) was used to calculate the wave amplitude

$$a_w = \sqrt{2 \left(\frac{1}{2\pi} \int_0^{2\pi} \eta^2(\theta) d\theta \right)} \quad (2.21)$$

The wave amplitude varied along the meadow, not only decreasing but also exhibiting a beat pattern associated with the reflected wave (Fig. 2.3). To calculate the wave decay coefficient, K_D , the evolution of wave amplitude along the meadow was fitted using a cosine relationship to account for the beat pattern. For simplicity we ignored changes in K_D associated with the change in wave amplitude over the meadow. Wave decay due to the channel walls and bed was tested with empty baseboards and determined to be negligible (<10% of the values recorded with the meadow). During each experiment, the amplitude measured at the reference gauge varied by less

than 0.5%, indicating stationary conditions. For the two largest currents, turbulence generated at the flow inlet created surface agitation that resulted in a small (10%) decrease in the wave amplitude measured at the meadow leading edge, $a_{w,0}$, relative to pure wave conditions with the same wavemaker setting. As $U_c \ll C_g$, this modification of wave amplitude was not related to the Doppler effect. For these cases, a reference pure wave decay coefficient, $K_{D,pw}$, was defined in the following way. A power function $K_{D,pw} = f(a_{w,0})$ was fit to the measured pure wave cases and used to estimate $K_{D,pw}$ for $a_{w,0}$ corresponding to the wave-current conditions.

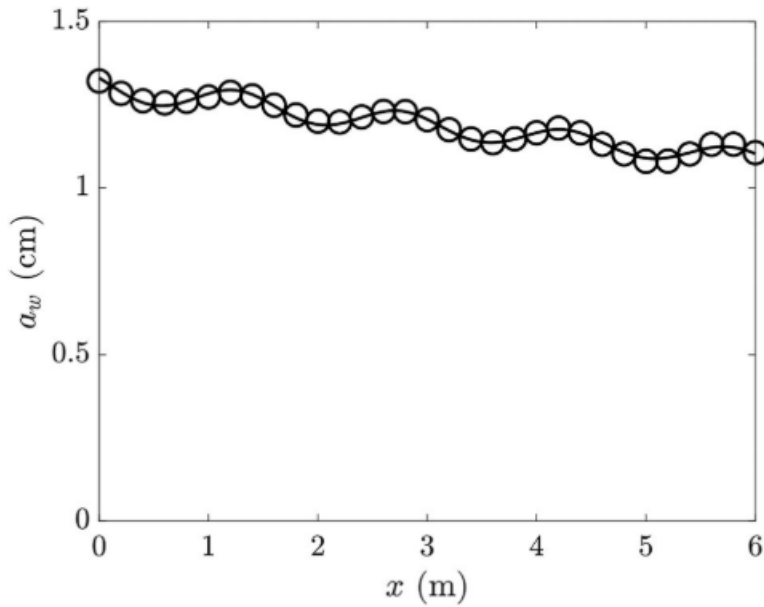


Figure 2.3: Measured wave amplitude (circles) along the length of the meadow for case W2C1S (see Table 2.S.2), for which wave amplitude $a_{w,0} = 1.3$ cm, wave period $T = 2$ s, imposed current $U_c = 4.0$ cm s⁻¹, and wavelength $\lambda = 3.1$ m. The solid black curve denotes predicted $a_w(x)$ for the fitted $K_D = 2.6 \pm 0.1$ m².

2.3.5 Parameter estimation

The Cauchy number (Eqns. (2.1), (2.2), and (2.7)) and wave decay coefficient K_D (Eqns. (2.15) and (2.16)) were defined using the drag coefficients of fully rigid blades, estimated from previous studies of flat plates as a function of the Keulegan-Carpenter number, $KC = U_w T / w_b$. Based on data reported in Keulegan and Carpenter (1958) and Graham (1980), Luhar and Nepf (2016) defined the wave drag coefficient $C_{D,w} = \max(10KC^{-1/3}, 1.95)$. For simplicity, we neglected any increase in C_D with distance into the meadow due to the reduction in wave amplitude. The current drag coefficient for flat plates is $C_{D,c} = 1.95 + 50/Re$ (Ellington 1991), with Reynolds number $Re = U_c w_b / \nu$, in which ν is the kinematic viscosity of water. Sarpkaya and Storm (1985) observed that the presence of a current could modify $C_{D,w}$, but that drag coefficients in combined wave-current conditions converged with pure wave values for $KC > 15$, and current had negligible impact on drag coefficient for $KC > 30$. In the present experiments $KC > 24$, so $C_{D,wc}$ was assumed to equal $C_{D,w}$. Wave-current Reynolds numbers $Re = \left(U_c^2 + \frac{1}{2} U_w^2 \right)^{1/2} w_b / \nu$ ranged from 100 to 600. Finally, the rigid sheath length of the physical model, l_{sh} , was used for l_r in Eqns. (2.9) and (2.10). The assumption $l_r = l_{sh}$ produced good agreement between predicted and measured wave amplitude decay in a *Posidonia oceanica* meadow (Lei and Nepf 2019a).

2.4 Results and Discussion

2.4.1 Influence of current on measured wave decay coefficient

The measured wave decay coefficient for each wave-current case, $K_{D,wc}$, was normalized by the wave decay coefficient for the corresponding (same $a_{w,0}$) pure wave case, $K_{D,pw}$ (Fig. 2.4). For weak currents, $U_c/U_w < \approx 0.5$, the addition of current had negligible impact and $K_{D,wc}/K_{D,pw}$ was approximately one or just below one within uncertainty. However, for $U_c/U_w > \approx 0.5$, the addition of current reduced the wave decay coefficient relative to pure wave conditions by as much as 40% percent. Similarly, Paul et al. (2012) observed that a following current of magnitude $U_c/U_w \approx 0.3$ reduced wave attenuation by a flexible model meadows by up to 30%. Paul et al. (2012) suggested that shoots might reach a maximum deflection above a critical current threshold, and that wave attenuation would not change above that current threshold. In the present study, the reduction in the wave decay coefficient plateaued at $K_{D,wc}/K_{D,pw} = 0.6$ for $U_c/U_w > 1$. However, in contrast to Paul et al. (2012)'s suggestion, this plateau was not associated with the maximum deflection limit. For example, posture W1C4D (Fig. 2.4(c)), was not at the maximum deflection, but for this case $K_{D,wc}/K_{D,pw}$ was at the plateau (0.6).

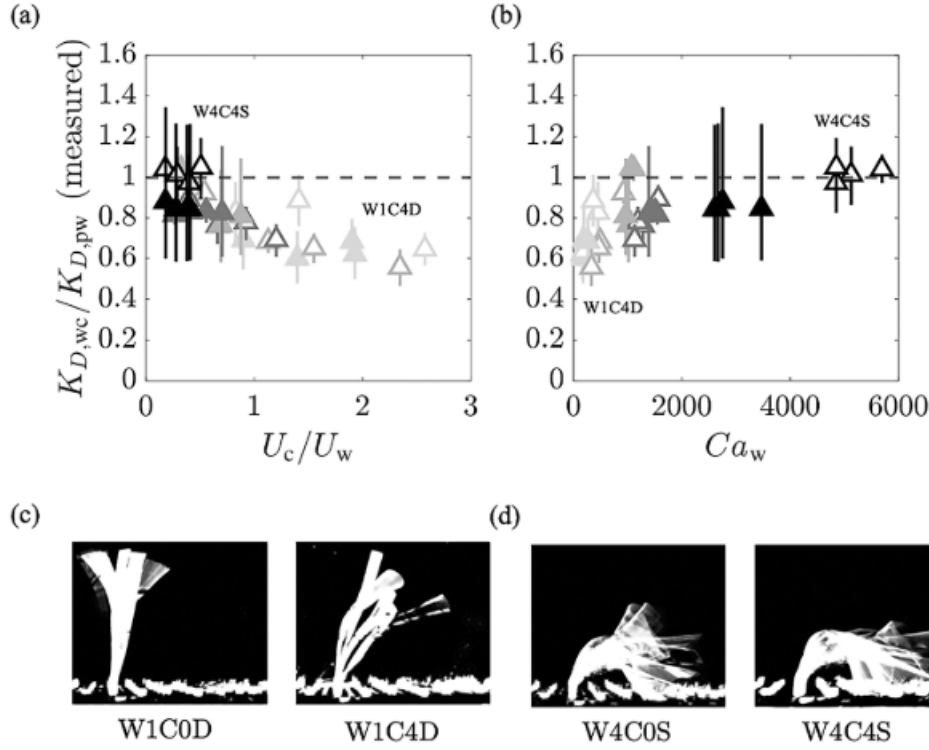


Figure 2.4: Measured wave decay coefficient $K_{D,wc}$ for combined wave and current conditions normalized by $K_{D,pw}$ for pure wave conditions with the same wave amplitude at the meadow leading edge, $a_{w,0}$, and as a function of (a) current-to-wave velocity ratio U_c/U_w and (b) wave Cauchy number Ca_w . Larger $a_{w,0}$ are denoted with darker shades. Open and filled symbols denote water depths $D = 27$ and 45 cm, respectively. Composite images of blade posture over six wave cycles corresponding to (c) $a_{w,0} = 1.0$ cm pure wave (case W1C0D) and with imposed current velocity $U_c = 6.8$ cm s^{-1} (case W1C4D) and (d) $a_{w,0} = 3.9$ cm pure wave (case W4C0S) and with $U_c = 10.4$ cm s^{-1} (case W4C4S). The labels in (c) and (d) are also shown in (a) and (b).

The impact of current on wave decay was dependent on the wave condition. Specifically, when the wave Cauchy number was small, so that the blades exhibited limited wave-induced motion (W1C0D in Fig. 2.4(c)), the addition of a current enhanced the blade pronation (W1C4D in Fig. 2.4(c)), which decreased the wave decay coefficient, $K_{D,wc}/K_{D,pw} < 1$. However, for large wave Cauchy number ($Ca_w \gtrsim 2000$), the wave alone produced significant reconfiguration of the blades (W4C0S in Fig. 2.4(d)), so that the additional reconfiguration

generated by the current was negligible, and the wave decay coefficient was not changed by the addition of current ($K_{D,wc}/K_{D,pw} = 1$). Note that even pure wave conditions can produce a blade posture with downstream bias (W4C0S in Fig. 2.4(d)). This is due both to the vertical component of the wave velocity (see the descriptions in Döbken 2015; Zhu et al. 2020) and to the wave-induced current in the canopy (Luhar et al. 2010; Abdolahpour et al. 2017; Luhar 2021).

The addition of current increases the maximum total (wave + current) velocity, which can increase the maximum drag force and wave energy dissipation, as has been observed for rigid meadows (Li and Yan 2007; Hu et al. 2014, 2021; Zhang and Nepf 2021). In contrast, for the present flexible meadow the addition of current was, for some cases, associated with a decrease in the wave decay coefficient, which can be attributed to current-induced reconfiguration of the blades, which both reduces the frontal area and makes the blades more streamlined, reducing the stem-normal relative velocity along the tilted part of the blade (above the sheath).

The measured wave decay coefficient in combined wave-current conditions, $K_{D,wc}$, decreased with increasing wave-current Cauchy number, Ca_{wc} , consistent with the expected impact of reconfiguration. For example, for the shallower water depth, $K_{D,wc} \sim Ca_{wc}^{-0.39 \pm 0.09}$, which was consistent with Eqn. (2.8), $l_e \sim Ca_{wc}^{-0.33}$ (see additional details in Section 2.8.4) and gives support to the effective meadow height as a predictor of the impact of reconfiguration on meadow drag and wave decay coefficient.

2.4.2 K_D prediction

Predictions based on different choices for meadow height are compared in Fig. 2.5. First, Losada et al. (2016) suggested using the observed deflected meadow height, $l = h_d$, in Eqn. (2.15). This

significantly overestimated $K_{D,wc}$ (Fig. 2.5(a)). While h_d accounts for the reduction in canopy frontal area, which contributes to the reduction in drag, it does not account for blade motion, which also reduces drag by reducing the relative velocity between the blade and water. The deflected height also does not account for the streamlining of the blade shape.

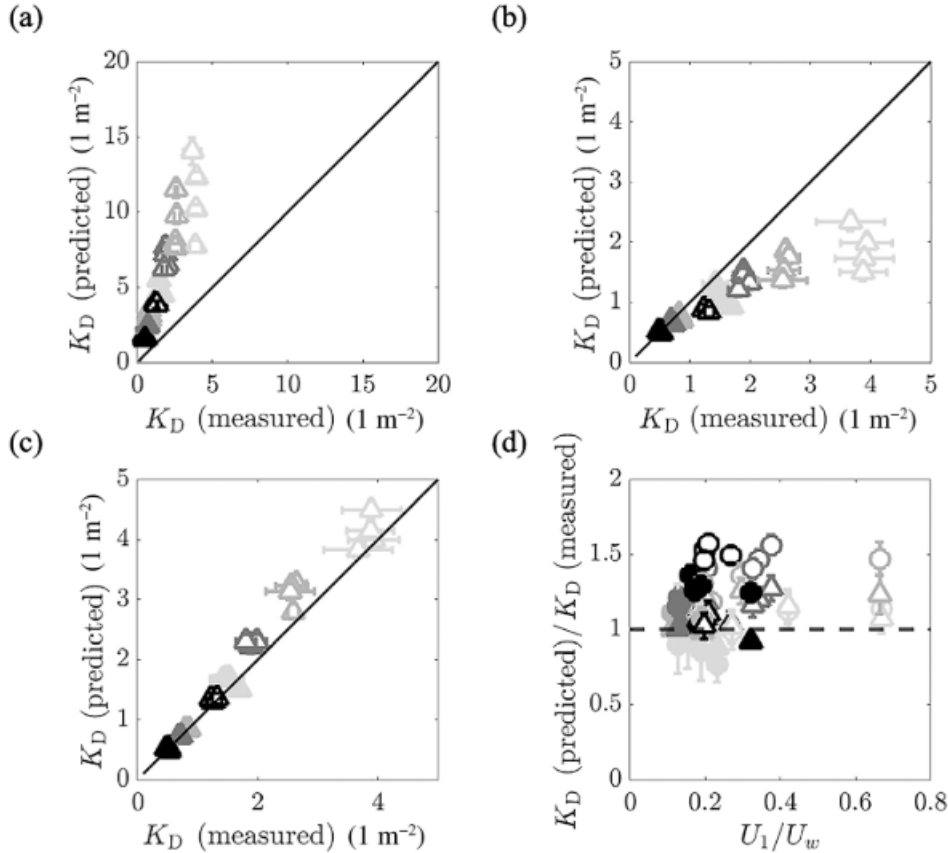


Figure 2.5: Predicted wave decay coefficient $K_{D,wc}$ vs. measured $K_{D,wc}$ using the following length scales in Eq. 2.15: (a) measured mean deflected height h_d , (b) wave-current effective meadow height $l_{e,m,wc}$ (Eqn. 2.10) using imposed depth-averaged current U_c , and (c) wave-current $l_{e,m,wc}$ scaling (Eqn. 2.10) using in-canopy time-averaged velocity U_1 . Open and filled symbols denote cases with depths $D = 27$ and 45 cm, respectively. (d) Ratio of predicted to measured $K_{D,wc}$ using wave-current $l_{e,m}$ scaling (Eq. 19, triangles) and wave-only $l_{e,m}$ scaling (Eq. 2.9, circles) as a function of $U_1 = U_w$. Larger wave amplitudes $a_{w,0}$ denoted with darker shades.

Second, we considered the effective meadow height defined by Eqn. (2.10). For simplicity, $l_{e,m,wc}$ was estimated using wave conditions at the leading edge of the meadow, which neglected the change in Ca_{wc} and KC with wave amplitude decay along the meadow. Initially $l_{e,m,wc}$ was predicted from Ca_{wc} defined with depth-averaged current U_c , which tended to underestimate $K_{D,wc}$ (Fig. 2.5(b)). This was because U_c was larger than the time-averaged velocity in the meadow ($U_1 < U_c$), so that U_c overestimated the degree of reconfiguration and thus the degree of drag reduction. Defining Ca_{wc} with U_1 improved the prediction (Fig. 2.5(c)), compared to Ca_{wc} defined by U_c (Fig. 2.5(b)). Specifically, using U_1 , $K_{D,wc}$ (predicted) = $(1.11 \pm 0.03)K_{D,wc}$ (measured).

Because the meadow modifies the current exposure of individual blades ($U_1 < U_c$), the meadow regulates the degree to which current modifies wave damping (Zhang and Nepf 2021). That is, by reducing the current to which individual blades are exposed, the meadow reduces Ca_{wc} , which increases $l_{e,m,wc}$ and $K_{D,wc}$. Though not tested in the present study, this implies that the impact of current on wave dissipation will depend on meadow density, because in general meadows of higher density more significantly reduce U_1 relative to U_c .

Given that the velocity relevant to blade drag and wave dissipation is U_1 , the transition between a pure wave (Eqn. (2.9)) and wave-current (Eqn. (2.10)) scaling should be described by U_1/U_w . Replacing U_c with U_1 in the limits described in Lei and Nepf (2019a), the wave-only scaling should be reasonable for $U_1/U_w < 0.25$. This is generally supported by Fig. 2.5(d), which compares predictions using $l_{e,m,w}$ and $l_{e,m,wc}$ (using U_1) as a function of U_1/U_w . Specifically, the wave-only scaling (circles) does reasonably well for $U_1/U_w < 0.2$, but

overpredicted $K_{D,wc}$ by as much as 50% for $U_1/U_w > 0.2$. The wave-current scaling (triangles in Fig. 2.5(d)) provided a better agreement across the full range of conditions.

2.4.3 Extension to field application

A better prediction of wave dissipation was possible using the in-canopy time-averaged velocity U_1 (Fig. 2.5). However, U_1 may not be readily available in field studies and is not simulated by depth-averaged numerical models. Therefore, it is useful to consider the prediction of U_1 from U_c and U_w , as discussed in this section. The deflected meadow height h_d can be predicted from U_c using the empirical fit presented in Luhar and Nepf (2013), shown in Fig. 2.6(a). See Section 2.8.5 for more details. The deflected meadow height can then be used to predict the in-canopy time-mean velocity $U_{1,c}$ from Eqn. (2.17). We must additionally consider the contribution from the wave-induced current. Noting that Eqn. (2.18) defines the maximum wave-induced current, we used pure wave measurements to modify Eqn. (2.18) to predict the canopy-averaged wave-induced current. Specifically, using pure wave cases, the measured canopy- and time-averaged velocity, $U_{1,w}$, was correlated with \bar{U}_{max} (Section 2.8.5), with a linear fit $U_{1,w}(measured) = (0.7 \pm 0.2) \bar{U}_{max}(predicted)$. Note that this fit averages over the vertical variation in wave-induced current within the canopy and is based on a single meadow density (5700 blades m^{-2}). Finally, the total in-canopy velocity was predicted as a linear combination of $U_{1,c}$ and $U_{1,w}$.

$$U_1 = (0.7 \pm 0.2)\bar{U}_{max} + \frac{U_c}{1 - \frac{h_d}{D}\phi + \sqrt{\frac{C_{D,c}a_v l_{e,m}}{2C(1-\phi)}\left(\frac{D-h_d}{D}\right)^3}} \quad (2.22)$$

Eqn. (2.22) assumes that the waves do not alter the momentum exchange between the meadow and overflow (C unchanged by waves) and that the wave-induced current ($U_{1,w}$) was not altered by presence of imposed current. These assumptions were validated by the good agreement between predicted and measured U_1 (Fig. 2.6(b)). Note that Eqn. (2.22) represents the fully developed flow condition, which occurs after flow development distance $X_D \approx 7l + 3(C_D a_v)^{-1}$ (Eqn. (10) in Chen et al. 2013). Higher in-canopy current may influence wave energy dissipation closer to the leading edge of the meadow ($x < X_D$).

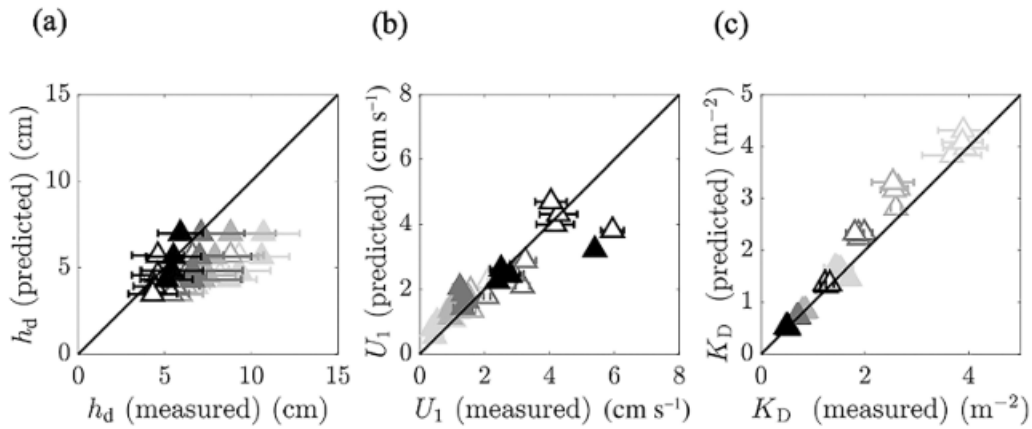


Figure 2.6: Predicted vs. measured (a) mean deflected height h_d , predicted from imposed current U_c (see Section 2.8.5), (b) in-canopy time-averaged velocity U_1 , predicted from Eq. 2.22 using predicted h_d , and (c) wave decay coefficient K_D , predicted using predicted U_1 to define the wave-current Cauchy number Ca_{wc} in Eq. 2.7. Larger wave amplitudes $a_{w,0}$ are denoted with darker shades. Open and filled symbols denote cases with depths $D = 27$ and 45 cm, respectively.

Finally, using the predicted U_1 to calculate $l_{e,m,wc}$ (Eqn. (2.10)) produced predictions of $K_{D,wc}$ (Eqn. (2.15), Fig. 2.6(c)) that were comparable to those made with measured U_1 (Fig. 2.5(c)). Specifically, as shown in Fig. 2.6(c), $K_{D,wc}$ (predicted) = $(1.10 \pm 0.04) K_{D,wc}$ (measured). In Eqn. (2.22), the relative contribution of $U_{1,c}$ to U_1 was between 15 and 85%, decreasing with increasing wave velocity. Excluding $U_{1,c}$ or $U_{1,w}$ led to worse

agreement (by about 8% and 3%, respectively) compared to including both components in Eqn. (2.22). The impact of the accuracy of Eqn. (2.22) on K_D prediction could become more important for higher U_1/U_w ratios than those tested here (through the wave-current Cauchy number, Eqn. (2.7)). The relatively poor prediction of h_d at low current velocity (Fig. 2.6(a)) did not have a significant impact on the prediction of $K_{D,wc}$. This was because small values of U_c were associated with small U_1 , which had little impact on wave damping, such that errors in h_d and U_1 had little impact on $K_{D,wc}$. The good agreement illustrated by Fig. 2.6(c) suggested that wave dissipation in the field or in numerical models could be predicted from the depth-averaged current (U_c), wave amplitude and dominant wave period, mean water depth (yielding U_w), and meadow properties (blade geometry and meadow density).

Note that the present study focused on a single meadow density and wave period, and only following collinear currents, and additional studies are needed to understand extensions to other meadow density and currents flowing opposite to or at oblique angles to the primary direction of wave propagation, which is also common in the field (e.g., Mullarney et al. 2017). In addition, spatial gradients in current are common near the edges of vegetation, and in those areas one should consider the work done by radiation stresses, S_{xx} , on spatially varying currents, $S_{xx} \frac{\partial U_c}{\partial x}$ (Longuet-Higgins and Stewart 1964). Although the impact of U_c on wave group velocity (Eqns. (2.11) and (2.12)) was negligible for the laboratory experiments ($U_c \leq 0.1 C_g$), it could be relevant in the field. For $U_c > 0.1 C_g$, Eqn. (2.10) can still be used to predict the effective meadow height, which would then be used in the modified prediction of $K_{D,wc}$ given in Losada et al. (2016); see also Section 2.8.3, which accounts for the Doppler shift in the wave group velocity.

2.5 Conclusions

Seagrass blades reconfigure in response to waves, which can reduce the drag on individual blades, which in turn reduces the rate of wave dissipation achieved by the meadow. For some conditions, the addition of a following current enhanced reconfiguration and reduced the wave decay coefficient, relative to pure waves. Specifically, the presence of a following current reduced K_D when $U_c/U_w > 0.5$. Current-induced pronation had the greatest impact on wave damping for small wave amplitude ($Ca_w < 2000$), for which wave-induced reconfiguration was weak. When wave-induced reconfiguration was strong ($Ca_w > 2000$), the additional reconfiguration provided by the current had a negligible impact on the wave decay coefficient.

The reduction in drag due to reconfiguration was described in terms of an effective length, l_e , which defined the length of rigid blade providing the same drag as a flexible blade of length l . In this study, descriptions of force and reconfiguration for individual blades were extended to meadow-scale dynamics to predict wave attenuation by a flexible seagrass meadow in combined wave-current conditions. Measurements validated the proposed prediction of wave decay coefficient. Importantly, the relevant velocity for reconfiguration, blade drag, and wave damping was shown to be the in-canopy velocity, U_1 , which, due to canopy drag, can be significantly smaller than the depth-averaged current, U_c . In this way, the impact of the meadow on current distribution reduces the impact of current on wave dissipation.

2.6 Acknowledgments

This material is based upon work supported by the National Science Foundation under Grant No. 1659923. R. Schaefer was supported in part by the Louis Berger Fellowship Fund in the Massachusetts Institute of Technology Department of Civil and Environmental Engineering, and by the National Science Foundation Graduate Research Fellowship under Grant No. 1745302.

The authors declare no conflict of interest.

2.7 References

- Abdolahpour, M., M. Hambleton, and M. Ghisalberti. 2017. The wave-driven current in coastal canopies. *J. Geophys. Res. Ocean.* 122: 3660–3674, doi:10.1002/2016JC012446
- Alben, S., M. Shelley, and J. Zhang. 2002. Drag reduction through self-similar bending of a flexible body. *Nature* 420: 479–481, doi:10.1038/nature01232
- Boese, B. L., B. D. Robbins, and G. Thursby. 2005. Desiccation is a limiting factor for eelgrass (*Zostera marina* L.) distribution in the intertidal zone of a northeastern Pacific (USA) estuary. *Bot. Mar.* 48: 274–283, doi:10.1515/BOT.2005.037
- Bradley, K., and C. Houser. 2009. Relative velocity of seagrass blades: Implications for wave attenuation in low-energy environments. *J. Geophys. Res. Earth Surf.* 114, doi:10.1029/2007JF000951
- Chen, Z., C. Jiang, and H. Nepf. 2013. Flow adjustment at the leading edge of a submerged aquatic canopy. *Water Resour. Res.* 49: 5537–5551, doi:10.1002/wrcr.20403
- Dalrymple, R. A., J. T. Kirby, and P. A. Hwang. 1984. Wave diffraction due to areas of energy dissipation. *J. Waterw. Port, Coastal, Ocean Eng.* 110: 67–79, doi:10.1061/(ASCE)0733-950X(1984)110:1(67)
- Döbken, J. W. D. 2015. Modeling the interaction of wave hydrodynamics with flexible aquatic vegetation. M.Sc. thesis. Delft Univ. of Technology.
- Ellington, C. P. 1991. Aerodynamics and the origin of insect flight. *Adv. In Insect Phys.* 23: 171–210, doi:10.1016/S0065-2806(08)60094-6

- Fourqurean, J. W., C. M. Duarte, H. Kennedy, and others. 2012. Seagrass ecosystems as a globally significant carbon stock. *Nat. Geosci.* 5: 505–509, doi:10.1038/ngeo1477
- Ginsburg, R., and H. Lowenstam. 1958. The influence of marine bottom communities on the depositional environment of sediments. *J. Geol.* 66: 310–318, doi:10.1086/626507
- Goda, Y., and Y. Suzuki. 1977. Estimation of incident and reflected waves in random wave experiments. *Proc. Fifteenth Coast. Eng. Conf.* 828–845, doi:10.9753/icce.v15.47
- Goring, D. G., and V. I. Nikora. 2002. Despiking acoustic Doppler velocimeter data. *J. Hydraul. Eng.* 128: 117–126, doi:10.1061/(ASCE)0733-9429(2002)128:1(117)
- Gosselin, F. P. 2019. Mechanics of a plant in fluid flow. *J. Exp. Bot.* 70: 3533–3548, doi:10.1093/jxb/erz288
- Graham, J. M. R. 1980. The forces on sharp-edged cylinders in oscillatory flow at low Keulegan-Carpenter numbers. *J. Fluid Mech.* 97: 331–346, doi:10.1017/S0022112080002595
- Henderson, S. M. 2019. Motion of buoyant, flexible aquatic vegetation under waves: Simple theoretical models and parameterization of wave dissipation. *Coast. Eng.* 152: 103497, doi:10.3354/meps338081
- Henderson, S. M., B. K. Norris, J. C. Mullarney, and K. R. Bryan. 2017. Wave-frequency flows within a near-bed vegetation canopy. *Cont. Shelf Res.* 147: 91–101, doi:10.1016/j.csr.2017.06.003
- Houser, C., S. Trimble, and B. Morales. 2015. Influence of blade flexibility on the drag coefficient of aquatic vegetation. *Estuaries Coast.* 38: 569–577, doi:10.1007/s12237-014-9840-3
- Hu, Z., S. Lian, H. Wei, Y. Li, M. Stive, and T. Suzuki. 2021. Laboratory data on wave propagation through vegetation with following and opposing currents. *Earth Syst. Sci. Data* 13: 4987–4999, doi:10.5194/essd-13-4987-2021
- Hu, Z., T. Suzuki, T. Zitman, W. Uittewaal, and M. Stive. 2014. Laboratory study on wave dissipation by vegetation in combined current-wave flow. *Coast. Eng.* 88: 131–142, doi:10.1016/j.coastaleng.2014.02.009
- Infantes, E., A. Orfila, G. Simarro, J. Terrados, M. Luhar, and H. Nepf. 2012. Effect of a seagrass (*Posidonia oceanica*) meadow on wave propagation. *Mar. Ecol. Prog. Ser.* 456: 63–72, doi:10.3354/meps09754
- Keulegan, G. H., and L. H. Carpenter. 1958. Forces on cylinders and plates in an oscillating fluid. *J. Res. Natl. Bur. Stand.* 60: 423, doi:10.6028/jres.060.043
- Leclercq, T., and E. De Langre. 2018. Reconfiguration of elastic blades in oscillatory flow. *J. Fluid Mech.* 838: 606–630, doi:10.1017/jfm.2017.910

- Lei, J., and H. Nepf. 2021. Evolution of flow velocity from the leading edge of 2-D and 3-D submerged canopies. *J. Fluid Mech.* 916: 1–27, doi:10.1017/jfm.2021.197
- Lei, J., and H. M. Nepf. 2019a. Wave damping by flexible vegetation: Connecting individual blade dynamics to the meadow scale. *Coast. Eng.* 147: 138–148, doi:10.1016/j.coastaleng.2019.01.008
- Lei, J., and H. M. Nepf. 2019b. Blade dynamics in combined waves and current. *J. Fluids Struct.* 87: 137–149, doi:10.1016/j.jfluidstructs.2019.03.020
- Li, C. W., and K. Yan. 2007. Numerical investigation of wave-current-vegetation interaction. *J. Hydraul. Eng.* 133: 794–803, doi:10.1061/(ASCE)0733-9429(2007)133:7(794)
- Longuet-Higgins, M. S., and R. W. Stewart. 1960. Changes in the form of short gravity waves on long waves and tidal currents. *J. Fluid Mech.* 8: 565–583, doi:10.1017/S0022112060000803
- Longuet-Higgins, M. S., and R. W. Stewart. 1964. Radiation stresses in water waves: a physical discussion, with applications. *Deep. Res.* 11: 529–562, doi:10.1016/0011-7471(64)90001-4
- Losada, I. J., M. Maza, and J. L. Lara. 2016. A new formulation for vegetation-induced damping under combined waves and currents. *Coast. Eng.* 107: 1–13, doi:10.1016/j.coastaleng.2015.09.011
- Lowe, R. J., J. R. Koseff, and S. G. Monismith. 2005. Oscillatory flow through submerged canopies: 1. Velocity structure. *J. Geophys. Res. Ocean.* 110: C10016, doi:10.1029/2004JC002788
- Luhar, M. 2012. Analytical and experimental studies of plant-flow interaction at multiple scales. Ph.D. thesis. Massachusetts Inst. of Technology.
- Luhar, M. 2021. Comment on “The wave-driven current in coastal canopies” by M. Abdolahpour et al. *J. Geophys. Res. Ocean.* 126: e2019JC015644, doi:10.1029/2019jc015644
- Luhar, M., S. Coutu, E. Infantes, S. Fox, and H. Nepf. 2010. Wave-induced velocities inside a model seagrass bed. *J. Geophys. Res. Ocean.* 115: C12005, doi:10.1029/2010JC006345
- Luhar, M., E. Infantes, and H. M. Nepf. 2017. Seagrass blade motion under waves and its impact on wave decay. *J. Geophys. Res. Ocean.* 122: 3736–3752, doi:10.1002/2017JC012731
- Luhar, M., and H. M. Nepf. 2011. Flow-induced reconfiguration of buoyant and flexible aquatic vegetation. *Limnol. Oceanogr.* 56: 2003–2017, doi:10.4319/lo.2011.56.6.2003
- Luhar, M., and H. M. Nepf. 2013. From the blade scale to the reach scale: A characterization of aquatic vegetative drag. *Adv. Water Resour.* 51: 305–316, doi:10.1016/j.advwatres.2012.02.002
- Luhar, M., and H. M. Nepf. 2016. Wave-induced dynamics of flexible blades. *J. Fluids Struct.* 61: 20–41, doi:10.1016/j.jfluidstructs.2015.11.007

- Mendez, F. J., and I. J. Losada. 2004. An empirical model to estimate the propagation of random breaking and nonbreaking waves over vegetation fields. *Coast. Eng.* 51: 103–118, doi:10.1016/j.coastaleng.2003.11.003
- Mullarney, J. C., S. M. Henderson, J. A. H. Reynolds, B. K. Norris, and K. R. Bryan. 2017. Spatially varying drag within a wave-exposed mangrove forest and on the adjacent tidal flat. *Cont. Shelf Res.* 147: 102–113, doi:10.1016/j.csr.2017.06.019
- Nepf, H., M. Ghisalberti, B. White, and E. Murphy. 2007. Retention time and dispersion associated with submerged aquatic canopies. *Water Resour. Res.* 43: 1–10, doi:10.1029/2006WR005362
- Orth, R. J., T. J. B. Carruthers, W. C. Dennison, and others. 2006. A global crisis for seagrass ecosystems. *Bioscience* 56: 987–996, doi:10.1641/0006-3568(2006)56[987:agcfse]2.0.co;2
- Paul, M., T. J. Bouma, and C. L. Amos. 2012. Wave attenuation by submerged vegetation: Combining the effect of organism traits and tidal current. *Mar. Ecol. Prog. Ser.* 444: 31–41, doi:10.3354/meps09489
- Pedersen, M. F., and J. Borum. 1992. Nitrogen dynamics of eelgrass *Zostera marina* during a late summer period of high growth and low nutrient availability. *Mar. Ecol. Prog. Ser.* 80: 65–73, doi:10.3354/meps080065
- Pollard, D. A. 1984. A review of ecological studies on seagrass-fish communities, with particular reference to recent studies in Australia. *Aquat. Bot.* 18: 3–42, doi:10.1016/0304-3770(84)90079-2
- Sarpkaya, T., and M. Storm. 1985. In-line force on a cylinder translating in oscillatory flow. *Appl. Ocean Res.* 7: 188–196, doi:10.1016/0141-1187(85)90025-2
- Schaefer, R. B., and H. M. Nepf. 2022a. Flow structure in an artificial seagrass meadow in combined wave-current conditions. *Front. Mar. Sci.* 9: 1–12, doi:10.3389/fmars.2022.836901
- Schaefer, R.B., Nepf, H.M. 2022b. Wave damping by seagrass meadows in combined wave-current conditions. *Limnol. Oceanogr.* 67: 1554–1565, doi:10.1002/lno.12102
- Ward, L. G., W. M. Kemp, and W. R. Boynton. 1984. The influence of waves and seagrass communities on suspended particulates in an estuarine embayment. *Mar. Geol.* 59: 85–103, doi:10.1016/0025-3227(84)90089-6
- Waycott, M., C. M. Duarte, T. J. B. Carruthers, and others. 2009. Accelerating loss of seagrasses across the globe threatens coastal ecosystems. *Proc. Natl. Acad. Sci. U. S. A.* 106: 12377–12381, doi:10.1073/pnas.0905620106
- Yin, Z., Y. Wang, Y. Liu, and W. Zou. 2020. Wave attenuation by rigid emergent vegetation under combined wave and current flows. *Ocean Eng.* 213: 107632, doi:10.1016/j.oceaneng.2020.107632

Zhang, J., J. Lei, W. Huai, and H. Nepf. 2020. Turbulence and particle deposition under steady flow along a submerged seagrass meadow. *J. Geophys. Res. Ocean.* 125: e2019JC015985, doi:10.1029/2019JC015985

Zhang, X., and H. Nepf. 2021. Wave damping by flexible marsh plants influenced by current. *Phys. Rev. Fluids* 6: 1–17, doi:10.1103/PhysRevFluids.6.100502

Zhang, Y., C. Tang, and H. Nepf. 2018. Turbulent kinetic energy in submerged model canopies under oscillatory flow. *Water Resour. Res.* 54: 1734–1750, doi:10.1002/2017WR021732

Zhao, C., J. Tang, Y. Shen, and Y. Wang. 2021. Study on wave attenuation in following and opposing currents due to rigid vegetation. *Ocean Eng.* 236: 109574, doi:10.1016/j.oceaneng.2021.109574

Zhu, L., Q. P. Zou, K. Huguenard, and D. W. Fredriksson. 2020. Mechanisms for the asymmetric motion of submerged aquatic vegetation in waves: A consistent-mass cable model. *J. Geophys. Res. Ocean.* 125: 1–23, doi:10.1029/2019JC015517

2.8 Supplementary Information

2.8.1 Compiled *Zostera marina* characteristics

Table 2.S.1: Compilation of field observations in *Zostera marina* meadows and comparison to experimental conditions in this study. The upper limit of Cauchy numbers in the field is associated with species with the longest blades. Sources: (Olesen and Sand-Jensen 1994; Lee et al. 2004; Moore 2004; Fonseca and Koehl 2006; Abdelrhman 2007; Fonseca et al. 2007; McKone 2009; Krause-Jensen et al. 2011; Stevens and Lacy 2012; Fonseca et al., 2019)

Parameter	<i>Zostera marina</i>	Experimental study
Shoot density n_s (shoots/m ²)	350 to 2,200	950
Blade length l_b (m)	0.1 to 1.1	0.136
Sheath length l_{sh} (m)	0.03 to 0.32	0.06

Blade width w_b (mm)	2 to 6	3.3
Blade thickness t_b (mm)	0.1 to 0.4	0.1
Number of blades per shoot	2 to 7	6
Blade stiffness EI (Nm ²)	8.0×10^{-8} to 2.8×10^{-7}	8.0×10^{-8}
Wave amplitude a_w (cm)	4 to 60	0.9 to 4
Wave velocity amplitude U_w (cm/s)	7 to 120	4 to 23
Current velocity U_c (cm/s)	1 to 55	2 to 10.5
Wave period T (s)	2 to 9	2
Mean water depth D (m)	0.4 to 11	0.27 (S) and 0.45 (D)
Wave-current Cauchy number Ca_{wc}	350 to 150,000+	150 to 3,000

References

- Abdelrhman, M. A. 2007. Modeling coupling between eelgrass *Zostera marina* and water flow. Mar. Ecol. Prog. Ser. 338: 81–96, doi:10.3354/meps338081
- Fonseca, M. S., J. W. Fourqurean, and M. A. R. Koehl. 2019. Effect of seagrass on current speed: Importance of flexibility vs. shoot density. Front. Mar. Sci. 6: 1–13, doi:10.3389/fmars.2019.00376
- Fonseca, M. S., and M. A. R. Koehl. 2006. Flow in seagrass canopies: The influence of patch width. Estuar. Coast. Shelf Sci. 67: 1–9, doi:10.1016/j.ecss.2005.09.018
- Fonseca, M. S., M. A. R. Koehl, and B. S. Kopp. 2007. Biomechanical factors contributing to self-organization in seagrass landscapes. J. Exp. Mar. Bio. Ecol. 340: 227–246, doi:10.1016/j.jembe.2006.09.015
- Krause-Jensen, D., J. Carstensen, S. L. Nielsen, T. Dalsgaard, P. B. Christensen, H. Fossing, and M. B. Rasmussen. 2011. Sea bottom characteristics affect depth limits of eelgrass *Zostera marina*. Mar. Ecol. Prog. Ser. 425: 91–102, doi:10.3354/meps09026

- Lee, K. S., F. T. Short, and D. M. Burdick. 2004. Development of a nutrient pollution indicator using the seagrass, *Zostera marina*, along nutrient gradients in three New England estuaries. *Aquat. Bot.* 78: 197–216, doi:10.1016/j.aquabot.2003.09.010
- McKone, K. 2009. Light available to the seagrass *Zostera marina* when exposed to currents and waves. M.Sc. thesis. Univ. of Maryland, College Park.
- Moore, K. A. 2004. Influence of seagrasses on water quality in shallow regions of the Lower Chesapeake Bay. *J. Coast. Res.* 2009: 162–178, doi:10.2112/si45-162.1
- Olesen, B., and K. Sand-Jensen. 1994. Demography of shallow eelgrass (*Zostera marina*) populations--Shoot dynamics and biomass development. *Br. Ecol. Soc.* 82: 379–390, doi:10.2307/2261305
- Stevens, A. W., and J. R. Lacy. 2012. The influence of wave energy and sediment transport on seagrass distribution. *Estuaries Coast.* 35: 92–108, doi:10.1007/s12237-011-9435-1

2.8.2 Experimental parameters and measurements

Table 2.S.2: Experimental parameters and measurements.

Final row indicates typical uncertainties.

Column 1: ‘PW’ indicates a pure wave case. ‘WC’ indicates a combined wave-current case. ‘PC’ indicates a pure current case.

Column 2: Case names. The wave condition (‘W’) was denoted 1 through 4 in order of increasing amplitude. The imposed current condition (‘C’) was denoted by 1 through 4 in order of increasing velocity. The number 0 indicated the absence of waves or imposed current. ‘S’ indicates shallower depth and ‘D’ indicates deeper depth.

Column 3: D is the water depth.

Column 4: $a_{w,0}$ is the wave amplitude measured at the meadow leading edge.

Column 5: T is the wave period.

Column 6: U_c is the time- and depth-averaged velocity measured upstream of meadow.

Column 7: U_1 is the time- and canopy-averaged velocity, which reflects both the current and wave-induced components.

Column 8: K_D is the wave decay coefficient reported with 95% confidence interval.

Type	Case	D (cm)	$a_{w,0}$ (cm)	T (s)	U_c (cm/s)	U_1 (cm/s)	K_D (1/m ²)
PW	W1C0S	27	0.9	2	0	0	4.4±0.4
PW	W2C0S	27	1.3	2	0	0.5	2.81±0.13
PW	W3C0S	27	1.8	2	0	1.9	2.11±0.08
PW	W4C0S	27	3.9	2	0	3.5	1.21±0.05
PC	W0C1S	27	0	N/A	4.0	0.7	N/A
PC	W0C2S	27	0	N/A	6.1	0.9	N/A
PC	W0C3S	27	0	N/A	8.2	1.5	N/A
PC	W0C4S	27	0	N/A	10.4	1.7	N/A
WC	W1C1S	27	0.9	2	4.0	1.0	3.7±0.6
WC	W1C2S	27	0.8	2	6.1	1.2	3.9±0.4
WC	W1C3S	27	0.6	2	8.2	1.3	3.9±0.5
WC	W1C4S	27	0.6	2	10.4	2.1	3.9±0.4
WC	W2C1S	27	1.3	2	4.0	1.6	2.60±0.10
WC	W2C2S	27	1.0	2	6.1	1.0	2.64±0.17
WC	W2C3S	27	0.9	2	8.2	1.6	2.6±0.3
WC	W2C4S	27	0.8	2	10.4	3.0	2.5±0.4
WC	W3C1S	27	1.8	2	4.0	2.1	1.89±0.10
WC	W3C2S	27	1.6	2	6.1	3.2	1.88±0.16
WC	W3C3S	27	1.6	2	8.2	2.9	1.99±0.16
WC	W3C4S	27	1.5	2	10.4	3.3	1.81±0.17

WC	W4C1S	27	3.9	2	4.0	5.9	1.26±0.07
WC	W4C2S	27	3.7	2	6.1	4.2	1.25±0.07
WC	W4C3S	27	3.6	2	8.2	4.3	1.23±0.08
WC	W4C4S	27	3.6	2	10.4	4.0	1.32±0.08
PW	W1C0D	45	1.0	2	0	-0.1	1.9±0.2
PW	W2C0D	45	1.9	2	0	1.0	0.79±0.04
PW	W3C0D	45	2.3	2	0	0.6	0.84±0.04
PW	W4C0D	45	4.1	2	0	2.1	0.56±0.03
PC	W0C1D	45	0	N/A	2.7	0.3	N/A
PC	W0C2D	45	0	N/A	4.1	0.3	N/A
PC	W0C3D	45	0	N/A	5.5	0.5	N/A
PC	W0C4D	45	0	N/A	6.8	0.7	N/A
WC	W1C1D	45	0.8	2	2.7	0.5	1.4±0.2
WC	W1C2D	45	0.7	2	4.1	0.4	1.4±0.2
WC	W1C3D	45	0.6	2	5.5	0.5	1.5±0.2
WC	W1C4D	45	0.6	2	6.8	0.8	1.71±0.10
WC	W2C1D	45	1.9	2	2.7	0.9	0.83±0.03
WC	W2C2D	45	1.8	2	4.1	0.9	0.83±0.03
WC	W2C3D	45	1.8	2	5.5	1.1	0.80±0.03
WC	W2C4D	45	1.7	2	6.8	1.5	0.86±0.03
WC	W3C1D	45	2.3	2	2.7	1.3	0.69±0.03
WC	W3C2D	45	2.2	2	4.1	1.5	0.70±0.02

WC	W3C3D	45	2.2	2	5.5	1.3	0.70±0.02
WC	W3C4D	45	2.1	2	6.8	1.2	0.73±0.02
WC	W4C1D	45	3.8	2	2.7	2.4	0.48±0.03
WC	W4C2D	45	3.4	2	4.1	2.8	0.51±0.02
WC	W4C3D	45	3.3	2	5.5	2.5	0.52±0.02
WC	W4C4D	45	3.2	2	6.8	5.4	0.53±0.02
Typical		0.2	0.1	0.02 s	5%	10-20%	
Uncertainties		cm	cm				

2.8.3 Accounting for current-induced modification of waves

Losada et al. (2016) used the energy density in combined wave-current conditions laid out in Longuet-Higgins & Stewart (1960) and expanded on in Baddour & Song (1990) to derive a wave decay coefficient in combined wave-current conditions,

$K_D = 2 \frac{A}{B}$, in which

$$A = \frac{2}{3\pi} \rho C_{D,wc} a_v a_{w,0} \left(\frac{gk}{2(\sigma - U_c k)} \right)^3 \frac{(\sinh(kl))^3 + 3 \sinh(kl)}{3k(\cosh(kD))^3} \quad (2.8.3.1)$$

and

$$B = \left(\frac{1}{4} \rho g C_g + \frac{1}{8} \rho g U_c \left(3 + \frac{4kD}{\sinh(2kD)} \right) + \frac{3}{8} \rho k U_c^2 \left(\frac{g}{k} \coth(kD) \right)^{\frac{1}{2}} \right) (U_c + C_g) \quad (2.8.3.2)$$

See the main text for variable definitions. Note that the Doppler shift modifies the wave number k in the presence of current. As indicated by the wave energy conservation described by Eqn. (2.11) in the main text, an increase in group velocity C_g due to a following current would be expected to decrease the spatial rate of meadow-induced energy dissipation. Conversely, a decrease in group velocity C_g due to opposing current would be expected to increase the spatial rate of meadow-induced energy dissipation.

If $C_g = \frac{1}{2} \left(1 + \frac{2kH}{\sinh(2kH)} \right) \left(\frac{g}{k} \tanh(kH) \right)^{\frac{1}{2}} \gg U_c$, the impact of the current on the group velocity is negligible, the terms in Eqns. (2.8.3.1) and (2.8.3.2) containing U_c drop out, and the wave decay coefficient simplifies to Eqn. (2.15) in the main text. In the present laboratory experiments, $C_g \gg U_c$ for all cases. When C_g and U_c are comparable, we propose using Eqns. (2.8.3.1) and (2.8.3.2) to predict wave decay coefficient, but replacing l with $l_{e,m}$ for a flexible meadow.

References

- Baddour, R. E., and S. Song. 1990. On the interaction between waves and currents. *Ocean Eng.* 17: 1–21, doi:10.1016/0029-8018(90)90011-T
- Longuet-Higgins, M. S., and R. W. Stewart. 1960. Changes in the form of short gravity waves on long waves and tidal currents. *J. Fluid Mech.* 8: 565–583, doi:10.1017/S0022112060000803
- Losada, I. J., M. Maza, and J. L. Lara. 2016. A new formulation for vegetation-induced damping under combined waves and currents. *Coast. Eng.* 107: 1–13, doi:10.1016/j.coastaleng.2015.09.011

2.8.4 Measured $K_{D,wc}$ as a function of Ca_{wc}

Wave and current conditions with greater total velocity (larger wave-current Cauchy number Ca_{wc}) produced greater blade reconfiguration and smaller values of wave decay coefficient ($K_{D,wc}$, Fig. 2.S.1). This was consistent with studies of pure waves, for which $K_{D,w}$ decreased with increasing wave Cauchy number Ca_w (Luhar et al., 2017). In addition, $K_{D,wc}$ was greater for the shallower depth $D = 27$ cm (open symbols in Fig. 2.S.1), reflecting that the meadow occupied a larger fraction of the water column. This dependence has also been noted for pure wave conditions (Anderson & Smith, 2014; Luhar et al., 2017; Stratigaki et al., 2011). The power fits to the shallower and deeper depth cases were $K_{D,wc} \sim Ca_{wc}^{-0.41 \pm 0.09}$ and $K_{D,wc} \sim Ca_{wc}^{-0.37 \pm 0.06}$, respectively. These dependences predominantly reflect changes in the effective meadow height. To show this, it is useful to consider a simplified version of Eqn. (2.16) in the main text. Specifically, since $kl_{e,m,wc}$ is small (less than 0.3), $\sinh(kl_{e,m,wc}) \approx kl_{e,m,wc}$. Grouping cases by water depth and wave period (T) fixes the wave number (k). In addition, the constant meadow density fixes α^3 and a_v . Then, the variation in wave decay coefficient is reduced to $K_{D,wc} \sim C_{D,wc} l_{e,m,wc}$. Recall that $l_e \sim Ca_{wc}^{-1/3}$ (Eqn. (2.8) in main text). Combining Eqns. (2.8) and (2.16) in the main text and assuming a constant drag coefficient, $K_{D,wc} \sim Ca_{wc}^{-0.33}$. Deviation from this scaling can be attributed to the drag coefficient $C_{D,wc}$, which can have a weak inverse dependence on velocity and thus Ca_{wc} . Specifically, $C_D \propto KC^{-1/3} \propto U_w^{-1/3} \propto Ca_{wc}^{-1/6}$. Combining with $l_e \sim Ca_{wc}^{-1/3}$, we anticipate $K_{D,wc} \sim C_{D,wc} l_{e,m,wc} \sim Ca_{wc}^{-1/2}$. The measured power-law dependence falls between the limits of -0.33 and -0.5, giving support to the effective meadow height as a predictor of the impact of reconfiguration on meadow drag and wave dissipation.

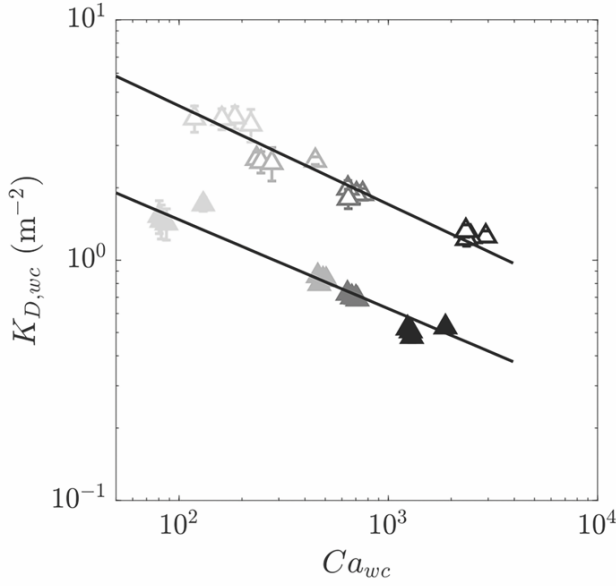


Figure 2.S.1: Measured wave damping coefficient $K_{D,wc}$ as a function of the wave-current Cauchy number Ca_{wc} for all wave-current cases. Larger wave amplitudes $a_{w,0}$ denoted with darker shades. Open and filled symbols denote water depths $D = 27$ cm and $D = 45$ cm, respectively. Solid black lines denote best fits for each depth.

Next, consider the wave attenuation parameter $K_D a_{w,0}$, which relates to the physical distance of wave attenuation $1/(K_D a_{w,0})$. Fig. 2.S.2 illustrates the dependence of $K_D a_{w,0}$ on wave amplitude at the leading edge of the meadow, $a_{w,0}$. To highlight the impact of reconfiguration, a prediction of $K_D a_{w,0}$ for pure waves propagating over a rigid meadow with the same characteristics is included for reference (dashed curves, based on Eqn. (2.15) in main text). Notably, wave attenuation for the flexible meadow (denoted by circles) was nearly an order of magnitude smaller than for a rigid meadow, highlighting the important role of reconfiguration.

Wave attenuation had a weak dependence on wave amplitude, the limits of which can be described as follows. In the limit of large wave velocity ($U_w \gg U_c$), $Ca_{wc} \sim C_D U_w^2 \sim a_{wc}^{5/3}$, such that $K_{D,wc} \sim C_D l_{e,m} \sim C_D Ca_{wc}^{-1/3} \sim a_w^{-0.9}$, which implies $K_D a_{w,0} \sim a_w^{0.1}$. In the limit of strong

current ($U_w \ll U_c$), $Ca_{wc} \sim U_c^2 \sim a_{wc}^0$, such that $K_{D,wc} \sim a_w^{-1/3}$ and $K_D a_{w,0} \sim a_w^{2/3}$. Consistent with this, the measured $K_D a_{w,0}$ showed a weak positive dependence on $a_{w,0}$.

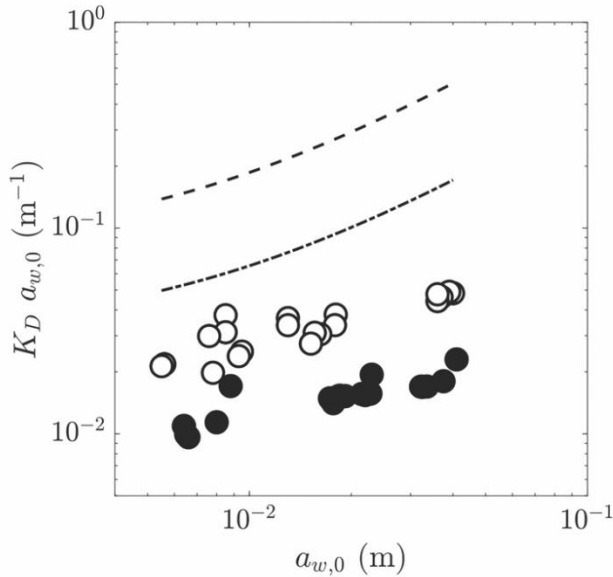


Figure 2.S.2: Measured wave decay coefficient multiplied by wave amplitudes at the leading edge, $K_D a_{w,0}$, versus wave amplitudes at the leading edge $a_{w,0}$. Open and filled symbols denote cases with water depths $D = 27$ cm and $D = 45$ cm, respectively. The dashed and dashed-dotted curves correspond to predicted $K_D a_{w,0}$ for a meadow consisting of rigid blades that cannot reconfigure, based on Eqn. (2.15) in main text and assuming pure wave conditions for water depths $D = 27$ cm and $D = 45$ cm, respectively.

References

- Anderson, M. E., and J. M. Smith. 2014. Wave attenuation by flexible, idealized salt marsh vegetation. *Coast. Eng.* 83: 82–92, doi:10.1016/j.coastaleng.2013.10.004
- Luhar, M., E. Infantes, and H. M. Nepf. 2017. Seagrass blade motion under waves and its impact on wave decay. *J. Geophys. Res. Ocean.* 122: 3736–3752, doi:10.1002/2017JC012731
- Stratigaki, V., E. Manca, P. Prinios, and others. 2011. Large-scale experiments on wave propagation over *Posidonia oceanica*. *J. Hydraul. Res.* 49: 31–43, doi:10.1080/00221686.2011.583388

2.8.5 Predicting the in-canopy time-averaged velocity

As a precursor to predicting the in-canopy time-averaged velocity U_1 (Eqn. (2.17) in main text), we first predict the deflected height of the canopy h_d . Lei & Nepf (2019) showed that the deflected height of an isolated blade in combined wave-current conditions followed the empirical relation for pure current provided in Eqn. (4) of Luhar & Nepf (2013). We modified this equation by including a sheath of height l_{sh} , and we neglected buoyancy effects (set the buoyancy parameter $B = 0$), which is appropriate for seagrass as discussed in the main text.

$$\frac{h_d - l_{sh}}{l_b} = 1 - \frac{1 - Ca_c^{-\frac{1}{4}}}{1 + 4Ca_c^{-\frac{3}{5}} + 8Ca_c^{-2}} \quad (2.8.5.1)$$

The depth-averaged current U_c would be the practical choice to define the current Cauchy number Ca_c in Eqn. (2.8.5.1), but U_1 was also considered. For the same U_c , the measured h_d showed variation with wave amplitude (Fig. 2.S.3(a)). In contrast, measured h_d collapsed to a single curve when plotted with measured U_1 . This made sense because the blades are predominantly exposed to U_1 . However, the measured h_d versus U_1 fell below predictions using Eqn. (2.8.5.1), which was based on studies of isolated blades. This reflects the influence of the shear layer at the top of the canopy, which exposes the top of the blades to velocities much higher than U_1 .

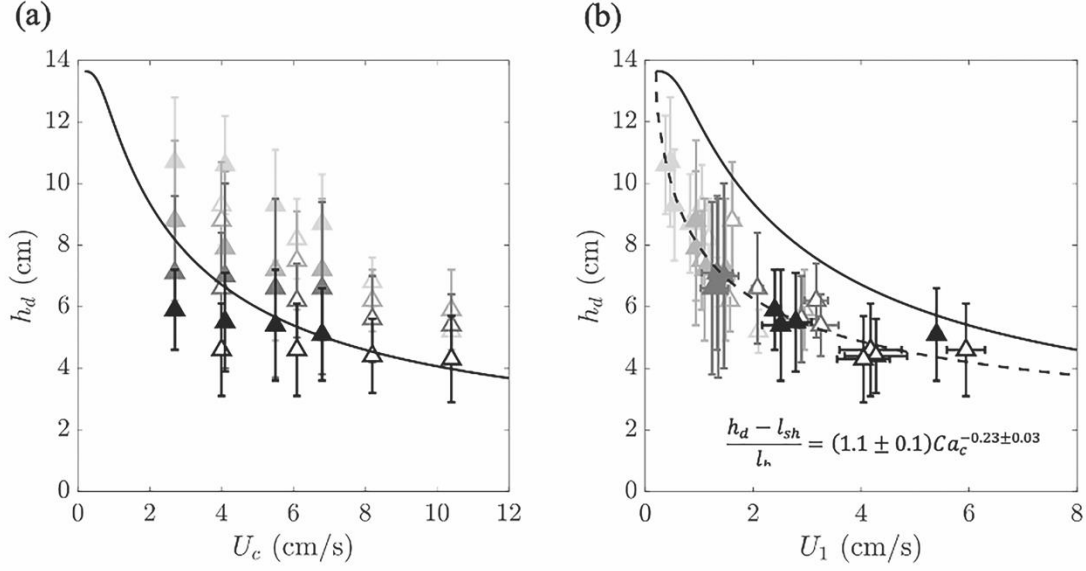


Figure 2.S.3: Measured deflected canopy height h_d as a function of (a) measured imposed depth-averaged current velocity U_c and (b) measured in-canopy time-averaged velocity U_1 . Larger wave amplitudes $a_{w,0}$ are denoted with darker shades. Open and filled symbols denote cases with water depths $D = 27$ cm and $D = 45$ cm, respectively. The solid black curves in (a) and (b) denote Eqn. (2.1). In (b) the dashed curve denotes the fit $\frac{h_d - l_{sh}}{l_b} = (1.1 \pm 0.1) C a_c^{-0.23 \pm 0.03}$. We caution that this relation may be valid only for the specific shoot density tested.

Next, considering only pure wave cases, the maximum wave-induced current \bar{U}_{max} predicted from Eqn. (2.18) in the main text, using $l_{e,m,w}$ from Eqn. (2.9) in the main text, agreed with measured \bar{U}_{max} within uncertainty, $\bar{U}_{max}(measured) = (1.2 \pm 0.1) \bar{U}_{max}(predicted)$. See Fig. 2.S.4(a). In addition, the canopy-averaged wave-induced current $U_{1,w}$, was shown to scale with \bar{U}_{max} . The subscript ‘w’ denotes the wave-induced current within the canopy. Using only pure wave cases, $U_{1,w}(measured) = (0.7 \pm 0.2) \bar{U}_{max}(predicted)$. Note that these fits could be different for other meadow densities.

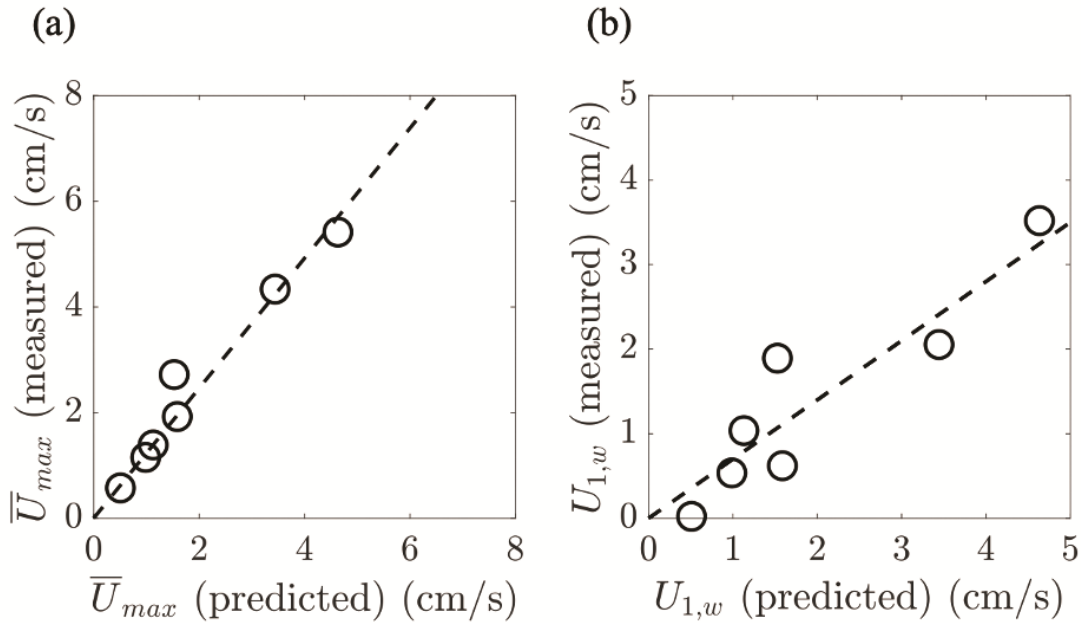


Figure 2.S.4: Measured versus predicted (a) maximum wave-induced current \bar{U}_{max} and (b) meadow-averaged time-averaged velocity $U_{1,w}$ for all pure wave cases. Dashed lines denote lines of best fit. Only positive values of $U_{1,w}$ are included.

References

- Lei, J., and H. M. Nepf. 2019. Blade dynamics in combined waves and current. *J. Fluids Struct.* 87: 137–149, doi:10.1016/j.jfluidstructs.2019.03.020
- Luhar, M., and H. M. Nepf. 2013. From the blade scale to the reach scale: A characterization of aquatic vegetative drag. *Adv. Water Resour.* 51: 305–316, doi:10.1016/j.advwatres.2012.02.002

Chapter 3

Movement of and drag force on slender flat plates in an array exposed to combinations of unidirectional and oscillatory flow²

Abstract:

When flexible structures deflect under unidirectional flow or sway under oscillatory flow, their hydrodynamic drag forces are reduced. The flow-induced motion of a structure is governed by the balance between hydrodynamic forces and restoring forces due to stiffness (a ratio known as the Cauchy number, Ca). Movement of and drag on structures under unidirectional (current) and oscillatory (wave) flow have often been studied separately, but such flows frequently coexist. In this study, a simple numerical model of a slender flexible plate, which can represent a seagrass blade, was used to investigate how the posture of and drag on the plate in oscillatory flow was

² This chapter was published as Schaefer and Nepf (2024).

impacted by collinear currents moving in the same (following) and opposite (opposing) directions, relative to the wave propagation. The rate of work done against hydrodynamic drag forces defines the rate of wave energy dissipation, $E_{D,w}$. The velocity acting on the blade was modeled as if the blade existed in a canopy of blades. For conditions in which blade motion was observed, added currents influenced $E_{D,w}$ in two ways. When the ratio of the time-averaged velocity within the canopy, U_1 , to the wave velocity amplitude, U_w , was less than 0.33 ± 0.05 , $E_{D,w}$ was reduced relative to the pure wave condition, which was attributed to current-induced deflection. However, when U_1/U_w exceeded 0.33 ± 0.05 , $E_{D,w}$ increased. While the blade increasingly deflected with increasing current, higher currents also limited wave-induced reconfiguration, increasing the relative motion between the blade and fluid and therefore increasing drag. While Ca can predict the drag reduction associated with weak current, it cannot predict the increase in drag for $U_1/U_w > 0.33$. Finally, the model was used to explore the influence of current on wave amplitude evolution across a seagrass meadow. Relative to pure wave conditions, opposing currents enhanced wave damping, but following currents had little impact on wave damping.

3.1 Introduction

The function of many natural structures is linked to their flexibility. For example, the flexibility of cilia can generate fluid flows (e.g., metachronal waves, Brumley et al., 2015); the flexibility of kelp fronds can reduce drag and enhance nutrient flux (e.g., Rominger and Nepf, 2014), and the flexibility of bird wings can enable flight control (e.g., Tobalske, 2007). The design of

biomimetic structures harnesses these functions for engineering purposes (e.g., magnetically actuated arrays of model cilia in Shields et al., 2010; kelp-inspired wave energy harvesters in Wang et al., 2019; air vehicles inspired by bird wings in Ward et al., 2015). The present study considered a slender flexible plate, which can, for example, represent an individual seagrass blade or cilium. A slender, flexible structure deflects under continuous unidirectional flow (current) and passively sways back and forth under oscillatory flow (waves). Current-induced deflection reduces drag by reducing the projected area and streamlining the object's shape (Gosselin, 2019; Vogel, 1984). The swaying motion under oscillatory flow reduces the relative velocity between the structure and the fluid, thereby reducing hydrodynamic forces (Bradley and Houser, 2009; Méndez and Losada, 1999; Mullarney and Henderson, 2010).

Understanding the structural response to flow, known as reconfiguration, and its impact on hydrodynamic forces is necessary to properly model natural flexible structures, such as plants, and to inform the design of bio-inspired structures. Natural systems are subjected to unidirectional flows, oscillatory flows, and combinations of the two. In unidirectional flow, the degree of bending in response to flow is governed by the balance between hydrodynamic forces and the restoring force due to the structure's stiffness (commonly represented by the dimensionless Cauchy number), and the balance between buoyancy and the restoring force due to stiffness (Alben et al., 2002; Luhar and Nepf, 2011). However, in the present study we do not consider buoyancy. In oscillatory flow, the ratio of the length of the structure to the excursion length of the fluid motion, e.g., the radius of a wave orbital, also influences the structure's motion and thus drag (Luhar and Nepf, 2016; Mullarney and Henderson, 2010). In combined conditions, reconfiguration depends on the relative magnitude of the unidirectional (current) and oscillating (wave) components.

Because reconfiguration influences drag, it influences the dissipation of wave energy. The dissipation of wave energy by coastal vegetation has recently drawn attention for its potential to provide nature-based coastal protection against flooding enhanced by storm waves. The numerical model presented in this study describes a generic flexible plate clamped at its base, but the parameters were mostly drawn from measured properties of seagrass blades for the purpose of using the model to investigate wave energy dissipation across a seagrass meadow. Seagrass meadows can be found on every continent except Antarctica (e.g., Unsworth et al., 2019) and therefore are exposed to a wide range of wave and current velocity magnitudes. Seagrasses provide a wide range of economically valuable ecosystem services (Costanza et al., 1997), which include coastal protection (e.g., Infantes et al., 2012), habitat for a myriad of species (e.g., Hemminga & Duarte, 2000), improved water quality (e.g., Fonseca & Fisher, 1986), and retention of sediment and organic carbon (e.g., Gacia et al., 2002). In particular, it is the ability of seagrass meadows to damp waves that enhances their ability to shelter other species and retain organic carbon (e.g., Koch, 2001). Protocols to quantify the value of these ecosystem services continue to evolve and would benefit from a quantitative physical model, such as developed in this study (e.g., Costanza et al., 2017; Liquete et al., 2013). Failure to account for the influence of current on seagrass-induced wave damping could misvalue the benefits of seagrass meadows. Therefore, the influence of current on wave energy propagation across seagrass meadows demands further investigation.

To properly quantify the reduction in wave energy achievable by vegetation, one must understand the role of reconfiguration under the range of combined wave-current conditions that exist in nature. Schaefer and Nepf (2022) demonstrated that the presence of a weak current travelling in the same direction as waves (known as a following current) decreased the wave

damping achieved by a model seagrass meadow, which they attributed to the current-induced reduction in frontal area of the individual seagrass blades. However, they only tested a limited range of wave-current conditions. The present study considered a wider range of conditions, including opposing currents (currents travelling in the opposite direction as the waves) and currents of greater magnitude, which revealed that the addition of current could either *increase* or *decrease* the rate of wave dissipation, depending on the ratio of wave to current velocity. Because the seagrass blade was modeled as a simple flexible plate, these results can be extended to other geometries of flexible structures in combined steady-unsteady flow conditions. We end by considering the implications for wave evolution across a seagrass meadow.

3.2. Reconfiguration of individual blades

The hydrodynamic drag experienced by a rigid body is commonly described using the quadratic drag law, $F_D = \frac{1}{2} C_D \rho u_r^2 A$, in which C_D is the drag coefficient, ρ is the density of the fluid, u_r is the relative velocity between the fluid and the object, and A is the area of the solid normal to the flow. However, if the structure is flexible and deforms, A will decrease in response to increasing u_r , and F_D will scale on u_r to a power weaker than 2 that depends on the geometry of the deformation (de Langre et al., 2012; Vogel, 1984). Past studies of flexible plants have described this drag reduction using modified drag coefficients calibrated for specific plants, keeping A as the undeflected area and u_r equal to the flow velocity (e.g., Kobayashi et al., 1993; Sand-Jensen, 2003). As an alternative to using a calibrated drag coefficient, Alben et al. (2002) introduced the concept of a bending length to describe how the competing effects of hydrodynamic forces and structural stiffness determine the degree of bending of a flexible fiber pinned at its midpoint.

Specifically, when the fiber deformed in unidirectional flow, the hydrodynamic drag was concentrated in a small section of the fiber near the midpoint, which was termed the bending length. The bending length depends on the dimensionless Cauchy number, which describes the competition between hydrodynamic drag and restoring force due to stiffness,

$$Ca = \frac{C_D \rho w_b l_b^3 u^2}{(2EI)}, \quad (3.1)$$

in which u is the characteristic velocity, E is the Young's modulus of elasticity, w_b is the characteristic width, l_b is the characteristic length, and I is the bending moment of inertia. If $Ca \ll 1$, stiffness dominates, and the structure does not reconfigure, while for $Ca > 1$ the extent of reconfiguration scales with Ca . Luhar and Nepf (2011) extended the work of Alben et al. (2002) to flexible plants, such as seagrass, and proposed the concept of an effective length, l_e , defined as the length of a rigid structure that induces the same horizontal drag force as a flexible structure of a given length, such that in the quadratic drag law $A = w_b l_e$. For a flexible structure of length l_b subjected to unidirectional flow,

$$l_e \sim l_b (Ca_c)^{-\frac{1}{3}}, \quad (3.2)$$

in which the subscript 'c' denotes that u in Eqn. 3.1 is the current velocity, defining the current Cauchy number, Ca_c . Refer to Luhar and Nepf (2011) for details of their experimental and modeling results. The effective blade length is generally smaller than the visible height of the deflected blade h_d , because the bent blade has a more streamlined shape than the rigid equivalent (Figure 3.1a).

While the balance between hydrodynamic drag and blade stiffness dictate reconfiguration in unidirectional flow, when considering oscillatory flow an additional inertial force due to flow

acceleration must also be considered (Morison et al., 1950). The relative importance of drag and inertial forces in oscillatory flow is represented by the Keulegan-Carpenter number, $KC = U_w T / w_b$, in which U_w is the wave velocity amplitude and T is the wave period (Keulegan and Carpenter, 1958). In general, for $KC \gg 1$, drag dominates, and for $KC \ll 1$, inertia dominates. For many slender (small w_b) flexible structures such as seagrass, KC has been observed to be much greater than 1, such that inertia may be neglected. Assuming $KC \gg 1$, Mullarney and Henderson (2010) proposed a model for the reconfiguration of flexible beams subjected to oscillatory flow. Their model, which assumed the beam experienced only small deflections (deflections much smaller than the beam length), showed that relative motion and therefore drag is concentrated within a thin region near the bed known as the elastic boundary layer. Luhar and Nepf (2016) extended the model in Mullarney and Henderson (2010) to describe the effective length in oscillatory flows. Specifically, when the horizontal wave excursion $A_w = U_w T_w / (2\pi)$ is less than the blade length (illustrated in Figure 3.1b), the horizontal excursion of the blade tip will be comparable to the orbital excursion, such that the blade bending angle can be related to wave excursion. Under these conditions, the balance of hydrodynamic drag and restoring force due to stiffness yields the scaling

$$l_e \sim l_b (Ca_w L)^{-\frac{1}{4}} \quad (3.3)$$

in which $L = 2\pi l_b / (U_w T_w)$ is the ratio of the blade length to the wave orbital excursion. The ‘w’ subscript denotes that u in Eqn. 3.1 is the wave velocity, defining the wave Cauchy number, Ca_w . Consistent with this, Lei and Nepf (2019b) used force measurements on individual blades to show that $l_e = 1.1 l_b (Ca_w L)^{-1/4}$. In contrast, when the horizontal wave excursion is much greater than the blade length ($L \ll 1$), the blade will reach its full extension early within each

half-cycle of the wave period, resembling its response to steady flow for most of the wave cycle, such that the scaling from Eqn. 3.2 is recovered, but with the Cauchy number defined by the wave velocity. Specifically, $l_e/l_b \sim Ca_w^{-1/3}$ (Luhar & Nepf, 2016; Lei and Nepf 2019a).

In combined wave-current conditions (Figure 1c), Lei and Nepf (2019a) suggested that the characteristic velocity u be defined by the time-averaged drag, which is proportional to $u^2 = U_1^2 + \frac{1}{2}U_w^2$, resulting in a wave-current (' wc ') Cauchy number Ca_{wc} using $u = \sqrt{U_1^2 + \frac{1}{2}U_w^2}$ in Eqn. 3.1, in which U_1 is the time-averaged velocity. Lei and Nepf (2019a) observed through laboratory experiments and numerical modeling of the absolute mean force on a blade that across a range of current-to-wave velocity ratios, $0 < U_1/U_w < 4$, the measured effective length followed the relationship

$$\frac{l_e}{l_b} = 0.9 Ca_{wc}^{-\frac{1}{3}}. \quad (3.4)$$

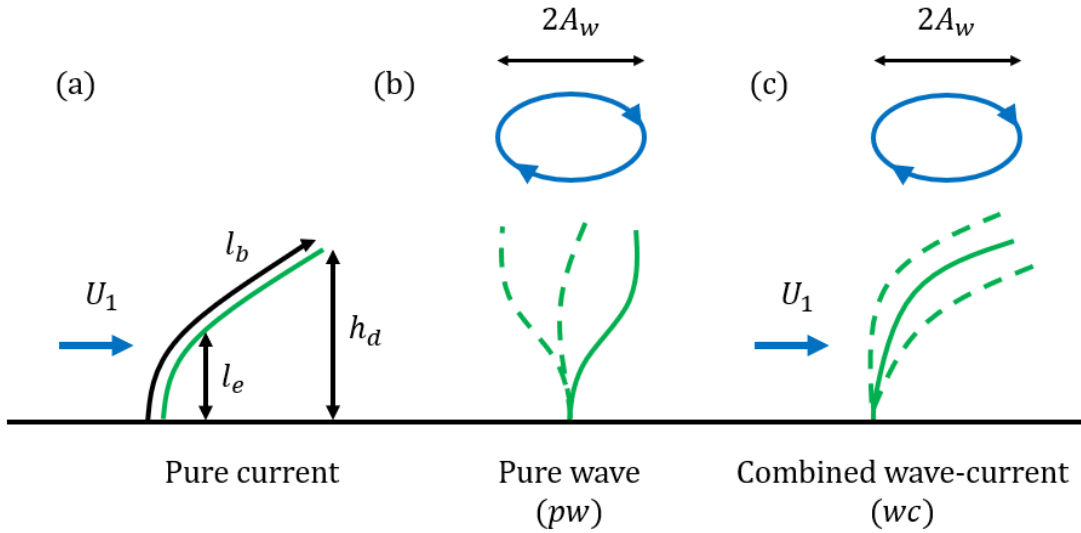


Figure 3.1: Depictions of blade reconfiguration under (a) pure current (unidirectional flow); (b) pure wave (oscillatory flow); and (c) combined wave-current conditions. The curved green lines represent a flexible blade clamped at the base. In (a) and (c), the blade experiences a time-averaged velocity U_1 . In (b) and (c), the blade experiences a wave velocity with amplitude U_w , and a wave orbital with diameter $2A_w = 2U_w T / (2\pi)$, depicted with blue circles. The differences between the blade length l_b , deflected blade height h_d , and effective blade length l_e are illustrated in (a).

3.3 Modeling Framework

3.3.1 Blades within a canopy

Section 3.2 reviewed the reconfiguration of isolated blades. In this study, the reconfiguration of blades is examined in a more natural context, i.e., within a canopy of identical blades (Figure 3.2). Fonseca et al. (1982) observed that seagrass plants only survive within meadows of a minimum size and suggested that the size was dictated by the meadow's ability to reduce the hydrodynamic stress felt by the individual plants. This community benefit is known as ecosystem engineering (e.g., Jones et al., 1994; Licci et al., 2019). An array formation (canopy) changes the

hydrodynamic exposure (waves and currents) of constituent individual structures (blades). We will use the flow conditions within the canopy to drive our blade reconfiguration model.

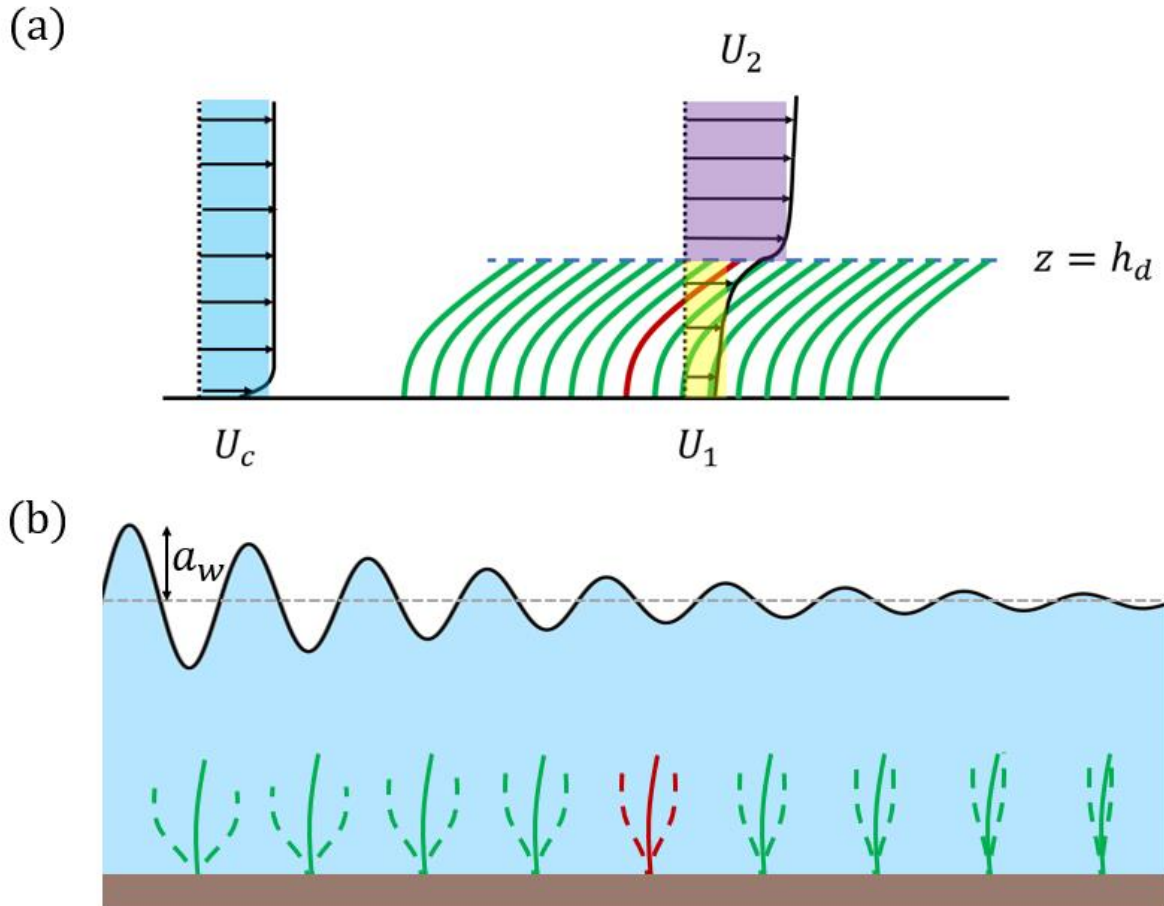


Figure 3.2: (a) Idealized vertical profiles of velocity upstream of and within a canopy of slender, flexible structures, such as a seagrass meadow, under unidirectional flow. Individual blades are represented by solid green lines. The mean deflected height of the canopy, $z = h_d$, defines the interface between two layers of different time-averaged velocity, with $U_{1,c}$ (yellow shading) and $U_{2,c}$ (purple shading) within and above the canopy, respectively. The depth-averaged velocity is U_c (blue shading). (b) The amplitude a_w of the wave decreases as the wave propagates across a canopy of blades. Each set of three curved green lines represents the range of individual blade position during a wave period. The numerical blade model simulates one blade (denoted by the red element in (a) and (b)) within an array of similar elements.

In a terrestrial or submerged canopy subjected to unidirectional flow, the canopy drag results in a time-averaged velocity above the canopy that is larger than the time-averaged velocity within the canopy (e.g., Raupach et al., 1996). For modeling purposes, the vertical profile of velocity is divided into a canopy layer with vertically-averaged velocity $U_{1,c}$ and an above-canopy layer with vertically-averaged velocity $U_{2,c}$ (e.g., Huthoff et al., 2007), as illustrated in Figure 3.2a. Based on continuity and layer-averaged momentum, the canopy velocity in pure current can be defined in terms of the depth-averaged current U_c (Eqn. 21 in Chen et al. for rigid canopies, 2013; Eqn. 2.30 in Lei & Nepf, 2021 for flexible canopies) as

$$U_{1,c} = \frac{U_c}{1 - \frac{h_d}{D} \phi + \sqrt{\frac{C_D n_b w_b l_e}{2C(1-\phi)} \left(\frac{D-h_d}{D}\right)^3}}, \quad (3.5)$$

in which D is the water depth, h_d is the mean deflected canopy height, ϕ is the element solid volume fraction, and n_b is the number of blades per bed area, each with width w_b (Chen et al., 2013; Lei and Nepf, 2021). The length scale δ_e represents the vertical distance from the top of the canopy over which turbulent momentum flux impacts in-canopy momentum. The coefficient $C = K_c(\delta_e/D)^{1/3}$ is the friction coefficient for the turbulent stress at the top of the canopy.

When $D/h_d > 2$, $\delta_e = 0.23(C_{D,c} a_v)^{-1}$ (Nepf et al., 2007), and otherwise $\delta_e =$

$0.23 \left(\frac{D}{h_d} - 1\right) (C_{D,c} a_v)^{-1}$ (Chen et al., 2013). Chen et al. (2013) estimated the empirical factor

$K_c = 0.07 \pm 0.02$.

A key result from Eqn. 3.5 is $\frac{U_{1,c}}{U_c} < 1$, i.e., the grouping of structures into a canopy decreases the steady velocity experienced by the structures within the canopy ($U_{1,c}$) compared to the velocity experienced by isolated structures (U_c). In contrast, for purely oscillatory flow, the

wave velocity in a submerged canopy compared to that above the canopy is generally not reduced to the same degree as the current velocity (Lowe et al., 2005), and specifically for seagrass canopies, the reduction is negligible (see Table 3.3 in Luhar et al., 2010). However, as waves propagate across a canopy, they lose energy to the work done against the canopy drag, such that the wave velocity decreases with distance over the meadow (Dalrymple et al., 1984; Figure 3.2b). Thus, a meadow of sufficient size can reduce both the steady and unsteady fluid forces on structures within a canopy, increasing their chance of survival.

For this study, the wave velocity experienced by a single blade within the canopy was described using linear wave theory, for which the horizontal wave orbital velocity is

$$u_w(t, z) = \frac{2\pi a_w}{T_w} \frac{\cosh(kz)}{\sinh(kD)} \sin\left(\frac{2\pi}{T_{wc}} t\right), \quad (3.6)$$

in which a_w is the wave amplitude, k is the wave number, t is time, z is the height above the bed, and $T_{wc} = 2\pi/T_w + kU_c$ is the apparent wave period experienced by the blade in the presence of current (Peregrine and Jonsson, 1983). When defining Cauchy numbers, the characteristic wave velocity amplitude U_w was defined by Eqn. 3.6 at the full height of the blade, $z = l_b$.

The interaction of a wave with a meadow also generates a time-averaged current. Specifically, canopy drag produces a nonzero correlation between horizontal and vertical components of wave velocity, generating a wave stress that drives a mean current within the canopy, which has its maximum magnitude near the time-averaged deflected height of the canopy (Luhar, 2021; Luhar et al., 2010). Luhar (2021) derived and validated a prediction for the

maximum wave-induced current, which Schaefer and Nepf (2022) converted to a prediction of canopy-averaged wave-induced current,

$$U_{wic} = (0.5 \pm 0.2) U_w \sqrt{\frac{n_b w_b k l_e T_w}{2\pi}} U_w, \quad (3.7)$$

in which T_w is the wave period. For simplicity, in defining the canopy-averaged velocity, the impact of time-varying reconfiguration on the canopy height was neglected.

3.3.2 Blade model setup

The motion of and forces acting along individual blades was evaluated using a two-dimensional slender blade model (Figure 3.3), as presented in Luhar and Nepf (2016) and adapted in Lei and Nepf (2019a). A fixed $x - z$ coordinate system represents the horizontal and vertical dimensions, respectively, with the origin defined at the clamped end (base) of the blade. The coordinate s aligned with the blade, with $s = 0$ at the base and $s = l_b$ at the tip. Using complex notation, the position along the blade was defined as $\tilde{x} = x(s) + iz(s)$, in which $i = \sqrt{-1}$. The blade was assumed to have a constant width w_b , thickness t_b , material density ρ_v , Young's modulus of elasticity E , and bending moment of inertia $I = w_b t_b^3 / 12$ along its length. The aspect ratio was $l_b \gg w_b \gg t_b$. Curvature along the length of the blade was defined by the angle with the vertical axis $\theta(s)$. The blade motion and hydrodynamic forces predicted by the numerical model were previously validated by laboratory measurements for pure wave, pure current, and combined wave-current conditions (Lei and Nepf, 2019b; Luhar and Nepf, 2016).

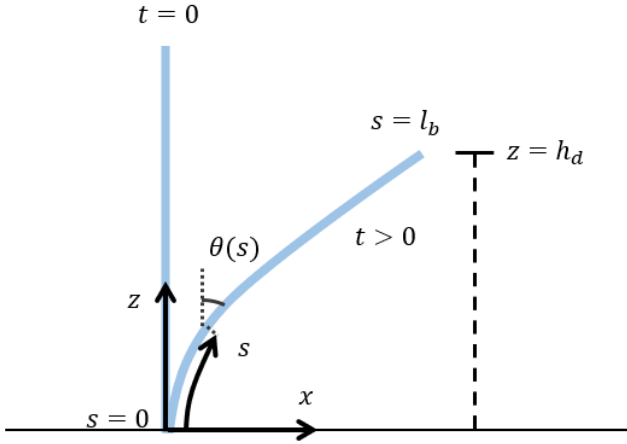


Figure 3.3: Schematic of numerical blade model. x and z are fixed horizontal and vertical coordinates, respectively. s is the position along the blade, with $s = 0$ at the bed where the blade is clamped. θ is the angle of the blade with the z -axis. The blade begins in an upright posture at time $t = 0$. h_d is the mean deflected blade height.

The model blade was exposed to a velocity field as if it existed within a canopy of identical blades, as discussed in section 3.3.1 and Figure 3.2. Specifically, the velocity field consisted of three components: the current ($U_{1,c}$, as in Eqn. 3.5), the wave velocity (Eqn. 6), and the wave-induced current U_{wic} (Eqn. 3.7):

$$\tilde{u}(t, z) = U_{1,c} + U_{wic} + u_w(t, z) = U_1 + u_w(t, z). \quad (3.8)$$

To simplify the notation, we defined $U_1 = U_{1,c} + U_{wic}$ as the total time-averaged velocity in the canopy. The simulated blade was divided into 1024 evenly spaced segments along its length, and the time evolution was divided into 60 time-steps per second. These increments were chosen to optimize the balance between model convergence and computation time. The model solved the force balance for each blade segment in each time step. Table 3.1 lists the vertical and horizontal forces, using Euler's rule $e^{i\theta} = \cos(\theta) + i \sin(\theta)$ to represent the force direction.

Table 3.1. Forces included in simulation of blade motion, defined per unit length of blade (see Figure 3.3, and Luhar and Nepf, 2016). \Re indicates the real component. \Im indicates the imaginary component. The relative velocity $\tilde{u}_r = \tilde{u} - \partial x / \partial t$. C_F ($= 0.1$) and C_M ($= 1$) are the skin friction and added mass coefficients, respectively, following Luhar and Nepf (2016).

Term	Description
$F_D = \frac{1}{2} C_D \rho w_b \Re(\tilde{u}_r e^{i\theta}) \Re(\tilde{u}_r e^{i\theta})$	Form drag force
$F_{SF} = \frac{1}{2} C_F \rho w_b \Im(\tilde{u}_r e^{i\theta}) \Im(\tilde{u}_r e^{i\theta})$	Skin friction force
$F_B = (\rho - \rho_v) g w_b t_b$	Net buoyancy force
$F_{FK} = \rho w_b t_b \frac{\partial \tilde{u}}{\partial t}$	Froude-Krylov force
$F_{AM} = \frac{\pi}{4} C_M \rho w_b^2 \Re\left(\frac{\partial \tilde{u}_r}{\partial t}\right)$	Added mass force
$V = -\frac{\partial}{\partial s} \left(EI \frac{\partial \theta}{\partial s} \right)$	Shear force (internal)
T	Tension (internal)

The force balance per unit blade length is (e.g., Luhar and Nepf 2016)

$$\frac{\partial}{\partial s} \left((V + iT) e^{-i\theta} \right) + iF_B + (F_D + iF_F + F_{AM}) e^{-i\theta} + F_{FK} = \rho_v w_b t_b \frac{\partial x^2}{\partial t^2}. \quad (3.9)$$

Multiplying Eqn. 3.9 by $e^{i\theta}$ rotates the forces such that the real part is the blade-normal force balance, and the imaginary part is the blade-parallel force balance. Eqn. 3.9 was solved across discretized space using a central finite-difference scheme of second-order accuracy, and across discretized time using a forward Euler method of first-order accuracy. The blade tension force was solved using a backward difference method applied to the blade-parallel component of the force balance. See Appendix C of Luhar (2012) for further details of the numerical procedures. Each condition was simulated for ten wave periods, which was enough time for the blade to converge to a consistent behavior throughout a wave period.

Luhar and Nepf (2016) used drag coefficients measured for rigid plates in Keulegan and Carpenter (1958) and Graham (1980) to produce an empirical description of the time-averaged wave drag coefficient $C_{D,w} = \max(10KC^{-\frac{1}{3}}, 1.95)$. For $KC > 25$, the combined wave-current drag coefficient converges with the pure wave drag coefficient (Sarpkaya and Storm, 1985). As $KC > 60$ for cases explored in this study, we assumed $C_{D,wc} = C_{D,w}$. Further, we assumed the drag coefficient was constant along the blade length. Following Luhar and Nepf (2016), we defined $C_M = 1$ and $C_F = 0.1$. We used a material density $\rho_v = 700 \text{ kg/m}^3$, based on measured material densities of *Zostera marina* seagrass blades (Abdelrhman, 2007).

One of the objectives of this study was to use the blade model to predict wave energy dissipation across a canopy of flexible structures (such as seagrass) in combined wave-current conditions. As mentioned in section 3.3.1, the decay in wave amplitude across a meadow is the result of work done against vegetation drag, which was assumed to be dominated by the blade-normal drag force, F_D , which is a reasonable assumption for $KC > 1$ (see discussion in Section 3 of Lei & Nepf, 2019). For a meadow of n_b blades per unit bed area, the rate of work done (energy extracted) by the meadow, $E_{D,total}$, was calculated by integrating the product of the drag force, F_D , and the velocity along the blade length and through a wave period:











$$E_{D,total} = \frac{n_b}{T} \int_{t=0}^T \int_{s=0}^{l_b} F_D \tilde{u} ds dt . \quad (3.10)$$

Only the horizontal component of the drag force was used in Eqn. 10, consistent with previous studies (e.g., Lei & Nepf, 2019b; Luhar et al., 2017). The vertical component of was consistently small relative to the horizontal component. The rate of work done by drag can be divided into oscillatory and steady components, $E_{D,total} = E_D + E_{D,c}$ (Li and Yan, 2007; Zhang and Nepf,

2021). Following the validation in Li and Yan (2007), the steady component was assumed to equal the time-averaged drag, $\overline{F_D}$, multiplied by the time-averaged velocity, $E_{D,c} = U_1 \int_{s=0}^{l_b} \overline{F_D} ds$.

A variety of cases was simulated to represent a range of stiffness, wave velocity, and current velocity parameters. For each set of runs, the wave amplitude was held constant, and the imposed current was varied. Maximum wave and current conditions were constrained by model convergence. Larger wave and current velocities led to numerical instability and model blow-up. Specifically, we only considered conditions for which the simulation produced stationary blade behavior over multiple wave periods. Three meadow blade densities were considered, $n_b = 1200$, 2500, and 3800 blades/m², chosen from common blade densities in coastal vegetation (e.g., (e.g., James et al., 2004, 2008; Olesen & Sand-Jensen, 1994; Orth & Moore, 1986). Further details of the cases described in this study are shown in Table 3.2.

Table 3.2: Test case conditions defined by wave amplitude a_w , wave velocity amplitude U_w , blade thickness t_b , Young's modulus of elasticity E , blade stiffness EI , wave Cauchy number Ca_w , and the ratio of the blade length l_b to the wave orbital excursion $L = 2\pi l_b / (U_w T_w)$. For all cases, the blade width $w_b = 0.33$ cm, the blade length $l_b = 13$ cm, the water depth $D = 45$ cm, and the wave period $T_w = 2$ s. The depth-to-blade length ratio was $D/l_b = 3.5$. The imposed current velocity $U_{1,c}$ ranged from 0.025 cm/s to 30 cm/s. Three meadow blade densities n_b were used: 1200, 2500, and 3800 blades/m². The symbols shown in this table correspond to the symbols used throughout the figures.

Case/ Symbol	a_w (cm)	U_w (cm s ⁻¹)	t_b (mm)	E (kg m ⁻¹ s ⁻²)	EI (kg m ³ s ⁻¹)	Ca_w	L
B1 	2.5	10	0.075	$2.4 \cdot 10^8$	$2.8 \cdot 10^{-8}$	3400	4.1
B2 	2.5	10	0.084	$2.4 \cdot 10^8$	$3.9 \cdot 10^{-8}$	2400	4.1
B3 	2.5	10	0.1	$2.4 \cdot 10^8$	$6.6 \cdot 10^{-8}$	1400	4.1
B4 	2.5	10	0.15	$2.4 \cdot 10^8$	$2.2 \cdot 10^{-7}$	420	4.1
B5 	2.5	10	0.2	$2.4 \cdot 10^8$	$5.3 \cdot 10^{-7}$	180	4.1
B6 	2.5	10	0.25	$2.4 \cdot 10^8$	$1.0 \cdot 10^{-6}$	91	4.1
B7 	2.5	10	0.3	$2.4 \cdot 10^8$	$1.8 \cdot 10^{-6}$	53	4.1
B8 	2.5	10	0.4	$2.4 \cdot 10^8$	$4.2 \cdot 10^{-6}$	22	4.1
B9 	5	20	0.2	$1.8 \cdot 10^8$	$4.0 \cdot 10^{-7}$	750	2.0
B10 	7.5	30	0.3	$2.4 \cdot 10^8$	$1.8 \cdot 10^{-6}$	360	1.4

3.3.3 Model limitations

The numerical model balanced simplicity, accuracy and computational expense. Several complexities were neglected. First, the model did not account for blade-blade interaction within a canopy. Under waves, seagrass blades are generally in synchronous motion, which naturally reduces blade-to-blade contact and its influence on blade motion (see the discussion in Lei and

Nepf, 2019b). Second, the model does not account for vortex shedding or vortex-induced vibrations, which may be important when the wave-current Cauchy number approaches 1, and the restoring force due to stiffness becomes more comparable to the hydrodynamic forcing (see Luhar & Nepf, 2016). Vortex generation and stability would likely be a function of the relative current and wave strengths (Zhou and Graham, 2000). Third, only collinear waves and currents were considered, which is representative of locally wind-generated currents and waves. However, conditions with waves and current obliquely oriented to each other also occur in the field, which would produce more complex reconfiguration. Field studies of kelp showed that oblique wave-current incidence angles may cause the kelp to spend less time in a fully extended position during a wave period, and may therefore reduce drag forces (Gaylord et al., 2003). Finally, the model blade has a uniform, rectangular cross-section. The structural cross-section influences the drag coefficient C_D and the bending moment of inertia I , which would be reflected in the specific Cauchy numbers, which could influence the extension of results to other plant morphology. However, this does not impact comparisons between wave-current and pure wave cases with the same geometry, as done in this study.

3.4 Results and Discussion

3.4.1 Blade reconfiguration and relative velocities

Blade reconfiguration influences the relative velocity between the blade and fluid, which determines the magnitude of the hydrodynamic drag force (F_D). Because the blade was clamped at the bed, which enforced zero blade motion at the bed, the relative velocity between the blade

and fluid was maximum at the bed. For example, consider the relative velocity in case B3 ($U_w = 10$ cm/s, $Ca_w = 1400$), shown in Figure 3.4 with selected following currents of 0, 1, 5, and 15 cm/s. The highest relative velocities occurred at the bed and were associated with the wave phase with the maximum total velocity $U_1 + U_w$, which occurred when the blade was at its maximum extension. For reference, the posture of the blade corresponding to the wave phase with the highest (dotted curves) and lowest (solid curves) relative velocity are shown in the top row of Figure 4. Relative velocities are shown as absolute values for easier visualization of magnitude, and are normalized by the wave velocity amplitude. The minimum relative velocity occurred at the minimum total velocity $U_1 + u_w$ when the blade was recovering from its maximum extension.

The portion of the blade with higher relative velocities (and therefore higher drag) initially decreased with increasing current velocity (note the decreasing heights of the green contours from Figure 3.4a-c), but at the highest current velocity (Figure 3.4c and 3.4d) showed little additional change. However, the peak magnitude of relative velocity, and therefore drag, continued to increase (blue and pink colors appearing in Figure 3.4d).

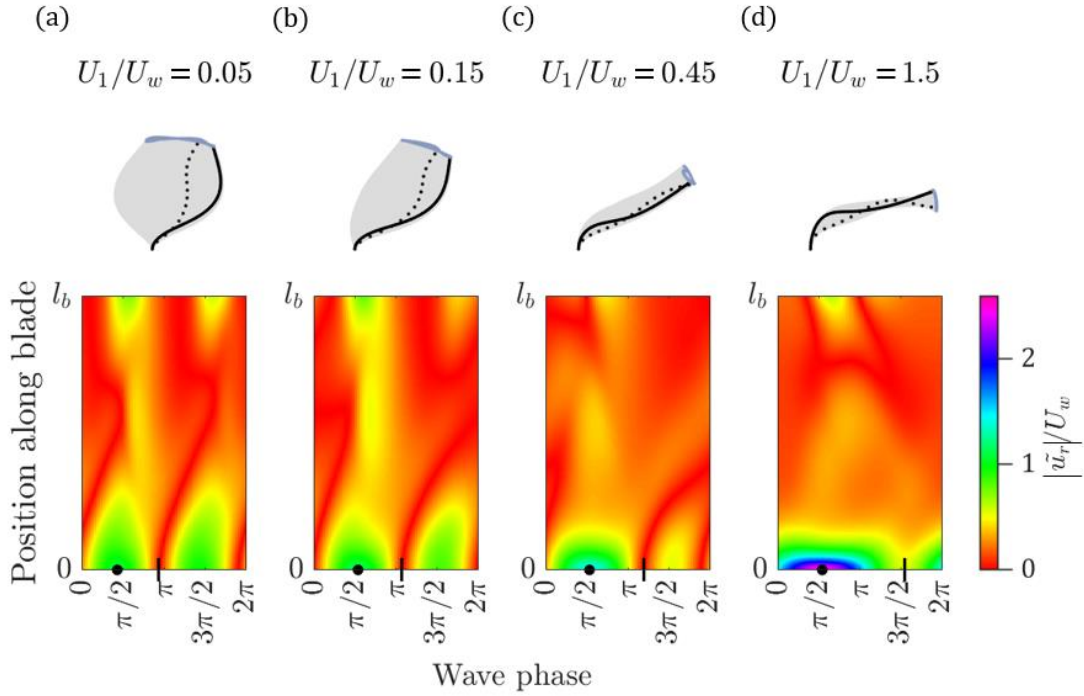


Figure 3.4: Case B3 ($Ca_w = 1400$) with following currents and a meadow of 2800 blades per square meter. Reconfiguration of the blade through a wave period (grey shading), and blade posture corresponding to the highest (dotted curves) and lowest (solid curves) relative velocity are shown in the top row. The corresponding heat maps indicate absolute value of relative velocity normalized by wave velocity amplitude $|\tilde{u}_r|/U_w$ for (a) pure waves, associated with wave-induced current $\frac{U_1}{U_w} = 0.05$; and cases with imposed currents (b) $\frac{U_1}{U_w} = 0.15$; (c) $\frac{U_1}{U_w} = 0.45$; (d) $\frac{U_1}{U_w} = 1.5$. The dot and line markers along the x-axes correspond to the phase with highest (dots) and lowest (vertical lines) relative velocity. Blade postures were rescaled for clarity of detail. The light blue curves in the blade posture plots trace the paths of the blade tips.

Next consider the stiffer blade (lower Ca_w) in case B7 ($Ca_w=53$, Figure 5), which had the same wave amplitude as case B3, but the blade was three times as thick, resulting in a bending moment of inertia (I) twenty-seven times higher than case B3. As expected, the motion of the blade was more restricted, resulting in larger portions of the blade length experiencing high relative velocity, compared to case B3 (compare the green contours in Figures 3.4 and 3.5).

In addition, with the stiffer blade (B7), the fraction blade length experiencing high relative velocity (green to pink shading) did not decrease with the addition of current, as it did for case B3.

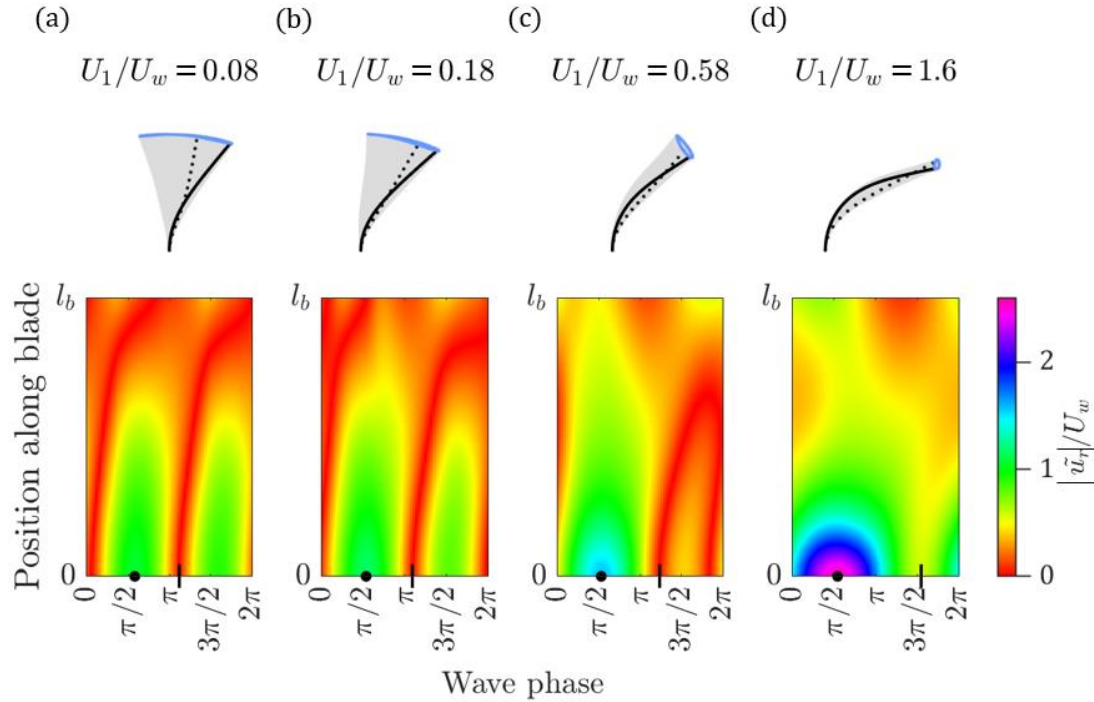


Figure 3.5: Case B7 ($Ca_w = 53$) with following currents and a meadow of 2800 blades per square meter. Reconfiguration of the blade through a wave period (grey shading), and blade posture corresponding to the highest (dotted curves) and lowest (solid curves) relative velocity are shown in the top row. The corresponding heat maps indicate absolute value of relative velocity normalized by wave velocity amplitude $|\tilde{u}_r|/U_w$ for (a) pure waves, but with wave-induced current $\frac{U_1}{U_w} = 0.08$; (b) $\frac{U_1}{U_w} = 0.18$; (c) $\frac{U_1}{U_w} = 0.58$; (d) $\frac{U_1}{U_w} = 1.6$. The dot and line markers along the x-axes correspond to the phase with highest (dots) and lowest (vertical lines) relative velocity. Blade postures were rescaled for clarity of detail. The light blue curves in the blade posture subplots trace the paths of the blade tips.

As the time-averaged velocity (U_1) increased, two changes to blade reconfiguration were observed, which had opposing impacts on the hydrodynamic drag. First, as the time-averaged

velocity increased, the time-averaged pronation of the blade increased (Figures 3.4 and 3.5), which tended to reduce the instantaneous force on the same segment of the blade. Second, as the time-averaged velocity increased, the degree of wave-following reconfiguration decreased. This is illustrated by the reduction in the distance traced by the blade tips (blue curve in blade posture insets in Figures 3.4 and 3.5), resulting in higher relative velocities and drag forces. The tension imposed by the current constrained the motion of the blade and inhibited its ability to follow the wave velocity field.

The time-averaged blade pronation increased (associated with a decreasing h_d) with increasing time-averaged velocity in a manner consistent with Eqn. 3.2. Specifically, the ratio of h_d to blade length l_b decreased with increasing Cauchy number Ca_{c,U_1} (Figure 3.6a), and for $Ca_{c,U_1} > 100$, $h_d/l_b = (3.4 \pm 0.9)(Ca_{c,U_1})^{-0.38 \pm 0.03}$, similar to the scaling for l_e/l_b in Eqn. 2. Between $Ca_{c,U_1} = 1$ to 100, mean pronation was also a function of wave Cauchy number (Ca_w in color bar), with greater deflection associated with greater Ca_w . The two largest wave amplitudes (B9 and B10, see Table 3.2) were separated into Figure 3.6b, because of the greater influence of the waves on mean deflected height, i.e., the deflected height decreased more rapidly with increasing Ca_{c,U_1} (compare subplots 3.6a and 3.6b). This was due to the greater impact of the vertical component of the wave orbital velocities on blade motion. Specifically, the downward velocity following the crest contributed to the reduction in mean deflected height (see the discussions in Döbken, 2015 and Gijón Mancheño, 2016). For these cases, a tendency toward $h_d/l_b \sim Ca_{c,U_1}^{-1/3}$ at large Ca_{c,U_1} was suggested (see inset line), but not captured within the range of conditions considered.

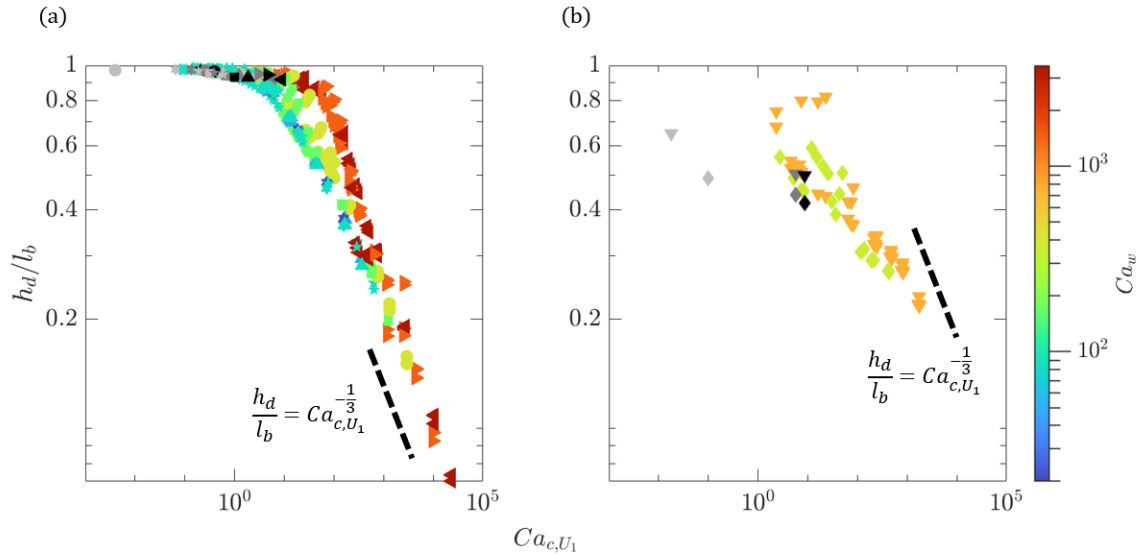


Figure 3.6: The ratio of mean deflected height h_d to full blade length l_b versus the current Cauchy number Ca_{c,U_1} for (a) cases B1-B8 and (b) cases B9 and B10. The color represents the wave Cauchy number Ca_w (note the color bar is in log scale). Grayscale markers denote pure wave cases (light gray symbols denote the lowest canopy density of 1200 blades m^{-2} , the dark gray symbols denote 2500 blades m^{-2} , and the black symbols denote 3800 blades m^{-2}). See Table 3.2 for symbol shape definitions.

As illustrated with the blade postures shown in Figures 3.4 and 3.5, with increasing current velocity there was a transition from unsteady reconfiguration (left-most blades in Figures 3.4 and 3.5) to steady reconfiguration (right-most blades in Figures 4 and 5). This transition can be quantified using the horizontal excursion of the blade tip, defined as $|x_{b,max} - x_{b,min}|$ (e.g., Luhar & Nepf, 2016), in which the subscripts ‘ b,max ’ and ‘ b,min ’ denote the maximum and minimum x positions reached by the blade tip in a wave period, respectively (Figure 3.7). Traces of the blade tip over a wave cycle are also shown in Figure 3.7, set near the blade excursion (symbols), for cases B3 (Figure 3.4) and B7 (Figure 3.5). The blade motion dropped off rapidly between pure wave conditions (denoted by red markers in Figure 3.7) and $U_1/U_w \approx 0.8$, and then leveled off to a nearly stationary condition (i.e., negligible blade motion) at higher current

magnitudes. This shift to an effectively stationary blade was associated with an increase in relative velocity (Figures 3.4 and 3.5).

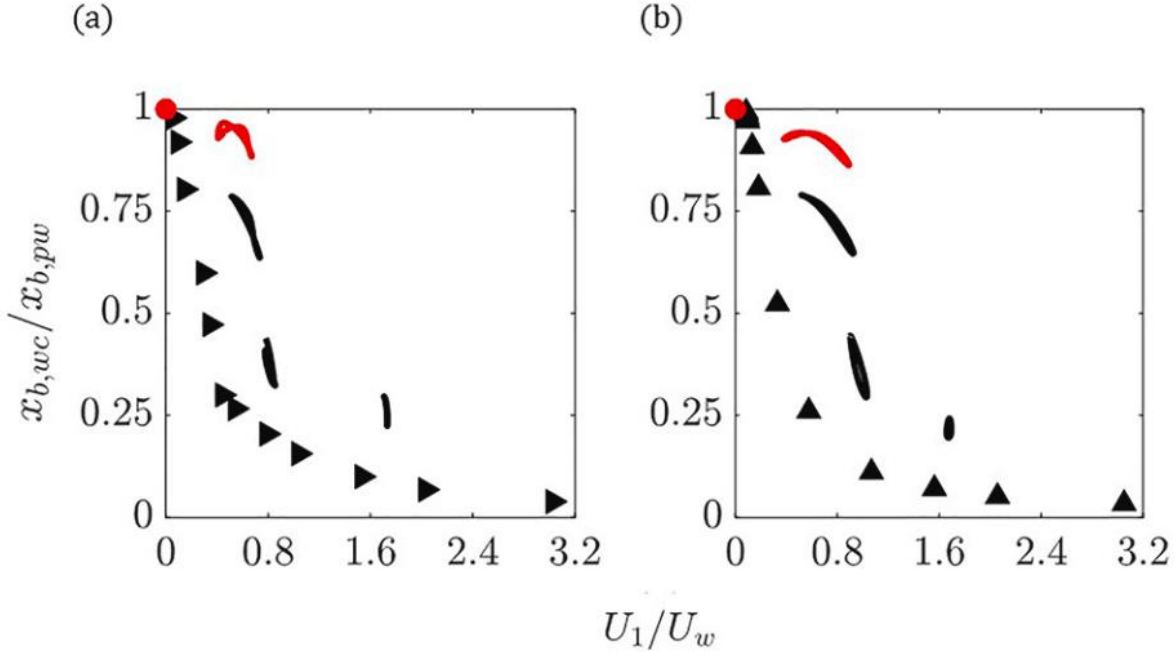


Figure 3.7: Symbols indicate horizontal blade excursion in combined wave-current conditions, $x_{b,wc}$, normalized by the horizontal blade excursion in the corresponding pure wave conditions, $x_{b,pw}$, versus the ratio of the canopy- and time-averaged velocity U_1 to the wave velocity amplitude at the top of the canopy U_w . (a) and (b) correspond to cases B3 ($Ca_w = 1400$) and B7 ($Ca_w = 53$), respectively. The blade tip traces for selected conditions shown in Figures 3.4 and 3.5 are included near the corresponding points here. The red circles and red blade tip traces correspond to the pure wave conditions.

3.4.2 Impact of current on wave energy dissipation rate

The temporal rate of wave energy dissipation in combined wave-current conditions, $E_{D,wc}$, was compared to that of the corresponding pure wave conditions using the ratio $\beta = E_{D,wc}/E_{D,pw}$

(Figure 3.8). The general trends of β versus U_1/U_w are illustrated by case B3, shown in Figure 3.8a. The rate of wave energy dissipation was reduced ($\beta < 1$) with the addition of a small opposing or following current ($U_1/U_w < 0.8$). The minimum β value (denoted by the vertical dashed line in Figure 3.8a) occurred at $U_1/U_w = 0.35$, and β increased with a further increase in current, eventually exceeding 1, indicating that the rate of wave energy dissipation was higher than the pure wave case. This nonlinear trend can be explained by the transition from unsteady to steady reconfiguration described in Figures 3.4 and 3.5. Specifically for case B3 (Figure 3.4, Figure 3.7a, and Figure 3.8a), for a small current (Figure 3.4b), the blade was pronated by the current, i.e., h_d decreased, which reduced the drag, but it still moved freely through the wave cycle (unsteady reconfiguration seen in Figure 3.4b). As a result of the decrease in h_d , wave dissipation was reduced by the current (to a minimum $\beta = 0.7$). In contrast, for a large current (Figure 3.4d), the blade was pronated by the current to such a strong degree that it no longer moved freely through the wave cycle (steady reconfiguration seen in Figure 3.4d), making it effectively rigid. As a result of being effectively rigid, the wave dissipation was increased by the current ($\beta > 1$). This was consistent with previous observations of rigid cylinder arrays, for which the addition of current was observed to increase wave dissipation (e.g., Li and Yan, 2007). For rigid elements there is no reconfiguration, so that the drag dependence on velocity is simply $E_D \sim |(U_w + U_1)^3| - U_c^3 = |U_w^3| + 3U_w^2|U_1| + 3U_1^2|U_w|$, which is greater than $E_{D,pw} \sim |U_w^3|$ (Li and Yan, 2007; Zhang and Nepf, 2021)

The behavior exhibited in case B3 was modified by the base wave condition as described by the wave Cauchy number. Specifically, as the wave Cauchy number decreased (stiffer blade behavior), the reduction in β below 1 was diminished, resulting in a larger value of minimum β , which is illustrated by comparing Figure 3.8a, 3.8b, and 3.8c, corresponding to $Ca_w = 1400, 180,$

and 53, respectively. In particular, note that for case B7 (Figure 3.8c), the blade behaves effectively rigid, with $\beta > 1$ for all currents. In addition, as Ca_w decreased, the minimum β occurred at lower values of U_1/U_w (compare the vertical dashed lines in Figures 3.8a, 3.8b, and 3.8c).

The time rate of wave energy dissipation was also enhanced ($\beta > 1$) for a narrow range of small magnitude opposing currents (Figure 3.8b), for which the imposed current ($U_{1,c} < 0$) balanced the wave-induced current (U_{wic}), producing a time-averaged velocity ($U_1 = U_{1,c} + U_{wic}$) that was smaller in the wave-current case than in the pure-wave case. This resulted in the blade having an overall more upright posture (larger h_d) with the addition of a small opposing current (black inset blade sequence in Figure 3.8b) than with a pure wave (red inset blade sequence). Note that the inset blade postures in Figure 3.8b depict the full swath of blade postures. While at some point during a wave period, the blade under the pure wave condition reached to a higher height than the blade under the wave-current condition (compare the maximum heights of red and black blades), the blade overall experienced greater mean deflection under the pure wave condition, i.e., smaller h_d . The more upright posture under the wave-current condition was associated with higher drag and thus higher wave energy dissipation ($\beta > 1$).

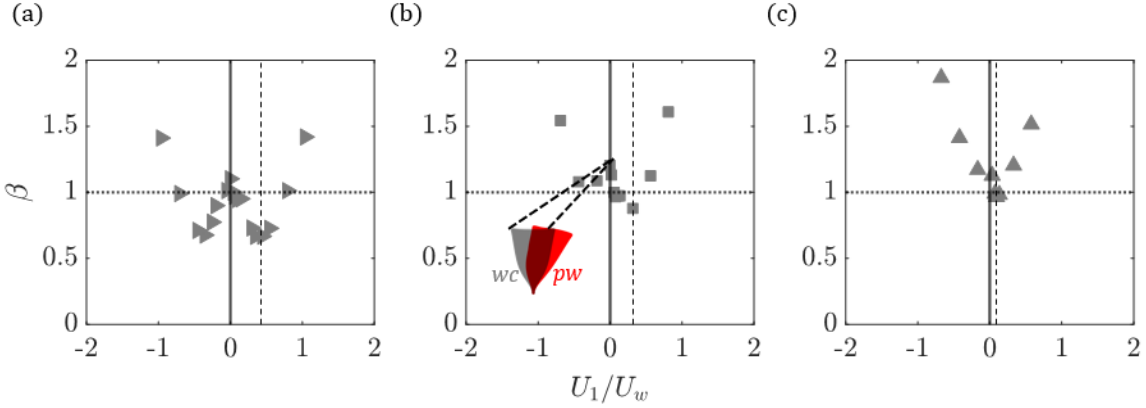


Figure 3.8: The temporal rate of wave energy dissipation in combined wave-current conditions normalized by the rate in corresponding pure wave conditions $\beta = E_{D,wc}/E_{D,pw}$, versus the ratio of the time-averaged velocity U_1 to the wave velocity amplitude at the top of the canopy U_w for (a) case B3; (b) case B5; and (c) case B7 for a canopy density of 2500 blades per square meter. The vertical dashed lines denote the U_1/U_w associated with the minimum β for that case. The inset figures in (b) illustrate blade motion over a wave period for a pure wave condition (red) and a small imposed current (gray) approximately equal in magnitude to U_{wic} for that condition. Small negative imposed currents offset the wave-induced current U_{wic} , reducing the mean pronation of the blade, which enhanced the wave dissipation ($\beta > 1$). See Table 3.2 for symbol shape definitions. Axes are truncated to show more details.

For a wide range of wave Cauchy numbers (Ca_w), the greatest reduction in wave energy dissipation rate, i.e., minimum β , occurred at a similar velocity ratio (Figure 3.9a). Specifically, for $Ca_w > 100$, the minimum β occurred at $U_{1,\min\beta}/U_w = 0.33 \pm 0.05$ (Figure 3.9a, mean \pm standard deviation). For $U_1/U_w < 0.33 \pm 0.05$, unsteady reconfiguration followed the fluid wave orbital motion (Figures 4a and 5a), with $x_{b,wc}/x_{b,pw} \approx 1$ (Figure 3.7). As U_1 increased, the mean deflected height of the blades decreased (Figure 3.6), which decreased the horizontal drag felt by the wave, resulting in a decreased rate of wave energy dissipation, relative to a wave without current, and decreased β for $U_1/U_w < 0.33 \pm 0.05$. For $U_1/U_w > 0.33 \pm 0.05$, the

wave-following reconfiguration was drastically reduced ($x_{b,wc}/x_{b,pw} < 0.25$ for $U_1/U_w > U_{1,\min\beta}/U_w$, Figure 3.7), which increased the relative velocity, with little additional reduction in h_d (compare Figure 3.4c and 3.4d with Figure 3.5c and 3.5d). Beyond this point, the enhanced relative velocity had a greater influence than the reduced h_d on wave hydrodynamic drag, such that the drag on the blade increased with increasing magnitudes of U_1/U_w . Because the transition in blade reconfiguration associated with β_{\min} occurred at a similar value of U_1/U_w (Figure 3.9a), the value of the current Cauchy number ($Ca_{c,U_1} = \left(\frac{U_1}{U_w}\right)^2 Ca_w$) at the transition increased with increasing wave Cauchy number. This meant that the degree of mean pronation ($h_d/l_b \sim Ca_{c,U_1}^{-\frac{1}{3}}$) at β_{\min} was greater for larger Ca_w , leading to a smaller value of β_{\min} . In other words, the β_{\min} decreased with increasing Ca_w (Figure 3.9b). Finally, for $Ca_w < 100$, the velocity associated with the minimum wave dissipation decreased toward zero as Ca_w approached zero, which was consistent with the rigid behavior limit.

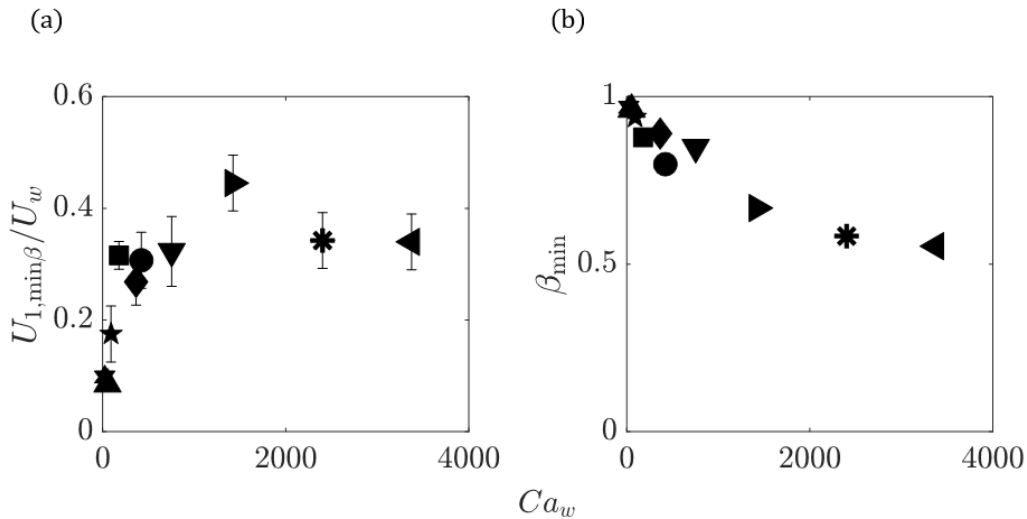


Figure 3.9: (a) For a given wave Cauchy number, the canopy-averaged current corresponding to the lowest β (*i. e.*, β_{\min}) was defined as $U_{1,\min\beta}$. The ratio of $U_{1,\min\beta}$ to the wave velocity

amplitude at the top of the canopy U_w initial increased with increasing wave Cauchy number Ca_w , but then became a constant. Uncertainty in $U_{1,\min\beta}$ arose from the flatness of the β versus U_1 curve, which is reflected in the vertical error bars. (b) the minimum value of β (β_{\min}) versus Ca_w , both for the 2500 blades per square meter canopy density. See Table 3.2 for symbol shape definitions.

3.4.3 Wave damping by seagrass meadow

One of the aims of this study was to extend the results from the flexible blade model to examine spatial wave energy dissipation across a seagrass meadow. Recall that the flexible blades in this study were modeled as if they existed in meadows of identical blades (Section 3.3.1). Assuming that bed-generated drag is negligible compared to meadow-generated drag (which is typical), the time- and blade-averaged rate of wave energy dissipation $E_{D,wc}$ describes the spatial evolution of wave amplitude, a_w , across a meadow (e.g., Dalrymple et al., 1984),

$$E_{D,wc} = E_{D,total} - E_{D,c} = -\frac{\partial}{\partial x_m} \left(\frac{1}{2} C_g \rho g a_w^2 \right), \quad (3.11)$$

in which C_g is the group velocity and x_m is the distance across the meadow. The group velocity C_g describes the speed at which wave energy travels and is a function of both wave properties and depth-averaged current U_c (e.g., Kamphuis, 2010; Peregrine & Jonsson, 1983),

$$C_g = U_c + \frac{1}{2} \left(1 + \frac{2kD}{\sinh(2kD)} \right) \sqrt{\frac{g}{k} \tanh(kD)}. \quad (3.12)$$

Although time-averaged velocity shear is generated by the meadow (see Section 3.3.1), Nepf and Monismith (1994) observed that vertical shear had minimal effect on the group velocity of shallow and intermediate waves, such that Eqn. 3.12 remains valid. It is important to note that the addition of current has two distinct influences on the spatial evolution of wave amplitude

$\frac{da_w}{dx_m}$. First, it modifies the reconfiguration of individual blades, which in turn modifies $E_{D,wc}$ (Figure 3.8). Second, the addition of current changes the speed at which wave energy is translated over the meadow (Eqn. 3.12). Note that the group velocity depends on the time- and depth-averaged current U_c , as opposed to the time- and canopy-averaged current U_1 (see Figure 3.2a). The wave-induced current can also contribute to U_c . Discretizing Eqn. 3.11, the evolution of wave amplitude can be predicted by marching in small spatial steps of size dx across the meadow:

$$a_{w,ndx} = \sqrt{a_{w,(n-1)dx}^2 - \frac{E_{D,wc,(n-1)dx} dx}{2\rho g C_g}}. \quad (3.13)$$

As the wave amplitude decreases across the meadow, the wave velocity also decreases, which reduces the wave Cauchy number and changes $E_{D,wc}$. Therefore, $E_{D,wc}$ was recalculated at set increments over the meadow. The increment was chosen to be 1/5 the expected distance required to reduce the wave amplitude by 50%, based on the wave Cauchy number at the initial position ($x_m = 0$ m).

Parameters were chosen based on the seagrass *Posidonia oceanica*, with a blade length of 40 cm, blade width of 1 cm, blade thickness of 0.35 mm, Young's modulus of 0.5 GPa, water depth of 1.2 m, blade densities of 2450 and 4900 blades per square meter, a wave period of 2 s, and an initial wave amplitude of 15 cm (Dalla Via et al., 1998; Folkard, 2005; Infantes et al., 2012; Pergent-Martini et al., 1994). The parameters for this field condition are shown in Table 3.3. Specifically, the wave Cauchy number was 3700, comparable to case B1. The blade length ratio L was 4.5, and the ratio of water depth to blade length was $D/l_b = 3$. The depth-averaged current was kept below 1 m/s, based on typical limits in *Posidonia oceanica* habitats (e.g.,

Ciraolo et al., 2006; Granata et al., 2001; Poulain et al., 2012). Due to the longer blade length, a simulation of 20 wave periods was needed for the blade behavior over a wave period to converge.

Table 3.3: Test parameters simulating *Posidonia oceanica* blades, with wave amplitude a_w , wave period T_w , wave velocity amplitude U_w , blade length l_b , blade width w_b , blade thickness t_b , Young's modulus of elasticity E , blade stiffness EI , wave Cauchy number Ca_w , and the ratio of the blade length l_b to the wave orbital excursion $L = 2\pi l_b / (U_w T_w)$. Two meadow blade densities were tested: 2450 and 4900 blades per square meter. The ratio of water depth to blade length $D/l_b = 3$. The imposed current velocities $U_{1,c}$ included 0.5 cm/s, 1 cm/s, 2 cm/s, 3 cm/s, 4 cm/s, 5 cm/s, 6 cm/s, 7 cm/s, 7.5 cm/s, and 10 cm/s, with U_c limited to below 1 m/s for each blade density.

D (m)	a_w (cm)	T_w (s)	U_w (cm/s)	l_b (cm)	w_b (cm)	t_b (mm)	E (kg m ⁻¹ s ⁻²)	EI (kg m ³ s ⁻¹)	Ca_w	L
1.2	15	2	28	40	1	0.35	$5 \cdot 10^8$	$1.8 \cdot 10^{-5}$	3700	4.5

When considering the influence of current on wave damping across a seagrass meadow, it is important to emphasize the distinction between 1) the in-canopy, time-mean velocity U_1 , which influences the blade-scale drag and the temporal rate of wave energy dissipation ($E_{D,wc}$), and 2) the depth-averaged, time-mean current U_c , which alters the group velocity (Eqn. 3.12), which in turn determines the conversion from the temporal to spatial rate of wave energy dissipation (Eqn. 3.11). Because of the meadow drag, U_1 is much smaller in magnitude than U_c (Figure 3.10a). Further, as meadow density increases (black to gray symbols in Figure 3.10a), the time-averaged current is diminished (smaller $U_{1,c}$, Eqn. 3.5), but the wave-induced current is increased (larger U_{wic} , Eqn. 3.7), such that a stronger opposing current is required for the time-

mean, in-canopy velocity ($U_1 = U_{1,c} + U_{wic}$) to reach zero. Specifically, for the wave considered in Figure 10, $U_1 = 0$ for $U_c = 70$ cm/s for the denser meadow (grey circles), compared to $U_c = 30$ cm/s for the sparser meadow (black circles).

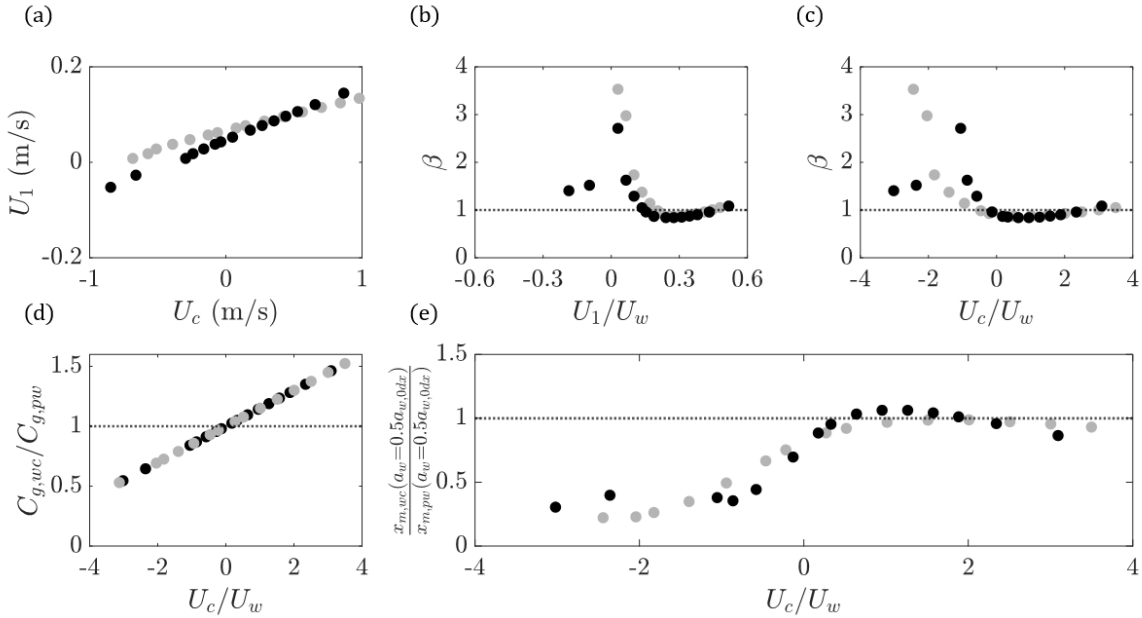


Figure 3.10: Modelling the influence of a *Posidonia oceanica* meadow on wave dissipation in the presence of current. Black and gray circles denote blade densities of 2450 blades m^{-2} and 4900 blades m^{-2} , respectively. (a) Time-mean in-canopy velocity U_1 versus time-mean depth-averaged current velocity U_c . (b) Ratio of the temporal rate of wave energy dissipation in wave-current and pure wave conditions, β , versus ratio of U_1 to wave velocity amplitude U_w . (c) β versus U_c/U_w . (d) Ratio of wave-current group velocity to pure wave group velocity $C_{g,wc}/C_{g,pw}$ versus U_c/U_w . (e) Ratio of distances needed for wave amplitude to be reduced by 50% in wave-current and pure wave conditions versus U_c/U_w .

Compared to the previous test cases (Table 3.2, Figure 3.8), the variation in the temporal rate of wave energy dissipation was similar for the *Posidonia* blade (Figure 3.10b). Specifically, for following currents, the *Posidonia* blade exhibited a minimum β value at approximately $U_1/U_w = 0.3$ (Figure 3.10b), similar to Figure 3.9a. However, the minimum $\beta = 0.85$ for the

Posidonia blade ($l_b = 40$ cm) was greater than that observed for the shorter blade ($l_b = 13$ cm) with the most similar Ca_w (Case B1, $Ca_w = 3400$, $\beta_{\min} = 0.55$), suggesting that blade length influenced β . For opposing currents resulting in a near-zero in-canopy velocity ($U_1 \approx 0$), the *Posidonia* blade exhibited an elevated temporal rate of dissipation ($\beta > 1$). This was also observed for the shorter blades in Figure 8, but the enhancement was much greater for the longer *Posidonia* blade, which reached β values of 2.7 (black symbols) and 3.5 (grey symbols) in Figure 3.10b.

Next, consider how the time rate of wave energy dissipation varied with depth-averaged velocity (Figure 3.10c), which illustrates the impact of meadow density. Specifically, the denser meadow (grey symbols) exhibited high temporal rates of wave dissipation over a wider range of opposing current velocity, which can be attributed to a larger wave-induced current associated with the denser meadow (see discussion of Figure 3.10a). Finally, the trends in the temporal rate of wave dissipation (Figure 3.10c) and group velocity (Figure 3.10d) combine to explain how a depth-averaged current impacts spatial wave decay over a meadow. Specifically, we considered the distance needed to reduce the wave amplitude by 50% (Figure 3.10e). For most cases with opposing depth-averaged currents ($U_c < 0$), the addition of current reduced the distance for wave decay (ratio less than 1), indicating that an opposing current increased the spatial wave damping, i.e., it took a shorter distance to achieve the same wave amplitude reduction. This trend arose from the increased temporal rate of wave energy dissipation (Figure 3.10c) and decreased group velocity (Figure 10d) associated with an opposing current, both of which tended to increase the spatial rate of change in wave amplitude (Eqn. 3.11). In contrast, the presence of a following current ($U_c > 0$) had a negligible impact on the distance needed to reduce wave amplitude by 50%, with the distance ratio near or slightly above 1. This was attributed to the

small impact of following current on the temporal dissipation rate (Fig 3.10c). This result was consistent with Schaefer and Nepf (2022), who also observed that following currents had a negligible impact on the spatial decay of wave amplitude for $Ca_w > 2000$, consistent with the conditions considered here. They attributed the insensitivity to a following current to the strong degree of reconfiguration provided in response to the wave alone (see Figure 4 in Schaefer and Nepf (2022)). However, for $Ca_w < 2000$, weaker wave-induced refiguration provided the opportunity for current-induced reconfiguration to reduce wave amplitude decay (Figure 4 in Schaefer and Nepf, 2022).

3.4.4 Using effective blade length to predict wave dissipation

Previous studies developed scaling laws to describe the impact of reconfiguration on drag (Eqns. 3.3 and 3.4 in Section 3.2), and these have been applied with success to predict wave dissipation by adapting a prediction for a rigid canopy. For linear waves (Eqn. 6), the time-rate of dissipation can be described by integrating Eqn. 3.10 and substituting into Eqn. 3.11. Assuming a rigid meadow (Dalrymple et al 1984),

$$E_{D,w} = \frac{2}{3\pi} C_D \rho n_b w_b \left(\frac{2\pi a_w}{T_w \sinh(kD)} \right) \left(\frac{9 \sinh(kl_b) + \sinh(3kl_b)}{12k} \right). \quad (3.14)$$

For a flexible meadow, Luhar et al. (2017) proposed replacing the blade length l_b in Eqn. 3.14 with the effective length l_e . Using Eqn. 3.4 for pure wave conditions and Eqn. 3.3 for combined wave-current conditions, Eqn. 3.14 led to good predictions of measured wave dissipation for both pure waves and waves with following current (Lei and Nepf, 2019a; Schaefer and Nepf, 2022). However, the ratios of in-canopy current velocity to wave velocity were mostly below

$U_1/U_w = 0.4$, which is comparable to $U_{1,\min\beta}/U_w = 0.33 \pm 0.05$ (Figure 9). That is, the observed cases fell within the regime of unsteady reconfiguration (see the discussion of Figure 3.4 and 3.5). Importantly, the effective length scaling laws predict a monotonic decrease in effective blade length with increasing Cauchy number (see Eqns. 3.3 and 3.4), which can capture the trends of weak current, but cannot capture the transition between unsteady and steady reconfiguration for flexible structures observed in this study (Figure 3.8).

To explore the breakdown of the scaling laws, we used Eqn. 3.14 to infer the effective blade length associated with the wave dissipation $E_{D,wc}$ produced by the blade model (Figure 3.11). Figure 3.11a isolates the cases with following current and $U_1/U_w \leq U_{1,\min\beta}/U_w$, for which the inferred values of l_e agreed with Eqn. 4 ($l_e/l_b = 0.9Ca_{wc}^{-1/3}$, dashed line in Figure 3.11a), consistent with previous experimental results (Lei and Nepf, 2019b; Schaefer and Nepf, 2022). For cases with opposing current and $U_1/U_w > U_{1,\min\beta}/U_w$, the scaling law significantly underpredicted the drag (Figure 3.11b). In Figure 3.11c-d we show comparisons of the inferred l_e/l_b against Ca_wL , with the dashed lines corresponding to Eqn. 3.3, $l_e/l_b = 1.1(Ca_wL)^{-1/4}$. The cases with following current and $U_1/U_w \leq U_{1,\min\beta}/U_w$ (Figure 3.11c) had reasonable agreement with Eqn. 3.3, even though Ca_wL does not account for the presence of current. This was likely due to U_1/U_w being close to or within the wave-dominated regime ($U_1/U_w < 0.25$) identified in Lei and Nepf (2019a).

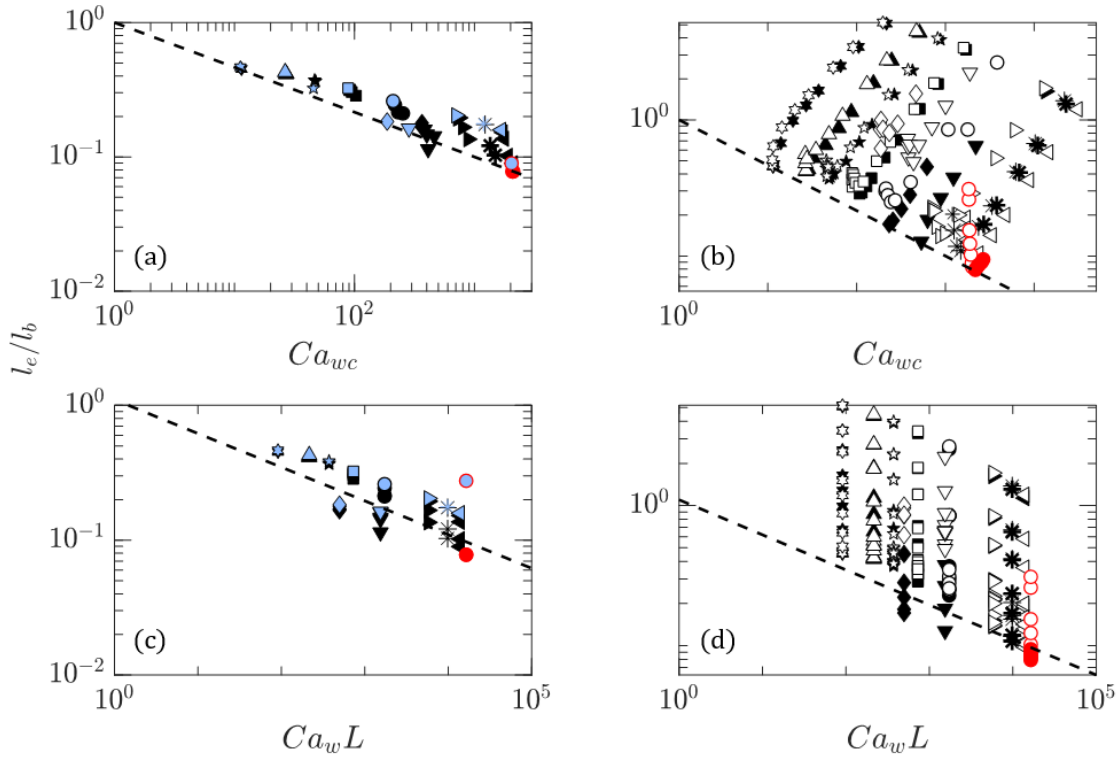


Figure 3.11: Ratio of effective blade length inferred from Eqn. 3.14 to the blade length, l_e/l_b , versus (a) the wave-current Cauchy number Ca_{wc} , for following current and $U_1/U_w \leq U_{1,\min}\beta/U_w$; (b) Ca_{wc} , for follow current and $U_1/U_w > U_{1,\min}\beta/U_w$ as well as opposing current cases (empty and less bold symbols); (c) the wave Cauchy number multiplied by the blade length ratio $Ca_w L$, for following current and $U_1/U_w \leq U_{1,\min}\beta/U_w$; and (d) $Ca_w L$, for following current and $U_1/U_w > U_{1,\min}\beta/U_w$ as well as opposing current cases (empty and less bold symbols). The black symbols denote cases from Table 3.2 with a blade density of 3800 per square meter. The red circles denote the *Posidonia* cases (with a blade density of 4900 per square meter) discussed in Section 3.4.3. The blue filled symbols denote pure wave cases. See Table 3.2 for symbol shape definitions. The dashed curves in (a) and (b) represent $l_e/l_b = 0.9Ca_{wc}^{-1/3}$ (Eqn. 3.4). The dashed curves in (c) and (d) represent $l_e/l_b = 1.1(Ca_w L)^{-1/4}$ (Eqn. 3.3).

The disagreement between cases in Figure 3.11b and 3.11d and Eqns. 3.4 and 3.3 can be explained by considering the physics driving the scaling relationships. Eqn. 3.4 quantifies the drag-reducing change in plant posture in response to flow, such that it predicts decreasing wave

dissipation with increasing current or wave velocity. However, Eqn. 3.4 does not take into account aspects of reconfiguration that would increase drag, and thus cannot account for the transition from unsteady to steady reconfiguration and the impact on wave dissipation observed in this study. Due to the unsteady to steady reconfiguration transition described in Sections 3.4.1 and 4.2, Eqn. 3.4 becomes less accurate as U_1/U_w increases above the mean $U_{1,\min\beta}/U_w = 0.33 \pm 0.05$ (for $Ca_w > 100$).

3.5 Conclusions

A numerical model was used to illustrate the impact of unidirectional current on the motion of and drag on a slender flexible blade exposed to an unsteady velocity field. The model revealed a transition in blade motion and drag with increasing current. Specifically, when a small following current was imposed ($U_1/U_w < 0.33$), the drag, relative to a rigid structure, decreased, but the drag, relative to a rigid structure, increased for current of larger magnitude. This nonlinear trend was explained by a transition from unsteady (wave-following) reconfiguration, which diminished drag (relative to a rigid structure) and wave dissipation, to a steady reconfiguration, which enhanced relative velocity, drag, and wave dissipation. Scaling laws that describe the reduction in drag associated with increasing reconfiguration were shown to be valid only within the regime of unsteady reconfiguration ($U_1/U_w < 0.33$), but significantly underpredicted drag outside this regime. Finally, the wave-induced time-averaged current within a meadow can be offset by an opposing current, resulting in more vertical blade posture that enhanced drag and enhanced wave dissipation. As a result, wave amplitude was reduced more rapidly over a meadow in the present of an opposing current. This study focused on parameters common to coastal vegetation such as

seagrass. However, the overall trends are relevant to any array of flexible structures exposed to combinations of steady and unsteady flow.

3.6 Acknowledgments

R.S. was supported in part by the National Science Foundation Graduate Research Fellowship under Grant No. 2141064, and by the Massachusetts Institute of Technology Department of Civil and Environmental Engineering.

3.7 References

- Abdelrhman, M.A., 2007. Modeling coupling between eelgrass *Zostera marina* and water flow. *Mar Ecol Prog Ser* 338, 81–96. <https://doi.org/10.3354/meps338081>
- Alben, S., Shelley, M., Zhang, J., 2002. Drag reduction through self-similar bending of a flexible body. *Nature* 420, 479–481. <https://doi.org/10.1038/nature01232>
- Bradley, K., Houser, C., 2009. Relative velocity of seagrass blades: Implications for wave attenuation in low-energy environments. *J Geophys Res Earth Surf* 114. <https://doi.org/10.1029/2007JF000951>
- Brumley, D.R., Polin, M., Pedley, T.J., Goldstein, R.E., 2015. Metachronal waves in the flagellar beating of *Volvox* and their hydrodynamic origin. *J R Soc Interface* 12. <https://doi.org/10.1098/rsif.2014.1358>
- Chen, Z., Jiang, C., Nepf, H., 2013. Flow adjustment at the leading edge of a submerged aquatic canopy. *Water Resour Res* 49, 5537–5551. <https://doi.org/10.1002/wrcr.20403>
- Ciraolo, G., Ferreri, G.B., La Loggia, G., 2006. Flow resistance of *Posidonia oceanica* in shallow water. *Journal of Hydraulic Research* 44, 189–202. <https://doi.org/10.1080/00221686.2006.9521675>
- Costanza, R., de Groot, R., Braat, L., Kubiszewski, I., Fioramonti, L., Sutton, P., Farber, S., Grasso, M., 2017. Twenty years of ecosystem services: How far have we come and how far do we still need to go? *Ecosyst Serv* 28, 1–16. <https://doi.org/10.1016/j.ecoser.2017.09.008>

- Costanza, R., J. R.A., Groot, R. De, Farberll, S., Grassot, M., Hannon, B., Limburg, K., Naeem, S., Neilltt, R.V.O., J, J.P.J., Raskin, R.G., Suttonllll, P., Belt, M. van den, 1997. The value of the world's ecosystem services and natural capital. *Nature* 387, 253–260.
<https://doi.org/https://doi.org/10.1038/387253a0>
- Dalla Via, J., Sturmbauer, C., Schönweger, G., Sötz, E., Mathekowitsch, S., Stifter, M., Rieger, R., 1998. Light gradients and meadow structure in *Posidonia oceanica*: Ecomorphological and functional correlates. *Mar Ecol Prog Ser* 163, 267–278.
<https://doi.org/10.3354/meps163267>
- Dalrymple, R.A., Kirby, J.T., Hwang, P.A., 1984. Wave diffraction due to areas of energy dissipation. *J Waterw Port Coast Ocean Eng* 110, 67–79.
[https://doi.org/10.1061/\(ASCE\)0733-950X\(1984\)110:1\(67\)](https://doi.org/10.1061/(ASCE)0733-950X(1984)110:1(67))
- de Langre, E., Gutierrez, A., Cossé, J., 2012. On the scaling of drag reduction by reconfiguration in plants. *Comptes Rendus Mecanique* 340, 35–40.
<https://doi.org/10.1016/j.crme.2011.11.005>
- Döbken, J.W.D., 2015. Modeling the interaction of wave hydrodynamics with flexible aquatic vegetation (M.Sc). Delft University of Technology.
- Folkard, A.M., 2005. Hydrodynamics of model *Posidonia oceanica* patches in shallow water. *Limnol Oceanogr* 50, 1592–1600. <https://doi.org/10.4319/lo.2005.50.5.1592>
- Fonseca, M.S., Fisher, J.S., 1986. A comparison of canopy friction and sediment movement between four species of seagrass with reference to their ecology and restoration. *Mar Ecol Prog Ser* 29, 15–22. <https://doi.org/10.3354/meps029015>
- Fonseca, M.S., Fisher, J.S., Zieman, J.C., Thayer, G.W., 1982. Influence of the seagrass, *Zostera marina* L., on current flow. *Estuar Coast Shelf Sci* 15, 351–364.
[https://doi.org/10.1016/0272-7714\(82\)90046-4](https://doi.org/10.1016/0272-7714(82)90046-4)
- Gacia, E., Duarte, C.M., Middelburg, J.J., 2002. Carbon and nutrient deposition in a Mediterranean seagrass (*Posidonia oceanica*) meadow. *Limnol Oceanogr* 47, 23–32.
<https://doi.org/10.4319/lo.2002.47.1.0023>
- Gaylord, B., Denny, M.W., Koehl, M.A.R., 2003. Modulation of wave forces on kelp canopies by alongshore currents. *Limnol Oceanogr* 48, 860–871.
<https://doi.org/10.4319/lo.2003.48.2.0860>
- Gijón Mancheño, A., 2016. Interaction between wave hydrodynamics and flexible vegetation. Delft University of Technology.
- Gosselin, F.P., 2019. Mechanics of a plant in fluid flow. *J Exp Bot* 70, 3533–3548.
<https://doi.org/10.1093/jxb/erz288>
- Graham, J.M.R., 1980. The forces on sharp-edged cylinders in oscillatory flow at low Keulegan-Carpenter numbers. *J Fluid Mech* 97, 331–346. <https://doi.org/10.1017/S0022112080002595>

- Granata, T.C., Serra, T., Colomer, J., Casamitjana, X., Duarte, C.M., Gacia, E., 2001. Flow and particle distributions in a nearshore seagrass meadow before and after a storm. *Mar Ecol Prog Ser* 218, 95–106. <https://doi.org/10.3354/meps218095>
- Hemminga, M.A., Duarte, C.M., 2000. Fauna associated with seagrass systems, in: *Seagrass Ecology*. Cambridge University Press, Cambridge, pp. 199–247. <https://doi.org/10.1017/cbo9780511525551.007>
- Huthoff, F., Augustijn, D.C.M., Hulscher, S.J.M.H., 2007. Analytical solution of the depth-averaged flow velocity in case of submerged rigid cylindrical vegetation. *Water Resour Res* 43, 1–10. <https://doi.org/10.1029/2006WR005625>
- Infantes, E., Orfila, A., Simarro, G., Terrados, J., Luhar, M., Nepf, H., 2012. Effect of a seagrass (*Posidonia oceanica*) meadow on wave propagation. *Mar Ecol Prog Ser* 456, 63–72. <https://doi.org/10.3354/meps09754>
- James, C.S., Birkhead, A.L., Jordanova, A.A., O’Sullivan, J.J., 2004. Flow resistance of emergent vegetation. *Journal of Hydraulic Research* 42, 390–398. <https://doi.org/10.1080/00221686.2004.9728404>
- James, C.S., Goldbeck, U.K., Patini, A., Jordanova, A.A., 2008. Influence of foliage on flow resistance of emergent vegetation. *Journal of Hydraulic Research* 46, 536–542. <https://doi.org/10.3826/jhr.2008.3177>
- Jones, C.G., Lawton, J.H., Shachak, M., Organisms, M., 1994. Organisms as Ecosystem Engineers. *Oikos* 69, 373–386.
- Kamphuis, J.W., 2010. *Introduction to Coastal Engineering and Management*, 2nd ed. WORLD SCIENTIFIC. <https://doi.org/10.1142/7021>
- Keulegan, G.H., Carpenter, L.H., 1958. Forces on cylinders and plates in an oscillating fluid. *J Res Natl Bur Stand (1934)* 60, 423. <https://doi.org/10.6028/jres.060.043>
- Kobayashi, N., Raichle, A.W., Asano, T., 1993. Wave attenuation by vegetation. *J Waterw Port Coast Ocean Eng* 119, 30–48. [https://doi.org/10.1061/\(ASCE\)0733-950X\(1993\)119:1\(30\)](https://doi.org/10.1061/(ASCE)0733-950X(1993)119:1(30))
- Koch, E.W., 2001. Beyond Light: Physical, Geological, and Geochemical Parameters as Possible Submersed Aquatic Vegetation Habitat Requirements. *Estuaries* 24, 1–17. <https://doi.org/10.2307/1352808>
- Lei, J., Nepf, H., 2021. Evolution of flow velocity from the leading edge of 2-D and 3-D submerged canopies. *J Fluid Mech* 916, 1–27. <https://doi.org/10.1017/jfm.2021.197>
- Lei, J., Nepf, H.M., 2019a. Wave damping by flexible vegetation: Connecting individual blade dynamics to the meadow scale. *Coastal Engineering* 147, 138–148. <https://doi.org/10.1016/j.coastaleng.2019.01.008>

- Lei, J., Nepf, H.M., 2019b. Blade dynamics in combined waves and current. *J Fluids Struct* 87, 137–149. <https://doi.org/10.1016/j.jfluidstructs.2019.03.020>
- Li, C.W., Yan, K., 2007. Numerical investigation of wave - current - vegetation interaction. *Journal of Hydraulic Engineering* 133, 794–803. [https://doi.org/10.1061/\(ASCE\)0733-9429\(2007\)133:7\(794\)](https://doi.org/10.1061/(ASCE)0733-9429(2007)133:7(794))
- Licci, S., Nepf, H., Delolme, C., Marmonier, P., Bouma, T.J., Puijalon, S., 2019. The role of patch size in ecosystem engineering capacity: a case study of aquatic vegetation. *Aquat Sci* 81, 1–11. <https://doi.org/10.1007/s00027-019-0635-2>
- Liquete, C., Piroddi, C., Drakou, E.G., Gurney, L., Katsanevakis, S., Charef, A., Egoh, B., 2013. Current Status and Future Prospects for the Assessment of Marine and Coastal Ecosystem Services: A Systematic Review. *PLoS One* 8. <https://doi.org/10.1371/journal.pone.0067737>
- Lowe, R.J., Koseff, J.R., Monismith, S.G., 2005. Oscillatory flow through submerged canopies: 1. Velocity structure. *J. Geophys. Res.: Oceans* 110. <https://doi.org/10.1029/2004JC002788>
- Luhar, M., 2021. Comment on “The wave-driven current in coastal canopies” by M. Abdollahpour et al. *J Geophys Res Oceans* 126, 1–6. <https://doi.org/10.1029/2019jc015644>
- Luhar, M., 2012. Analytical and experimental studies of plant-flow interaction at multiple scales (Ph.D). Massachusetts Institute of Technology.
- Luhar, M., Coutu, S., Infantes, E., Fox, S., Nepf, H., 2010. Wave-induced velocities inside a model seagrass bed. *J Geophys Res Oceans* 115, 1–15. <https://doi.org/10.1029/2010JC006345>
- Luhar, M., Infantes, E., Nepf, H.M., 2017. Seagrass blade motion under waves and its impact on wave decay. *J Geophys Res Oceans* 122, 3736–3752. <https://doi.org/10.1002/2017JC012731>
- Luhar, M., Nepf, H.M., 2016. Wave-induced dynamics of flexible blades. *J Fluids Struct* 61, 20–41. <https://doi.org/10.1016/j.jfluidstructs.2015.11.007>
- Luhar, M., Nepf, H.M., 2011. Flow-induced reconfiguration of buoyant and flexible aquatic vegetation. *Limnol Oceanogr* 56, 2003–2017. <https://doi.org/10.4319/lo.2011.56.6.2003>
- Méndez, F.J., Losada, I.J., 1999. Hydrodynamics induced by wind waves in a vegetation field. *J Geophys Res* 104, 18383–18396. <https://doi.org/10.1029/1999JC900119>
- Morison, J.R., Johnson, J.W., Schaaf, S.A., 1950. The force exerted by surface waves on piles. *Journal of Petroleum Technology* 2, 149–154. <https://doi.org/10.2118/950149-g>
- Mullarney, J.C., Henderson, S.M., 2010. Wave-forced motion of submerged single-stem vegetation. *J Geophys Res Oceans* 115, 1–14. <https://doi.org/10.1029/2010JC006448>
- Nepf, H., Ghisalberti, M., White, B., Murphy, E., 2007. Retention time and dispersion associated with submerged aquatic canopies. *Water Resour Res* 43, 1–10. <https://doi.org/10.1029/2006WR005362>

- Nepf, H.M., Monismith, S.G., 1994. Wave dispersion on a sheared current. *Applied Ocean Research* 16, 313–315. [https://doi.org/10.1016/0141-1187\(94\)90019-1](https://doi.org/10.1016/0141-1187(94)90019-1)
- Olesen, B., Sand-Jensen, K., 1994. Demography of shallow eelgrass (*Zostera marina*) populations--Shoot dynamics and biomass development. *British Ecological Society* 82, 379–390. <https://doi.org/10.2307/2261305>
- Orth, R.J., Moore, K.A., 1986. Seasonal and year-to-year variations in the growth of *Zostera marina* L. (eelgrass) in the lower Chesapeake Bay. *Aquat Bot* 24, 335–341. [https://doi.org/10.1016/0304-3770\(86\)90100-2](https://doi.org/10.1016/0304-3770(86)90100-2)
- Peregrine, D.H., Jonsson, I.G., 1983. Interaction of waves and currents.
- Pergent-Martini, C., Rico-Raimondino, V., Pergent, G., 1994. Primary production of *Posidonia oceanica* in the Mediterranean Basin. *Mar Biol* 120, 9–15. <https://doi.org/10.1007/BF00381936>
- Poulain, P.M., Menna, M., Mauri, E., 2012. Surface geostrophic circulation of the mediterranean sea derived from drifter and satellite altimeter data. *J Phys Oceanogr* 42, 973–990. <https://doi.org/10.1175/JPO-D-11-0159.1>
- Raupach, M.R., Finnigan, J.J., Brunet, Y., 1996. Coherent eddies and turbulence in vegetation canopies: the mixing-layer analogy. *Boundary Layer Meteorol* 78, 351–382. <https://doi.org/10.1007/BF00120941>
- Rominger, J.T., Nepf, H.M., 2014. Effects of blade flexural rigidity on drag force and mass transfer rates in model blades. *Limnol Oceanogr* 59, 2028–2041. <https://doi.org/10.4319/lo.2014.59.6.2028>
- Sand-Jensen, K., 2003. Drag and reconfiguration of freshwater macrophytes. *Freshw Biol* 48, 271–283. <https://doi.org/10.1046/j.1365-2427.2003.00998.x>
- Sarpkaya, T., Storm, M., 1985. In-line force on a cylinder translating in oscillatory flow. *Applied Ocean Research* 7, 188–196. [https://doi.org/10.1016/0141-1187\(85\)90025-2](https://doi.org/10.1016/0141-1187(85)90025-2)
- Schaefer, R.B., Nepf, H.M., 2022. Wave damping by seagrass meadows in combined wave-current conditions. *Limnol Oceanogr* 67, 1554–1565. <https://doi.org/10.1002/lno.12102>
- Schaefer, R., & Nepf, H, 2024. Movement of and drag force on slender flat plates in an array exposed to combinations of unidirectional and oscillatory flow. *J Fluid Struct*, 124, 104044. <https://doi.org/10.1016/j.jfluidstruct.2023.104044>
- Shields, A.R., Fiser, B.L., Evans, B.A., Falvo, M.R., Washburn, S., Superfine, R., 2010. Biomimetic cilia arrays generate simultaneous pumping and mixing regimes. *Proc Natl Acad Sci U S A* 107, 15670–15675. <https://doi.org/10.1073/pnas.1005127107>
- Tobalske, B.W., 2007. Biomechanics of bird flight. *Journal of Experimental Biology* 210, 3135–3146. <https://doi.org/10.1242/jeb.000273>

- Unsworth, R.K.F., McKenzie, L.J., Collier, C.J., Cullen-Unsworth, L.C., Duarte, C.M., Eklöf, J.S., Jarvis, J.C., Jones, B.L., Nordlund, L.M., 2019. Global challenges for seagrass conservation. *Ambio* 48, 801–815. <https://doi.org/10.1007/s13280-018-1115-y>
- Vogel, S., 1984. Drag and Flexibility in Sessile Organisms 1 44, 37–44. <https://doi.org/https://doi.org/10.1093/icb/24.1.37>
- Wang, N., Zou, J., Yang, Y., Li, X., Guo, Y., Jiang, C., Jia, X., Cao, X., 2019. Kelp-inspired biomimetic triboelectric nanogenerator boosts wave energy harvesting. *Nano Energy* 55, 541–547. <https://doi.org/10.1016/j.nanoen.2018.11.006>
- Ward, T.A., Rezadad, M., Fearday, C.J., Viyapuri, R., 2015. A review of biomimetic air vehicle research: 1984-2014. *International Journal of Micro Air Vehicles* 7, 375–394. <https://doi.org/10.1260/1756-8293.7.3.375>
- Zhang, X., Nepf, H., 2021. Wave damping by flexible marsh plants influenced by current. *Phys Rev Fluids* 6, 1–17. <https://doi.org/10.1103/PhysRevFluids.6.100502>
- Zhou, C.Y., Graham, J.M.R., 2000. A numerical study of cylinders in waves and currents. *J Fluids Struct* 14, 403–428. <https://doi.org/doi:10.1006/jfls.1999.0276>

Chapter 4

Flow structure in an artificial seagrass meadow in combined wave-current conditions³

Abstract:

Experiments in a laboratory flume were conducted using an artificial seagrass meadow, modeled after *Zostera marina*, to examine the impact of waves on the vertical structure of time-averaged current, Reynolds stress, and turbulent kinetic energy (TKE) under combined wave-current conditions within the meadow. With the addition of smaller waves, defined using a ratio of wave velocity to current velocity $U_w/U_c < 2.5$, the time-averaged velocity peaked above the meadow, which was similar to pure current conditions. When $U_w/U_c > 2.5$, the presence of waves caused the time-averaged velocity to peak near the top of the meadow. Meanwhile, when $U_w/U_c > 1$ the presence of waves reduced the magnitude of peak Reynolds stress. For all conditions considered,

³ This chapter was published as Schaefer and Nepf (2022a).

the wake production of turbulence dominated the shear production of turbulence in the meadow. However, the wave velocity was less efficient than the current velocity in generating TKE in the meadow because the movement of the blades forced by the oscillatory fluid motion reduced the relative velocity between the blades and the wave. A modified hybrid model for wake production of TKE in a flexible canopy under combined wave-current conditions was proposed to account for the relative contributions of waves and currents. Wake production of TKE was dominated by waves when $U_w/U_c > 1$ and dominated by currents when $U_w/U_c < 1$. The models and observations proposed in this study contribute to an enhanced understanding of the relative influences of waves and currents on seagrass meadow flow structure in realistic combined wave-current conditions.

4.1 Introduction

Meadows of submerged aquatic vegetation, such as seagrass, can damp wave energy (e.g., Knutson et al. 1982; Fonseca and Cahalan 1992), reduce erosion, and improve water quality (e.g., Ginsburg and Lowenstam 1958; Ward et al. 1984; Moore 2004). The reduction of current velocity within the meadow enhances the creation of near-bed habitat relative to unvegetated regions (e.g., Fonseca et al. 1982; Homziak et al. 1982). These ecosystem services depend on the interactions between the meadow, waves, and current. For example, hydrodynamic intensity impacts seagrass nutrient uptake (e.g., Lei and Nepf 2016; Gillis et al. 2017) and overall seagrass survival (Fonseca et al. 2007; Peralta et al. 2006). Furthermore, the initiation of sediment transport within vegetated regions has been linked to exceeding thresholds of vegetation-

generated turbulence in pure current (Yang et al. 2016) and pure wave (Tang et al. 2019; Tinoco and Coco 2018; Zhang and Nepf 2019) conditions. This paper describes mean and turbulent flow within submerged aquatic vegetation under combined wave-current conditions, which can provide a deeper understanding of meadow hydrodynamics and enable a more accurate assessment of ecosystem services.

Under unidirectional flow, vegetation drag reduces velocity within the meadow and redirects some flow over the top of the meadow, creating a shear layer with an inflection point in the vertical profile of time-averaged velocity (Brunet et al. 1994; Ghisalberti and Nepf 2006; Raupach et al. 1996). The shear layer at the top of the meadow, as well as the wakes of individual shoots and leaves, can convert mean kinetic energy into turbulent kinetic energy (e.g., Nepf 1999; Nepf and Vivoni 2000; Tanino and Nepf 2008). In pure wave conditions, stem wake turbulence is generated in proportion to the wave velocity squared (Tang et al. 2019; Zhang et al. 2018; Zhang and Nepf 2019), but shear layer turbulence is only generated for long waves for which the wave excursion significantly exceeds the drag length scale of the canopy (Ghisalberti and Schlosser 2013).

Turbulence has been studied in pure current and pure wave conditions separately, but waves and currents can coexist in seagrass meadows (e.g., Koch et al. 2006). Multiple studies have considered turbulence in combined wave-current conditions in rigid and flexible meadows of model vegetation. Both Lou et al. (2018) and Chen et al. (2020) observed that the addition of waves increased turbulent kinetic energy (TKE) within dense arrays of rigid cylinders relative to pure currents. In a flexible meadow, the individual plants may deflect under currents and sway under waves, changing the structure of time-averaged and turbulent velocities. For example, in pure current conditions, oscillations in the meadow height (known as *monami*) decrease the

sharpness of the drag interface at the top of the canopy and the magnitude of peak Reynolds stress, relative to stationary canopies (Ghisalberti and Nepf 2006). The presence of waves can cause a mean pronation in the direction of wave propagation (e.g., Zhang et al. 2018). Paul and Gillis (2015) subjected a transplanted meadow of *Zostera noltei* to both pure current and combined wave-current conditions and observed no differences in time-averaged velocity, but observed a reduction in TKE in combined wave-current conditions relative to corresponding pure current conditions, which is opposite to the trend observed for rigid models (e.g., Chen et al. 2020; Lou et al. 2018). In a field study on a floodplain of the Yangtze River and for multiple species of flexible vegetation, Zhang et al. (2021) observed little impact of waves on the magnitude of TKE associated with the current, but observed that the presence of waves increased the shear layer penetration depth, δ_e , relative to that predicted for pure current (Nepf et al. 2007), and they attributed this to the waving of the flexible leaves.

The primary goal of this study was to observe the influence of wave amplitude on time-mean flow structure, Reynolds stress, and TKE in combined wave-current conditions within a flexible meadow, including an evaluation of TKE prediction in combined wave-current conditions. Understanding how the combination of waves and currents impacts flow structure and turbulence in a seagrass meadow can improve the description of seagrass meadow hydrodynamics and the ecosystem services those conditions facilitate.

4.2 Theoretical background for predicting velocity and turbulence in meadow

Several studies have described unidirectional flow over a rigid submerged meadow using a two-layer model: an overflow layer, with depth- and time-averaged velocity U_2 , and a canopy layer of height h , with depth- and time-averaged velocity U_1 (e.g., Chen et al. 2013; Cheng 2011; Huthoff et al. 2007; see **Figure 1**). This was modified for a flexible meadow by Lei and Nepf (2021), who incorporated the impact of plant reconfiguration by using the deflected canopy height, h_d , and the effective blade length, l_e , defined in Luhar and Nepf (2011, 2013) as the length of rigid blade that provides the equivalent drag to a flexible blade of length l . Specifically, for a depth-averaged velocity U_c in total water depth D , the in-canopy velocity is

$$U_1 = \frac{U_c}{1 - \frac{h_d}{D} \phi + \sqrt{\frac{C_D a_v l_e}{2C(1-\phi)} \left(\frac{D-h_d}{D}\right)^3}} \quad (4.1)$$

in which ϕ is the solid volume fraction and a_v is the frontal area per canopy volume. C_D is the canopy drag coefficient. (See Appendix B for a dictionary of symbols.) C is a coefficient representing the efficiency of turbulent momentum transfer between the canopy and overflow layers:

$$C = K_c \left(\frac{\delta_e}{D}\right)^{\frac{1}{3}} \quad (4.2)$$

in which K_c is an empirical coefficient. For rigid canopies, Chen et al. (2013) found $K_c = 0.07 \pm 0.02$. The penetration length scale δ_e describes the vertical distance into the canopy over which turbulent momentum flux is significant, and it is defined as the distance from the top of the

canopy at which the Reynolds stress decays to 10% of the peak magnitude. The penetration length depends on the canopy height and drag length scale $(C_D a_v)^{-1}$, specifically $\delta_e = \min\left(\frac{0.23 \pm 0.06}{C_D a_v}, D - h, h\right)$ (Konings et al. 2012; Nepf and Vivoni 2000). Shear is highest near the top of the canopy, such that the Reynolds shear stress $\overline{u'w'}$ reaches a peak magnitude at the canopy height (Figure 4.1), with u' and w' the velocity fluctuations in the streamwise and vertical directions, respectively, and the overbar denoting the time-averaging operation. The peak magnitude of Reynolds stress, assumed to occur at the top of the canopy, scales with the velocity difference between the overflow and canopy layers (Chen et al. 2013; Konings et al. 2012):

$$\tau_{h(max)} = \rho \overline{u'w'}|_{z=h} = \rho C (U_2 - U_1)^2 \quad (4.3)$$

in which ρ is the density of water.

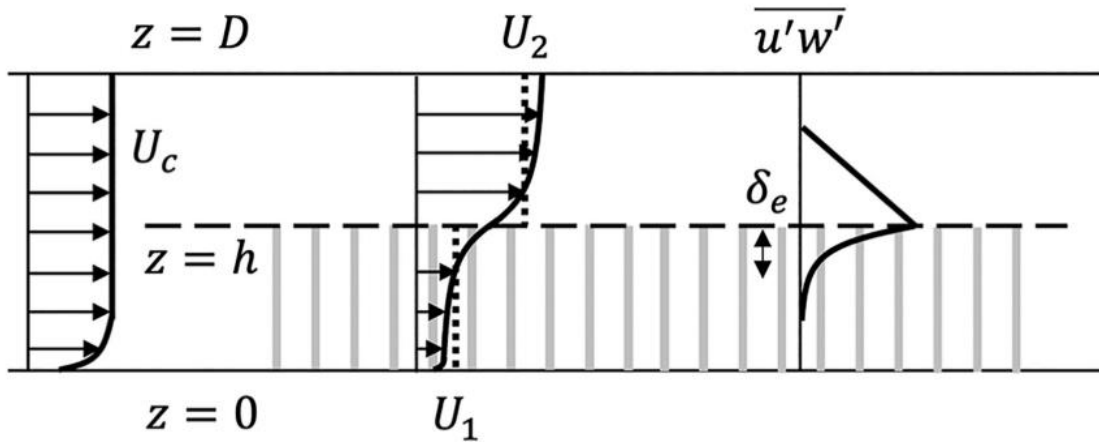


Figure 4.1: Simplified sketch of time-averaged velocity profiles (denoted by arrows) and Reynolds stress $\overline{u'w'}$ profile in a submerged canopy (with canopy elements represented by vertical gray rectangles). The dotted vertical lines within and above the canopy in the time-averaged velocity profiles denote the spatial vertically averaged time-averaged velocity within and above the canopy (U_1 in the canopy and U_2 above the canopy).

In the presence of waves, Schaefer and Nepf (2022) proposed an extension to Equation 4.1 to account for the wave-induced current in the meadow:

$$U_1 = (0.6 \pm 0.3)\bar{U}_{max} + \frac{U_c}{1 - \frac{h_d}{D}\phi + \sqrt{\frac{C_D a_v l_e}{2C(1-\phi)} \left(\frac{D-h_d}{D}\right)^3}} \quad (4.4)$$

The maximum wave-induced current \bar{U}_{max} is (Luhar 2021)

$$\bar{U}_{max} = (1.2 \pm 0.2) U_w \sqrt{\frac{a_v k l_e}{\sigma}} U_w \quad (4.5)$$

in which U_w is the wave velocity amplitude, k is the wave number, and σ is the wave angular frequency. The addition in Equation 4.4 assumes that the waves do not modify the momentum transfer between the meadow and overflow layers (i.e., C is effectively unchanged), and that the generation of wave-induced current is not altered by presence of an imposed current.

In addition to predicting the reduction of velocity, it is also important to predict the intensity of turbulence generated in the meadow. For unidirectional flow, a submerged meadow contributes two sources of turbulence production: shear production P_s , associated with the shear at the top of the meadow, and stem production P_w , associated with the wakes of individual stems and leaves. The shear production is

$$P_s(z) = -\overline{u'w'} \frac{\partial \bar{u}}{\partial z} \quad (4.6)$$

in which z is the elevation above the bed and \bar{u} is the time-averaged velocity. For a stem diameter d and stem density m_s (number of stems per unit bed area), the wake production is (e.g., Nepf 2012).

$$P_w(z) = \frac{1}{2} C_D \frac{m_s d}{1 - \phi} \bar{u}(z)^3 \quad (4.7)$$

Averaged over the meadow height, Equation 4.7 is approximated as

$$\langle P_w \rangle = \frac{1}{2} C_D \frac{m_s d}{1 - \phi} U_1^3 \quad (4.8)$$

Angle brackets indicate a canopy vertical spatial average. A prediction of TKE, k_t , is possible by equating the rates of turbulence production to the rate of turbulence dissipation, $\varepsilon \sim k_t^{3/2} / l_t$, with l_t the turbulence integral length scale (e.g., Tennekes and Lumley 1972). Tanino and Nepf (2008) considered this model for an array of rigid emergent cylinders, for which the shear production can be neglected. Zhang et al. (2018) extended the Tanino and Nepf (2008) model to a flexible seagrass meadow with blades of width w_b and blade density m_b (number of blades per unit bed area). For shoot spacing $S > 1.8w_b$, $l_t \sim w_b$, such that $\langle P_w \rangle \sim \varepsilon$, from which

$$\frac{\sqrt{\langle k_t \rangle}}{U_1} = \delta \left(C_D \frac{m_b w_b^2}{2(1 - \phi)} \right)^{\frac{1}{3}} \quad (4.9)$$

The scale factor $\delta = 1.1$ for unidirectional flow in an emergent rigid meadow, as shown in Tanino and Nepf (2008). Equation 9 with $\delta = 1.1$ has also been validated for pure wave conditions in rigid canopies, but with the velocity scale replaced with the root-mean-squared wave velocity, $U_{w,RMS}$ (Tang et al. 2019) or the wave velocity amplitude U_w (Chen et al. 2020; Tinoco and Coco 2018). However, Zhang et al. (2018) found that the scale coefficient δ was reduced for a submerged flexible artificial seagrass meadow, and this was attributed to the motion of the blades reducing the relative velocity between the waves and the blade.

4.3 Materials and methods

Experiments were performed in a 24 m long, 38 cm wide, and 60 cm deep laboratory flume (Figure 4.2). A piston-type paddle wavemaker controlled by a Syscomp WGM-101 waveform signal generator (refer to Appendix A in Luhar, 2012 for details) produced waves of period $T=2$ s and varying amplitude. To reduce wave reflection, a 1:5 sloped aluminum ramp covered with rubberized coconut fiber was placed at the downstream end of the flume. The upstream edge of the ramp was lifted to allow for the passage of current. The ramp reduced wave reflection to below 11%, based on the analysis described in Goda and Suzuki (1977). Currents of varying speeds were recirculated through an inlet pipe (8 cm inner diameter) 0.8 m downstream of the wavemaker and an outlet drain downstream of the ramp. Currents of varying speeds were recirculated through an inlet pipe (8 cm inner diameter) 0.8 m downstream of the wavemaker and an outlet drain downstream of the ramp.

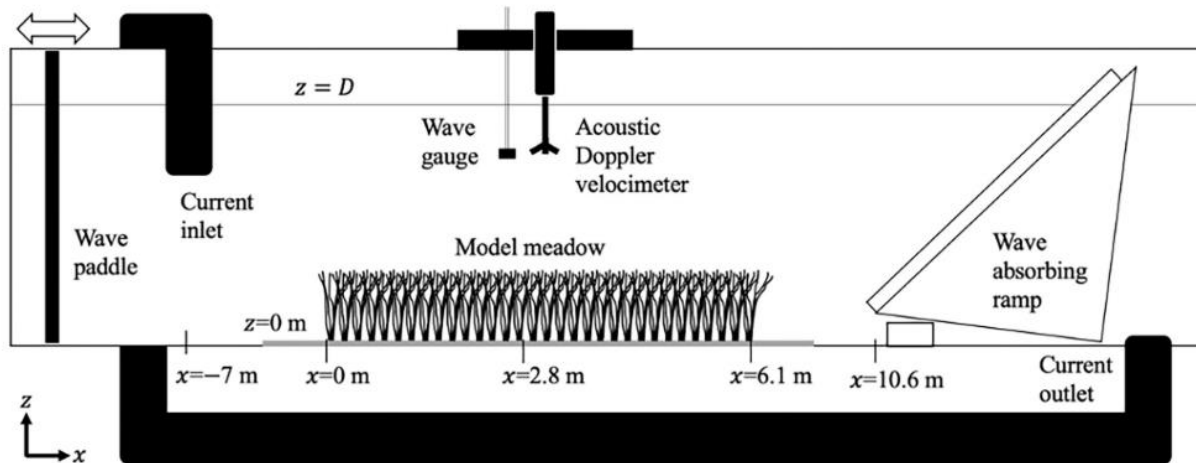


Figure 4.2: Sketch of experimental setup, not drawn to scale. The streamwise direction x is zero at leading edge of the model meadow, and the vertical direction z is zero at the bed and positive upward.

4.3.1 Construction of artificial seagrass shoot and meadow

A seagrass shoot model was constructed to be geometrically and dynamically similar to *Zostera marina*, (e.g., Ghisalberti and Nepf 2002). Each model shoot had six blades laser-cut from low-density polyethylene (LDPE). Each blade was 13 cm long, 0.3 cm wide, and 0.1 mm thick. The blades were wrapped around the upper half of a 0.6 cm diameter, 1.3 cm long cylindrical dowel using tape, which increased the diameter by 0.1 cm. The erect height of each shoot was $h = 13.6$ cm.

The shoots were inserted in a staggered pattern into pre-drilled holes in polyvinyl chloride boards such that the rigid dowels, representing the seagrass sheaths, extended 0.6 cm above the baseboards. The shoot density $m_s = 950$ shoots per square meter, and the blade density $m_b = 5700$ blades per square meter. A bare baseboard (1.2 m in length) was placed at the upstream and downstream ends of the 6.1 m long meadow. Experiments were performed with mean water depths $D = 27$ cm and 45 cm above the baseboards. For each water depth, four pure wave cases, four pure current cases, and sixteen combined wave-current cases were considered (see Appendix B). Turbulence generated at the current inlet slightly modified the wave amplitude relative to pure wave conditions with the same wavemaker setting.

4.3.2 Velocity measurements, wave gauge measurements, and meadow imaging

The velocities in the streamwise (x), lateral (y), and vertical (z) directions were defined as (u, v, w) , respectively. Instantaneous velocities were measured with a Nortek Vectrino three-

dimensional acoustic velocimeter, which was centered longitudinally between successive shoot rows and laterally between adjacent shoots, at the spanwise center of the flume. This position within a staggered array has been shown to offer accurate estimates of the laterally averaged velocity and turbulence in current and wave conditions (see Figure 2 in Chen et al. 2013 and Figure 2 in Zhang et al. 2018). To minimize interference with the measurement volume, blades were removed from shoots within a 10 cm diameter circle around the probe (see Luhar et al. 2010). Measurements were taken along a vertical transect in 1 cm intervals above the bed at the longitudinal center of the meadow ($x = 2.8$ m), for 240 s at 200 Hz for each case.

Velocity records were cleaned using the acceleration thresholding methods described in Goring and Nikora (2002). Each component of velocity was decomposed into the summation of the time-averaged (denoted by an overbar), phase-averaged (denoted by a tilde), and turbulent (denoted by prime) velocity. For example, for the streamwise component,

$$u(t, z) = \bar{U}(z) + \tilde{U}(t, z) + u'(t, z) \quad (4.10)$$

in which t is time. The number of samples n_s in each wave period was estimated through autocorrelation. The phase-averaged velocity $\tilde{U}(\theta)$ was calculated for each of the $n_s = 403$ phase bins, in which θ is the wave phase. The time-averaged velocity was calculated as

$$\bar{U} = \frac{1}{2\pi} \int_0^{2\pi} \tilde{U}(\theta) d\theta \quad (4.11)$$

The depth-averaged imposed current U_c was defined by integrating \bar{U} over depth upstream of the meadow. The time-averaged TKE was calculated as

$$TKE = k_t = \frac{1}{4\pi} \int_0^{2\pi} [u'_{RMS}(\theta)^2 + v'_{RMS}(\theta)^2 + w'_{RMS}(\theta)^2] d\theta \quad (4.12)$$

Water surface displacement η was measured with a wave gauge (1000 Hz for 90 seconds) at the longitudinal center of the meadow, which provided both the wave amplitude and confirmed stationary wave conditions. The wave-to-wave variation in wave amplitude was less than 1% of the phase-averaged wave amplitude, determined using $\frac{1}{2\pi} \int_0^{2\pi} \eta_{RMS}(\theta) d\theta / \eta_{w,RMS}$, as described in Zhang et al (2018). This indicated that the variation in wave form made negligible impact on the estimation of the turbulence within the phase-averaged method (Equation 4.12).

The in-canopy velocity U_1 for each case was estimated as a vertical average of the time-mean velocity between the bed and the time-mean deflected canopy height, h_d . Mean deflected heights were estimated from digital videos of six blades painted black at the longitudinal center of the meadow collected using a Nikon D7500 camera. The videos were viewed and processed using MATLAB VideoReader, readFrame, and Sobel edge detection functions. A red-green-blue pixel identification algorithm was used to identify the painted blades. The vertical positions of the highest and lowest part of each blade were recorded for all cases under the wave crests and troughs. The mean deflected canopy height h_d was defined as the average across all six blades. The characteristic wave velocity amplitude U_w for each case was defined from Stokes second-order wave theory under the crest (LeMéhauté 1976; Dean and Dalrymple 1984) at the undeflected canopy height ($z = h$) using the measured wave amplitude at $x = 2.8$ m, the location of mid-meadow velocity measurements.

4.3.3 Drag coefficient

The drag coefficient C_D for the flat rectangular blades was assumed to be 1.95 (as in Zhang et al. 2018). Zhang et al. (2018) found that using a variable C_D to account for the impact of different

hydrodynamic conditions on blade reconfiguration did not improve TKE predictions, as the drag coefficient used in TKE predictions represents the drag along the vertical part of the plant. Furthermore, although Sarpkaya and Storm (1985) observed that the addition of a current to oscillatory flow could alter the drag coefficient, the impact depended on the Keulegan-Carpenter number $KC = U_w T / w_b$ (Keulegan and Carpenter 1958). They observed that the drag coefficients of cylinders in combined wave-current conditions converged for $KC > 15$, and the impact of current on drag coefficients became negligible for $KC > 30$. In this study all KC were greater than 24. Based on this, and for simplicity, in this study the drag coefficient in pure current, pure wave, and wave-current conditions was assumed to be 1.95.

4.4 Results

4.4.1 Time-averaged velocity profiles

Selected profiles of time-averaged velocity were used to illustrate the flow behavior (**Figure 4.3**), including the strongest imposed current in both depths. The full set of profiles is given in Appendix B. See Appendix B for details of all conditions. For pure current cases (red triangles in **Figure 4.3**), the time-averaged velocity profiles included a mixing-layer at or just above the meadow interface and a peak velocity well above the meadow (**Figure 4.3(A), (D)**). Wave-current cases (circles in **Figure 4.3**) with $U_w / U_c < 2.5$ retained this mixing-layer time-mean structure, but the center of the shear layer moved toward the bed as either the imposed current or wave velocity was increased, both of which were associated with a reduction in the canopy deflected height (horizontal dashed lines in **Figure 4.3**; see Appendix B).

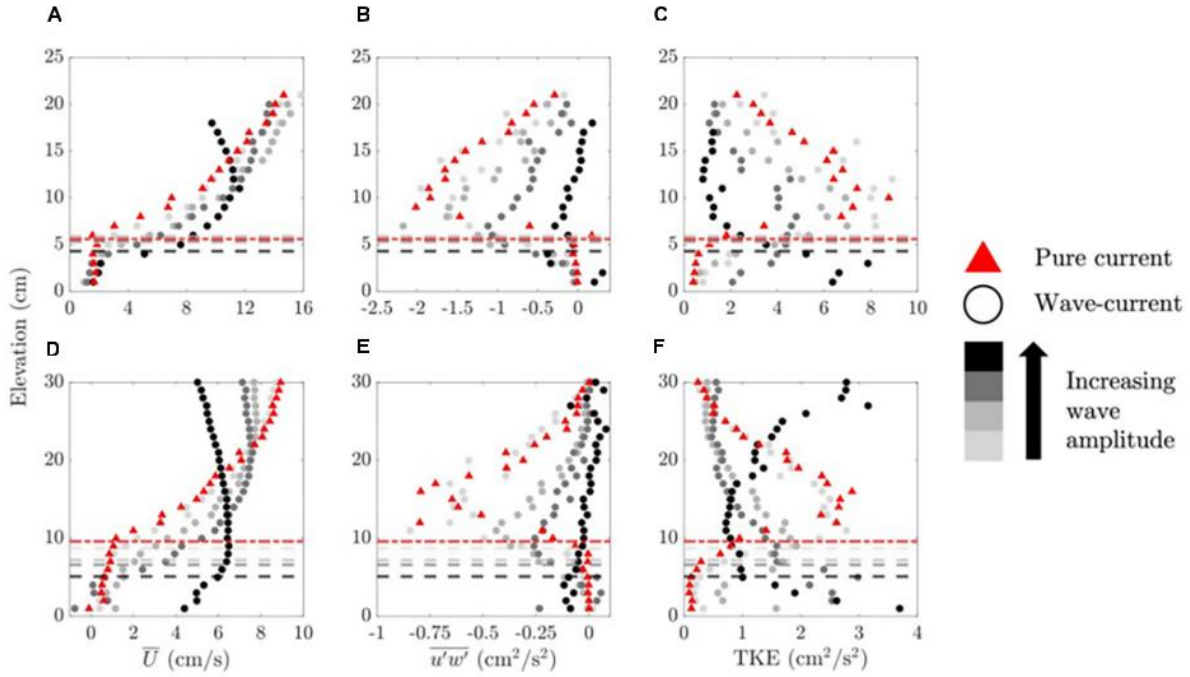


Figure 4.3: Distance above the bed (z) versus (A, D) time-averaged velocity (\bar{U}), (B, E) Reynolds stress ($\overline{u'w'}$), and (C, F) TKE for the largest imposed current and all waves for cases with (A-C) depth $D=27$ cm and (D-F) depth $D=45$ cm. In (A-C), $U_c=10.4$ cm s^{-1} and $U_w=3.2$ - 4.7 cm s^{-1} (lightest gray), $U_w=4.1$ - 7.4 cm s^{-1} (second-lightest gray), $U_w=8.9$ - 10.0 cm s^{-1} , (second-darkest gray), and $U_w=19.2$ - 21.8 cm s^{-1} (black). In (D-F), $U_c=6.8$ cm s^{-1} and $U_w=2.9$ - 3.9 cm s^{-1} (lightest gray), $U_w=8.1$ - 8.8 cm s^{-1} (second-lightest gray), $U_w=10.1$ - 11.1 cm s^{-1} , (second-darkest gray), and $U_w=15.4$ - 19.0 cm s^{-1} (black). (Turbulence at the current inlet pipe slightly modified wave amplitudes for higher currents relative to pure wave conditions for the same programmed wave.) Horizontal dashed lines denote measured h_d , with matching colors (dashed-dotted lines correspond to pure current). Profiles could not be extended over the entire depth due to limitations of the instrument and the presence of waves. Profiles for cases with depth $D=45$ cm are shortened to 30 cm to show detail within and above the canopy.

For most cases with $U_w/U_c > 2.5$, the time-mean velocity peaked at the top of the canopy, reflecting the contribution from the wave-induced current (discussed in Section 4.2 and predicted with Equation 4.5), so that these conditions were considered to be wave-dominated. The transition at approximately $U_w/U_c = 2.5$ is supported by **Figure 4.4**, which illustrates the

distribution of cases for which the time-averaged velocity peaked at the top of the canopy (wave-dominated, triangles) or for which the time-averaged velocity peaked above the canopy (circles). The transition was not a function of current Reynolds number ($U_c D / \nu$, in which ν is the kinematic viscosity of water). Finally, for the largest waves (black circles in **Figure 4.3**), the time-averaged current was reduced near the water surface. This was attributed to a wave-induced Eulerian drift, which has been observed in several previous studies in laboratory water channels and in the field (Gjørsund 2003; Monismith et al. 2007; Nepf et al. 1995; Smith 2006).

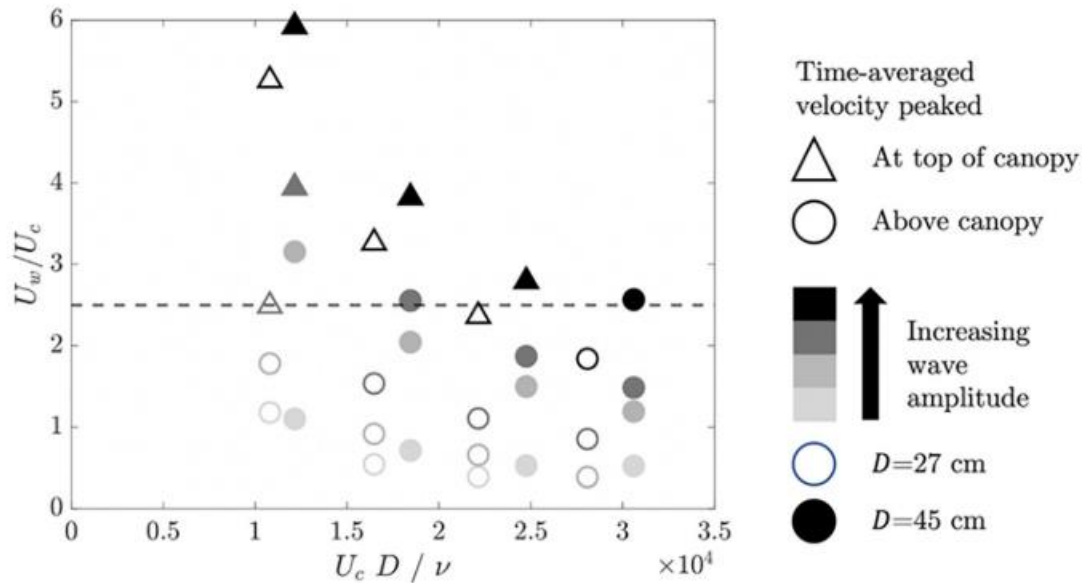


Figure 4.4: Wave-to-current velocity ratio (U_w/U_c) versus current Reynolds number ($U_c D / \nu$). Circles denote cases for which the time-averaged velocity peaked above the canopy, similar to pure current conditions. Triangles denote cases for which the time-averaged velocity peaked at the top of the canopy, indicating that the wave-induced mean current was significant within the meadow.

4.4.2 Reynolds stress and turbulence kinetic energy profiles

For pure current (red triangles in **Figure 4.3(B), (E)**) and wave-current (circles in **Figure 4.3(B), (E)**) cases with a clear mixing layer flow structure, the magnitude of the Reynolds stress was approximately zero near the bed, increased to a peak near the mean deflected meadow height (dashed horizontal lines in **Figure 4.3**), and then decreased with distance above the meadow. As the wave amplitude increased, the peak Reynolds stress magnitude decreased (**Figure 4.3(B), (E)**). A peak in TKE appeared near the top of the canopy (**Figure 4.3(C), (F)**), coincident with the peak in Reynolds stress, which was consistent with shear production (Equation 4.6). As the wave amplitude increased, this TKE peak was diminished, consistent with the decrease in Reynolds stress peak magnitude. The opposite trend was observed within the canopy. Specifically, as wave amplitude increased, TKE within the canopy increased (see the progression of light gray to darker gray to black symbols below the dashed lines in **Figure 4.3(C), (F)**), reflecting the contribution of wake production, which increased with the addition of waves. For larger waves, TKE in the upper water column increased toward the water surface (e.g., black circles in **Figure 4.3(F)**). The near-surface enhancement in TKE was attributed to a secondary circulation. Specifically, the interaction between progressive waves and vertical vorticity, here associated with the side-wall boundary layers, generated a secondary circulation by Langmuir instability, with downwelling at the channel center (Nepf and Monismith 1991). This circulation elevates near-surface turbulence (Nepf et al. 1995).

4.4.3 Predictions of magnitude of peak Reynolds stress

The addition of waves had little impact on the magnitude of peak Reynolds stress for $U_w/U_c < 1$, but for $U_w/U_c > 1$ the peak Reynolds stress magnitude decreased with increasing wave amplitude, compared to the corresponding pure current conditions (**Figure 4.5(A)**; also see the Reynolds stress profiles in Appendix C, noting the change in magnitude of the maximum Reynolds stress with increasing wave amplitude for each current). The reduction in Reynolds stress was predominantly associated with a decrease in velocity shear, rather than a change in the efficiency in turbulent momentum transport. This distinction was illustrated by considering the idealized two-layer model for canopy flow, which defines the Reynolds stress at the top of the meadow, $\tau_{h(max)}$, in terms of the layer-averaged time-averaged velocity within, U_1 , and above, U_2 , the meadow (Equation 4.3). When the momentum coefficient C ($= 0.014$ to 0.020) was estimated using Equation 4.2, then Equation 4.3 predicted the maximum magnitude of Reynolds stress within uncertainty (**Figure 4.5(B)**) for both pure current cases and the wave-current cases that exhibited shear layer behavior, indicating that the momentum coefficient was not significantly changed by the waves.

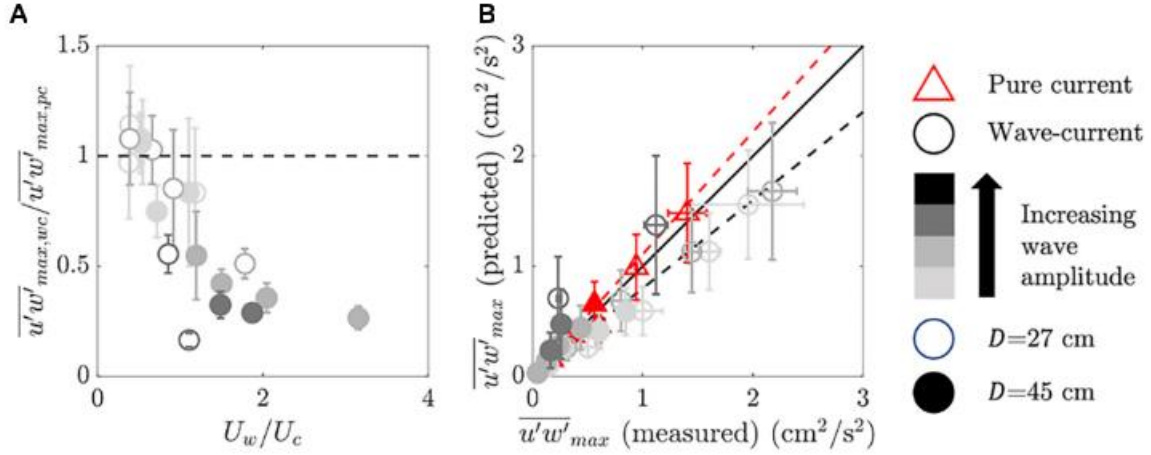


Figure 4.5: (A) Maximum magnitude of Reynolds stress in combined wave-current (subscript ‘wc’) conditions ($\overline{u'w'}_{max,wc}$) normalized by the maximum magnitude of Reynolds stress in corresponding pure current (subscript ‘pc’) conditions ($\overline{u'w'}_{max,pc}$) versus wave-to-current velocity ratio (U_w/U_c). (B) Predicted versus measured maximum magnitude of Reynolds stress ($\overline{u'w'}_{max}$). Cases that showed a shear layer flow structure were included. The dashed line in (A) denotes a ratio of 1. The red and black dashed lines in (B) denote the lines of best fit for pure current (red triangles) and combined wave-current (circles) cases, respectively. The solid black line in (B) is a one-to-one line. Error bars in (A) indicate uncertainties assessed using propagated uncertainties in the ratio of measured maximum magnitudes of Reynolds stress (single point measurements, using half of their range when the record was split in half) and in (B) indicate propagated uncertainties in the prediction of the maximum magnitude of Reynolds stress (from C [Equation 4.2], as well as U_2 and U_1 [in which the mean deflected height h_d measurements were the dominant source of uncertainty] in Equation 4.3).

However, note that the best fit line through the combined wave-current cases (black dashed line fitted to circles in **Figure 4.5(B)**, $\overline{u'w'}_{max} (predicted) = (0.80 \pm 0.09)\overline{u'w'}_{max} (measured)$) fell below that for the pure current cases (red dashed line fitted to triangles in **Figure 4.5(B)**, $\overline{u'w'}_{max} (predicted) = (1.11 \pm 0.07)\overline{u'w'}_{max} (measured)$), which suggested that Equation 4.2 underpredicted C by 20 to 30% for combined wave-current cases. This trend suggested that the presence of waves augmented the vertical turbulent transfer of momentum. However, this conclusion is only speculative, because in fact Equation 4.3 produced predictions consistent with the measured stress. The trends in **Figure 4.5** can be

explained as follows. The addition of waves reduced h_d , relative to pure current conditions, which increased the depth of overflow ($D - h_d$), which in turn decreased U_2 . The reduction in $U_2 - U_1$ led to a decrease in Reynolds stress. Because the efficiency of turbulent momentum change was not significantly altered (C was the same within uncertainty), the decrease in Reynolds stress was consistent with the decrease in velocity gradient (**Figure 4.5(B)**). It is important to note that if C is not impacted by waves (as suggested here), then two-layer models developed for pure current conditions can be used to predict the in-canopy velocity in combined wave-current conditions, using the deflected height (i.e., Equation 4.4), which is supported by analysis in Schaefer and Nepf (2022). This is a useful result for modeling flows through submerged meadows.

4.4.4 Canopy turbulent kinetic energy measurements and predictions

The canopy-averaged shear production $\langle P_s \rangle$ of turbulence was estimated by averaging Equation 4.6 over the deflected canopy height. The canopy-averaged wake production $\langle P_w \rangle$ of turbulence was estimated from Equation 4.7 using the in-canopy depth-averaged, time-averaged velocity, U_1 . This represents a lower bound on wake production, because $\langle \bar{u}(z)^3 \rangle > U_1^3$, and contributions from wave velocity were neglected. Even using an underestimate for $\langle P_w \rangle$, the ratio $\langle P_w \rangle / \langle P_s \rangle$ was greater than five for all but three cases and greater than 10 for all but eight cases (see Appendix B). Given this, it was reasonable to neglect the shear-production and thus to expect a form of Equation 8 to predict TKE within the canopy. However, we must determine the appropriate velocity scale for TKE prediction.

For combined wave-current conditions, Chen et al. (2020) proposed that stem-generated turbulence scaled with the sum of the wave velocity and imposed depth-averaged current velocity, i.e., with the maximum velocity in the wave period, U_{max} . Within a rigid submerged meadow, they observed a linear relationship between TKE and U_{max}^2 . Here, we considered a similar relationship in a flexible canopy, using the sum of the wave velocity U_w and in-canopy depth-averaged, time-averaged velocity U_1 . Recall that in the presence of waves, a wave-induced current will augment U_1 above the imposed current velocity (see Equation 4.4). Specifically, we considered the dependence of TKE and $(U_w + U_1)^2$, as shown in **Figure 4.6**.

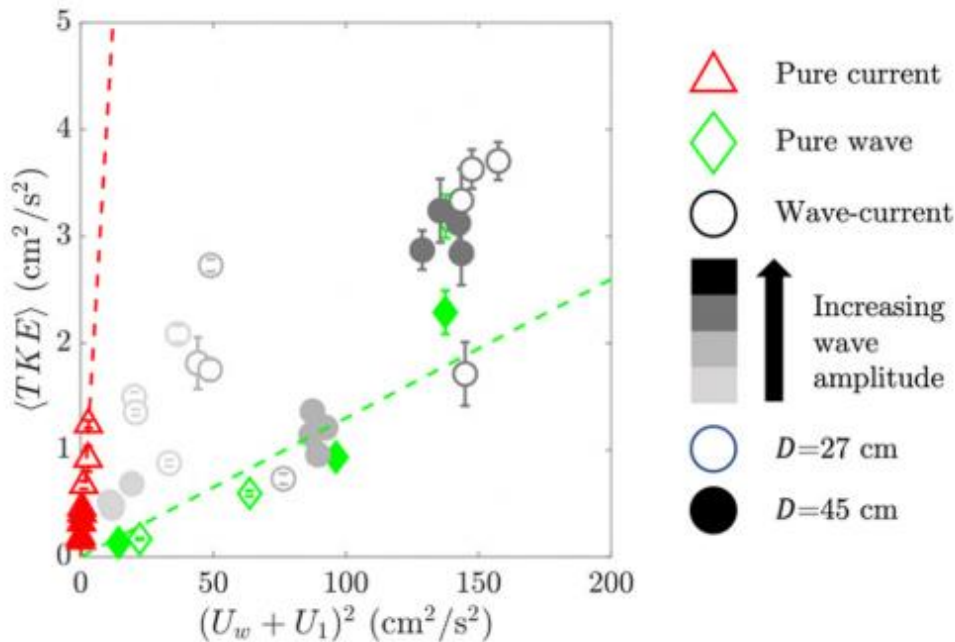


Figure 4.6: Measured canopy-averaged TKE ($\langle TKE \rangle$) versus the squared sum of the wave velocity and the in-canopy depth-averaged, time-averaged velocity ($(U_w + U_1)^2$). Red and green dashed lines denote best fit lines for pure current and pure wave cases, respectively. For clarity among the cases with smaller TKE, the highest TKE cases were excluded (see **Figure 4.7**). Error bars indicate uncertainties assessed in the canopy-averaged TKE (propagating uncertainties using half of the range from each measurement when the records were split in half).

First, note that there was a stronger dependence between TKE and velocity for pure current (red triangles in **Figure 4.6**) than for pure waves (green diamonds in **Figure 4.6**). Specifically, using the velocity scale ($U_w + U_1$) in Equation 4.9, the scale factor for pure current, $\delta_{pc} = 1.8 \pm 0.3$, was six times larger than for pure wave ($\delta_{pw} = 0.30 \pm 0.04$). This makes physical sense, because flexible blades can move with the wave orbital velocity, which reduces the relative velocity, the drag, and the wake turbulence production (Zhang and Nepf 2018). In pure current, the flexibility can allow plants to become more streamlined, but it cannot reduce the relative velocity. Zhang and Nepf (2018) also observed a smaller scale factor in Equation 4.9 for flexible blades under pure wave conditions. Specifically, using velocity scale $U_{w,RMS}$ in Equation 4.9 they found $\delta_{pw} = 0.44$, which converts to $\delta_{pw} = 0.22$ for the velocity scale U_w , as used here. Note that the pure current scale factor δ_{pc} was larger than the scale factor 1.1 found for rigid emergent cylinders (Tanino and Nepf 2008), which may be explained by the difference in morphology between emergent cylinders and submerged model plants. First, Equation 4.9 assumes that the integral length scale is equal to the blade width, $l_t = w_b$, which may not be appropriate in the lower canopy, where the blades are bundled into a sheath of larger dimension (sheath diameter = 0.7 cm), or near the top of the canopy where larger shear layer vortices are present (Poggi et al. 2004; Zhang et al. 2020). Second, Equation 4.9 uses the canopy-averaged velocity U_1 . However, for a submerged meadow the velocity varies over the canopy height, and U_1^2 will underestimate $\langle \bar{u}(z)^2 \rangle$, and this must be offset by a larger scale coefficient.

Next, consider the combined wave-current cases (gray to black circles in **Figure 4.6**), which predominantly fell in between the dependences observed for pure current (red triangles) and pure wave (green diamonds). This suggested that a simple hybrid wake production model

might collapse all of the cases. Specifically, we proposed the following modification to Equation 9 for wave-current conditions $\langle k_{t,wc} \rangle$:

$$\langle k_{t,wc} \rangle = \left(C_D \frac{m_b w_b^2}{2(1-\phi)} \right)^{\frac{2}{3}} (\delta_{pc}^2 U_1^2 + \delta_{pw}^2 U_w^2) \quad (4.13)$$

Indeed, this hybrid model collapsed most of the data (**Figure 4.7**).

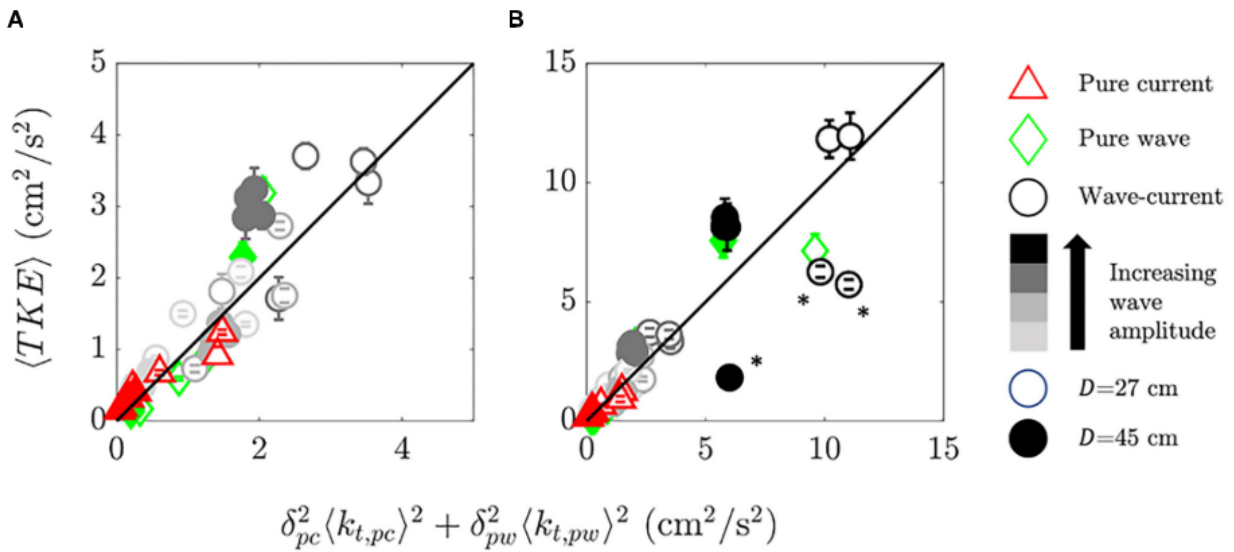


Figure 4.7: Measured canopy-averaged TKE ($\langle TKE \rangle$) versus the proposed hybrid model ($\delta_{pc}^2 \langle k_{t,pc} \rangle^2 + \delta_{pw}^2 \langle k_{t,pw} \rangle^2$, Equation 13) with (A) axes scaled to highlight that the majority of cases collapse reasonably well by the hybrid model and (B) showing all cases. The solid black lines denote one-to-one lines. In (B), asterisks denote cases involving the highest waves, but atypically low TKE, as discussed in Section 5.3 in the text. Error bars indicate uncertainties assessed in canopy-averaged TKE (as in **Figure 7**).

As an alternative to the hybrid model, it would be useful to evaluate when the canopy turbulence is dominated by either the current or the waves, allowing for prediction of $\langle k_t \rangle$ using only the wave or current velocity. Consider the ratio of canopy-averaged turbulence in wave-

current conditions $\langle TKE_{wc} \rangle$ normalized by corresponding TKE in pure current $\langle TKE_{pc} \rangle$ and pure wave $\langle TKE_{pw} \rangle$ versus U_w/U_c , as shown in **Figure 4.8**. For $U_w/U_c < 1$, increasing U_w/U_c had minimal impact on canopy turbulence relative to pure current conditions, compared to the increase in TKE observed with increasing U_w/U_c for $U_w/U_c > 1$ (**Figure 4.8(A)**). Alternatively, when current was added to waves, $\langle TKE_{wc} \rangle / \langle TKE_{pw} \rangle$ was greater than 1 for $U_w/U_c < 1$, but converged to 1 for $U_w/U_c > 1$ (**Figure 4.8(B)**). Together, these trends suggest that for $U_w/U_c > 1$, a good prediction of TKE can be made using just the wave velocity. Conversely, for $U_w/U_c < 1$, a good prediction of TKE can be made using just the current velocity.

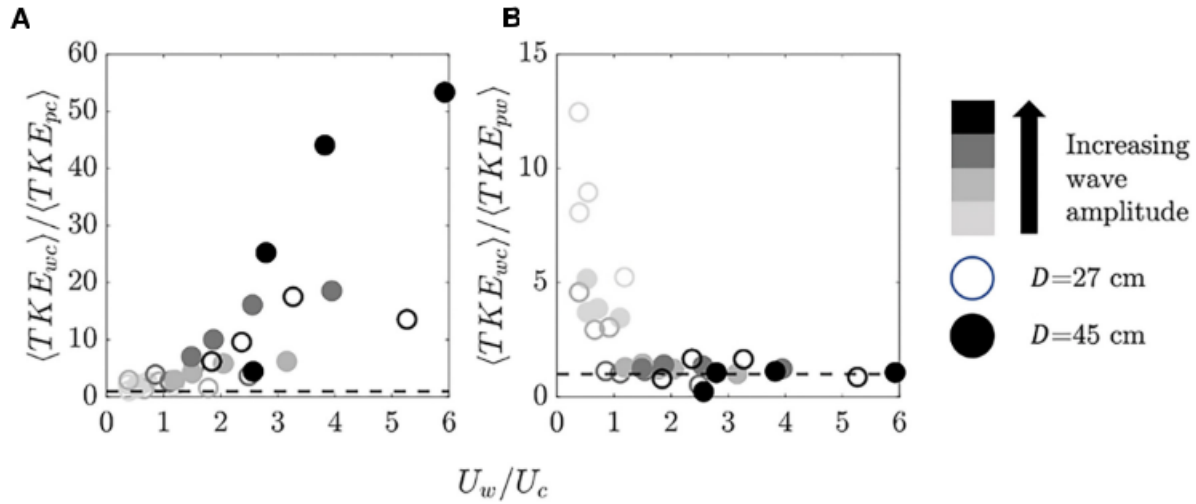


Figure 4.8: Canopy-averaged turbulent kinetic energy in wave-current (subscript ‘wc’) conditions ($\langle TKE_{wc} \rangle$) normalized by (A) canopy-averaged TKE in pure current (subscript ‘pc’) conditions ($\langle TKE_{pc} \rangle$) and (B) canopy-averaged TKE in pure wave (subscript ‘pw’) conditions ($\langle TKE_{pw} \rangle$), both versus the wave-to-current velocity ratio (U_w/U_c). The dashed horizontal lines are (A) $\langle TKE_{wc} \rangle / \langle TKE_{pc} \rangle = 1$ and (B) $\langle TKE_{wc} \rangle / \langle TKE_{pw} \rangle = 1$.

4.5 Discussion

Laboratory experiments with an artificial seagrass meadow described the impact of waves on the time-averaged velocity, Reynolds stress, and TKE within a flexible submerged meadow. The study considered a range of wave and current conditions for a single meadow density (950 shoots m^{-2} , 5700 blades m^{-2}). One major result of this study is that for a flexible meadow, wave velocity is less efficient in generating TKE (smaller scale coefficient), because wave-induced motion of the blades reduces the relative velocity between the blade and the waves. The resultant proposed hybrid model (Equation 4.13) is valid when wake production dominates shear production. Overall, this study provided important validation of models that predict Reynolds stress and turbulence within a submerged meadow in realistic conditions of combined waves and currents. These models provide a quantitative framework to predict ecosystem services facilitated by meadow-mediated hydrodynamic conditions.

4.5.1 Impact of waves on mean deflected height

The observed reduction in h_d in the presence of waves contrasted with observations in Paul and Gillis (2015), who observed that for combined wave and current conditions, the presence of a wave did not appear to impact the mean deflected canopy height. The discrepancy might be related to the fact that Paul and Gillis (2015) used the tip of the blade to estimate the canopy height, while the present study considered the highest position along the length of the blade. The pronation of blades in the direction of wave propagation, resulting in a decrease in mean deflected height, has been observed in previous studies and attributed to two mechanisms. First, observations showed that the vertical component of the wave orbital velocity induced

asymmetric blade motion and deflection in the direction of wave propagation (Döbken 2015). Second, the wave-induced current generated in the meadow can pronate the individual blades (Zhang and Nepf 2018).

4.5.2 Reynolds stress at the top of the canopy

The direct contribution of waves to shear and turbulent momentum exchange (i.e., Reynolds stress) at the top of the canopy is limited to long period waves, as described in Ghisalberti and Schlosser (2013). They defined a wave Reynolds number, $Re_w = 2U_w d / \pi \nu$, and a Keulegan-Carpenter number KC_s as the ratio of wave period to the time scale of vortex formation. Specifically, $KC_s = U_w T / L_D$, with $L_D = 2(C_D a_v)^{-1}(1 - \phi)$ (e.g., Chen et al. 2013). Pure waves can generate vortices at the top of a canopy only when both $KC_s > 5$ and Reynolds number $Re_w > 1000$. For the meadow in the present study, $KC_s < 2.2$ and $Re_w < 600$, indicating that the waves did not contribute to Reynolds stress or shear production at the top of the canopy, consistent with the fact that C was not impacted by the addition of waves.

In addition, note that the peak Reynolds stress did not always occur at the mean deflected height, but for most cases occurred within a few cm above the mean deflected height. This was in contrast to measurements in unidirectional flow made for a flexible meadow of lower density (230 shoot m^{-2}), for which the peak Reynolds stress was consistently at the canopy interface (Ghisalberti and Nepf 2006). The shoot density in the present study was much higher at 950 shoot m^{-2} , which may have reduced the shear penetration into the canopy, pushing the shear layer and peak Reynolds stress slightly above the canopy interface. Considering the measured

maximum deflected height instead of the measured mean deflected height, as in Ghisalberti and Nepf (2006), did not explain the slightly shifted position of the Reynolds stress peak.

4.5.3 Blade reconfiguration and wake production

For the three wave-current cases marked with asterisks in **Figure 4.7**, the canopy-averaged turbulence was noticeably lower than other wave-current cases of the same programmed wave amplitude and depth. Cases of the highest wave amplitudes had the smallest deflected heights (see Appendix B), with many blades touching the bed during the wave period (see the conceptual sketch in **Figure 4.9**). It was possible that the blades, which were in-line with the sheath, restricted flow around the sheath, which reduced or eliminated the shedding of vortices from the sheath for the marked cases. This is a potentially important observation, as it illustrates how wake turbulence can be eliminated when the meadow pronation due to reconfiguration becomes extreme. While this description does not fully explain the differences in canopy TKE among all of the strongest wave cases, it was likely a contributing factor.

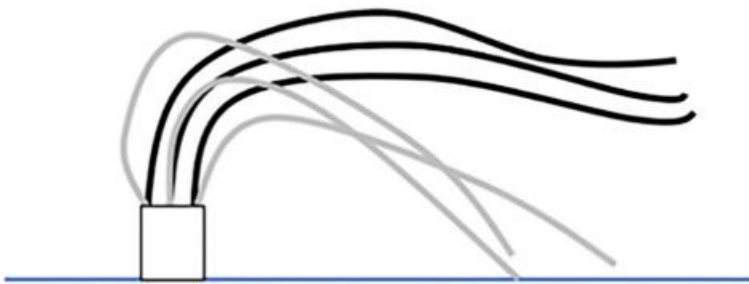


Figure 4.9: Conceptual sketch of the side view of a model seagrass plant showing blade motion under a wave crest (black curves) and wave trough (gray curves), corresponding to the strongest wave forcing (e.g., black circles in **Figure 4.7**). The rectangle represents the sheath.

4.5.4 Relative strengths of wave and current velocities

For clarity, we note that the aforementioned threshold of approximately $U_w/U_c = 2.5$ described changes in the time-mean velocity profile. Specifically, the time-mean velocity peaked above the canopy when $U_w/U_c < 2.5$, and peaked at the top of the canopy when $U_w/U_c > 2.5$.

Meanwhile, shifts in canopy turbulence were observed at a lower threshold $U_w/U_c = 1$.

Combining these, when $1 < U_w/U_c < 2.5$, the wave velocity dominated the production of TKE in the canopy, but did not significantly modify the current-induced time-mean flow structure behavior. We note that these transitions may have some dependence on canopy density, which was not explored in the present study. Finally, seagrass meadows exhibit a wide range of density (140 to 30000 blades per bed area; see Table 3 in Luhar et al. 2010), both more and less dense than the model canopy considered in this study (5700 blades m^{-2}). The assumption that wake production dominates shear production, which was validated in the present study, likely extends to denser meadows, but may not be valid in sparser meadows.

4.6 Acknowledgments

This material is based upon work supported by the National Science Foundation under Grant No. 1659923 and the National Science Foundation Graduate Research Fellowship under Grant No. 1122374. R. Schaefer was supported in part by the Louis Berger Fellowship Fund in the Massachusetts Institute of Technology Department of Civil and Environmental Engineering.

4.7 References

- Brunet, Y., Finnigan, J. J., and Raupach, M. R. (1994). A wind tunnel study of air flow in waving wheat: Single-point velocity statistics. *Boundary-Layer Meteorol.*, 70(1–2), 95–132. doi: 10.1007/BF00712525
- Carus, J., Arndt, C., Bouma, T. J., Schröder, B., and Paul, M. (2020). Effect of artificial seagrass on hydrodynamic thresholds for the early establishment of *Zostera marina*. *J. Ecohydraul.*, 0(0), 1–11. doi: 10.1080/24705357.2020.1858197
- Chen, M., Lou, S., Liu, S., Ma, G., Liu, H., Zhong, G., and Zhang, H. (2020). Velocity and turbulence affected by submerged rigid vegetation under waves, currents and combined wave-current flows. *Coast. Eng.*, 159. doi: 10.1080/10643389.2012.728825
- Chen, Z., Jiang, C., and Nepf, H. M. (2013). Flow adjustment at the leading edge of a submerged aquatic canopy. *Water Resour. Res.*, 49(9), 5537–5551. doi: 10.1002/wrcr.20403
- Cheng, N. S. (2011). Representative roughness height of submerged vegetation. *Water Resour. Res.*, 47(8), 1–18. doi: 10.1029/2011WR010590
- Dean, R. G., & Dalrymple, R. A. (1984). *Water Wave Mechanics for Engineers and Scientists*. Englewood Cliffs, NJ: Prentice-Hall.
- Döbken, J. W. D. (2015). Modeling the interaction of wave hydrodynamics with flexible aquatic vegetation. Master's Thesis. Delft (The Netherlands): Delft University of Technology.
- Fonseca, M. S., Fisher, J. S., Zieman, J. C., and Thayer, G. W. (1982). Influence of the seagrass, *Zostera marina* L., on current flow. *Estuar. Coast. Shelf. Sci.*, 15(4), 351–364. doi: 10.1016/0272-7714(82)90046-4
- Fonseca, Mark S., and Cahalan, J. A. (1992). A preliminary evaluation of wave attenuation by four species of seagrass. *Estuar. Coast. Shelf. Sci.*, 35(6), 565–576. doi: 10.1016/S0272-7714(05)80039-3
- Fonseca, Mark S., Koehl, M. A. R., and Kopp, B. S. (2007). Biomechanical factors contributing to self-organization in seagrass landscapes. *J. Exp. Mar. Biol. Eco.*, 340(2), 227–246. doi: 10.1016/j.jembe.2006.09.015
- Ghisalberti, M., and Nepf, H. M. (2006). The structure of the shear layer in flows over rigid and flexible canopies. *Environ. Fluid Mech.*, 6(3), 277–301. doi: 10.1007/s10652-006-0002-4
- Ghisalberti, M., and Nepf, H. M. (2002). Mixing layers and coherent structures in vegetated aquatic flows. *J. Geophys. Res.*, 107(C2), 3-1-3–11. doi: 10.1029/2001jc000871
- Ghisalberti, M., and Schlosser, T. (2013). Vortex generation in oscillatory canopy flow. *J. Geophys. Res. Oceans*, 118(3), 1534–1542. doi: 10.1002/jgrc.20073

- Gillis, L. G., Paul, M., and Bouma, T. (2017). Ammonium uptake rates in a seagrass bed under combined waves and currents. *Front. Mar. Sci.*, 4(JUN), 1–7. doi: 10.3389/fmars.2017.00207
- Ginsburg, R., and Lowenstam, H. (1958). The influence of marine bottom communities on the depositional environment of sediments. *J. Geol.*, 66(3), 310–318. doi: 10.1086/626507
- Gjørsund, S. H. (2003). A Lagrangian model for irregular waves and wave kinematics. *J. Offshore Mech. Arct. Eng.*, 125(2), 94–102. doi: 10.1115/1.1554702
- Goda, Y., and Suzuki, Y. (1977). Estimation of incident and reflected waves in random wave experiments. *Proc. Fifteenth Coastal Engng. Conf. (Hawaii Univ., U.S.A., Jul.11-17, 1976)*, 828–845. doi: 10.9753/icce.v15.47
- Goring, D. G., and Nikora, V. I. (2002). Despiking acoustic Doppler velocimeter data. *J. Hydraul. Eng.*, 117–126. doi: 10.1061/(ASCE)0733-9429(2002)128:1(117)
- Homziak, J., Fonseca, M., and Kenworthy, W. (1982). Macrobenthic community structure in a transplanted eelgrass (*Zostera marina*) meadow. *Mar. Ecol. Progr. Ser.*, 9(3), 211–221. doi: 10.3354/meps009211
- Huthoff, F., Augustijn, D. C. M., and Hulscher, S. J. M. H. (2007). Analytical solution of the depth-averaged flow velocity in case of submerged rigid cylindrical vegetation. *Water Resour. Res.*, 43(6), 1–10. doi: 10.1029/2006WR005625
- Infantes, E., Orfila, A., Bouma, T. J., Simarro, G., and Terrados, J. (2011). *Posidonia oceanica* and *Cymodocea nodosa* seedling tolerance to wave exposure. *Limnol. Oceanogr.*, 56(6), 2223–2232. doi: 10.4319/lo.2011.56.6.2223
- Keulegan, G. H., and Carpenter, L. H. (1958). Forces on cylinders and plates in an oscillating fluid. *J. Res. Natl. Bur. Stand.*, 60(5), 423. doi: 10.6028/jres.060.043
- Knutson, P. L., Brochu, R. A., and Seelig, W. N. (1982). Wave damping in *Spartina alterniflora* marshes. *Wetlands*, 2(1), 87–104. doi: 10.1007/BF03160548
- Koch, E. W., Verduin, J. J., Keulen, M. Van, and Orth, R. J. (2006). "Fluid Dynamics in Seagrass Ecology - from Molecules to Ecosystems," in *Seagrasses: Biology, Ecology and Conservation*, ed. A. W. D. Larkum, R. J. Orth, and C. M. Duarte (Dordrecht, The Netherlands: Springer), 193–225.
- Konings, A. G., Katul, G. G., and Thompson, S. E. (2012). A phenomenological model for the flow resistance over submerged vegetation. *Water Resour. Res.*, 48(2), 1–9. doi: 10.1029/2011WR011000
- Lei, J., and Nepf, H. M. (2021). Evolution of flow velocity from the leading edge of 2-D and 3-D submerged canopies. *J. Fluid Mech.*, 916, 1–27. doi: 10.1017/jfm.2021.197

- Lei, J., and Nepf, H. M. (2016). Impact of current speed on mass flux to a model flexible seagrass blade. *J. Geophys. Res. Oceans*, 121, 3372–3380. doi: 10.1002/2016JC011826
- LeMéhauté, B. (1976). *An Introduction to Hydrodynamics and Water Waves*. New York: Springer Science+Business Media.
- Lou, S., Chen, M., Ma, G., Liu, S., and Zhong, G. (2018). Laboratory study of the effect of vertically varying vegetation density on waves, currents and wave-current interactions. *Appl. Ocean Res.*, 79(July), 74–87. doi: 10.1016/j.apor.2018.07.012
- Luhar, M. (2012). Analytical and experimental studies of plant-flow interaction at multiple scales. Dissertation. Cambridge (MA): Massachusetts Institute of Technology
- Luhar, M. (2021). Comment on “The wave-driven current in coastal canopies” by M. Abdolahpour et al. *J. Geophys. Res. Oceans*, 126(8), 1–6. doi: 10.1029/2019jc015644
- Luhar, M., Coutu, S., Infantes, E., Fox, S., and Nepf, H. M. (2010). Wave-induced velocities inside a model seagrass bed. *J. Geophys. Res. Oceans*, 115(12), 1–15. doi: 10.1029/2010JC006345
- Luhar, M., and Nepf, H. M. (2011). Flow-induced reconfiguration of buoyant and flexible aquatic vegetation. *Limnol. Oceanogr.*, 56(6), 2003–2017. doi: 10.4319/lo.2011.56.6.2003
- Luhar, M., and Nepf, H. M. (2013). From the blade scale to the reach scale: A characterization of aquatic vegetative drag. *Adv. Water Resour.*, 51, 305–316. doi: 10.1016/j.advwatres.2012.02.002
- Monismith, S. G., Cowen, E. A., Nepf, H. M., Magnaudet, J., and Thais, L. (2007). Laboratory observations of mean flows under surface gravity waves. *J. Fluid Mech.*, 573, 131–147. doi: 10.1017/S0022112006003594
- Moore, K. A. (2004). Influence of seagrasses on water quality in shallow regions of the Lower Chesapeake Bay. *J. Coast. Res.* 2009(10045), 162–178. doi: 10.2112/si45-162.1
- Nepf, H. M., Ghisalberti, M., White, B., and Murphy, E. (2007). Retention time and dispersion associated with submerged aquatic canopies. *Water Resour. Res.*, 43(4), 1–10. doi: 10.1029/2006WR005362
- Nepf, H. M., Cowen, E. A., Kimmel, S. J., and Monismith, S. G. (1995). Longitudinal vortices beneath breaking waves. *J. Geophys. Res.*, 100(C8). doi: 10.1029/95jc01405
- Nepf, H. M., and Monismith, S. G. (1991). Experimental study of wave-induced longitudinal vortices. *J. Hydraul. Eng.*, 117(12), 1639–1649. doi: 10.1061/(ASCE)0733-9429(1991)117:12(1639)
- Nepf, H. M. (1999). Drag, turbulence, and diffusion in flow through emergent vegetation. *Water Resour. Res.*, 35(2), 479–489. doi: 10.1029/1998WR900069

- Nepf, H. M. (2012). Hydrodynamics of vegetated channels. *J. Hydraul. R.*, 50(3), 262–279. doi: 10.1080/00221686.2012.696559
- Nepf, H. M., and Vivoni, E. R. (2000). Flow structure in depth-limited, vegetated flow. *J. Geophys. Res.*, 105(C12), 28547–28557. doi: 10.1029/2000JC900145
- Paul, M., and Gillis, L. G. (2015). Let it flow: How does an underlying current affect wave propagation over a natural seagrass meadow? *Mar. Ecol. Progr. Ser.*, 523, 57–70. doi: 10.3354/meps11162
- Peralta, G., Brun, F. G., Pérez-Lloréns, J. L., and Bouma, T. J. (2006). Direct effects of current velocity on the growth, morphometry and architecture of seagrasses: A case study on *Zostera noltii*. *Mar. Ecol. Progr. Ser.*, 327, 135–142. doi: 10.3354/meps327135
- Poggi, D., Porporato, A., Ridolfi, L., Albertson, J. D., and Katul, G. G. (2004). The effect of vegetation density on canopy sub-layer turbulence. *Boundary-Layer Meteorol.*, 111(3), 565–587. doi: 10.1023/B:BOUN.0000016576.05621.73
- Raupach, M. R., Finnigan, J. J., and Brunet, Y. (1996). Coherent eddies and turbulence in vegetation canopies: the mixing-layer analogy. *Boundary-Layer Meteorol.*, 78(3–4), 351–382. doi: 10.1007/BF00120941
- Sarpkaya, T., and Storm, M. (1985). In-line force on a cylinder translating in oscillatory flow. *Appl. Ocean Res.*, 7(4), 188–196. doi: 10.1016/0141-1187(85)90025-2
- Schaefer, R. B., and H. M. Nepf. (2022). Flow structure in an artificial seagrass meadow in combined wave-current conditions. *Front. Mar. Sci.* 9, 1–12. doi: 10.3389/fmars.2022.836901
- Smith, J. A. (2006). Observed variability of ocean wave Stokes drift, and the Eulerian response to passing groups. *J. Phys. Oceanogr.*, 36(7), 1381–1402. doi: 10.1175/JPO2910.1
- Tang, C., Lei, J., and Nepf, H. M. (2019). Impact of vegetation-generated turbulence on the critical, near-bed, wave-velocity for sediment resuspension. *Water Resour. Res.*, 55(7), 5904–5917. doi: 10.1029/2018WR024335
- Tanino, Y., and Nepf, H. M. (2008). Lateral dispersion in random cylinder arrays at high Reynolds number. *J. Fluid Mech.*, 600, 339–371. doi: 10.1017/S0022112008000505
- Tennekes, H., and Lumley, J. L. (1972). *A First Course in Turbulence*. Cambridge, MA: The MIT Press.
- Tinoco, R. O., and Coco, G. (2018). Turbulence as the main driver of resuspension in oscillatory flow through vegetation. *J. Geophys. Res.: Earth Surf.*, 123(5), 891–904. doi: 10.1002/2017JF004504

- Ward, L. G., Kemp, W. M., and Boynton, W. R. (1984). The influence of waves and seagrass communities on suspended particulates in an estuarine embayment. *Mar. Geol.*, 59(1–4), 85–103. doi: 10.1016/0025-3227(84)90089-6
- Yang, J. Q., Chung, H., and Nepf, H. M. (2016). The onset of sediment transport in vegetated channels predicted by turbulent kinetic energy. *Geophys. Res. Lett.*, 43(21), 11,261–11,268. doi: 10.1002/2016GL071092
- Zhang, J., Lei, J., Huai, W., and Nepf, H. M. (2020). Turbulence and particle deposition under steady flow along a submerged seagrass meadow. *J. Geophys. Res.: Oceans*, 125(5), 1–19. doi: 10.1029/2019JC015985
- Zhang, Y., Lai, X., Ma, J., Zhang, Q., Yu, R., Yao, X., and Deng, H. (2021). Field study on flow structures within aquatic vegetation under combined currents and small-scale waves. *Hydrol. Process.*, 35(4). doi: 10.1002/hyp.14121
- Zhang, Y., and Nepf, H. M. (2019). Wave-driven sediment resuspension within a model eelgrass meadow. *J. Geophys. Res.: Earth Surf.*, 124(4), 1035–1053. doi: 10.1029/2018JF004984
- Zhang, Y., Tang, C., and Nepf, H. M. (2018). Turbulent kinetic energy in submerged model canopies under oscillatory flow. *Water Resour. Res.*, 54(3), 1734–1750. doi: 10.1002/2017WR021732

4.8 Supplementary Information

4.8.1 Dictionary of symbols

Table 4.S.1: Descriptions and units of symbols used in the main text.

Symbol	Description	Unit
$\bar{\quad}$	Time average	
$\langle \quad \rangle$	Canopy spatial vertical average	
U_w	Wave velocity amplitude	m s^{-1}
U_c	Depth-averaged imposed current velocity	m s^{-1}
U_1	Depth-averaged, time-averaged in-canopy velocity	m s^{-1}
U_2	Depth-averaged, time-averaged overflow layer velocity	m s^{-1}
D	Mean water depth	m
h	Undeflected canopy height	m
h_d	Deflected canopy height	m
C_D	Drag coefficient	
a_v	Canopy frontal area per canopy volume	m^{-1}
m_s / m_b	Number of stems / blades per unit bed area	m^{-2}
d / w_b	Stem diameter / blade width	m
δ_e	Shear layer penetration depth	m

ϕ	Canopy solid volume fraction	
l_e	Effective blade length	m
C	Coefficient of momentum exchange at the top of the canopy	
K_c	Empirical coefficient used in C	
$\tau_{h(max)}$	Reynolds shear stress at the top of the canopy	$\text{kg m}^{-1} \text{s}^{-2}$
ρ	Density of water	kg m^{-3}
u, v, w	Streamwise, lateral, and vertical velocity	m s^{-1}
u', v', w'	Fluctuations in streamwise, lateral, and vertical velocities	m s^{-1}
t	Time	s
z	Vertical coordinate (with $z = 0$ at the bed)	m
x	Streamwise coordinate (with $x = 0$ at the leading edge of the meadow)	m
$\overline{U_{max}}$	Maximum wave-induced current within the canopy	m s^{-1}
k	Wave number	m^{-1}
T / σ	Wave period / wave angular frequency	s / s^{-1}
P_s	Shear production	$\text{m}^2 \text{s}^{-3}$
P_w	Wake production	$\text{m}^2 \text{s}^{-3}$
ε	Turbulent dissipation rate	$\text{m}^2 \text{s}^{-3}$

TKE	Turbulent kinetic energy (observed)	$\text{m}^2 \text{s}^{-2}$
k_t	Turbulent kinetic energy (predicted)	$\text{m}^2 \text{s}^{-2}$
l_t	Integral length scale	m
δ	Scale factor	
ν	Kinematic viscosity of water	$\text{m}^2 \text{s}^{-1}$
L_D	Drag length scale	m

4.8.2 Experimental parameters

Table 4.S.2: Experimental parameters for pure wave ('PW'), pure current ('PC'), and combined wave-current ('WC') conditions. a_w is wave amplitude. The final row includes typical uncertainties.

Type	D (cm)	$a_{w,x=2.8 m}$ (cm)	T (s)	U_c (cm/s)	U_1 (cm/s)
PW	27	0.8	2	0	0
PW	27	1.3	2	0	0.5
PW	27	1.7	2	0	1.9
PW	27	3.6	2	0	3.5
PC	27	0	N/A	4.0	0.7
PC	27	0	N/A	6.1	0.9
PC	27	0	N/A	8.2	1.5

PC	27	0	N/A	10.4	1.7	
WC	27	0.8	2	4.0	1.0	
WC	27	0.6	2	6.1	1.2	
WC	27	0.6	2	8.2	1.3	
WC	27	0.7	2	10.4	2.1	
WC	27	1.2	2	4.0	1.6	
WC	27	1.0	2	6.1	1.0	
WC	27	0.9	2	8.2	1.6	
WC	27	0.7	2	10.4	3.0	
WC	27	1.7	2	4.0	2.1	
WC	27	1.6	2	6.1	3.2	
WC	27	1.6	2	8.2	2.9	
WC	27	1.5	2	10.4	3.3	
WC	27	3.5	2	4.0	5.9	
WC	27	3.3	2	6.1	4.2	
WC	27	3.2	2	8.2	4.3	
WC	27	3.2	2	10.4	4.0	
<hr/>						
PW	45	0.9	2	0	-0.1	
PW	45	1.9	2	0	1.0	
PW	45	2.4	2	0	0.6	
PW	45	4.0	2	0	2.1	
PC	45	0	N/A	2.7	0.3	
PC	45	0	N/A	4.1	0.3	

PC	45	0	N/A	5.5	0.5
PC	45	0	N/A	6.8	0.7
WC	45	0.7	2	2.7	0.5
WC	45	0.7	2	4.1	0.4
WC	45	0.6	2	5.5	0.5
WC	45	0.8	2	6.8	0.8
WC	45	1.9	2	2.7	0.9
WC	45	1.8	2	4.1	0.9
WC	45	1.8	2	5.5	1.1
WC	45	1.8	2	6.8	1.5
WC	45	2.3	2	2.7	1.3
WC	45	2.2	2	4.1	1.5
WC	45	2.2	2	5.5	1.3
WC	45	2.2	2	6.8	1.2
WC	45	3.4	2	2.7	2.4
WC	45	3.3	2	4.1	2.8
WC	45	3.3	2	5.5	2.5
WC	45	3.7	2	6.8	5.4
	0.2	0.1	0.02	0.2	0.1

4.8.3 Time-averaged velocity, Reynolds stress, and turbulent kinetic energy profiles for all cases

Time-averaged velocity profiles are shown in Figure 4.S.1. Pure waves (first column, Figure 4.S.1(A), (F)) produce wave-induced time-mean currents within the meadow (in the direction of wave propagation) and return currents above the meadow, resulting in a peak velocity near the top of the meadow. The magnitude of wave-induced current increased as the wave amplitude increased and agreed with the model prediction of Luhar (2021) (see Equation 5 in the main text, and Schaefer and Nepf, 2022, in review).

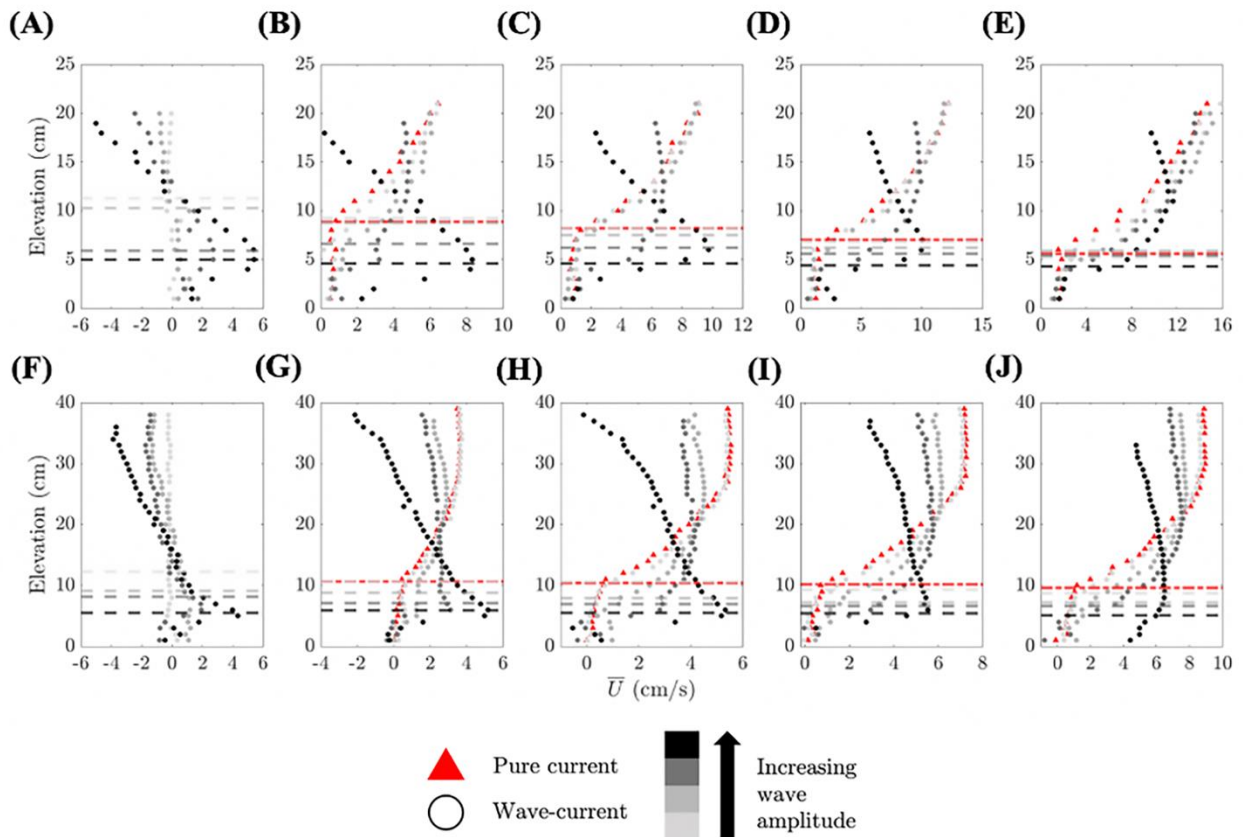


Figure 4.S.1: Distance above the bed (z) versus time-averaged streamwise velocity (\bar{U}) for depths (A-E) $D=27$ cm and (F-J) $D=45$ cm. The first column includes pure wave conditions, and

the imposed current increases from the second through fifth columns (see Table 4.S.2). Horizontal dashed lines denote measured h_d , with matching colors (dashed-dotted lines correspond to pure current cases). Profiles could not be extended over the entire depth due to limitations of the instrument and the presence of waves.

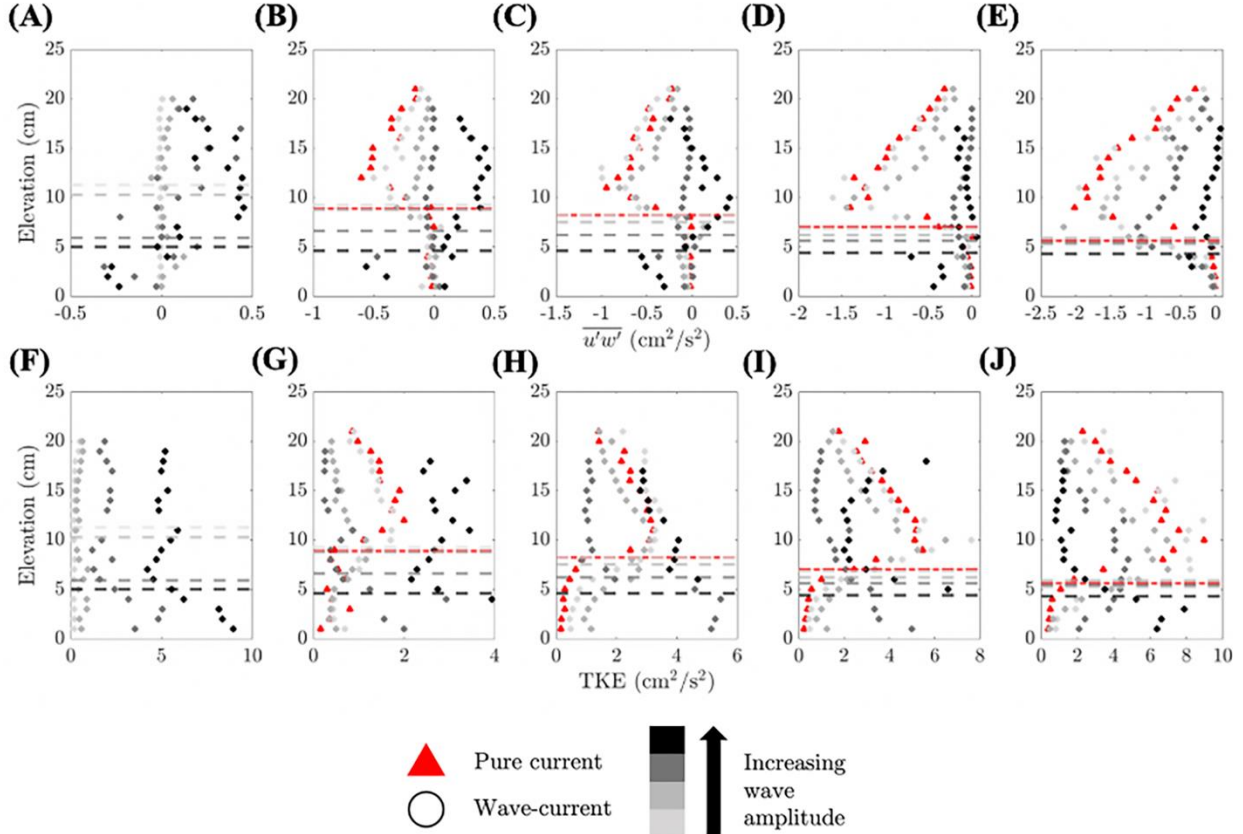


Figure 4.S.2: Distance above the bed (z) versus (A-E) Reynolds stress $\overline{u'w'}$ and (F-J) turbulent kinetic energy (TKE) profiles for the depth $D=27$ cm. The first column includes pure wave conditions, and the imposed current increases from the second through fifth columns (see Table 4.S.2). Horizontal dashed lines denote measured deflected meadow height h_d , with matching colors (dashed-dotted lines correspond to pure current cases). Profiles could not be extended over the entire depth due to limitations of the instrument and the presence of waves. Some points from cases involving the stronger two waves (black and darkest gray circles) are outside of the shown x-axis ranges in order to show the details of the other profiles.

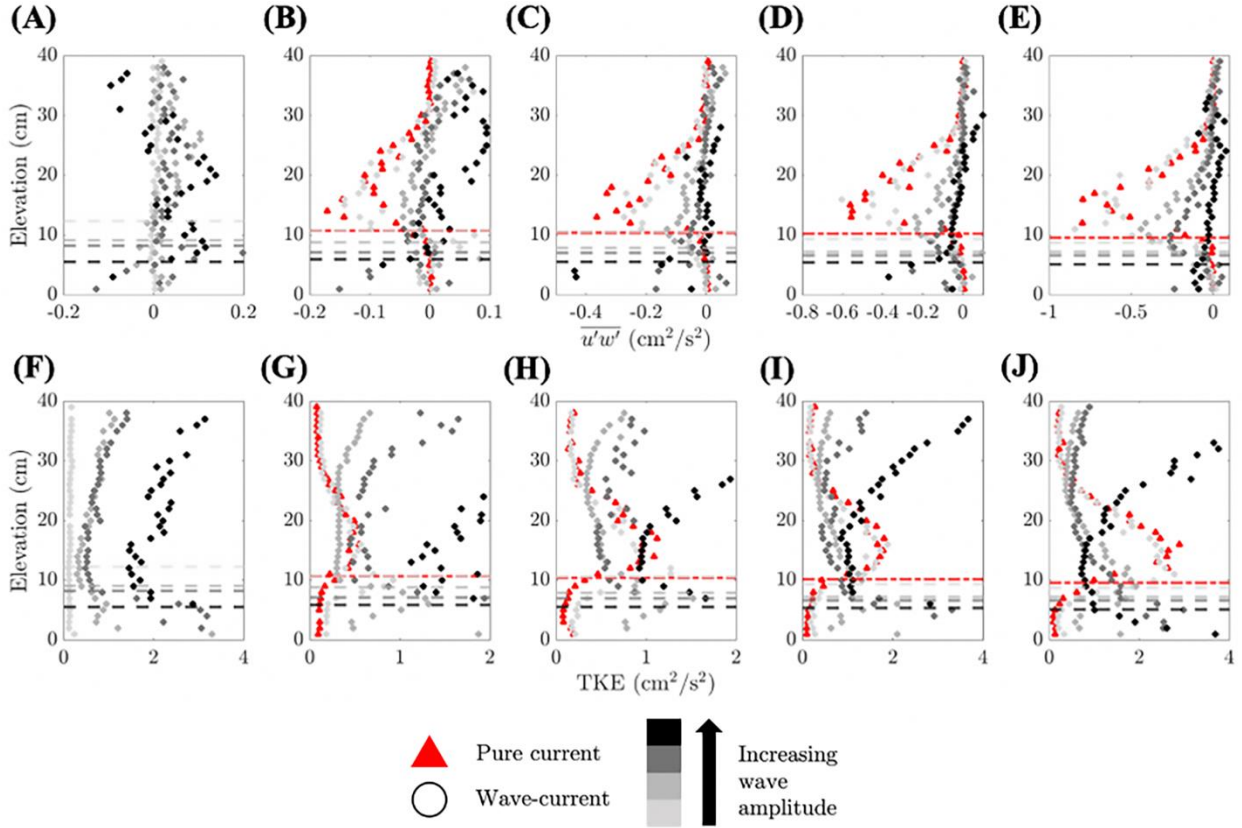


Figure 4.S.3: (A-E) Distance above the bed (z) versus Reynolds stress ($\overline{u'w'}$) and (F-J) turbulent kinetic energy (TKE) profiles for the depth $D=45$ cm. The first column includes pure wave conditions, and the imposed current increases from the second through fifth columns (Table 4.S.2). Horizontal dashed lines denote measured deflected meadow height h_d , with matching colors (dashed-dotted lines correspond to pure current cases). Profiles could not be extended over the entire depth due to limitations of the instrument and the presence of waves. Some points from cases involving the stronger two waves (black and darkest gray circles) are outside of the shown x-axes ranges in order to show the details of the other profiles.

4.8.4 Additional figures

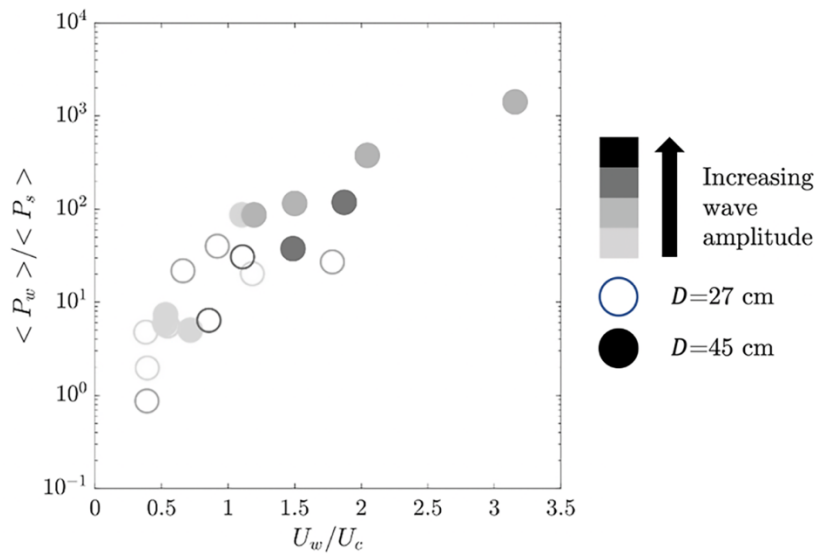


Figure 4.S.4: Ratio of lower-bound canopy-averaged wake production ($\langle P_w \rangle$) predicted using Equation 4.8 in the main text (using the in-canopy time-averaged velocity scale U_1) to canopy-averaged measured shear production ($\langle P_s \rangle$) using Equation 4.6 in the main text versus the wave-to-current velocity ratio (U_w/U_c), specifically for cases showing typical shear layer structure. Note the logarithmic scale on the y-axis. Ratios increased with increasing U_w/U_c due to the decrease in Reynolds stress peak magnitude (see Figure 4.5 in the main text).

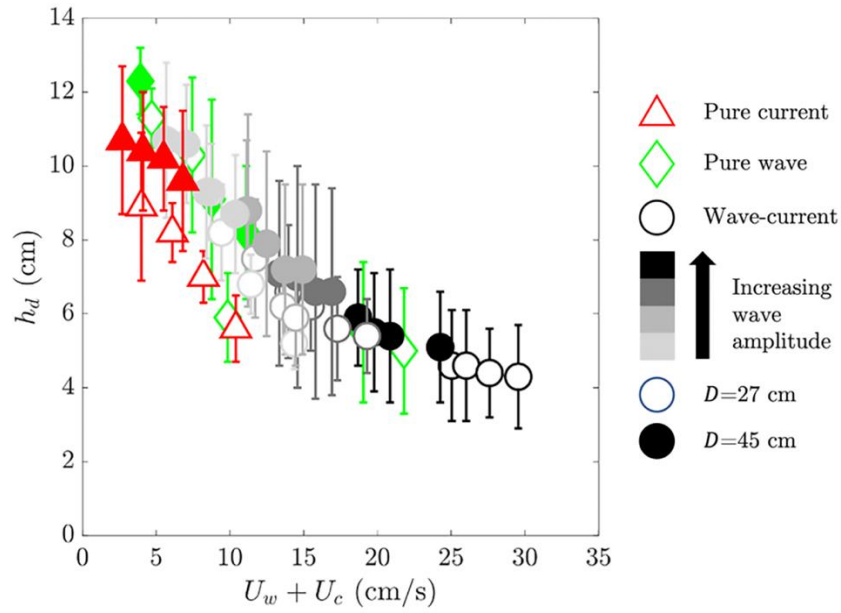


Figure 4.S.5: Measured mean deflected height (h_d) versus the sum of the wave and current velocity ($U_w + U_c$) for each case. Error bars denote standard deviation. The mean deflected height decreased with increasing current velocity, and decreased with increasing wave amplitude.

Chapter 5

Spatial heterogeneity in sediment and carbon accretion rates within a seagrass meadow correlated with the hydrodynamic intensity⁴

Abstract:

The majority of the carbon stored in seagrass sediments originates outside the meadow, such that the carbon storage capacity within a meadow is strongly dependent on hydrodynamic conditions that favor deposition and retention of fine organic matter within the meadow. By extension, if hydrodynamic conditions vary across a meadow, they may give rise to spatial gradients in carbon. This study considered whether the spatial gradients in sediment and carbon accretion

⁴ This chapter was co-authored and published as Lei et al. (2023). R. Schaefer is a co-first-author

rates correlated with the spatial variation in hydrodynamic intensity within a single meadow. Field measurements were conducted in three depth zones across a *Zostera marina* L. (eelgrass) meadow in Nahant Harbor, Massachusetts. Four sediment cores were collected in each zone, including one outside the meadow (control) and three within the meadow at increasing distances from the nearest meadow edge. Sedimentation and carbon accretion rates were estimated by combining the measurements of dry bulk density, organic carbon fraction (%OC), ^{210}Pb , and ^{226}Ra . Tilt current meters measured wave velocities within each zone, which were used to estimate turbulent kinetic energy (*TKE*). Both sediment and carbon accretion rates exhibited spatial heterogeneity across the meadow, which were correlated with the spatial variation in near-bed *TKE*. Specifically, both accretion rates increased with decreasing *TKE*, which was consistent with diminished resuspension associated with lower *TKE*. A method is proposed for using spatial gradients in hydrodynamic intensity to improve the estimation of total meadow accretion rates.

5.1 Introduction

Seagrass meadows are global hotspots for carbon storage (e.g., Kennedy et al., 2010; Duarte et al., 2010; Fourqurean et al., 2012). However, carbon stocks vary significantly between different seagrass sites. For example, Lavery et al. (2013) reported an 18-fold range in carbon stock measured across seventeen different seagrass habitats (260 to 4800 g C m⁻²). Similarly, Serrano et al. (2014) observed a 14-fold difference in carbon stock over a 10-fold difference in water

depth, which they attributed to gradients in light availability. The variability in carbon stock is a major source of uncertainty in assessing global seagrass carbon stocks; therefore, there is a need to understand the factors driving this variability (Lavery et al., 2013; Serrano et al., 2014).

More than 50% of the carbon stored in seagrass sediments originates outside the meadow (known as allochthonous carbon), so that the carbon storage capacity within a meadow is dependent on hydrodynamic conditions that favor deposition and retention of fine organic matter (e.g., Gacia and Duarte, 2001; Gacia et al., 1999; Kennedy et al., 2010). Therefore, hydrodynamic conditions should help to explain differences in measured seagrass carbon stocks and burial rates (Granata et al., 2001; Gruber and Kemp, 2010). For example, Oreska et al. (2017) observed that sediment organic carbon increased with distance from the meadow edge and attributed this to the attenuation of current by meadow drag forces. Ricart et al. (2020) attributed an increase in seagrass meadow carbon stocks between the lower and upper regions of an estuary to a decrease in hydrodynamic intensity. Similarly, Novak et al. (2020) observed higher carbon stocks at sites with lower wave and current exposure.

The correlation between hydrodynamic intensity and carbon stock is likely due to sediment resuspension. For example, Dahl et al. (2018) showed that sediment resuspension within a meadow led to a loss of carbon from the surface sediment. Previous studies have linked resuspension within a meadow to near-bed turbulent kinetic energy (*TKE*). Resuspension occurs when *TKE* increases above a critical magnitude, which depends on the median sediment grain size (e.g., Tinoco and Coco, 2018; Tang et al., 2019). For a unidirectional current interacting with a submerged meadow, spatial gradients in *TKE* have been correlated with spatial gradients of net deposition. Specifically, when a unidirectional current encounters a submerged meadow,

the hydrodynamic drag generated by the meadow causes the within-meadow current velocity and *TKE* to decrease with distance from the leading edge (e.g., Chen et al., 2013; Lei and Nepf, 2021). Zhang et al (2020) observed that net deposition increased with distance from the meadow leading edge, correlated with the progressive decrease in *TKE*.

In addition to reducing current velocity, seagrass meadows also attenuate wave energy, which may diminish near-bed wave velocity (e.g., Fonseca and Calahan, 1992; Mendez and Losada, 2004; Infantes et al., 2012; Lei and Nepf, 2019). The interaction between the wave velocity and the seagrass sheath generates turbulence near the bed (Zhang et al., 2018), which can trigger sediment resuspension (Tinoco and Coco, 2018; Tang et al., 2019). Combining these effects, Tang et al. (2019) predicted the meadow size needed to diminish wave energy enough to eliminate wave-induced resuspension and enhance particle retention.

Building on the studies described above, the present study used field observations at a wave-dominated site to examine the connection between sediment and carbon accretion rates, wave velocity, and *TKE* within a single meadow. An understanding of how resuspension may impose spatial gradients on carbon accretion could improve the assessment of carbon credit for seagrass meadows, as well as provide guidelines to optimize long-term carbon accretion potential. To this end, a method is proposed for using predicted gradients in hydrodynamic exposure to improve estimates of meadow-scale carbon accretion rates.

5.2 Methods

5.2.1 Meadow and sediment characteristics

This study was conducted in a meadow of *Zostera marina* in Nahant Harbor, Massachusetts (Figure 5.1), which is a wave-dominated site. Based on isotopic signature analysis, the carbon in this meadow has a significant allochthonous fraction (Figure 8 in Novak et al., 2020), so that the accretion rate of organic carbon was expected to be influenced, at least in part, by hydrodynamic conditions favorable for its retention. Meadow boundaries were delineated through a boat survey. In Figure 5.1, the outer edge of the meadow is shown with pink line segments, which enclose 14.3 acres (0.06 km²). A denser inner region (5.2 acres, 0.02 km²) is shown with green line segments. The meadow was divided into three depth zones, which were expected to experience different hydrodynamic conditions: Shallow (mean water depth = 2.2 m), Mid (mean depth = 3.2 m), and Deep (mean depth = 6.2 m). Mean water depths were measured with diver depth gauges and corrected for tidal phase. In July 2020, within each of the three depth zones, three cores were extracted within the meadow and a fourth reference core was collected from the adjacent bare bed, resulting in a total of 12 cores. A 50-cm core barrel with 7-cm diameter was manually driven to the point of refusal, which ranged from 24 cm to 30 cm. The core locations are shown in Figure 5.1.

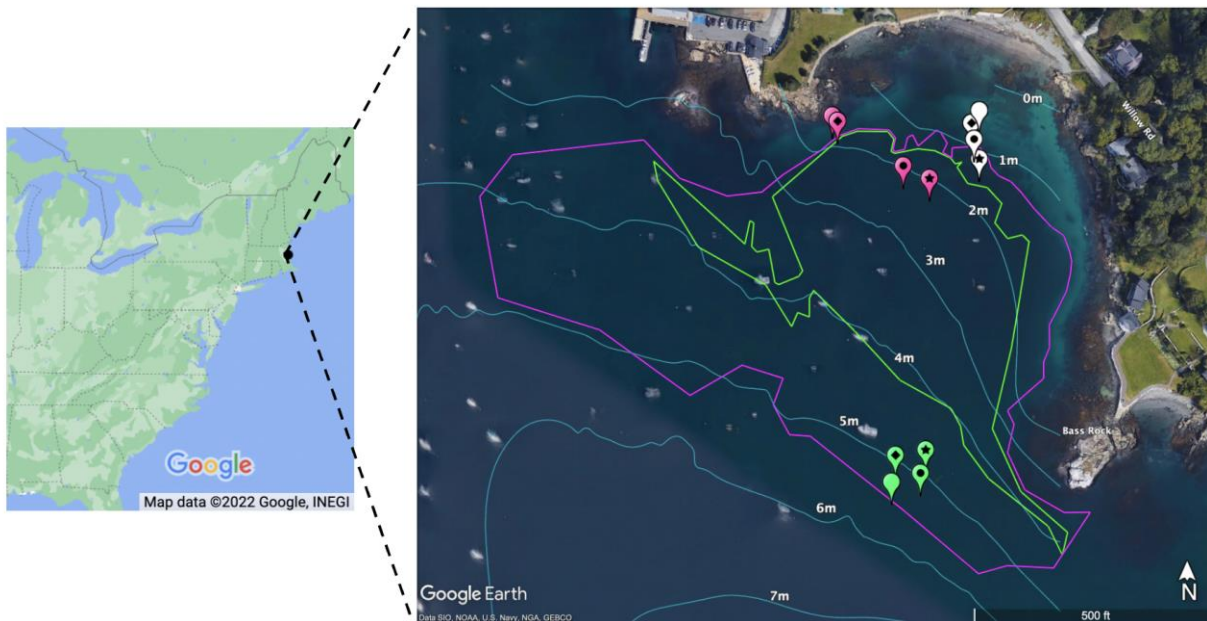


Figure 5.1: The field site in Nahant Harbor, Massachusetts, on the East Coast of the United States. Four cores were collected in each of three depth zones; three within the meadow at increasing distance from the nearest meadow edge, numbered 1 (diamonds), 2 (circles), 3 (stars), respectively, and one reference core outside of the meadow (“Ref,” blank markers). White, pink, and green denote the Shallow, Mid, and Deep depth zones, respectively. Green and magenta outlines show the regions of dense (shoot density $> 200 \text{ m}^{-2}$) and sparse (shoot density $< 200 \text{ m}^{-2}$) vegetation mapped using boat surveys in 2014. The bathymetry surveyed in 2014 is indicated by labeled blue contour lines.

After the cores were extracted, they were capped underwater and kept vertical during transport from the extraction sites to the beach. Depending on the core length, the cores were extruded into 22 to 25 sections, with 1-cm increments from 0 to 20 cm and 2-cm increments from 20 to 30 cm. The core subsamples were stored in Ziploc bags on ice in coolers and transported to the Novak Lab at Boston University in Boston, Massachusetts. Samples were put into a drying oven at $60 \text{ }^{\circ}\text{C}$ for seven days or until they attained a constant weight. The dry bulk density of each slice was calculated by dividing the dry mass of the sample by the volume. Next, the sediment samples were divided in half with a sediment splitter. One half of each sample was

placed in a muffle furnace at 450 °C for 16 h to determine the percent organic matter content (%OM) using the loss-on-ignition method (Howard et al., 2014). Percent organic carbon (%OC) was calculated assuming a linear dependence on %OM based on data from sites across New England reported in Novak et al. (2020). %OM, %OC, and bulk dry density were averaged over the top 15 cm of each core. These parameters showed no trends with depth into the cores. The grain size distribution was measured by combining samples from the top 5 cm and sieving from 0.5 mm to 0.0625 mm. The median grain size was calculated from the grain size distribution.

The second half of each sediment sample was shipped to Edith Cowan University in Joondalup, Australia for ^{210}Pb analysis to determine sediment accumulation rates (*SAR*) and mass accumulation rates (*MAR*). ^{210}Pb was determined by analyzing ^{210}Po using alpha spectrometry after the addition of ^{209}Po as an internal tracer and digestion in acid media using an analytical microwave (Sanchez-Cabeza et al., 1998). Gamma spectrometry measurements determined the concentration of ^{226}Ra in selected samples along each core. The excess ^{210}Pb was defined as the difference between the total ^{210}Pb and ^{226}Ra (i.e., supported ^{210}Pb). Using the ^{210}Pb concentration profiles, an average *MAR* was calculated using the Constant Flux and Constant Sedimentation (CF: CS, applied piecewise) model (e.g., Krishnaswami et al., 1971, Arias-Ortiz et al., 2018). Cores that indicated significant mixing were not analyzed for *MAR*. The carbon accretion rate (*CAR*) was estimated by combining *MAR* with %OC (see Table 5.1).

On the same day the cores were extracted, the shoot density was measured near each core site with three randomly placed quadrats (25 cm × 25 cm). The leaf width, length, sheath length, number of leaves, and shoot biomass were measured for five selected shoots within each quadrat.

Leaf area index (*LAI*) was calculated as the product of the mean leaf area per shoot (sheath included) and shoot density (see Table 5.1).

5.2.2 Velocity and turbulence

In August 2021, six tilt current meters (TCMs) designed and manufactured by Lowell Instruments, LLC (East Falmouth, Massachusetts) were deployed in Nahant Harbor at Shallow(Ref), Shallow1, Mid(Ref), Mid2, Deep(Ref), and Deep3. The TCM deployment sites were chosen because the extracted sediment cores at these sites yielded mass accretion rates from the ^{210}Pb analysis. Each TCM consisted of a cylindrical housing tethered by a short cord to an anchor, which in this study was a 20-lb, 12-in by 12-in by 2-in square concrete paving stone. In the absence of water motion, the long axis of the cylinder is vertical. The cylinder tilts in response to the wave and current velocities. An accelerometer and magnetometer within the cylinder measure the degree and direction of tilt, which is converted through factory calibration coefficients into velocity and heading. Data were recorded at 16 Hz for 60-s bursts every five minutes at all sites except Shallow(Ref). Due to concerns about boat traffic, the instrument at Shallow(Ref) recorded at 16 Hz continuously for 24 hours, at which point it was removed. The remaining TCMs were deployed for a minimum of two weeks. All TCMs were fully submerged during their deployment. The total height of each TCM setup was 33 cm, which was less than the observed meadow height at all sites, confirmed by measured shoot height and GoPro footage recorded at the Deep3 site. Although TCMs are primarily marketed to record unidirectional flow, a comparison with an acoustic Doppler velocimeter (Nortek Vectrino) in an experimental channel confirmed their ability to record wave velocity (see Appendix C). The average root-

mean-squared velocity, U_{RMS} , was estimated over each 1-hour interval, from which wave velocity amplitude was defined as $U_w = 2^{1/2}U_{RMS}$. Velocity records confirmed that this is a wave-dominated site, with wave velocity much larger than time-mean velocity. Tidal elevations at high and low tides were obtained from Nahant US Harbors data.

Because previous studies have correlated resuspension with near-bed turbulence, the measured near-bed wave velocity was used to estimate near-bed turbulence. Turbulence is generated by the interaction of the wave velocity with the bed and with the relatively stiff sheath of each seagrass shoot (Zhang et al., 2018; Tang et al., 2019). The vegetation-generated turbulent kinetic energy per fluid mass (TKE) can be predicted from a model based on the conversion of wave kinetic energy to TKE by canopy drag (Tanino and Nepf, 2008; Tang et al., 2019). The bed-generated turbulence is linearly proportional to the bed-generated shear stress, $\tau_w = \rho f_w U_w^2 / 2$, in which f_w is a wave friction factor (Tang et al., 2019). The sum of these predicts the total near-bed TKE :

$$\text{near - bed } TKE = \underbrace{\delta \left(C_D \frac{n_s b^2}{2(1 - \phi)} \right)^{\frac{2}{3}} U_{RMS}^2}_{\text{vegetation-generated turbulence}} + \underbrace{C_{b,w} U_{RMS}^2}_{\text{bed-generated turbulence}} \quad (5.1)$$

in which scale factor $\delta = 1.2 \pm 0.2$ is an average from two previous studies (Tanino and Nepf, 2008; Tang et al., 2019). n_s is the number of shoots per bed area. b is the sheath diameter (see section 3.2 in Zhang et al. 2018), which was assumed to be equal to the leaf width. Since the sheath has a nearly cylindrical geometry, the near-bed solid volume fraction $\phi = \frac{\pi}{4} n_s b^2$. C_D (=1.2) is the sheath drag coefficient, based on cylinder drag measurements in Keulegan and

Carpenter (1958). The bare-bed scale factor $C_{b,w}$, defined by measurements over bare bed, is a function of bed roughness. We used a value measured by Tang et al. (2019), $C_{b,w} = 0.02 \pm 0.01$ for $d_{50} = 85$ micron, which is close to the sediment grain size at Nahant ($d_{50} = 100$ micron).

The critical *TKE* threshold was estimated using the critical velocity for bare beds, modified for meadows (Tang et al. 2019). First, Komar and Miller (1973) showed that for a median grain size d_{50} less than 0.05 cm, the critical wave velocity for a bare bed, $U_{w,c,b}$, is given by

$$\frac{\rho U_{w,c,b}^2}{(\rho_s - \rho) g d_{50}} = 0.3 \sqrt{\frac{2A_{w,c,b}}{d_{50}}}, \quad (5.2)$$

in which ρ_s is the sediment density, g is the gravitational acceleration, $A_{w,c,b} = U_w T / (2\pi)$ is the critical wave excursion, and T is the wave period. The critical RMS wave velocity is then, $U_{RMS,c,b} = U_{w,c,b} / \sqrt{2}$. The critical velocity threshold within the meadow is reduced, relative to the bare bed, due to the contribution from vegetation-generated turbulence. Specifically, the critical rms wave velocity in a meadow, $U_{RMS,c,v}$, is (Tang et al., 2019)

$$\frac{U_{RMS,c,v}}{U_{RMS,c,b}} = \frac{1}{\sqrt{1 + \frac{\delta^2}{C_{b,w}} \left(\frac{2C_D}{\pi}\right)^{\frac{2}{3}} \left(\frac{\phi}{1-\phi}\right)^{\frac{2}{3}}}}. \quad (5.3)$$

The critical RMS wave velocity can be used in Equation (5.1) to estimate the critical *TKE*. We emphasize that this prediction is for near-bed, wave-generated turbulence. This is our focus because near-bed turbulence has been shown to correlate with resuspension (Tang et al 2019). The vertically-averaged, wave-driven turbulence within a meadow is much smaller, because the

turbulence decays sharply with distance from the bed (see Figure 3(f) in Zhang and Nepf, 2018). This is because bed-generated turbulence is limited by a thin wave-boundary-layer, and because the seagrass leaves can easily move with the waves, reducing relative motion and thus reducing vegetation-generated turbulence above the sheath region (see discussions in Zhang and Nepf, 2018 and Tang et al., 2019).

5.3 Results and Discussion

3.1 Meadow structure and sediment characteristics

The measured meadow structure and sediment characteristics are summarized in Table 5.1. The shoot density was highest in the Mid zone and lowest in the Deep zone. The measured leaf width averaged over all quadrats was $b = 0.47 \pm 0.09$ cm. The median grain size was comparable across the meadow, increasing by just 20% between the Shallow and Deep zones. The nearly uniform grain size across the meadow can be attributed to a common source of suspended material, derived from a nearby marsh.

Table 5.1: Summary of measured meadow structure and sediment characteristics averaged over the top 15 cm of the sediment cores, consistent with the depth of cores that was used to assess *MAR* and *SAR* (Figure 2). Standard deviations among quadrat samples (shoot density) and over sediment profiles (dry bulk density, %OC, *SAR*) are reported. Derived quantities (*LAI*, organic carbon, *CAR*) include propagated uncertainty.

	Distance to edge	Mean water depth	Dry bulk density	%OC	Shoot density	<i>LAI</i>	OC	Median grain size	<i>MAR</i>	<i>SAR</i>	<i>CAR</i>
	<i>m</i>	<i>m</i>	$\frac{g}{cm^3}$	%	m^2	$\frac{m^2}{m^2}$	$\frac{g C}{cm^2}$	<i>mm</i>	$\frac{g}{cm^2 yr}$	$\frac{mm}{yr}$	$\frac{g C}{m^2 yr}$
D1	11	6.3	1.54 ± 0.13	0.33±0.08	91 ± 46	0.9 ± 0.5	0.0051 ± 0.0012	0.11			15 ± 5
D2	19	6.2	1.53 ± 0.14	0.35 ± 0.04	59 ± 9	0.69 ± 0.11	0.0054 ± 0.0007	0.11			16 ± 4
D3	29	6.0	1.45 ± 0.20	0.42 ± 0.07	85 ± 18	0.74 ± 0.16	0.0062 ± 0.0013	0.11	0.45±0.10	3.1 ± 0.7	19 ± 5
DR	1	6.5	1.41 ± 0.19	0.29 ± 0.07			0.0040 ± 0.011	0.12			

M1	5	3.0	1.21 ± 0.19	0.68 ± 0.25	261 ± 9	3.04 ± 0.11	0.008 ± 0.003	0.10			14 ± 6
M2	54	3.3	1.36 ± 0.17	0.47 ± 0.16	331 ± 76	7.9 ± 1.8	0.007 ± 0.002	0.10	0.21 ± 0.04	1.6 ± 0.3	10 ± 4
M3	72	3.3	1.39 ± 0.16	0.47 ± 0.11	261 ± 65	4.3 ± 1.1	0.0065 ± 0.0017	0.09			10 ± 3
M R	1	3.0	1.36 ± 0.14	0.21 ± 0.03			0.0028 ± 0.0005	0.10			
S1	11	2.0	1.41 ± 0.18	0.21 ± 0.08	240 ± 48	3.7 ± 0.7	0.0030 ± 0.0011	0.10	0.12 ± 0.02	0.90 ± 0.18	2.5 ± 1.0
S2	19	2.3	1.41 ± 0.17	0.20 ± 0.04	251 ± 76	4.8 ± 1.4	0.0027 ± 0.0006	0.09			2.3 ± 0.6
S3	29	2.6	1.33 ± 0.39	0.23 ± 0.05	176 ± 55	1.2 ± 0.4	0.0031 ± 0.0011	0.10			2.8 ± 0.8
SR	8	1.7	1.33 ± 0.22	0.29 ± 0.08			0.0039 ± 0.0013	0.07			

In the Deep zone, the total ^{210}Pb concentrations decreased with depth in the meadow cores (green, blue, and red symbols in Figure 5.2(a)) from around 25 Bq/kg at the surface down to a constant of 14.9 ± 1.6 Bq/kg below 10 to 12 cm. Based on the Deep1, Deep2, and Deep3 cores, the mass accretion rate was $MAR = 0.45 \pm 0.01$ g cm^{-2} yr^{-1} , and the sedimentation accretion rate was $SAR = 3.1 \pm 0.7$ mm/yr (Figure 5.2(a)). In the meadow Mid zone, $MAR = 1.6 \pm 0.3$ g cm^{-2} yr^{-1} and $SAR = 1.6 \pm 0.3$ mm/yr based on the Mid2 core (Figure 5.2(b)). In the meadow Shallow zone, $MAR = 0.90 \pm 0.18$ g cm^{-2} yr^{-1} and $SAR = 0.90 \pm 0.18$ mm/yr based on the Shallow1 core (Figure 5.2(c)).

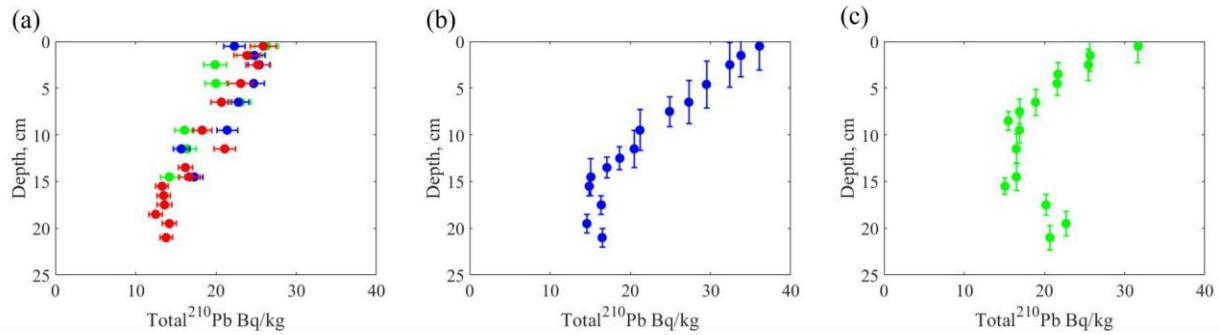


Figure 5.2: Total ^{210}Pb and ^{226}Ra versus depth from the surface of the meadow sediment cores for the (a) Deep zone, (b) Mid zone, and (c) Shallow zone. Only profiles without mixing from which SAR and MAR were determined are included. Colors correspond to the site distance from the nearest edge of the meadow. Green, blue, and red denote meadow sites at increasing distances from the nearest edge of the meadow, respectively.

5.3.2 Velocity, turbulent kinetic energy, and sediment accumulation rate

Wind speeds observed during the deployment were typical of historical wind conditions (based on records from the weather station at the Boston Logan International Airport), so that the observed spatial trends in hydrodynamic intensity were considered to be representative of the

long-term conditions that produced the recorded spatial trend in mass accretion. Power spectra of velocity records indicated dominant wave periods between 6 and 10 s, which was consistent with historical data from the National Oceanic and Atmospheric Administration National Data Buoy Center (NOAA NDBC) Station 44013 buoy in Massachusetts Bay. For this wave period and local depth range, the near-bed wave velocity is sensitive to depth, specifically increasing as depth decreases. As a result, the magnitude of the near-bed U_{RMS} was correlated with the tidal phase (Figure 5.3), with peak U_{RMS} values associated with low tide (vertical gray lines in Figure 5.3), which was particularly evident at the Shallow1 site (black curve in Figure 5.3). Over the two-week deployment, the average RMS velocity was highest at the Shallow1 site (6.6 cm/s), less at the Mid2 site (5.3 cm/s), and smallest at the Deep3 site (4.7 cm/s). Within each depth zone, the RMS velocity measured just outside the meadow differed from the in-meadow velocity by less than 10% (data not shown). That is, the meadow did not locally diminish the wave velocity within the meadow compared to just outside of the meadow. This was consistent with the prediction of wave velocity attenuation described in Lowe et al. (2005). Specifically, based on the meadow density and wave period, the in-canopy wave velocity attenuation factor $\alpha \approx 1$ for all depth zones. Large wave events on Days 2, 7, and 13 were correlated with stormy weather reported on Logan International Airport wind speed and precipitation data.

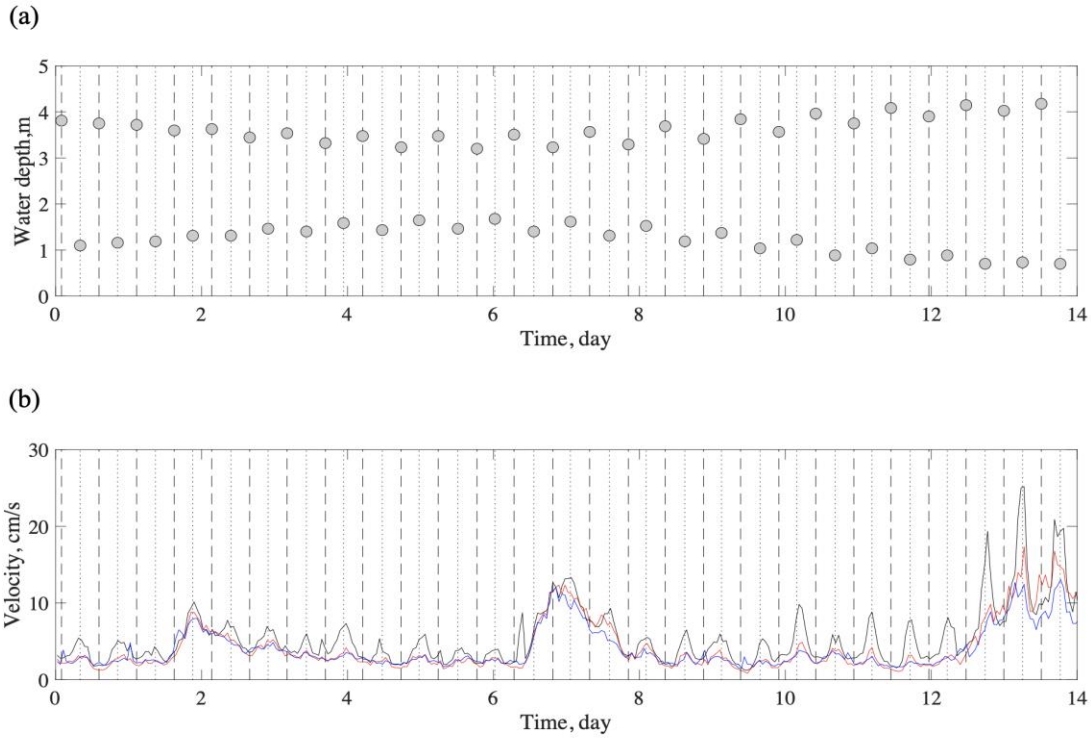


Figure 5.3: (a) Water depths at the Shallow site at high and low tides, and (b) hourly-averaged U_{RMS} over two weeks. The black curve denotes the Shallow zone (Shallow1). The red curve denotes the Mid zone (Mid2). The blue curve denotes the Deep zone (Deep3). Vertical dotted and dashed lines denote times of low and high tide, respectively.

The near-bed TKE was estimated from measured U_{RMS} using Equation (5.1). We considered the strong wave conditions observed during low tides on Days 2, 7, and 13, referred to as Storms 1, 2, and 3. Consistent with the spatial variation in U_{RMS} in Figure 3, the Shallow1 site experienced the highest TKE while the Deep3 site experienced the lowest TKE (Figure 4). The critical TKE threshold for sediment resuspension (based on Equations (5.1), (5.2), and (5.3)) are indicated with horizontal lines in Figure 5.4(a). During Storm 3, the TKE at the Shallow1 and Mid2 sites exceeded the thresholds, while the thresholds were barely crossed at the Shallow1 and Mid2 sites during Storms 1 and 2. Based on this, we infer that events with velocity magnitude

similar to or greater than that of Storm 3 control resuspension within the meadow and influence the spatial distribution of sediment carbon within the meadow. With this in mind, in the next phases of analysis we focus on Storm 3.

The *SAR* (Table 5.1, Figure 5.4(b)) varied inversely with near-bed *TKE* during Storm 3, which can be explained by resuspension triggered by near-bed turbulence, i.e., resuspension diminished particle retention and thus sediment accretion rate. This was consistent with previous laboratory studies, which found sediment resuspension increased as near-bed *TKE* increased in pure wave and pure current conditions (Tinoco and Coco, 2018; Tang et al., 2019; Zhang et al., 2020). The spatial gradient of *TKE* results in a spatial gradient of exceedance of the critical *TKE* threshold, and therefore a spatial gradient of resuspension. Consistent with this, previous sediment trap measurements within the Nahant meadow indicated significantly higher resuspension both within and adjacent to the meadow in the Shallow zone compared to the other depth zones (data not shown). Assuming sediment supply was the same across the meadow, an increase in resuspension would lead to a lower net sedimentation rate, so that the correlation observed between sedimentation rate and near-bed *TKE* was consistent with the impact of resuspension (Figure 5.4).

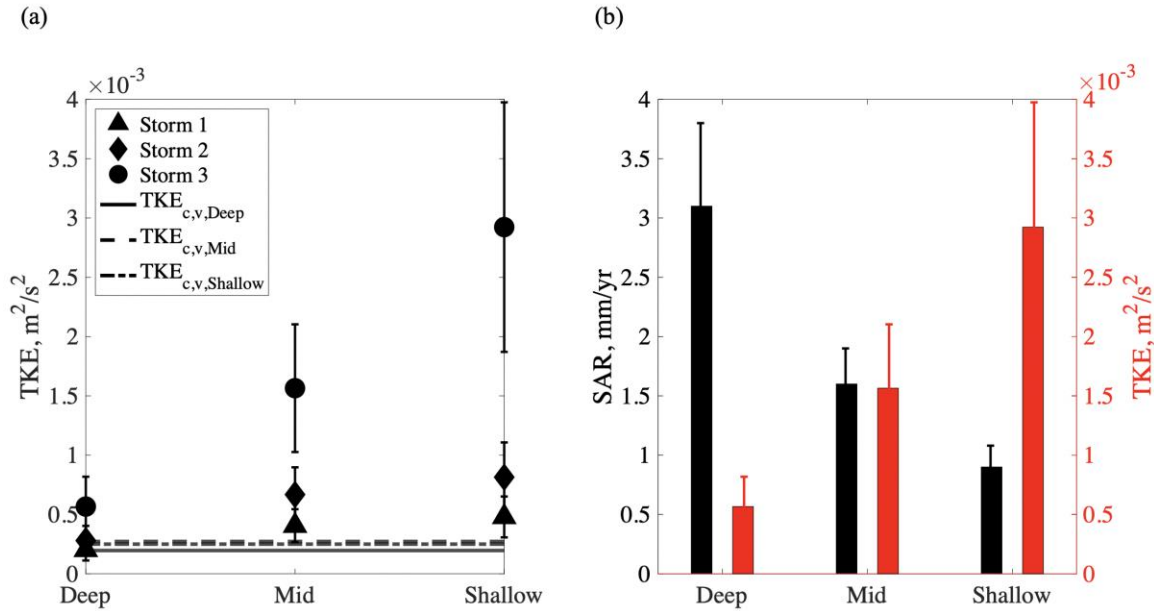


Figure 5.4: (a) Turbulent kinetic energy (TKE at Deep3, Mid2, and Shallow1 for Storms 1, 2, and 3 (Days 2, 7, and 13 events). The horizontal lines indicate the critical TKE thresholds for each meadow site. The thresholds varies between sites due to the different meadow densities, i.e. n_b in Equation (1). (b) Sediment accretion rate (SAR , black bars, left-hand axis) and near-bed turbulent kinetic energy (TKE , red bars, right-hand axis) at Deep3, Mid2, and Shallow1 during Storm 3.

5.3.3 Sediment organic carbon content and carbon accretion rates

The measured CAR values in the Nahant meadow were typical of those observed in other meadows of the same seagrass species. Specifically, previous studies report a range of CAR in *Zostera marina* L meadows from 3.1 to $93.0 \text{ gCm}^{-2}\text{yr}^{-1}$ (Poppe and Rybczyk, 2018; Prentice et al. 2020). The CAR in the Shallow zone is at the low end of this range, while the CAR in the Deep zone is close to the average.

The mean sediment organic carbon fractions (%OC) were statistically significantly different between the Shallow and Mid Zones but not between the Mid and Deep or Shallow and

Deep zones (see Figure C.2 in Appendix C). However, differences in sedimentation rates generated differences in *CAR* among all three depth zones. Specifically, *CAR* were statistically significantly different at each depth zone (see Figure C.3 in Appendix C).

Organic carbon accretion might differ between depth zones due to differences in seagrass productivity. For example, Dennison and Alberte (1986) observed that at the deepest sites within a *Zostera marina* L. meadow at Woods Hole, Massachusetts, productivity was controlled by light availability for photosynthesis, whereas light availability was not a major factor in productivity differences in shallower regions of the meadow. However, previous measurements in the Nahant meadow (April to October of 1999 and 2000) did not indicate a dependence of seagrass productivity on water depth (Colarusso, 2006).

Furthermore, the three-fold spatial variation in sediment organic carbon did not have a significant relationship with spatial variation in shoot density, and *CAR* had a negative correlation with shoot density (see Figure C.4 in Appendix C). Specifically, *CAR* was highest where the shoot density was lowest (Table 5.1). While surprising for autochthonous carbon, this is consistent with allochthonous carbon, which tends to be more significantly influenced by hydrodynamic factors. Recall that Nahant has a significant allochthonous fraction (Figure 8 in Novak et al., 2020). Specifically, within this wave-dominated meadow, the near-bed velocity, which controls resuspension, has little dependence on local shoot density but instead depends on the integration of shoot density (which determines meadow drag) along the trajectory of the wave. However, shoot density can be an important metric when comparing carbon accretion rates between different meadows. Denser and larger meadows diminish wave energy to a greater degree and thus have a greater ability to curtail resuspension, which would enhance *SAR* and

CAR (Tang et al., 2019). In contrast to an oscillating wave velocity, a steady current velocity is more directly influenced by a spatial variation in shoot density (e.g., see the discussions in Lowe et al., 2005 and Luhar et al., 2008). Therefore, at current-dominated sites with a patchy meadow structure, one would expect spatial variation in shoot density to be associated with spatial variation in velocity, and thus, potentially, with spatial variation in sediment carbon.

The distance from the meadow edge is another physical factor that can influence the spatial heterogeneity in carbon within a meadow. For example, at a current-dominated site, Oreska et al. (2017) observed that sediment carbon increased with distance from the meadow's leading edge, and they attributed this to the attenuation of current within the meadow due to meadow drag. Specifically, when a current encounters a submerged meadow with a sufficient shoot density, the velocity within the meadow decreases with distance from the leading edge over an adjustment length-scale that is dependent on the meadow height and shoot density (Chen et al., 2013).

At the Nahant site, neither sediment organic carbon nor *CAR* had a significant correlation with distance to the nearest meadow edge, and the highest and lowest *CAR* occurred at similar distances to the nearest edge of the meadow (Figure 5.5(a) and 5.5(c)). The meadow sites were not within the expected current adjustment length-scale of the meadow (up to 2.5 m, based on Equation (10) in Chen et al., 2013), such that the distance to the nearest meadow edge was not expected to be a factor. Furthermore, at this wave-dominated site, the distance measured along the direction of wave propagation is more relevant than the distance to the nearest meadow edge. Since the waves transform across the meadow in response to changes in water depth and to dissipation by meadow drag, one should consider the direction of wave propagation and measure

the distance from the offshore edge of the meadow. The *CAR* had a significant relationship with distance to the offshore meadow edge (Figure 5.5(d)). Specifically, *CAR* decreased with distance from the offshore edge. This was consistent with the increased near-bed wave velocity associated with shoaling, which would tend to produce greater resuspension at sites closer to the shore, which in turn influenced carbon accretion. That is, moving toward shore, the near-bed wave velocity increased, promoting resuspension and diminishing carbon accretion. Consistent with this, Dahl et al. (2018) observed that resuspension removed organic material from the bed within a meadow. Resuspension can also enhance oxygen within the bed, which would tend to diminish carbon retention through increased rates of mineralization by aerobic microbes (e.g., Ståhlberg et al., 2006).

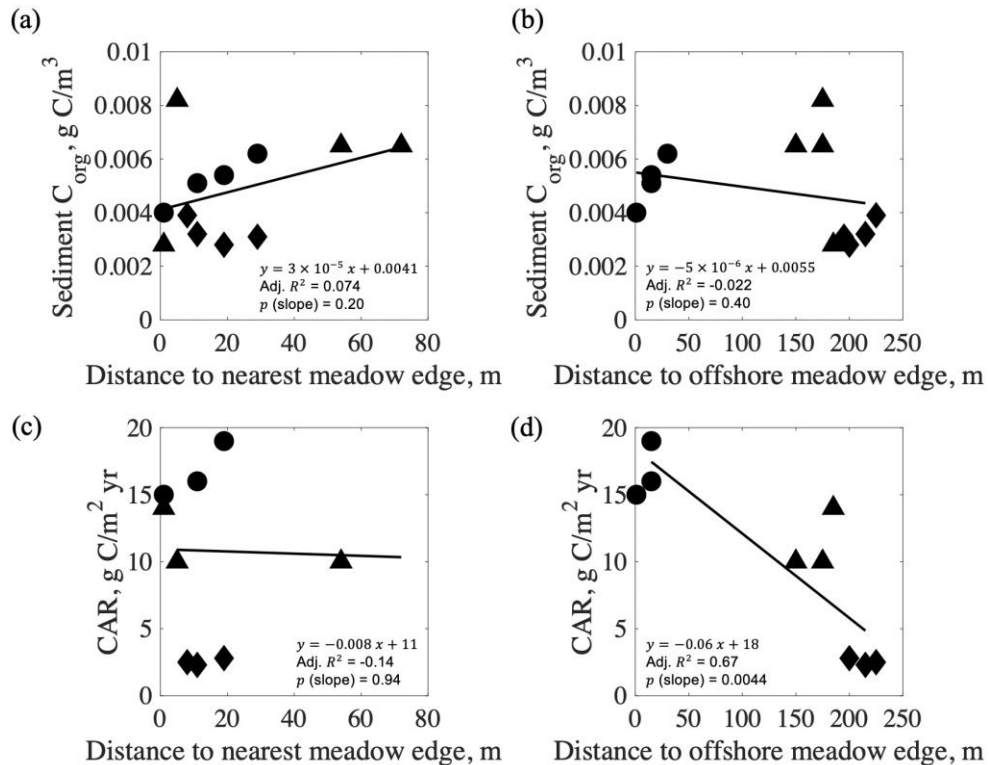


Figure 5.5: (a)(b) Sediment organic carbon and (c)(d) carbon accretion rate (*CAR*) versus the distance from nearest meadow edge (a and c) and the distance from offshore meadow edge (b

and d). Circles, triangles, and diamonds denote the Deep, Mid, and Shallow zones, respectively. The solid curves denote the lines of best fit.

5.3.4 Using hydrodynamic gradients to constrain meadow-scale estimates of carbon

The carbon accretion rates were inversely correlated with hydrodynamic exposure expressed in terms of near-bed *TKE* (Figure 5.6), with the following linear best-fit based on Storm 3 (90% CI, Figure 5.6).

$$CAR \left(\frac{g C}{m^2 yr} \right) = (-0.69 \pm 0.17) TKE \left(\frac{cm^2}{s^2} \right) + (21 \pm 3) \quad (5.4)$$

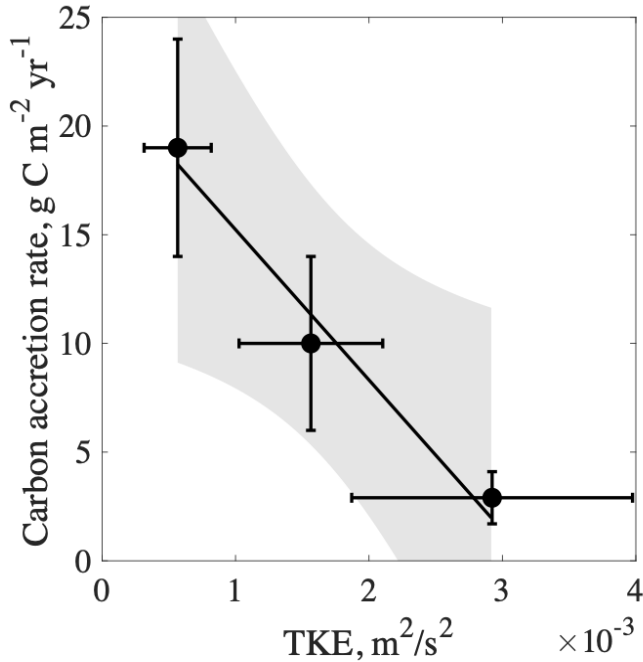


Figure 5.6: Carbon accretion rate (*CAR*) as a function of near-bed turbulent kinetic energy (*TKE*) during Storm 3. The black curve denotes the linear best fit (Equation (5.4)). The shaded region shows the 90% confidence interval bounds for the fit.

At this wave-dominated site, the near-bed *TKE* can be predicted from wave mechanics. Specifically, wave evolution over the meadow can be described by the conservation of wave energy, including the influence of shoaling and vegetation-induced wave dissipation on the wave amplitude, a_w . Bed-induced wave dissipation was assumed to be negligible, compared to vegetation-induced dissipation. Since both shoaling and wave dissipation change with water depth, a marching solution was used to evaluate the wave amplitude at $\Delta x = 1$ -m steps across the meadow. Specifically, Equation (17) in Mendez and Losada (2004) was adapted to describe the change in wave amplitude over the meadow,

$$\frac{a_{w(i)}}{a_{w(i-1)}} = K_{v(i-1)} K_{s(i-1)} \quad (5.5)$$

in which $a_{w(i)}$, $K_{v(i)}$ and $K_{s(i)}$ are the wave amplitude, vegetation dissipation and shoaling coefficients at distance i from the offshore edge of the meadow, respectively, with i corresponding to the progression of 1-m steps (Δx). The change in wave amplitude due to wave energy dissipation by the meadow can be described as (e.g., Dalrymple et al., 1984)

$$K_{v(i)} = \frac{1}{1 + K_{D(i)} a_{w(i)} \Delta x} \quad (5.6)$$

in which the wave decay coefficient

$$K_{D(i)} = \frac{2}{9\pi} C_D n_{b(i)} b k_{(i)} \frac{9 \sinh(k_{(i)} l_{e,m}) + \sinh(3k_{(i)} l_{e,m})}{(\sinh(k_{(i)} D_{(i)})) (\sinh(2k_{(i)} D_{(i)}) + 2k_{(i)} D_{(i)})} \quad (5.7)$$

depends on water depth, D , wave number, k , number of leaves per bed area, n_b , and average leaf width, b . The drag coefficient $C_D = 2$ for flat leaf morphology (see Luhar and Nepf, 2016).

Because seagrass leaves are flexible, their tips can move with the waves, reducing the relative

velocity between the leaf and the water, which reduces the drag. The impact of this reconfiguration is characterized by the effective meadow height, l_{em} , which is the height of the meadow that contributes to the drag and wave dissipation. The effective meadow height depends on the morphology and material properties of the leaves and on the wave conditions (Luhar and Nepf, 2016; Luhar et al., 2017). Over a wide range of pure wave conditions, a simple but reasonable approximation for $l_{e,m}$ is 10% of the average shoot length (see Figure 5 in Lei and Nepf, 2019).

The group velocity, C_g , describes the speed of wave energy propagation (Kamphuis, 2010):

$$C_g = \frac{1}{2} \left(1 + \frac{2kD}{\sinh(2kD)} \right) \left(\frac{g}{k} \tanh(kD) \right)^{\frac{1}{2}} \quad (5.8)$$

As the water depth D decreases, C_g decreases which generally results in an increase in wave amplitude. This is captured by the shoaling coefficient, K_s (Kamphuis, 2010),

$$K_s = \left(\frac{C_{g(i-1)}}{C_{g(i)}} \right)^{\frac{1}{2}} \quad (5.9)$$

Based on the bathymetric survey, it was reasonable to assume a linear bottom slope across the meadow (Figure 5.1). The leaf density (n_b , number of leaves per bed area) was estimated from the shoot density (Table 5.1) and average number of leaves per shoot in each depth zone; both were assumed to vary smoothly across the meadow and interpolated between measurement sites. The initial wave amplitude at the outer edge of the meadow, $a_{w,0}$, was calculated from linear wave theory and the measured near-bed wave velocity amplitude, U_w ,

$$U_w = \frac{2\pi}{T} a_w \frac{\cosh \cosh(kz)}{\sinh \sinh(kD)} \quad (5.10)$$

in which T is the wave period, and $z = 16$ cm was the approximate distance above the bed corresponding to half of the vertical height of the TCM. For this analysis, we focused on Storm 3 conditions. Starting from the offshore edge (≈ 250 m in Figure 5.7), Equation (5.5) was evaluated in 1-m increments over the meadow, using Equations (5.6) through (5.9) to evaluate $K_v(i-1)$ and $K_s(i-1)$. Linear wave theory (Equation (5.10)) was used to convert the spatial evolution of wave amplitude to spatial variation in near-bed U_{RMS} , using $U_{RMS} = U_w/\sqrt{2}$ (Figure 5.7(a)). The near-bed U_{RMS} was used in Equation (5.1) to estimate near-bed vegetation-generated TKE (Figure 5.7(b)), assuming a smooth change in shoot density over the meadow. Finally, Equation (5.4) was used to predict the spatial variation in carbon accretion rate (Figure 5.7(c)). In this way, we used physical models of wave mechanics to interpolate the carbon accretion rate over the meadow. The estimation was made for two wave periods representing the bounds of the measured wave spectral peak ($T=6$ s and 10 s shown with black and red curves, respectively, in Figure 5.7), but the solution was not sensitive to wave periods in this range. Differences between predictions and measurements could be attributed to the assumed linearization of the bathymetry and smooth variation in the meadow structure. In summary, simple modeling tools performed well in predicting the observed spatial variation in hydrodynamic conditions and CAR .

Next, we considered the results from Storm 3 (Figure 5.7) in the broader context of conditions expected at the site. The average historic airport wind speed for August is 4.5 m/s, and the peak hourly airport wind speed on the stormy days (including Storm 3) was 9 m/s. The dominant wind direction is from the southwest, with a fetch of about 5 km. Assuming that the

airport wind speeds were representative of the wind speed 10 m above the water surface, we used the fetch-limited Joint North Sea Wave Project (JONSWAP) parameter equations (Kamphuis, 2010) to estimate a significant wave height H_{m0} of 16 cm (using a wind speed of 4.5 m/s) and 33 cm (using a wind speed 9 m/s). Wave heights estimated from the TCM velocity data during the stormy periods were between 20 and 32 cm, confirming that the range of observed conditions were representative of long-term conditions at the site.

To examine the impact of the meadow on the hydrodynamic conditions and CAR , we repeated the analysis without vegetation, setting $K_v=1$ and $n_b = 0$ (Figure 5.7(d-f)). Note that at the offshore edge of the meadow (≈ 250 m in Figure 5.7) the wave conditions are the same with and without the meadow, because this is the point at which the waves first encounter the meadow. Moving toward shore ($x < 250$ m), the wave velocity and near-bed TKE would be significantly higher without the meadow, with wave velocity increasing to more than twice the observed value (Figure 5.7(d)). The significant increase in near-bed TKE (Figure 5.7e), suggests that CAR would decrease to zero over most of the meadow (based on Equation (5.4)), which emphasizes the important role of wave dissipation by the meadow in creating conditions conducive to carbon accretion. We caution that Figure 5.7(e) is speculative because Equation (5.4) is based on only three points and does not resolve the transition to zero CAR at low values of near-bed TKE .

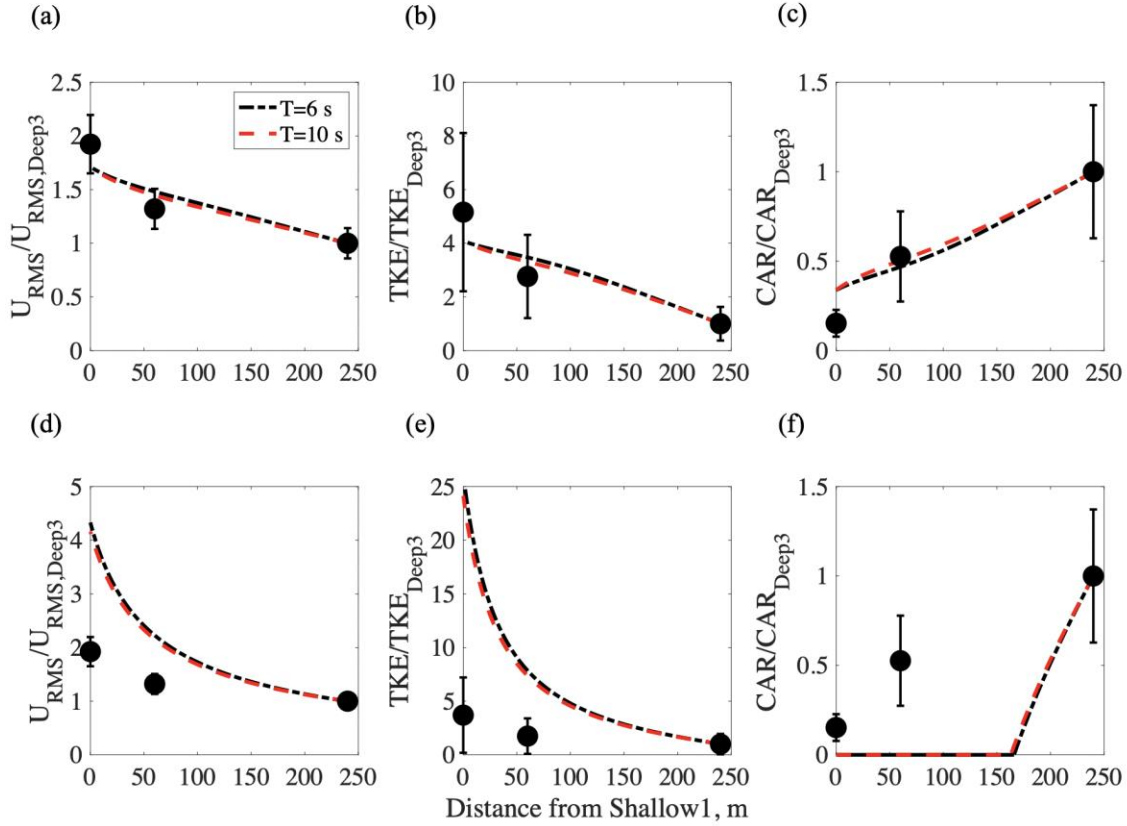


Figure 5.7: Evolution of (a,d) RMS wave velocity, (b,e) near-bed turbulent kinetic energy (TKE), and (c,f) carbon accretion rate (CAR) versus distance from the site Shallow1 ($x = 0$) during Storm 3. The top row includes the effects of the meadow on wave dissipation and near-bed TKE . The bottom row excludes the impact of the meadow by setting $K_v=1$ and $n_b=0$. Black circles represent measurements at Shallow1, Mid2, and Deep3. Dashed curves denote predictions based on physical models and the observed correlation between near-bed TKE and carbon accretion (Figure 5.6). Two wave periods were considered, $T = 6$ s (black dashed-dotted curve) and $T=10$ s (red dashed curve), to span the observed range of dominant wave periods at the site.

The predicted spatial variation in carbon accretion rate $CAR_{(i)}$ (Figure 5.7(c)) was used to calculate the total carbon accretion rate for the meadow, $TCAR$. Again using $\Delta x = 1$ m,

$$TCAR = \sum CAR_{(i)} \Delta x w_{(i)} \quad (5.11)$$

$w_{(i)}$ denotes the meadow width at distance i m from Shallow1. The meadow width was assumed to increase linearly from 100 m at Shallow1 to 500 m at Deep3, based on meadow contours developed from boat surveys (Figure 5.1). Using Equation (5.11), $TCAR = 9.2 \times 10^5 \text{ g } C_{\text{org}} \text{ yr}^{-1} = 1.0 \text{ short tons } C_{\text{org}} \cdot \text{yr}^{-1}$. For comparison, estimates using individual point measurements at the Deep, Mid, and Shallow zones were, respectively, 1.5 short tons $C_{\text{org}} \text{ yr}^{-1}$ (50% higher), 0.80 short tons $C_{\text{org}} \text{ yr}^{-1}$ (20% lower), and 0.20 short tons $C_{\text{org}} \text{ yr}^{-1}$ (80% lower). This comparison demonstrates that individual measurements of CAR do poorly in estimating the meadow average, and that the predictable variation in wave velocity over a meadow can constrain estimates of carbon accretion.

Finally, the potential for wave-driven resuspension to generate spatial gradients in CAR at other sites can be assessed using wind data and median grain size (d_{50}). Wind data and fetch provides an estimate of wave climate at the meadow edge, and the model described above can be used to describe the gradient in wave velocity across the meadow. For resuspension to drive spatial heterogeneity in sediment carbon, two conditions must be met. First, there is a gradient in near-bed wave velocity, and thus in near-bed TKE within the meadow. Second, the range of TKE within the meadow crosses the critical TKE threshold for resuspension, so that there will be a gradient in resuspension. The grain size, d_{50} , can be used in Equations (5.2) and (5.3) to infer the critical turbulence level for resuspension. Spatial gradients in resuspension can also be observed with sediment traps.

5.4 Conclusions

Measurements in a *Zostera marina* L. meadow in Nahant Harbor, Massachusetts, showed that spatial variation in sediment and carbon accretion rates correlated with the spatial variation in hydrodynamic intensity, which was characterized by near-bed turbulence. Specifically, sedimentation and carbon accretion rates both decreased as near-bed turbulence increased. This suggested that resuspension driven by turbulence provided a constraint on the rates of accretion. At wave-dominated sites, near-bed turbulence estimated from wave velocity and meadow morphology may provide a framework for describing spatial heterogeneity in carbon accretion and carbon sequestration within seagrass meadows, which could facilitate more accurate carbon measurements. More accurate carbon measurements could advance carbon credit assessment methods and improve the design of targeted seagrass conservation and restoration projects.

5.5 Acknowledgements

This study was supported by Shell International Exploration and Production through the MIT Energy Initiative. R. Schaefer was supported in part by the National Science Foundation Graduate Research Fellowship under Grant No. 1745302. We thank the U.S. Environmental Protection Agency dive team for their assistance in the field: Brent England, Jean Brochi, Chuck Protzmann, and Eric Nelson. The bathymetry and meadow mapping were collected by Mike Sacarny and Juliet C. Simpson under award NA18OAR4170105 from the National Sea Grant College Program of the U.S. Department of Commerce's National Oceanic and Atmospheric Administration. The International Atomic Energy Agency is grateful for the support provided by

the Government of the Principality of Monaco. Ved Ahuja assisted with processing sediment samples at Boston University.

5.6 References

- Arias-Ortiz, A., Masqué, P., Garcia-Orellana, J., Serrano, O., Mazarrasa, I., Marbà, N., Lovelock, C., Lavery, P., & C.M. Duarte (2018). Reviews and syntheses: 210Pb-derived sediment and carbon accumulation rates in vegetated coastal ecosystems – setting the record straight. *Biogeosciences*, 15, 6791-6818, doi:10.5194/bg-15-6791-2018.
- Chen, Z., C. Jiang, & H. Nepf (2013). Flow adjustment at the leading edge of a submerged aquatic canopy. *Water Resour. Res.*, 49(9), 5537-5551, doi:10.1002/wrcr.20403.
- Colarusso, Phil 2006. Natural and stress induced changes in non-structural carbohydrate concentrations in eelgrass (*Zostera marina* L.). Doctoral dissertation, Northeastern University.
- Dahl, M., Infantes, E., Clevesjö, R., Linderholm, H. W., Björk, M., & M. Gullström (2018). Increased current flow enhances the risk of organic carbon loss from *Zostera marina* sediments: Insights from a flume experiment. *Limnol. Oceanogr.*, 63(6), 2793-2805, doi:10.1002/lno.11009.
- Dalrymple, R. A., Kirby, J. T., & P.A. Hwang (1984). Wave diffraction due to areas of energy dissipation. *J. Waterw. Port. Coast. Ocean. Eng.*, 110(1), 67-79, doi:10.1061/(ASCE)0733-950X(1984)110:1(67).
- Dennison, W. C., & R.S. Alberte (1986). Photoadaptation and growth of *Zostera marina* L. (eelgrass) transplants along a depth gradient. *J. Exp. Mar. Biol. Ecol.*, 98, 265–282, doi:10.1016/0022-0981(86)90217-0.
- Duarte, C. M., Marbà, N., Gacia, E., Fourqurean, J. W., Beggins, J., Barrón, C., & E.T. Apostolaki (2010). Seagrass community metabolism: Assessing the carbon sink capacity of seagrass meadows. *Global Biogeochem. Cycles*, 24(4) 1–8, doi:10.1029/2010GB003793.
- Fonseca, M.S, & J.A. Cahalan (1992) A preliminary evaluation of wave attenuation by 4 species of seagrass. *Estuar. Coast. Shelf Sci.*, 35(6), 565-576, doi:10.1016/S0272-7714(05)80039-3.
- Fourqurean, J. W., Duarte, C. M., Kennedy, H., Marbà, N., Holmer, M., Mateo, M. A., Apostolaki, E. T., Kendrick, G. A., Krause-Jensen, D., & O. Serrano (2012). Seagrass ecosystems as a globally significant carbon stock. *Nature Geoscience*, 5, 505–509, doi:10.1038/ngeo1477.

- Gacia, E., & C. Duarte (2001), Sediment retention by a Mediterranean *Posidonia oceanica* meadow: the balance between deposition and resuspension. *Estuar. Coast. Shelf Sci.* 52, 505–514, doi:10.1006/ecss.2000.0753.
- Gacia, E., T. Granata, & C. Duarte (1999), An approach to measurement of particle flux and sediment retention within seagrass (*Posidonia oceanica*) meadows. *Aquat. Bot.* 65, 255–268, doi:10.1016/S0304-3770(99)00044-3.
- Granata, T., T. Serra, J. Colomer, X. Casamitjana, C. Duarte, & E. Gacia (2001), Flow and particle distributions in a nearshore seagrass meadow before and after a storm. *Mar. Ecol. Prog. Ser.* 218, 95–106, doi:10.3354/meps218095.
- Gruber, R., & W. M. Kemp (2010), Feedback effects in a coastal canopy-forming submersed plant bed. *Limnol. Oceanogr.*, 55(6):2285–2298, doi:10.4319/lo.2010.55.6.2285.
- Hansen, J.C.R., & M.A. Reidenbach (2012). Wave and tidally driven flows in eelgrass beds and their effect on sediment suspension. *Mar. Ecol. Prog. Ser.* 448, 271–287, doi:10.3354/meps09225.
- Howard, J., S. Hoyt, K. Isensee, E. Pidgeon, & M. Telszewski, eds. 2014. Coastal blue carbon: Methods for assessing carbon stocks and emissions factors in mangroves, tidal salt marshes, and seagrass meadows, Conservation International, Intergovernmental Oceanographic Commission of UNSECO, International Union for Conservation of Nature.
- Infantes, E., Orfila, A., Simarro, G., Terrados, J., Luhar, M., & H. Nepf (2012). Effect of a seagrass (*Posidonia oceanica*) meadow on wave propagation. *Mar. Ecol. Prog. Ser.*, 456, 63–72, doi:10.3354/meps09754.
- Kamphuis, J. William. (2010). Introduction to coastal engineering and management, Advanced Series on Ocean Engineering (Vol. 30). World Scientific Co. Pte. Ltd.
- Kennedy, H., J. Beggins, C. Duarte, J. Fourqurean, M. Holmer, N. Marbà, & J. Middelburg (2010), Seagrass sediments as a global carbon sink: Isotopic constraints, *Global Biogeochem. Cycles*, 24, GB4026, doi:10.1029/2010GB003848.
- Keulegan, G. H., & L.H. Carpenter (1958). Forces on cylinders and plates in an oscillating fluid. *J. Res. Natl. Bur. Stand.*, 60(5), 423–440, doi:10.6028/jres.060.043.
- Komar, P. D., & C.M. Miller (1973). The threshold of sediment movement under oscillatory water waves. *J. Sediment. Petrol.*, 43(4), 1101–1110, doi:10.1306/74D7290A-2B21-11D7-8648000102C1865D.
- Krishnaswami, S., Lal, D., Martin, J. M. & M. Meybeck (1971). Geochronology of lake sediments. *Earth Planet. Sci. Lett.*, 11, 407–414, doi:10.1016/0012-821X(71)90202-0.
- Lavery, P., M. Mateo, O. Serrano, & M. Rozaimi (2013), Variability in the carbon storage of seagrass habitats and its implications for global estimates of blue carbon ecosystem service. *PLoS One*, 8(9), e73748, doi:10.1371/journal.pone.0073748.

- Lei, J., & H. Nepf (2019). Wave damping by flexible vegetation: Connecting individual blade dynamics to the meadow scale. *Coast. Eng.*, 147, 138-148, doi:10.1016/j.coastaleng.2019.01.008.
- Lei, J., & H. Nepf (2021). Evolution of velocity from leading edge of 2D and 3D submerged canopies. *J. Fluid Mech.*, 916, 1-37, doi:10.1017/jfm.2021.197.
- Lei, J., Schaefer, R., Colarusso, P., Novak, A., Simpson, J. C., Masqué, P., & H. Nepf (2023). Spatial heterogeneity in sediment and carbon accretion rates within a seagrass meadow correlated with the hydrodynamic intensity. *Sci. Total Environ.*, 854, doi:10.1016/j.scitotenv.2022.158685.
- Lowe, R. J., Koseff, J. R., & S.G. Monismith (2005). Oscillatory flow through submerged canopies: 1. Velocity structure. *J. Geophysical. Res. Oceans*, 110(C10), doi:10.1029/2004JC002788.
- Luhar, M., J. Rominger, & H. Nepf (2008). Interaction between flow, transport and vegetation spatial structure. *Env. Fluid. Mech.* 8: 423-439, doi:10.1007/s10652-008-9080-9.
- Luhar, M., & H.M. Nepf (2016). Wave-induced dynamics of flexible blades. *J. Fluids. Struct.*, 61, 20-41, doi:10.1016/j.jfluidstructs.2015.11.007.
- Luhar, M., E. Infantes, & H. M. Nepf (2017). Seagrass blade motion under waves and its impact on wave decay. *J. Geophys. Res. Ocean.* 122: 3736–3752, doi:10.1002/2017JC012731
- Martins, M., Carmen, B., Masqué, P., Carrasco, A. R., Veiga-Pires, C., & R. Santos (2021). Carbon and nitrogen stocks and burial rates in intertidal vegetated habitats of a mesotidal coastal lagoon. *Ecosystems*, 1-15, doi:10.1007/s10021-021-00660-6.
- Mendez, F.J., & I.J. Losada (2004). An empirical model to estimate the propagation of random breaking and nonbreaking waves over vegetation fields. *Coast. Eng.* 51, 103–118, doi.org/10.1016/j.coastaleng.2003.11.003.
- Novak, A. B., Pelletier, M. C., Colarusso, P., Simpson, J., Gutierrez, M. N., Arias-Ortiz, A., Charpentier, M., Masqué, P., & P. Vella (2020). Factors influencing carbon stocks and accumulation rates in eelgrass meadows across New England, USA. *Estuaries Coast.* 43(8), 2076-2091, doi:10.1007/s12237-020-00754-9.
- Oreska, M. P. J., K. J. McGlathery, & J. H. Porter (2017). Seagrass blue carbon spatial patterns at the meadow-scale. *PLoS One* 12, doi:10.1371/journal.pone.0176630.
- Poppe, K. L., & J.M. Rybczyk (2018). Carbon sequestration in a pacific northwest eelgrass (*Zostera marina*) meadow. *Northwest Sci.*, 92(2), 80–91, doi:10.3955/046.092.0202.
- Prentice, C., Poppe, K. L., Lutz, M., Murray, E., Stephens, T. A., Spooner, A., HESSING-Lewis, M., Sanders-Smith, R., Rybczyk, J. M., Apple, J., Short, F. T., Gaeckle, J., Helms, A., Mattson, C., Raymond, W. W., & T. Klinger (2020). A synthesis of blue carbon stocks, sources, and accumulation rates in eelgrass (*Zostera marina*) meadows in the Northeast Pacific. *Global Biogeochem. Cycles*, 34(2), 1–16, doi:10.1029/2019GB006345.

- Ricart, A. M., P. H. York, C. V. Bryant, M. A. Rasheed, D. Ierodiaconou, & P. I. Macreadie. 2020. High variability of Blue Carbon storage in seagrass meadows at the estuary scale. *Sci. Rep.* 10, 1–12, doi:10.1038/s41598-020-62639-y.
- Ros, À., Colomer, J., Serra, T., Pujol, D., Soler, M., & X. Casamitjana (2014). Experimental observations on sediment resuspension within submerged model canopies under oscillatory flow. *Cont. Shelf Res.* 91, 220–231, doi.org/10.1016/j.csr.2014.10.004.
- Samper-Villarreal, J., Lovelock, C. E., Saunders, M. I., Roelfsema, C., & P.J. Mumby (2016). Organic carbon in seagrass sediments is influenced by seagrass canopy complexity, turbidity, wave height, and water depth. *Limnol. and Oceanogr.*, 61(3), 938-952, doi:10.1002/lno.10262.
- Sanchez-Cabeza, J. A., Masqué, P. & Ani-Ragolta, I. (1998). ²¹⁰Pb and ²¹⁰Po analysis in sediments and soils by microwave acid digestion. *J. Radioanal. Nuc. Chem.*, 227, 19–22, doi:10.1007/BF02386425.
- Serrano, O., Lavery, P. S., Rozaimi, M., & M. Á. Mateo (2014). Influence of water depth on the carbon sequestration capacity of seagrasses. *Global Biogeochem. Cycles*, 28(9), 950-961, doi:10.1002/2014GB004872.
- Ståhlberg, C., Bastviken, D., Svensson, B. H., & L. Rahm (2006). Mineralisation of organic matter in coastal sediments at different frequency and duration of resuspension. *Estuar. Coast. Shelf Sci.*, 70(1–2), 317–325, doi:10.1016/j.ecss.2006.06.022.
- Tang, C., Lei, J., & H.M. Nepf (2019). Impact of vegetation-generated turbulence on the critical, near-bed, wave-velocity for sediment resuspension. *Water Resour. Res.*, 55(7), 5904-5917, doi:10.1029/2018WR024335.
- Tanino, Y., & H.M. Nepf (2008). Lateral dispersion in random cylinder arrays at high Reynolds number. *J. Fluid Mech.*, 600, 339-371, doi:10.1017/S0022112008000505.
- Tinoco, R.O., & G. Coco (2018). Turbulence as the main driver of resuspension in oscillatory flow through vegetation. *J. Geophys. Res. Earth Surf.*, 123, 891-904, doi.org/10.1002/2017JF004504.
- Yang, J. Q., Chung, H., & H.M. Nepf (2016). The onset of sediment transport in vegetated channels predicted by turbulent kinetic energy. *Geophys. Res. Lett.*, 43(21), 11,261-11,268, doi.org/10.1002/2016GL071092.
- Zhang, J., Lei, J., Huai, W. & H. Nepf (2020). Turbulence and particle deposition under steady flow along a submerged seagrass meadow. *J. Geophys. Res. Oceans*, 125(5), doi:10.1029/2019JC015985.
- Zhang, Y., Tang, C., & H. Nepf (2018). Turbulent kinetic energy in submerged model canopies under oscillatory flow. *Water Resour. Res.*, 54(3), 1734-1750, doi:10.1002/2017WR021732.
- Zhang, Y., & H. Nepf (2019). Wave-driven sediment resuspension within a model eelgrass meadow. *J. Geophys. Res. Earth Surf.*, 124(4), 1035–1053, doi:10.1029/2018JF004984.

5.7 Supplementary Information

5.7.1 Tilt current meter measurements in the presence of waves

Tilt current meters (TCMs) are instruments with self-contained accelerometers and magnetometers that are marketed to measure time-mean currents. We ran a set of tests in a laboratory flume to compare velocities measured by a Lowell Instruments TCM and a Nortek Vectrino (acoustic Doppler velocimeter, ADV). We considered pure wave, combined wave-current, and pure current cases. The wave periods were 2.0 and 3.3 s. Waves were generated using a piston-type paddle wavemaker controlled by a Syscomp WGM-101 waveform signal generator. We tethered the TCM to the bottom of the flume and set up the Vectrino to measure at 15 cm above the bed, approximately half of the vertical height of the TCM.

Time-average (\bar{U}), peak (U_p), and root-mean-squared (RMS) (U_{RMS}) velocities recorded by the TCM and Vectrino are compared in Figure 5.S.1. The peak velocity was defined as the average of the highest 10% of velocity magnitudes. The TCM slightly over-estimated the time-mean velocity (Figure 5.S.1(a)), with $\overline{U_{TCM}} = (1.27 \pm 0.08)\overline{U_{ADV}}$. The best agreement was between peak velocity (Figure A.1(b)), with $U_{p,TCM} = (1.09 \pm 0.09)U_{p,ADV}$. The RMS velocity agreed to within 20%, $U_{RMS,TCM} = (0.9 \pm 0.2)U_{RMS,ADV}$. The velocity magnitudes were similar to those measured in the field (Figure 5.3 in the main text). TCMs are less expensive, sturdier, and easier to transport and set up compared to acoustic type velocity meters, providing a relatively inexpensive way to capture spatial variation in hydrodynamic intensity. These laboratory measurements indicate that TCMs could be reasonably used in field experiments for characterizing time-mean and wave velocities.

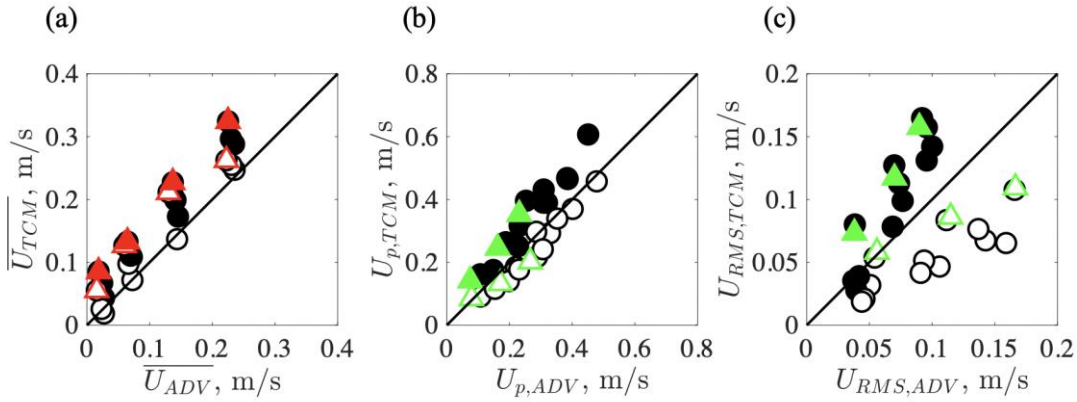


Figure 5.S.1: Comparison of TCM and ADV measurements. Open and filled symbols denote wave periods $T=2.0$ s and 3.3 s, respectively. (a) Time-averaged velocities, with pure current (red triangle) and combined wave-current (black circles) conditions. Linear fit: $\overline{U}_{TCM} = (1.27 \pm 0.08) \overline{U}_{ADV}$. (b) Peak velocities, with pure wave (green triangle) and combined wave-current (black circles) conditions. Linear fit: $U_{p,TCM} = (1.09 \pm 0.09) U_{p,ADV}$. The peak velocity is defined as the average of the highest 10% of velocity magnitudes. (c) RMS velocities, with pure wave (green triangle) and combined wave-current (black circles) conditions. Linear fit: $U_{RMS,TCM} = (0.9 \pm 0.2) U_{RMS,ADV}$.

5.7.2 Additional data analysis

For additional analysis, the nine meadow sites were grouped into the three depth zones: Shallow, Mid, and Deep. Statistical tests were carried out on meadow percentage organic carbon (%OC) and carbon accretion rate (CAR) to evaluate the influence of the depth zone. The significance level used in the following tests was 0.05. Tests for normality (Shapiro-Wilk test) and equal variance (Bartlett test) were satisfied before conducting ANOVA (analysis of variance) based on meadow measurements grouped by depth zone, with three sites in each group. For meadow %OC, the ANOVA p-value was 0.0049, indicating overall significance. Tukey's Honestly Significant Difference (HSD) post-hoc test was used for pairwise comparisons. The compact

letter display is shown in Figure B.1, indicating which depth zones were statistically significantly different in %OC. The Mid-Shallow comparison was statistically significant.

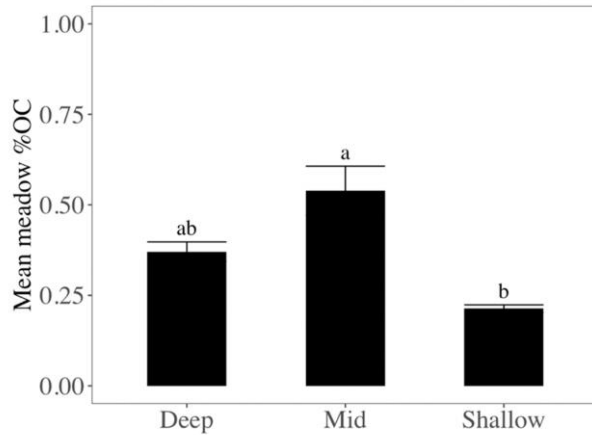


Figure 5.S.2: Mean meadow percent organic carbon %OC by depth zone. Letters indicate statistical differences among the depth zones.

Only one core in each of the Shallow and Mid depth zones yielded a sedimentation rate, such that sedimentation rates alone could not be statistically analyzed. *CAR* at each site were based on mean organic carbon measurements at each site and the sedimentation rate per depth zone reported in Table 5.1 in the main text. Tests for normality (Shapiro-Wilk test) and equal variance (Bartlett test) were satisfied before conducting ANOVA on *CAR*. The ANOVA p-value was 2.1×10^{-4} , indicating overall significance. Tukey's HSD post-hoc test indicated the carbon accretion rates by depth zones were statistically significantly different from each other (Figure 5.S.2).

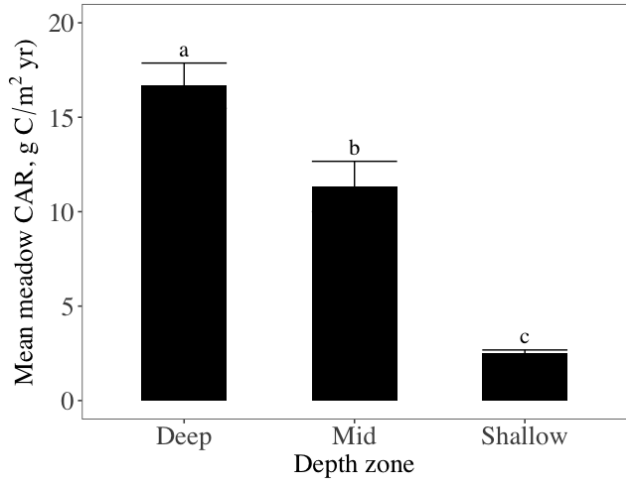


Figure 5.S.3: Mean meadow carbon accretion rate CAR by depth zone. Letters indicate statistical differences among the depth zones.

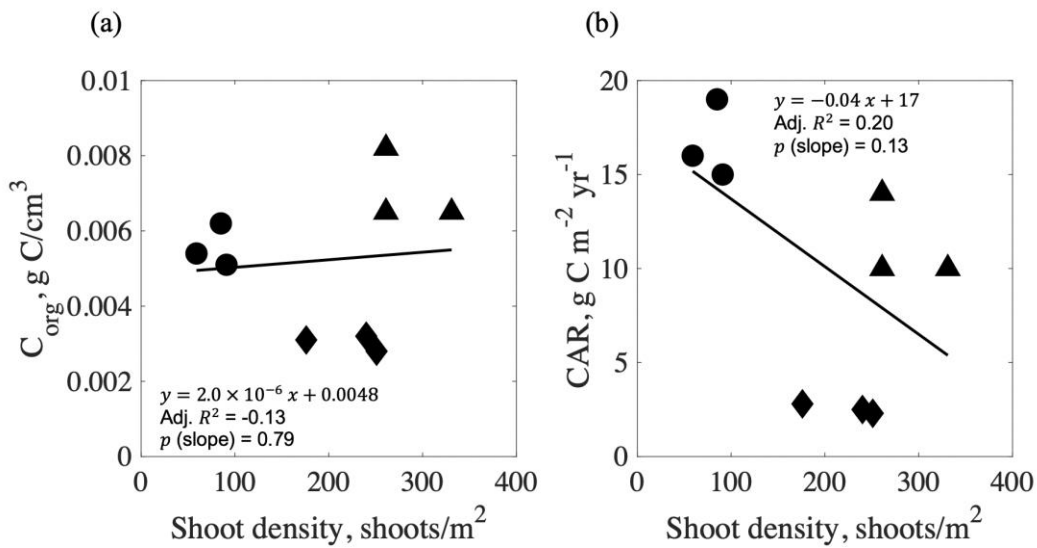


Figure 5.S.4: (a) Soil organic carbon C_{org} versus shoot density. (b) Carbon accretion rate CAR versus shoot density. Circles denote the Deep zone, triangles denote the Mid zone, and diamonds denote the Shallow zone. The solid curves denote the lines of best fit.

Chapter 6

Proximity to inlet channel drives spatial variation in sediment organic carbon across a lagoonal seagrass meadow

Abstract:

Seagrass meadows are known to be efficient sinks for organic carbon, but estimates of global carbon stocks are complicated by substantial spatial variability in organic carbon burial within a single meadow and among different meadows of the same species. This study investigated relationships between spatial patterns in sediment organic carbon accretion rates and stocks, hydrodynamics, and proximity to the expected dominant source of carbon in a current-dominated *Zostera marina* Linnaeus meadow in Menemsha Pond, Martha's Vineyard, Massachusetts, USA.

Sediment and velocity measurements were carried out at six stations along a 150-m long transect in the meadow perpendicular to the pond's inlet channel. The edge of the meadow had higher surface organic matter content than the adjacent unvegetated inlet channel, and this was also the highest surface organic content in the meadow. With increasing distance from the inlet channel and into meadow, all of the following parameters decreased: sediment organic carbon content, sediment accretion rates, peak tidal velocity, sediment trap mass, and the relative contributions of allochthonous (non-seagrass) sources to sediment organic carbon. Lower tidal velocities farther from the inlet channel reduced resuspension, consistent with lower sediment trap mass, which should produce more effective carbon burial. However, the opposite trend of decreasing carbon content and accretion rates with distance from channel was observed. This suggested that local hydrodynamics was not controlling carbon accretion, which was instead constrained by supply limitation and controlled by the lagoon-scale circulation.

6.1 Introduction

Seagrasses are photosynthesizing plants found along coastlines throughout the world (Unsworth et al., 2019). They provide a variety of economically valuable ecosystem services, including habitat for fish and shellfish (e.g., Pollard, 1984), wave attenuation that protects shorelines (e.g., Infantes et al., 2012), water quality enhancement (e.g., Ward et al., 1984), and sediment organic carbon sequestration (e.g., Miyajima et al., 1998). Many of the ecosystem services provided by seagrass meadows are driven by the drag-induced attenuation of current velocity within the meadow (Fonseca et al., 1982). Specifically, a reduced near-bed current inhibits the

remobilization of sediment and promotes the retention of particles, which reduces turbidity and improves water quality. In addition, organic matter can be preserved through adsorption to predominantly fine sediments (Hemingway et al., 2019; Keil & Hedges, 1993), such that the enhancement of fine sediment deposition promotes sediment organic carbon burial.

There has been growing interest in the carbon sequestration provided by seagrass meadows, which might be used to compensate for anthropogenic greenhouse gas emissions (Nellemann et al., 2009). Seagrass meadows are estimated to have about twice as much sediment organic carbon content per unit area as terrestrial ecosystems (Fourqurean et al., 2012). At the same time, seagrass populations have been declining 7% per year globally since 1990 due to climate change and human activities (Orth et al., 2006; Waycott et al., 2009), leading to significant loss of carbon stores that were previously protected by the disappearing seagrass meadows (Salinas et al., 2020). Projects to restore degraded seagrass meadows or protect existing meadows can prevent those meadows from changing from carbon sinks into carbon sources (e.g., Greiner et al., 2013).

An assessment of the carbon credit-worthiness of a particular seagrass restoration project, which is based on quantifying how the restoration enhances carbon stocks compared to a baseline degraded or unvegetated condition (e.g., Lafratta et al., 2020), has been hindered by the significant spatial variability observed in sediment organic carbon stocks and accumulation rates between different meadows (Lavery et al., 2013; Mazarrasa et al., 2021; Ricart et al., 2020) and also within the same meadow (Lei et al., 2023; Oreska et al., 2017). To improve estimates of carbon stocks, it is necessary to understand the causes of the spatial heterogeneity.

Some recent studies have considered how spatial gradients in hydrodynamic conditions drive spatial gradients in carbon stock and accretion rate. For example, at a wave-dominated seagrass site, Lei et al. (2023) showed that spatial variation in wave velocity, resulting from a combination of seagrass-induced wave dissipation and wave shoaling, produced spatial variation in carbon accumulation rates. Specifically, they observed that accretion rates decreased as wave velocity increased, which was associated with higher resuspension at sites with higher wave velocity. At a current-dominated site, Oreska et al. (2017) determined that proximity to the edges of a seagrass meadow was the major factor in kilometer-scale spatial gradients in sediment organic carbon content, with higher carbon content measured farther from the meadow edge. The spatial gradients in organic carbon content were correlated with spatial gradients in sediment grain size and hydrodynamic intensity, both of which decreased with distance from meadow edge. Specifically, finer sediments, which are associated with high carbon content, were carried farther into a seagrass meadow before depositing, and the finer sediment was protected from resuspension by the lower hydrodynamic intensity farther from the meadow edge.

This aim of this study was to contribute additional understanding of hydrodynamic controls on carbon storage and accretion by relating spatial patterns in sediment organic carbon content and accumulation rates across a seagrass meadow to several environmental parameters, including the distance to potential sources of carbon, as well as peak tidal velocity. The seagrass meadow is located adjacent to the lagoon's inlet channel, which is flanked by wetlands, such that the channel is likely the dominant source of fine sediments and carbon to the lagoon.

6.2. Materials and Methods

6.2.1 Field site

The study was conducted in a *Zostera marina* Linnaeus meadow in Menemsha Pond on the island of Martha's Vineyard in Massachusetts, on the East Coast of the United States of America (Figure 6.1). Menemsha Pond, approximately 1.9 km by 1.5 km in area, is a tidal lagoon connected to the ocean through a regularly dredged inlet channel. Six measurement stations were chosen along a transect in the meadow that was approximately perpendicular to the inlet channel. Stations were labeled MP1, MP2, MP3, MP4, MP5, and MP6 (Figure 6.1), with MP1 located at the meadow edge closest to the inlet channel, and MP6 located at the farther end of the transect, 150 m from the meadow edge. Mean water depths at the stations were estimated from National Oceanic and Atmospheric Administration (NOAA) National Ocean Science nautical charts.



Figure 6.1: The right image shows a map of the Menemsha Pond seagrass meadow field site, in Massachusetts, United States of America. Circles denote measurement station locations. Diamonds denote locations from which surface sediment samples were taken in the channel. October, 2022 image copyright Airbus, 2024. The gray rectangle in the bottom left image of Menemsha Pond (October, 2022 image copyright Airbus, 2024) corresponds to the right image (copyright Airbus, 2024). The top left image of the United States East Coast is copyright Landsat/Copernicus.

6.2.2 Sediment sample collection

In October 2022, one sediment core was extracted at each measurement station by scientific divers using a manual T-handled driver to drive a 7.0 cm outer diameter, 6.7 cm inner diameter polycarbonate tubes to the point at which it could not go deeper. Sediment compression that occurred during the core extraction process was measured by marking the level of the outside sediment surface on the tube before the core was pulled from the sediment. Sediment cores were

kept vertical while being transported by boat to the dock, where they were systematically extruded into 1-cm thick cylindrical slices up to 20 cm depth and 2-cm thick slices for deeper sediment. Estimated sediment core compression resulting from coring and extrusion ranged from 13% to 16%, with the S4 core being an exception with 27% compression due to removal of a large quahog from the core. Sediment core slices were placed into separate pre-weighed, labeled Whirl-Pak bags, which were stored in a cooler until arrival at a laboratory.

A sediment trap was deployed at each station, comprised of a frame with three cylindrical polyvinyl chloride (PVC) tubes of length 15 cm and inner diameter 5 cm that rested on the bed, following common practice discussed in Blomqvist & Kofoed (1981). A honeycomb baffle (Plascore, Zeeland, Michigan) was installed in each tube to reduce sediment resuspension out of the tube. The sediment traps were deployed for three weeks in September to October 2022.

To produce a higher resolution map of organic carbon content along the transect, surface sediment samples were collected every 5 m between MP1 and MP5 (0 to 100 m) and every 3 m between MP5 and MP6. 20-mL lined scintillation vials were pushed 2 to 3 cm into the sediment surface, capped, and labeled with the position along the transect. There were several small bare regions within the meadow on the transect. Whether the sampling location was bare or vegetated was recorded at the time of sample collection. Collected vials were stored in a cooler during transport to a laboratory.

6.2.3 Seagrass parameters and sample collection

The shoot density at each station was measured using three haphazardly placed 25 cm × 25 cm quadrats near the sediment core locations. At least fourteen shoots were randomly removed from each station to measure leaf length, sheath length, and shoot width. Fifteen shoots were transported to a laboratory, where the second leaf of each shoot was detached, dried, and homogenized into powder.

6.2.4 Laboratory sample analyses

Once uncapped, the material in the sediment trap tubes was allowed to settle before water was decanted. The sediment from each tube was placed into a separate pre-weighed Whirl-Pak bag. Shellfish, arthropods, shell fragments, and plant matter were carefully removed from each sample to capture the long-term carbon storage compartment (e.g., Greiner et al., 2013).

Sediment trap and sediment core samples were dried to constant mass in a 60°C drying oven and then homogenized with a mortar and pestle. Sediment samples were not pre-washed with acid due to the physical removal of shells, low inorganic carbon measured in similar *Z. marina* L. meadows in the northeastern USA (based on US Environmental Protection Agency surveys in the region), as well as the possibility of biasing stable isotope ratios and elemental analyses (Brodie et al., 2011). Subsamples from the top 5 cm of the crushed sediment core slices were combined and dry sieved with size fractions from the Krumbein ϕ scales of 0.5 to 3.5 (equivalent to diameters of 0.71 mm to 0.089 mm) to quantify the near-surface sediment grain size distribution at each station.

Elemental analyses for organic carbon content (%OC) and nitrogen content (%N) as well as stable isotope ratios $\delta^{13}\text{C}$ (relative to the Vienna Pee Dee Belemnite [VPDB] international standard) and $\delta^{15}\text{N}$ (relative to atmospheric air) were performed on tinned subsamples of the homogenized sediment trap and sediment core samples and tinned homogenized seagrass leaf samples using the Isoprime 100 isotope ratio mass spectrometer (IRMS) interfaced with a Micro Vario Elemental Analyzer (Elementar Americas, Mt. Laurel, New Jersey). In-house laboratory standards (peptone and glycine) were processed every 10 to 20 samples for quality control. A large quahog occupied part of the MP4 core near the surface, likely affecting the top 8 cm. Each sediment core was at least 20 cm long. For the purpose of accurate comparison across the transect, averages of %OC, %N, $\delta^{13}\text{C}$, and $\delta^{15}\text{N}$ were taken of core slices at each measurement station between 10 cm and 20 cm sediment depth.

The surface sediment collected in vials was dried to constant mass at 60°C. Plant material and shell fragments were removed before the samples were crushed into homogeneous powder. Two subsamples from each vial were ignited in crucibles in a furnace at 450°C for 6 hours to optimize the complete loss of organic carbon and preservation of inorganic carbon (Dean, Jr., 1974; Froelich, 1980). The loss in mass during the burning process was used to calculate the percentage of organic matter (%OM) in the subsample. Organic matter content measurements were converted to organic carbon content (%OC) estimates based on a linear regression compiled from measurements in other similar *Zostera marina* L. meadows in Massachusetts, USA, $\%OC = (0.338 \pm 0.034) \%OM - (0.138 \pm 0.010)$ (Novak et al., 2020).

Finally, to obtain estimates of mass accumulation rates, one subsample from what remained of each sediment core slice was analyzed for ^{210}Pb radioisotope activity. To reduce

delays, two different laboratories were employed, so that three cores were analyzed using gamma spectrometry (using a Canberra GL 2020 Low Energy Germanium detector for the MP1, MP3, and MP6 cores) and two cores with alpha spectrometry (using an EG&G Ortec Octet alpha spectrometer for the MP2 and MP5 cores). The MP4 core was not analyzed due to heavy mixing and loss of sediment volume in the top 10 cm associated with the large quahog lodged in that section of the core. The MP1, MP3, and MP6 core subsamples were packed into Petri dishes and sealed with electrical tape and paraffin wax 30 days prior to analysis to allow for equilibration between ^{226}Ra and its daughter isotopes, ^{214}Pb and ^{214}Bi (Martz & Langner, Jr, 1991). The activities of ^{214}Pb and ^{214}Bi were then used to determine the background levels of ^{210}Pb . ^{210}Pb activities were corrected for detector efficiency and self-attenuation using the point-source method (Cutshall et al., 1983). For the MP2 and MP5 cores, total ^{210}Pb activities were measured through ^{210}Po as a proxy (based on Eakins & Morrison, 1978), and background ^{210}Pb activities were measured through ^{226}Ra , which was derived from measurements of ^{222}Rn using a SPECTECH UCS-30 alpha spectrometer (based on Mathieu et al., 1988).

For all cores, the concentrations of excess ^{210}Pb were determined as the difference between total ^{210}Pb and background ^{210}Pb (for the MP2 and MP5 cores, the nearest neighboring ^{226}Ra measurement). A constant flux-constant sedimentation model (CFCS; Corbett & Walsh, 2015) was used to calculate mass accumulation rates *MAR*. The *MAR* values were multiplied by the respective average sediment organic carbon content in the sediment cores to yield carbon accretion rates *CAR*. The excess ^{210}Pb profiles in the MP3 core did not yield conclusive results, likely due to sediment mixing. Finally, while ^{137}Cs activity profiles are commonly used to confirm results from ^{210}Pb results, the sediment core ages inferred from the ^{210}Pb modelling indicated that the cores were not long enough to include the assumed 1963 peak in ^{137}Cs

associated with bomb-produced radionuclides (Nittrouer et al., 1984; Pennington et al., 1973; Ritchie & McHenry, 1990) Preliminary ^{137}Cs measurements indeed did not show any peaks in activity.

6.2.5 Velocity data collection and processing

Tilt current meters (Lowell Instruments, Massachusetts) anchored to square paving stones were used to record flow velocity at each transect station for three weeks in September to October 2022, i.e., the same deployment period as the sediment traps. Velocity was recorded at 16 Hz for 60-second bursts every five minutes. Velocity data were divided into two bins according to the instantaneous flow direction, with flood velocities directed toward the west-southwest and denoted as positive, and ebb velocities directed toward the east and denoted as negative. The tidal velocity peaks were found by applying the MATLAB *findpeaks* function to a moving average of velocity with a 60-minute window. The peak velocities were separately averaged for the flood and ebb phases, denoted as $\overline{U_{c,peak}}$. As the deployment occurred over approximately three weeks, the velocity record was biased toward neap tides. To account for this bias, the velocity record was divided into neap and spring phases (assuming the divisions of spring and neap tides coincided with the lunar quarter phases) so that both phases contributed equally to $\overline{U_{c,peak}}$.

Tidal currents deflected both the tilt current meter and the surrounding flexible seagrass shoots, such that at peak tidal velocity the height of the deflected meadow was lower than the height of the deflected tilt current meter. Consequently, the velocity both within and above the meadow contributed to the TCM measurement. To isolate the flow conditions near the bed,

which are more important for sediment retention and carbon sequestration, we applied a two-layer velocity model to estimate the average peak tidal velocity inside the meadow, $\overline{U_{1,peak}}$, from the average peak velocity $\overline{U_{c,peak}}$ and meadow characteristics. See the Supplemental Information of Lei et al. (2023) and Schaefer et al. (2024, in review) for more details on the processing of the tilt current meter data. Due to the absence of *in situ* measurements of the number of leaves per seagrass shoot, we assumed an average of four leaves per shoot based on measurements from other Massachusetts *Z. marina* L. meadows reported in Lei et al. (2023) and Schaefer et al. (2024, in review).

6.3 Results

The measurement locations at the field site were chosen with the expectation of observing trends in sediment organic carbon content and sediment carbon accretion rates with increasing distance away from the inlet channel, resulting from a balance of gradients in hydrodynamic intensity against proximity to the likely dominant source of carbon in the wetlands along the inlet channel. We will next describe the experimental results, which will then direct our discussion of these ideas.

6.3.1 Seagrass and sediment characteristics

Seagrass and sediment properties, mean water depths, D , and station distances from MP1 are reported in Table 6.1. Shoot density m_s and blade length l_b were somewhat smaller at MP1, but otherwise did not show any systematic variation across the transect. Average shoot widths were

higher at MP5 and MP6 compared to the rest of the stations. The one-sided leaf area index LAI (assuming four leaves per shoot, as in Section 6.2.5) was similar within uncertainty for MP1 through MP5, and slightly higher at MP6. The percentage of near-surface sediment finer than the Krumbein scale $\phi = 3.5$ (equivalent to $89 \mu\text{m}$, and the finest categorical scale used in the grain size measurements) increased between MP1 and MP3 and decreased between MP3 and MP6. See Figure S1 in the Supplementary Information for the sediment grain size distributions.

Station	L_{MP1} (m)	D (m)	m_s (m^{-2})	w_b (cm)	l_b (cm)	LAI	l_s (cm)	$\phi \geq 3.5$ (%)
MP1	0	0.6	160 ± 19	0.25 ± 0.02	17.5 ± 1.9	0.28 ± 0.05	6.3 ± 0.4	1.4
MP2	10	0.6	280 ± 70	0.25 ± 0.02	19 ± 2	0.52 ± 0.16	5.5 ± 0.3	1.6
MP3	20	0.6	200 ± 20	0.22 ± 0.018	20 ± 2	0.35 ± 0.06	6.8 ± 0.6	2.1
MP4	50	0.7	220 ± 40	0.24 ± 0.02	23 ± 2	0.48 ± 0.11	7.5 ± 0.6	0.59
MP5	100	0.8	91 ± 5	0.46 ± 0.02	24 ± 2	0.40 ± 0.08	8.4 ± 0.2	0.50
MP6	150	0.9	180 ± 30	0.46 ± 0.02	22 ± 2	0.72 ± 0.16	7.1 ± 0.5	0.28

Table 6.1: Parameters of Menemsha Pond transect stations, with distance to station MP1 L_{MP1} , mean water depth D , seagrass shoot density m_s , shoot width w_b , leaf length l_b , one-sided leaf area index LAI (assuming four leaves per shoot as in Section 2.5), sheath length l_s (such that the total shoot height is $l_b + l_s$), and percentage of near-surface sediment finer than the Krumbein scale $\phi=3.5$, equivalent to $89 \mu\text{m}$. Averages are reported with standard errors and propagated standard errors.

Considering how sediment carbon and nitrogen stable isotope ratios change across the meadow can provide insight into how the relative contributions of potential sources of carbon change across the meadow. Carbon stable isotope ratios $\delta^{13}\text{C}$ and nitrogen stable isotope ratios

$\delta^{15}N$ are shown in Figure 6.2 for the sediment trap (circles), sediment core (triangles), and seagrass leaf (square). In the sediment cores $\delta^{13}C$ was similar at 0m (MP1) and 20m (MP2) from the meadow edge, but became less depleted with farther distance into the meadow (between 20 and 150 m, triangles in Figure 6.2a). In addition, between 0 and 50 m sediment cores became more depleted in ^{15}N with distance from the channel, but remained constant between 50 m and 150 m (triangles in Figure 6.2d). The spatial variation in $\delta^{13}C$ and $\delta^{15}N$ indicated shifts in the relative contributions of different carbon and nitrogen sources. Spatial variation in $\delta^{13}C$ and $\delta^{15}N$ in the sediment traps were similar to, but less dramatic than, those in the sediment cores (compare circles and triangles in Figure 6.2a, 6.3d). In all cases, $\delta^{13}C$ in the sediment samples was substantially more depleted than that of the seagrass leaves (Figure 6.2c). While the dominant seagrass contribution to sediment $\delta^{13}C$ is expected to be from the more refractory rhizomes, which were not collected in this study, for *Z. marina* L., $\delta^{13}C$ in leaves (collected in this study) are typically similar to $\delta^{13}C$ in rhizomes (Kim et al., 2014; Xu et al., 2021). Therefore, sources more depleted in $\delta^{13}C$ than the seagrass, such as some types of wetland vegetation that are found on Martha's Vineyard (which have $\delta^{13}C$ values between -27‰ and -14‰, Bouillon & Boschker, 2006), were contributing to sediment ^{13}C .

Meanwhile, the average organic carbon and nitrogen content in the sediment traps and sediment cores generally decreased with distance from the channel, except at the MP6 sediment trap (left and right axes in Figure 6.2b; e). See the Supplementary Information for sediment core profiles of %OC, %N, $\delta^{13}C$, and $\delta^{15}N$. Lastly, the average mass of sediment deposited in the sediment traps over the three-week deployment decreased between 0 and 20 m and then remained the same within uncertainty between 20 m and 150 m (Figure 6.2f).

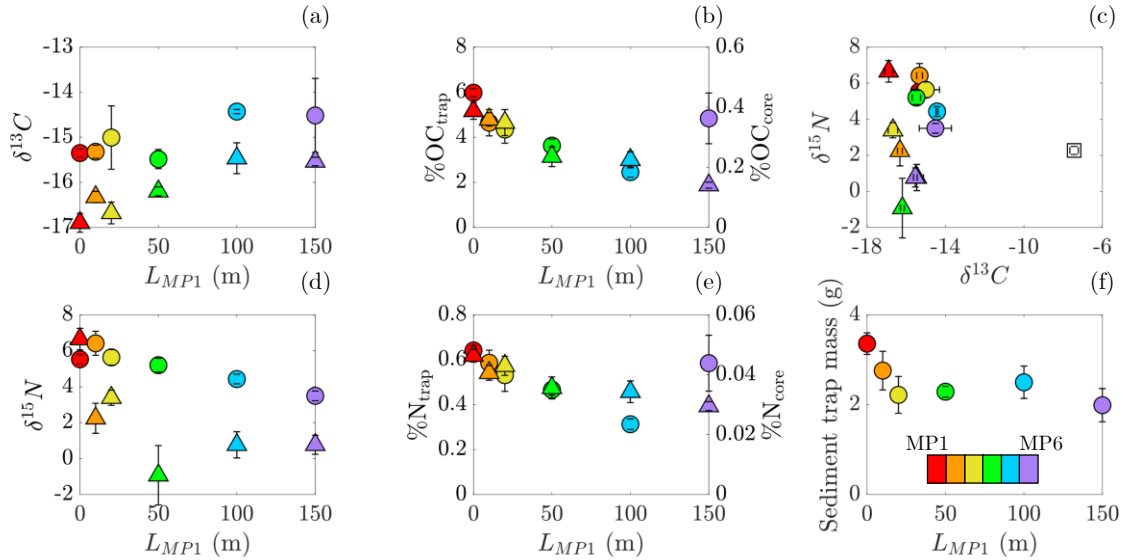


Figure 6.2: Triangle symbols denote sediment cores and circles denote sediment traps. (a) Average carbon stable isotope ratio $\delta^{13}C$ (‰, relative to VPDB) and (b) average organic carbon content %OC versus distance from station MP1 L_{MP1} (note the different y-axis scales for sediment cores and traps). (c) Average $\delta^{15}N$ (‰, relative to atmospheric air) versus average $\delta^{13}C$ for sediment and seagrass leaf samples. (d) Average $\delta^{15}N$, (e) average nitrogen content %N (note the different y-axis scales for sediment cores and traps), and (f) average sediment trap mass versus L_{edge} . Colors distinguish stations for visual clarity, with the legend in (f). The square symbol in (c) represents seagrass leaf samples. Error bars represent standard errors.

The presence of the meadow generally increased the sediment organic carbon content, especially near the meadow edge. Specifically, the surface %OC at the edge of the meadow (near MP1, Figure 6.3) was significantly higher than in the unvegetated channel. The organic carbon content decreased over the first 20 m into the meadow and then was approximately constant between 20 m and 150 m, with some lower points near bare regions (open circles in Figure 6.3). The small red symbols in Figure 6.3 denote a 15-m moving average of the measurements, excluding bare patches (open circles), e.g. near $L_{edge}=100$ m. The diamonds denote sediment samples taken from the unvegetated inlet channel near MP1. Finally, the squares denote the

average %OC in the top 3 cm of the sediment core for all stations except MP4, due to the quahog near the surface of that core. Noting the uncertainty in the conversion from %OM to %OC, the near-surface sediment core %OC measurements compared well within uncertainty with the vial sample measurements except at the edge of the meadow.

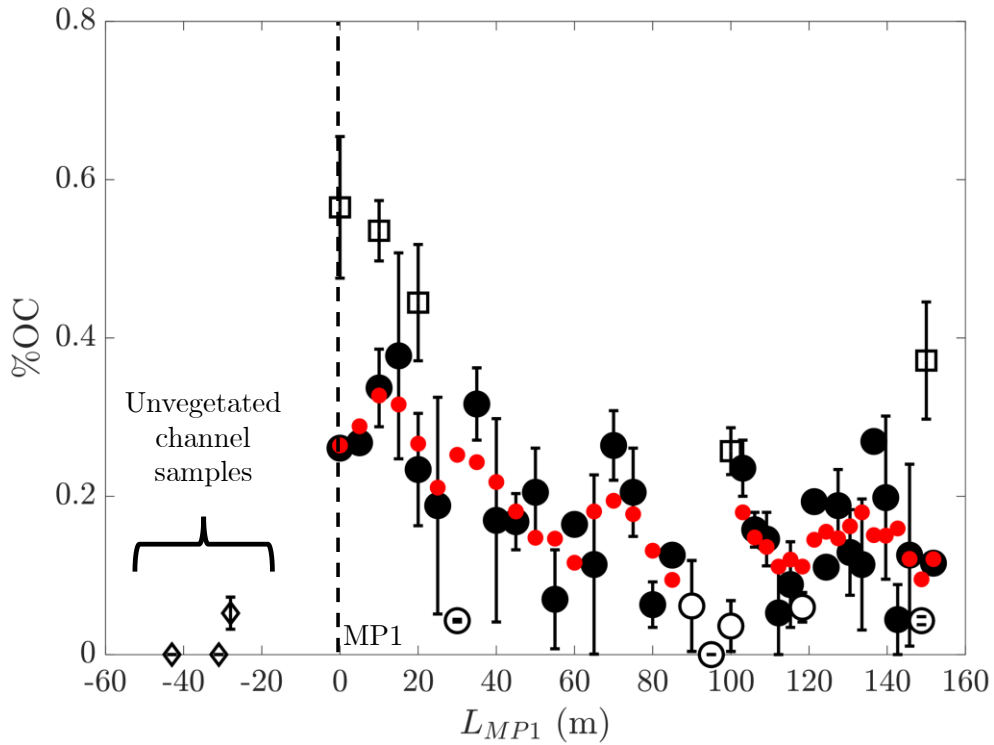


Figure 6.3: Black symbols represent converted percentage organic matter (%OC) obtained from loss-on-ignition measurements in surface sediment samples taken between MP1 and MP6 (circles) and three samples taken from the inlet channel (diamonds). Filled symbols denote measurements in vegetated regions, and open symbols are bare regions. Red circles are a 15-m moving average of measurements. Empty square symbols denote the average %OC in the top 3 cm slices of the sediment cores (excluding MP4, due to a quahog near the surface of that core). Error bars denote standard errors based on the two subsamples from each sediment sample.

6.3.2 Mass and carbon accumulation rates

Mass accumulation rates MAR and carbon accretion rates CAR were determined from four of the sediment cores (Figure 6.4). See Figure 6.S.6 in the Supplementary Information for the sediment core ^{210}Pb measurements and regressions. MAR was lowest at MP1, was the same within uncertainty at MP2 and MP5, and decreased between MP5 and MP6. CAR , which reflects the sediment core organic carbon content, was low directly at the meadow edge (MP1), increased rapidly within the meadow (MP2), then progressively decreased with distance from the channel edge (MP2 to MP6).

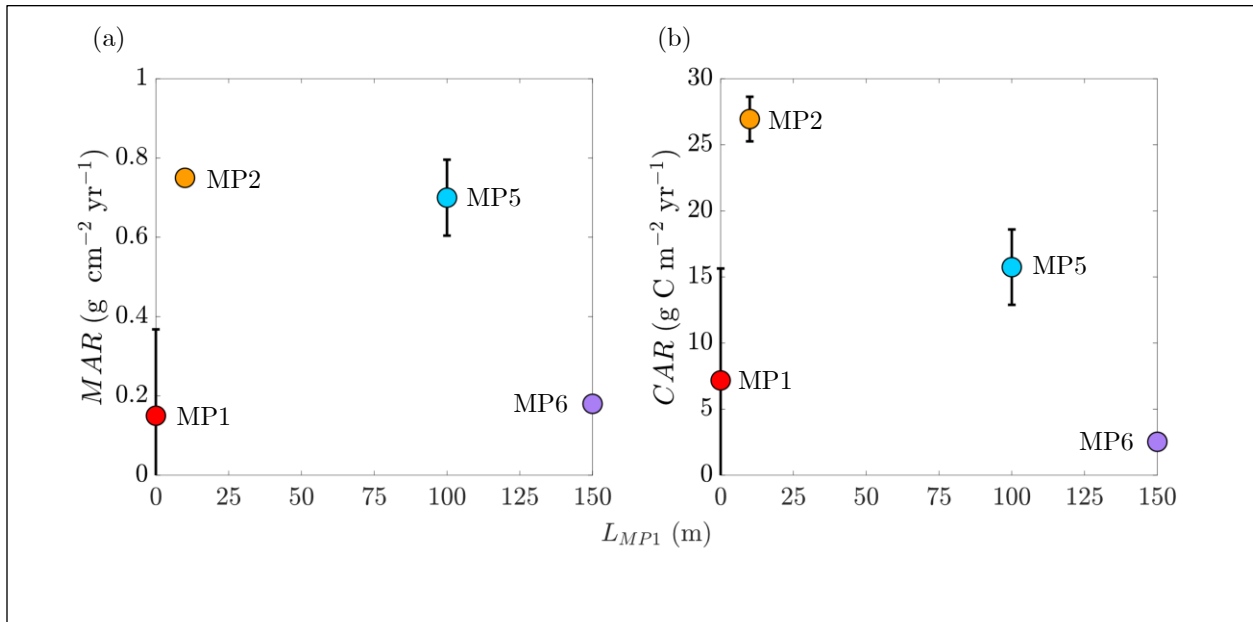


Figure 6.4: (a) mass accumulation rates MAR and (b) organic carbon accumulation rates CAR versus distance from MP1, denoted L_{MP1} . MAR error bars in (a) denote standard errors of the excess ^{210}Pb profile regressions (Arias-Ortiz et al., 2018). CAR error bars in (b) denote the MAR uncertainty propagated with the standard errors of the average sediment core organic carbon content.

6.3.3 Exposure to waves and currents

Peak tidal velocities were between 11 cm/s and 24 cm/s and decreased with distance from the channel (Figure 6.5a). Hourly-averaged wave velocities were typically 2 to 6 cm/s during the deployment (Figure 6.5b), reflecting the limited fetch. The hydrodynamics were current-dominated. During flood (water entering the pond), the flow direction rotated across the transect (Figure 6.6a and b), while during ebb (water leaving the pond), flow direction was similar across the transect (Figure 6.6c and d). Spring flood tidal velocity was similar to neap flood tidal velocity (compare Figure 6.6a and b), but spring ebb tidal velocity was typically higher than neap ebb velocity (compare Figure 6.6c and d).

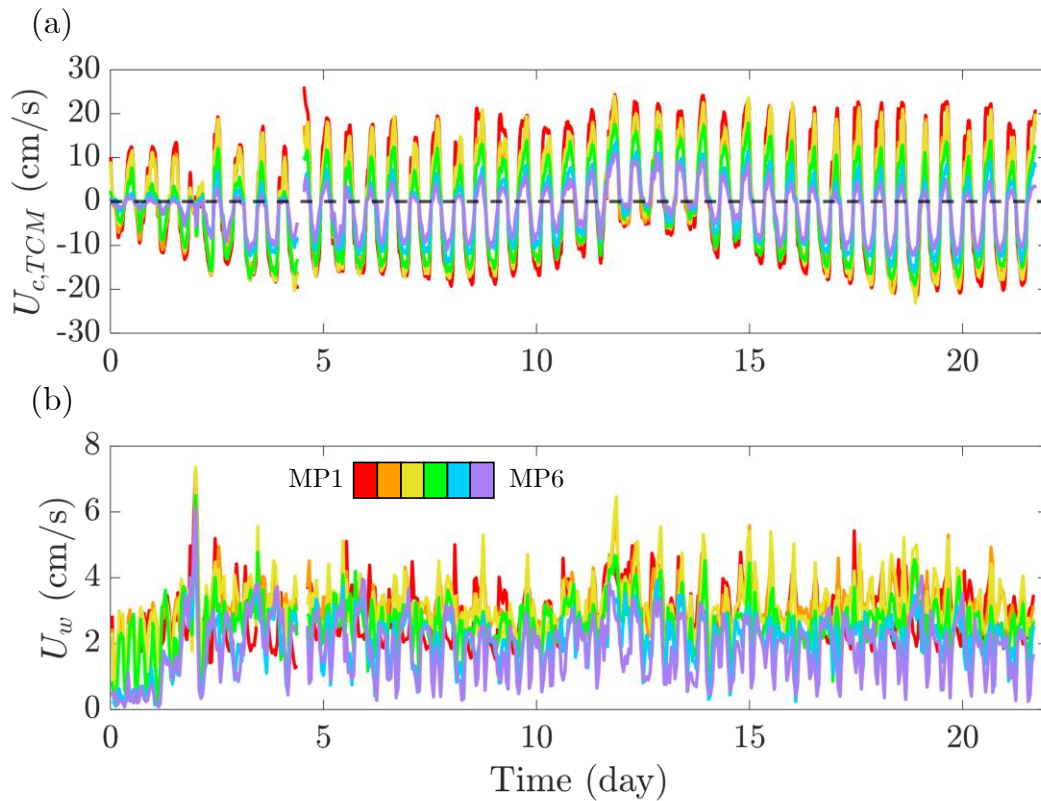


Figure 6.5: (a) Sixty-minute moving average velocities recorded by the tilt current meters $U_{c,TCM}$ over time. (b) Hourly-averaged wave velocities U_w over time. Colors denote stations.

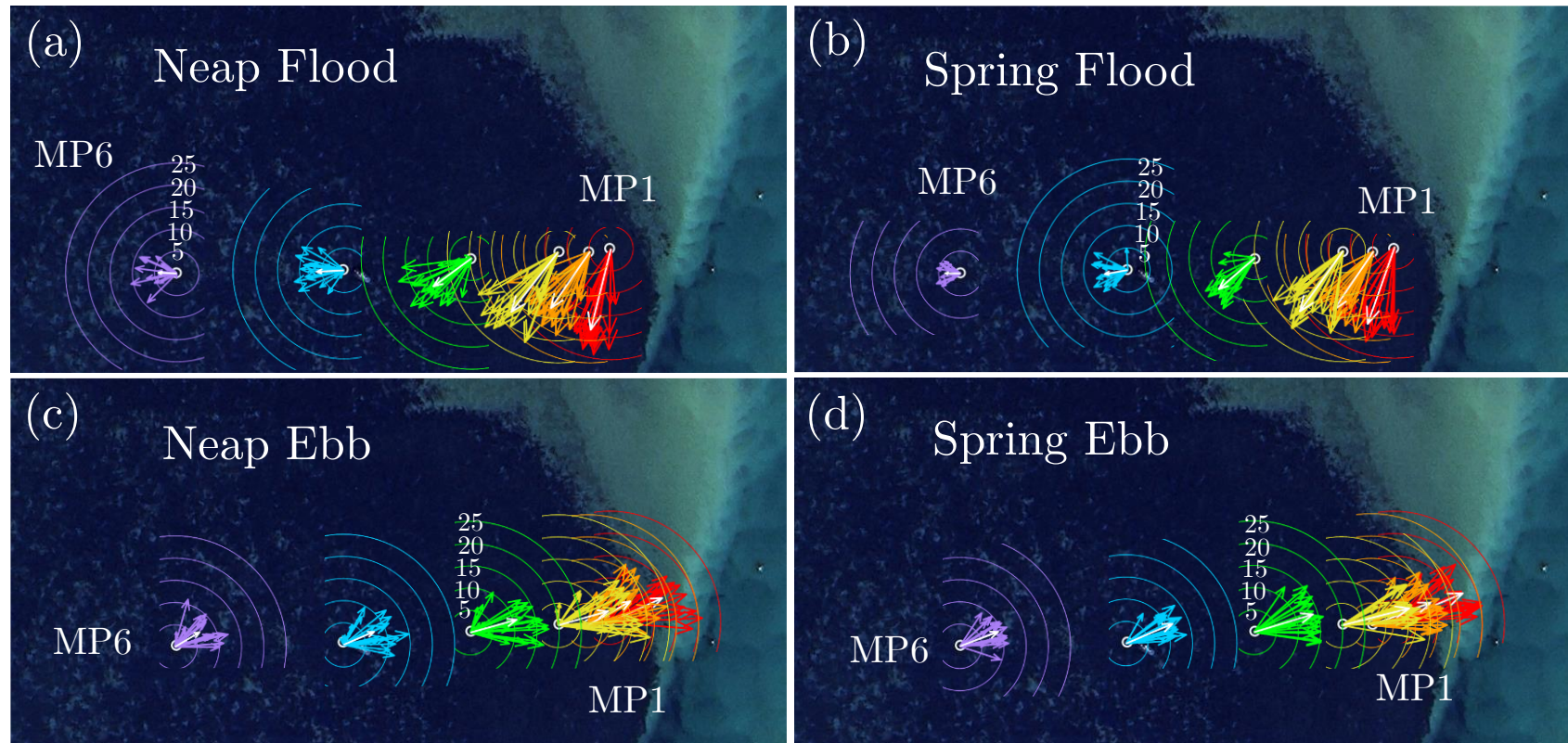


Figure 6.6: Polar compass plots of the magnitude and direction of the peak tidal velocity from (a) neap flood tides and (b) spring flood tides as well as (c) neap ebb tides and (d) spring ebb tides, overlaid on a map of the measurement transect. White circles denote measurement station locations. The inlet channel is to the right side of the image. The length of each arrow represents the magnitude, with radial axes labels given in cm/s, and the direction of the arrowhead denotes the direction of flow. The white arrow within each plot represents the average flow magnitude and direction among the respective peaks. For visual clarity, measurement stations were distinguished by color in rainbow order (red for MP1, orange for MP2, yellow for MP3, green for MP4, blue for MP5, purple for MP6). October, 2022 background image copyright Airbus, 2024.

Peak in-canopy velocities $\overline{U_{1,peak}}$, were 40-60% of TCM velocities and decreased with distance from the channel, with peak velocities about 80% lower at MP6 compared to MP1 (Figure 6.7a). The average organic carbon content in the cores increased with increasing $\overline{U_{1,peak}}$ (Figure 6.7b). The average sediment trap mass also increased with increasing $\overline{U_{1,peak}}$, although MP3 ($x = 20$ m, light blue symbol) had a slightly higher $\overline{U_{1,peak}}$ or lower sediment trap mass than the trend would suggest (Figure 6.7c). Finally, $\overline{U_{1,peak}}$ did not appear to be correlated with CAR (Figure 6.7d).

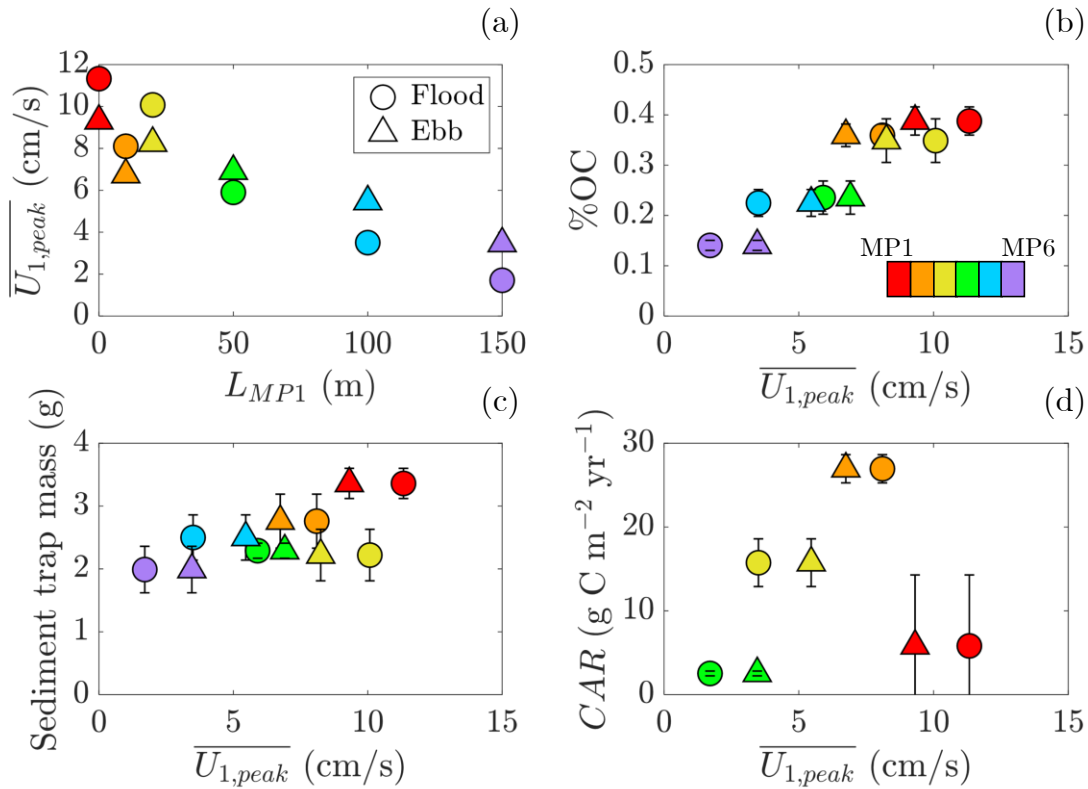


Figure 6.7: (a) Average peak in-canopy velocity $\overline{U_{1,peak}}$ versus distance from station MP1 L_{MP1} . (b) Average sediment core carbon content %OC, (c) average sediment trap mass, and (d) average carbon accumulation rate CAR versus $\overline{U_{1,peak}}$. Error bars represent standard errors. Colors distinguish stations for visual clarity.

6.4. Discussion

6.4.1 Drivers of spatial gradients in sediment carbon

Next, we consider the possible environmental factors contributing to the observed spatial variability in sediment carbon content and accretion rates, focusing on hydrodynamic intensity and sediment supply. In a current-dominated meadow, currents can reduce sediment organic carbon content by selectively resuspending organic material, such that organic carbon content decreases with increasing current velocity (Dahl et al., 2018). Consistent with this, Oreska et al. (2017) observed that sediment carbon content increased with distance from the edge of a *Z. marina* L. meadow, which they attributed to current velocity decreasing from the meadow edge. The opposite trend was observed in Menemsha Pond. Organic carbon content within the cores was higher at sites with higher near-bed peak tidal velocity (Figure 6.7b), and the carbon content decreased with distance from the meadow edge (Figure 6.2b). This suggested that resuspension and removal of organic carbon was not an important driver at this site. That is, the local hydrodynamic exposure at each site was not the main driver determining the %OC at that site. It is likely that the positive correlation between peak velocity and %OC is an artifact of the correlation between velocity and distance from the channel (Figure 6.7a), and that the distance from the channel is the explanatory variable.

The situation in Menemsha Pond suggests that the carbon stock distribution was controlled by supply. Specifically, the supply of carbon and fine sediments was progressively diminished with distance from the channel and into the meadow, such that carbon accretion declined with distance into the meadow (Figure 6.4b). The one exception is site MP1, which had a distinctly smaller mass accretion rate, which then resulted in a low carbon accretion rate

(Figure 6.4). The lower accretion rates at MP1 were likely due to higher velocity at this station promoting resuspension and inhibiting sediment accumulation.

Non-seagrass organic carbon entering the pond likely originates from wetlands located along the inlet channel (some of which are noted in Figure 6.1). During flood tide, the inflow stays largely within the channel, carrying most of the new carbon toward the deep basin at the southern end of the pond. The inflow jet spreads laterally (Figure 6.8a), producing high velocity at stations MP1 to MP3, but velocity at stations MP4 to MP6 remains small (Figure 6.6). As the flood phase begins, new water carrying a new supply of carbon reaches stations MP1 to MP3 first, with significantly less transport reaching stations MP4 to MP6. Later during the ebb phase, which follows a slack water period that allows sediment to slow down and settle to the bed, flow throughout Menemsha Pond moves toward the point where the inlet channel enters the pond inlet (known as a point sink flow, Figures 6.7 and 6.8b). Water parcels traveling across the transect during the ebb phase likely circulated around the pond through the deep inner basin after entering the lagoon during a previous flood tidal phase, and as a result will likely be carrying low concentrations of carbon.

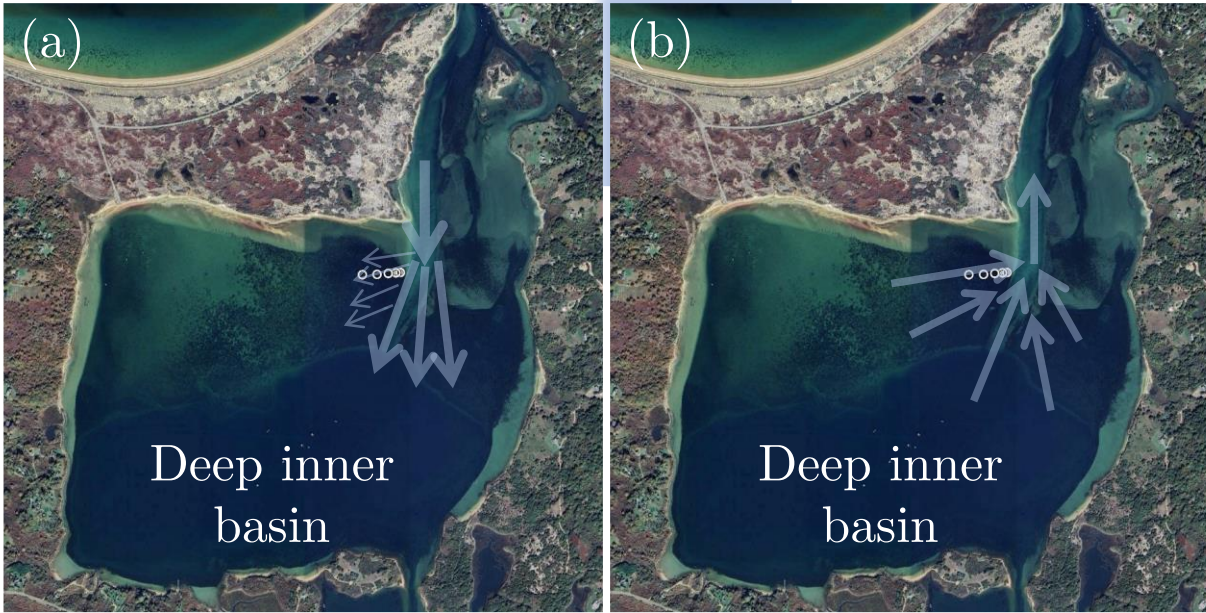


Figure 6.8: Sketches of flow circulation patterns near the inlet to Menemsha Pond during (a) flood tides and (b) ebb tides. Map images copyright 2024 Airbus.

To examine the potential for sediment supply limitation, we compared the time-scale for a sediment particle to travel across the transect (T_a) during flood tide (when new sediment is delivered to the pond) to the time-scale for it to settle to the bed (T_s). First, we isolated the component of flood tide velocity perpendicular to the channel $U_{\perp channel}$, i.e., entering the meadow (aligned with the direction of flood tidal velocities at MP5 and MP6, Figure 6.9). The measured velocity components showed more spatial variation during spring tides than during neap tides (compare Figure 6.9b and 6.9c), likely due to changes in frictional influences on the shoal near the inlet (Figure 6.1) on tidal flow associated with the changing tidal range. Note that $U_{\perp channel}$ at MP1 shifted from positive (in the direction of MP6) to negative (in the opposite direction) during the flood phase, likely due to its proximity to the channel. We will therefore excluded MP1 from the time-scale analysis.

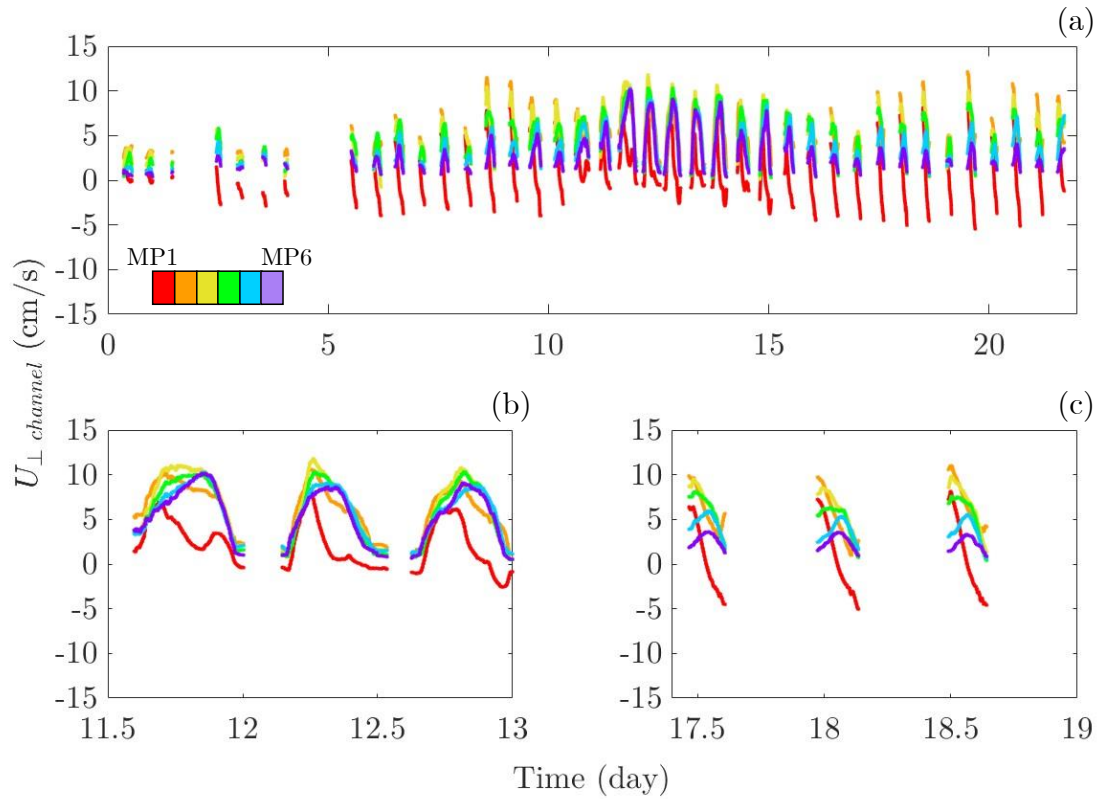


Figure 6.9: (a) 60-minute moving average of velocity component perpendicular to inlet channel during the flood phase, $U_{\perp channel}$, uncorrected for meadow presence. (b) Example segment of neap tidal cycles. (c) Example segment of spring tidal cycles. Colors distinguish stations.

To estimate the time scales for sediment advection across the transect, we first calculated the average velocity component $\overline{U_{\perp channel}}$ for each station during spring and neap tides (Figure 6.10a). Piecewise linear fits were used to describe $\overline{U_{\perp channel}}$ in between individual stations. The time scale for a sediment particle to travel from the edge of the meadow (MP1) to a particular station, T_a , was calculated using the piecewise fit of $\overline{U_{\perp channel}}$ and the distances between stations. To estimate the time scale of settling, we considered clay particles, which have greater sorptive capacity than coarser sand particles due in large part to their higher specific surface area (e.g., Keil & Hedges, 1993). When clay particles and organic matter particles collide with each

other in saline conditions, they form porous flocs (Abolfazli & Strom, 2023; Sutherland et al., 2015). Based on the compilation of floc settling velocities in Droppo (2004), a typical floc settling velocity in an estuarine environment, such as at Menemsha Pond, would be roughly 0.6 mm/s. We used this settling velocity combined with the mean water depth over meadow to estimate the settling time-scale T_s . Considering both neap and spring cycles, the ratio T_s/T_a decreased below a value of one at station MP3, indicating that an organic matter floc could settle before arriving at MP3, which suggests that stations MP3 through MP6 experienced a reduced supply of suspended material supply carbon to the bed (Figure 6.10b). In other words, with increasing distance from the channel, the sediment supply and therefore the sediment organic carbon that can be accumulated diminishes as sediment settles out.

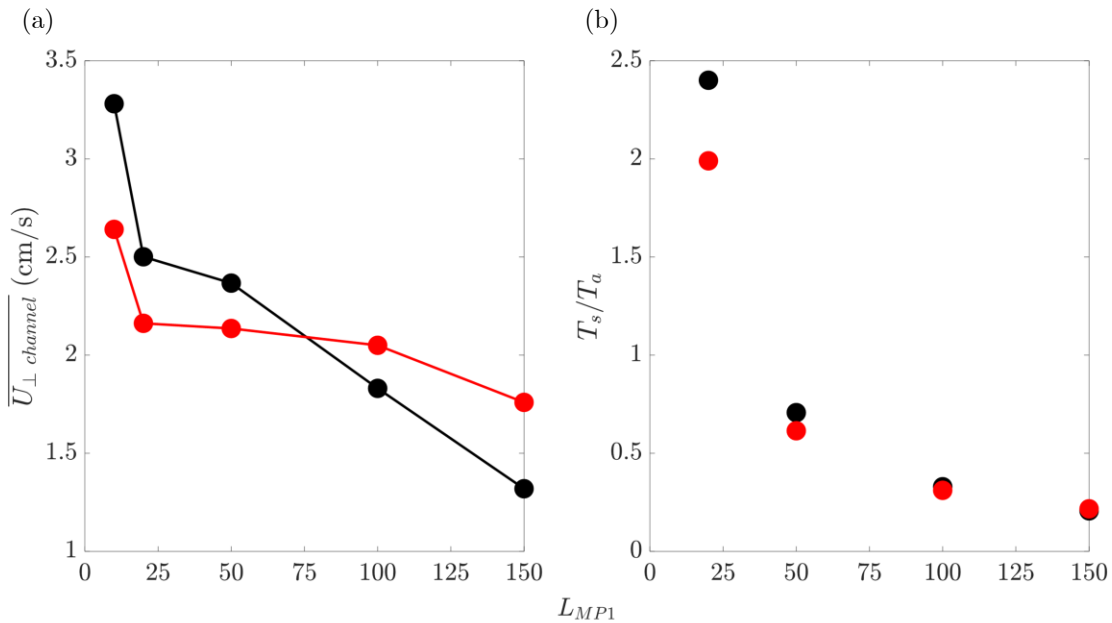


Figure 6.10: (a) Average component of flood tidal velocities (60-minute moving averages) perpendicular to the channel $\overline{U}_{\perp channel}$ versus distance from the edge of the meadow L_{MP1} , with piecewise linear fits. (b) Ratios of advection time scales T_a (how long it would take a particle to travel from the edge of the meadow to each station, based on the piecewise fits in (a)) to settling

time scales T_s (how long it would take a particle to fall through the mean water depth at each station). Note that mean water depths increased between MP1 and MP6 (Table 6.1) . The red symbols and curves denote spring tides and the black symbols and curves denote neap tides.

A diminishing supply of new sediment with increasing distance from the inlet channel can also explain why sediment farther from the channel edge was less depleted in ^{13}C (Figure 6.2a). Sediment organic carbon at the stations closer to the channel likely had higher proportions of non-seagrass sources, which is transported into the meadow predominantly during flood, while seagrass biomass likely contributed more to the sediment organic carbon closer to MP6 due to the lower availability and retention of other carbon sources. Meanwhile, the lower fines percentage toward the MP6 end of the transect could partly explain the contrast between Figures 6.2a and 6.3, in that the average sediment core organic carbon content at MP6 was lower than at MP5, but the near-surface organic matter content was similar across the gap between MP5 and MP6. Organic matter deposited near MP6, as measured in the surface samples, may have a lower probability of burial due to the lower available long-term protection provided by fine sediments (e.g., Hemingway et al., 2019).

An inverse relationship between sediment organic carbon content and the proximity to the dominant source of carbon was also observed in a tidal estuary in Ricart et al. (2020). Ricart et al. (2020) measured sediment organic carbon content in multiple seagrass meadows from the upper reaches of a tidal estuary to the mouth, and they found that sediment organic carbon content increased with distance from the mouth of the estuary. The authors proposed that the observed spatial gradient in organic carbon content was related to proximity to the dominant sources of fine sediment and carbon in the upper estuary. Similarly, in Menemsha Pond the inlet

channel is likely the dominant source of organic carbon, so that sediment organic carbon was higher closer to the channel and lower toward the interior of the pond, even though the area closer to the inlet channel experienced greater hydrodynamic intensity.

6.5 Conclusions

A field study of a *Z. marina* L. meadow within a tidal lagoon demonstrated a strong spatial dependence of sediment organic carbon content and carbon accumulation rates (*CAR*) on proximity to the lagoon's inlet channel that could not be explained by the observed gradient in hydrodynamic intensity. Specifically, the tidal velocity decreased with increasing distance from the inlet channel, which was expected to promote increasing carbon content and *CAR* with increasing distance from the channel due to decreasing resuspension. However, the opposite trend was observed. Carbon content and *CAR* decreased with distance from the channel edge, which was attributed to limitation in suspended sediment supply. This was supported by a comparison of advection and settling time scales that suggested that the concentration of carbon particles in the water column decreased with distance from the channel. The station (MP1) closest to the channel was an exception to this trend. Despite the high sediment carbon content near the inlet channel, the sediment accumulation rate was lowest at this station, resulting in low *CAR*. This was likely due to exposure to the highest velocity causing the highest rates of resuspension at this station. This field study demonstrated that hydrodynamic controls on the supply of carbon can generate spatial variation in sediment organic carbon over a length scales as small as 150 m, which illustrates that an assessment of meadow-scale carbon storage using a single point measurement could lead to considerable error.

6.6 Acknowledgments

This study was supported by Shell International Exploration and Production through the MIT Energy Initiative. R. Schaefer was supported by the National Science Foundation Graduate Research Fellowship under Grant No. 2141064 and the Massachusetts Institute of Technology Department of Civil and Environmental Engineering. Andrew Jacobs and Isaiah Schaeffer provided boats and boat operation support. Dr. Gary Lei and Alley McConnell assisted with the field work. We thank the U.S. Environmental Protection Agency divers Eric Nelson and Danielle Gaito for their assistance.

6.7 References

- Abolfazli, E., & Strom, K. (2023). Salinity impacts on floc size and growth rate with and without natural organic matter. *Journal of Geophysical Research: Oceans*, *128*(7), 1–16. <https://doi.org/10.1029/2022JC019255>
- Anderson, S. M., & Charters, A. C. (1982). A fluid dynamics study of seawater flow through *Gelidium nudifrons*. *Limnology and Oceanography*, *27*(3), 399–412. <https://doi.org/10.4319/lo.1982.27.3.0399>
- Arias-Ortiz, A., Masqué, P., Garcia-Orellana, J., Serrano, O., Mazarrasa, I., Marbá, N., Lovelock, C. E., Lavery, P. S., & Duarte, C. M. (2018). Reviews and syntheses: 210Pb-derived sediment and carbon accumulation rates in vegetated coastal ecosystems - Setting the record straight. *Biogeosciences*, *15*(22), 6791–6818. <https://doi.org/10.5194/bg-15-6791-2018>
- Blomqvist, S., & Kofoed, C. (1981). Sediment trapping—A subaquatic in situ experiment. *Limnology and Oceanography*, *26*(3), 585–590. <https://doi.org/10.4319/lo.1981.26.3.0585>
- Bos, A. R., Bouma, T. J., de Kort, G. L. J., & van Katwijk, M. M. (2007). Ecosystem engineering by annual intertidal seagrass beds: Sediment accretion and modification. *Estuarine, Coastal and Shelf Science*, *74*(1–2), 344–348. <https://doi.org/10.1016/j.ecss.2007.04.006>
- Bouillon, S., & Boschker, H. T. S. (2006). Bacterial carbon sources in coastal sediments: a review based on stable isotope data of biomarkers. *Biogeosciences*, *3*, 175–185.

- Brodie, C. R., Leng, M. J., Casford, J. S. L., Kendrick, C. P., Lloyd, J. M., Yongqiang, Z., & Bird, M. I. (2011). Evidence for bias in C and N concentrations and $\delta^{13}\text{C}$ composition of terrestrial and aquatic organic materials due to pre-analysis acid preparation methods. *Chemical Geology*, 282(3–4), 67–83. <https://doi.org/10.1016/j.chemgeo.2011.01.007>
- Brunet, Y., Finnigan, J. J., & Raupach, M. R. (1994). A wind tunnel study of air flow in waving wheat: Single-point velocity statistics. *Boundary-Layer Meteorology*, 70(1–2), 95–132. <https://doi.org/10.1007/BF00712525>
- Costanza, R., de Groot, R., Sutton, P., van der Ploeg, S., Anderson, S. J., Kubiszewski, I., Farber, S., & Turner, R. K. (2014). Changes in the global value of ecosystem services. *Global Environmental Change*, 26(1), 152–158. <https://doi.org/10.1016/j.gloenvcha.2014.04.002>
- Cutshall, N. H., Larsen, I. L., & Olsen, C. R. (1983). Direct analysis of ^{210}Pb in sediment samples: Self-absorption corrections. *Nuclear Instruments and Methods In Physics Research*, 206, 309–312. [https://doi.org/10.1016/0167-5087\(83\)91273-5](https://doi.org/10.1016/0167-5087(83)91273-5)
- Dahl, M., Infantes, E., Clevesjö, R., Linderholm, H. W., Björk, M., & Gullström, M. (2018). Increased current flow enhances the risk of organic carbon loss from *Zostera marina* sediments: Insights from a flume experiment. *Limnology and Oceanography*, 63(6), 2793–2805. <https://doi.org/10.1002/lno.11009>
- Dalrymple, R. A., Kirby, J. T., & Hwang, P. A. (1984). Wave diffraction due to areas of energy dissipation. *Journal of Waterway, Port, Coastal, and Ocean Engineering*, 110(1), 67–79. [https://doi.org/10.1061/\(ASCE\)0733-950X\(1984\)110:1\(67\)](https://doi.org/10.1061/(ASCE)0733-950X(1984)110:1(67))
- Dean, Jr., W. E. (1974). Determination of carbonate and organic matter in calcareous sediments and sedimentary rocks by loss on ignition: comparison with other methods. *Journal of Sedimentary Petrology*, 44(I), 242–248.
- Droppo, I. G. (2004). Structural controls on flocculation strength and transport. *Canadian Journal of Civil Engineering*, 31(4), 569–578. <https://doi.org/10.1139/L04-015>
- Eakins, J. D., & Morrison, R. T. (1978). A new procedure for the determination of lead-210 in lake and marine sediments. *The International Journal Of Applied Radiation And Isotopes*, 29(9–10), 531–536. [https://doi.org/10.1016/0020-708X\(78\)90161-8](https://doi.org/10.1016/0020-708X(78)90161-8)
- Fonseca, M. S., & Cahalan, J. A. (1992). A preliminary evaluation of wave attenuation by four species of seagrass. *Estuarine, Coastal and Shelf Science*, 35(6), 565–576. [https://doi.org/10.1016/S0272-7714\(05\)80039-3](https://doi.org/10.1016/S0272-7714(05)80039-3)
- Fonseca, M. S., Fisher, J. S., Zieman, J. C., & Thayer, G. W. (1982). Influence of the seagrass, *Zostera marina* L., on current flow. *Estuarine, Coastal and Shelf Science*, 15(4), 351–364. [https://doi.org/10.1016/0272-7714\(82\)90046-4](https://doi.org/10.1016/0272-7714(82)90046-4)
- Fourqurean, J. W., Duarte, C. M., Kennedy, H., Marbà, N., Holmer, M., Mateo, M. A., Apostolaki, E. T., Kendrick, G. A., Krause-Jensen, D., & Serrano, O. (2012). Seagrass

- ecosystems as a globally significant carbon stock. *Nature Geoscience*, 5, 505–509. <https://doi.org/10.1038/ngeo1477>
- Froelich, P. N. (1980). Analysis of organic carbon in marine sediments. *Limnology and Oceanography*, 25(3), 564–572. <https://doi.org/10.4319/lo.1980.25.3.0564>
- Gosselin, F. P. (2019). Mechanics of a plant in fluid flow. *Journal of Experimental Botany*, 70(14), 3533–3548. <https://doi.org/10.1093/jxb/erz288>
- Greiner, J. T., McGlathery, K. J., Gunnell, J., & McKee, B. A. (2013). Seagrass restoration enhances “blue carbon” sequestration in coastal waters. *PLoS ONE*, 8(8), 1–8. <https://doi.org/10.1371/journal.pone.0072469>
- Hemingway, J. D., Rothman, D. H., Grant, K. E., Rosengard, S. Z., Eglinton, T. I., Derry, L. A., & Galy, V. V. (2019). Mineral protection regulates long-term global preservation of natural organic carbon. *Nature*, 570(7760), 228–231. <https://doi.org/10.1038/s41586-019-1280-6>
- Infantes, E., Orfila, A., Simarro, G., Terrados, J., Luhar, M., & Nepf, H. (2012). Effect of a seagrass (*Posidonia oceanica*) meadow on wave propagation. *Marine Ecology Progress Series*, 456, 63–72. <https://doi.org/10.3354/meps09754>
- Irandi, E. A., & Peterson, C. H. (1991). Modification of animal habitat by large plants: mechanisms by which seagrasses influence clam growth. *Oecologia*, 87(3), 307–318. <https://doi.org/10.1007/BF00634584>
- Jones, C. G., Lawton, J. H., Shachak, M., & Organisms, M. (1994). Organisms as ecosystem engineers. *Oikos*, 69(3), 373–386. <https://doi.org/10.2307/3545850>
- Keil, R. G., & Hedges, J. I. (1993). Sorption of organic matter to mineral surfaces and the preservation of organic matter in coastal marine sediments. *Chemical Geology*, 107(3–4), 385–388. [https://doi.org/10.1016/0009-2541\(93\)90215-5](https://doi.org/10.1016/0009-2541(93)90215-5)
- Kim, M.-S., Lee, S.-M., Kim, H.-J., Lee, S.-Y., Yoon, S.-H., & Shin, K.-H. (2014). Carbon stable isotope ratios of new leaves of *Zostera marina* in the mid-latitude region: Implications of seasonal variation in productivity. *Journal of Experimental Marine Biology and Ecology*, 461, 286–296. <https://doi.org/10.1016/j.jembe.2014.08.015>
- Lafratta, A., Serrano, O., Masqué, P., Mateo, M. A., Fernandes, M., Gaylard, S., & Lavery, P. S. (2020). Challenges to select suitable habitats and demonstrate ‘additionality’ in Blue Carbon projects: A seagrass case study. *Ocean and Coastal Management*, 197. <https://doi.org/10.1016/j.ocecoaman.2020.105295>
- Lavery, P. S., Mateo, M. Á., Serrano, O., & Rozaimi, M. (2013). Variability in the carbon storage of seagrass habitats and its implications for global estimates of blue carbon ecosystem service. *PLoS ONE*, 8(9). <https://doi.org/10.1371/journal.pone.0073748>

- Lei, J., & Nepf, H. M. (2019). Wave damping by flexible vegetation: Connecting individual blade dynamics to the meadow scale. *Coastal Engineering*, *147*(October 2018), 138–148. <https://doi.org/10.1016/j.coastaleng.2019.01.008>
- Lei, J., Schaefer, R., Colarusso, P., Novak, A., Simpson, J. C., Masqué, P., & Nepf, H. (2023). Spatial heterogeneity in sediment and carbon accretion rates within a seagrass meadow correlated with the hydrodynamic intensity. *Science of the Total Environment*, *854*(April 2022). <https://doi.org/10.1016/j.scitotenv.2022.158685>
- Martz, D. E., & Langner, Jr, G. H. (1991). Half-lives of ²¹⁴Pb and ²¹⁴B1. *Health Physics*, *61*(4), 511–518. <https://doi.org/10.1097/00004032-199110000-00006>
- Mateo, M. A., Romero, J., Pérez, M., Littler, M. M., & Littler, D. S. (1997). Dynamics of millenary organic deposits resulting from the growth of the Mediterranean seagrass *Posidonia oceanica*. *Estuarine, Coastal and Shelf Science*, *44*(1), 103–110. <https://doi.org/10.1006/ecss.1996.0116>
- Mathieu, G. G., Biscaye, P. E., & Lupton, R. A. (1988). System for measurement of ²²²Rn at low levels in natural waters. *Health Physics*, *55*(6), 989–992. <https://doi.org/10.1097/00004032-198812000-00015>
- Mazarrasa, I., Lavery, P., Duarte, C. M., Lafratta, A., Lovelock, C. E., Macreadie, P. I., Samper-Villarreal, J., Salinas, C., Sanders, C. J., Trevathan-Tackett, S., Young, M., Steven, A., & Serrano, O. (2021). Factors determining seagrass blue carbon across bioregions and geomorphologies. *Global Biogeochemical Cycles*, *35*(6), 1–17. <https://doi.org/10.1029/2021GB006935>
- Miyajima, T., Koike, I., Yamano, H., & Iizumi, H. (1998). Accumulation and transport of seagrass-derived organic matter in reef flat sediment of Green Island, Great Barrier Reef. *Marine Ecology Progress Series*, *175*, 251–259. <https://doi.org/10.3354/meps175251>
- Nellemann, C., Corcoran, E., Duarte, C. M., Valdes, L., De Young, C., Fonseca, L., & Grimsditch, G. (Eds.). (2009). *Blue Carbon: A Rapid Response Assessment*. GRID-Arendal.
- Nittrouer, C. A., DeMaster, D. J., McKee, B. A., Cutshall, N. H., & Larsen, I. L. (1984). The effect of sediment mixing on Pb-210 accumulation rates for the Washington continental shelf. *Marine Geology*, *54*(3–4), 201–221. [https://doi.org/10.1016/0025-3227\(84\)90038-0](https://doi.org/10.1016/0025-3227(84)90038-0)
- Novak, A. B., Pelletier, M. C., Colarusso, P., Simpson, J., Gutierrez, M. N., Arias-Ortiz, A., Charpentier, M., Masque, P., & Vella, P. (2020). Factors influencing carbon stocks and accumulation rates in eelgrass meadows across New England, USA. *Estuaries and Coasts*, *43*(8), 2183–2184. <https://doi.org/10.1007/s12237-020-00815-z>
- Oreska, M. P. J., McGlathery, K. J., & Porter, J. H. (2017). Seagrass blue carbon spatial patterns at the meadow-scale. *PLoS ONE*, *12*(4), 1–18. <https://doi.org/10.1371/journal.pone.0176630>
- Orth, R. J., Carruthers, T. J. B., Dennison, W. C., Duarte, C. M., Fourqurean, J. W., Heck, K. L., Hughes, A. R., Kendrick, G. A., Kenworthy, W. J., Olyarnik, S., Short, F. T., Waycott, M.,

- & Williams, S. L. (2006). A global crisis for seagrass ecosystems. *BioScience*, 56(12), 987–996. [https://doi.org/10.1641/0006-3568\(2006\)56\[987:agcfse\]2.0.co;2](https://doi.org/10.1641/0006-3568(2006)56[987:agcfse]2.0.co;2)
- Orth, R. J., Harwell, M. C., & Fishman, J. R. (1999). A rapid and simple method for transplanting eelgrass using single, unanchored shoots. *Aquatic Botany*, 64(1), 77–85. [https://doi.org/10.1016/S0304-3770\(99\)00007-8](https://doi.org/10.1016/S0304-3770(99)00007-8)
- Orth, R. J., Luckenbach, M., & Moore, K. A. (1994). Seed dispersal in a marine macrophyte: implications for colonization and restoration. *Ecology*, 75(7), 1927–1939. <https://doi.org/10.2307/1941597>
- Pennington, W., Cambray, R. S., & Fisher, E. M. (1973). Observations on lake sediments using fallout ¹³⁷Cs as a tracer. *Nature*, 242(5396), 324–326. <https://doi.org/10.1038/242324a0>
- Pollard, D. A. (1984). A review of ecological studies on seagrass-fish communities, with particular reference to recent studies in Australia. *Aquatic Botany*, 18(1–2), 3–42. [https://doi.org/10.1016/0304-3770\(84\)90079-2](https://doi.org/10.1016/0304-3770(84)90079-2)
- Raupach, M. R., Finnigan, J. J., & Brunet, Y. (1996). Coherent eddies and turbulence in vegetation canopies: the mixing-layer analogy. *Boundary-Layer Meteorology*, 78(3–4), 351–382. <https://doi.org/10.1007/BF00120941>
- Reide Corbett, D., & Walsh, J. P. (2015). ²¹⁰Pb and ¹³⁷Cs: Establishing a chronology for the last century. *Handbook of Sea-Level Research*, 361–372. <https://doi.org/10.1002/9781118452547.ch24>
- Ricart, A. M., York, P. H., Bryant, C. V., Rasheed, M. A., Ierodiaconou, D., & Macreadie, P. I. (2020). High variability of Blue Carbon storage in seagrass meadows at the estuary scale. *Scientific Reports*, 10(1), 1–12. <https://doi.org/10.1038/s41598-020-62639-y>
- Ritchie, J. C., & McHenry, J. R. (1990). Application of radioactive fallout Cesium-137 for measuring soil erosion and sediment accumulation rates and patterns: A review. *Journal of Environmental Quality*, 19(2), 215–233. <https://doi.org/10.2134/jeq1990.00472425001900020006x>
- Salinas, C., Duarte, C. M., Lavery, P. S., Masque, P., Arias-Ortiz, A., Leon, J. X., Callaghan, D., Kendrick, G. A., & Serrano, O. (2020). Seagrass losses since mid-20th century fuelled CO₂ emissions from soil carbon stocks. *Global Change Biology*, 26(9), 4772–4784. <https://doi.org/10.1111/gcb.15204>
- Schaefer, R. B., & Nepf, H. M. (2022a). Flow Structure in an Artificial Seagrass Meadow in Combined Wave-Current Conditions. *Frontiers in Marine Science*, 9(February), 1–12. <https://doi.org/10.3389/fmars.2022.836901>
- Schaefer, R. B., & Nepf, H. M. (2022b). Wave damping by seagrass meadows in combined wave-current conditions. *Limnology and Oceanography*, 67(7), 1554–1565. <https://doi.org/10.1002/lno.12102>

- Schaefer, R., & Nepf, H. (2024). Movement of and drag force on slender flat plates in an array exposed to combinations of unidirectional and oscillatory flow. *Journal of Fluids and Structures*, 124(July 2023), 104044. <https://doi.org/10.1016/j.jfluidstructs.2023.104044>
- Sutherland, B. R., Barrett, K. J., & Gingras, M. K. (2015). Clay settling in fresh and salt water. *Environmental Fluid Mechanics*, 15(1), 147–160. <https://doi.org/10.1007/s10652-014-9365-0>
- Tan, Y. M., Dalby, O., Kendrick, G. A., Statton, J., Sinclair, E. A., Fraser, M. W., Macreadie, P. I., Gillies, C. L., Coleman, R. A., Waycott, M., van Dijk, K. J., Vergés, A., Ross, J. D., Campbell, M. L., Matheson, F. E., Jackson, E. L., Irving, A. D., Govers, L. L., Connolly, R. M., ... Sherman, C. D. H. (2020). Seagrass Restoration Is Possible: Insights and Lessons From Australia and New Zealand. *Frontiers in Marine Science*, 7(August). <https://doi.org/10.3389/fmars.2020.00617>
- Unsworth, R. K. F., McKenzie, L. J., Collier, C. J., Cullen-Unsworth, L. C., Duarte, C. M., Eklöf, J. S., Jarvis, J. C., Jones, B. L., & Nordlund, L. M. (2019). Global challenges for seagrass conservation. *Ambio*, 48(8), 801–815. <https://doi.org/10.1007/s13280-018-1115-y>
- van Katwijk, M. M., Thorhaug, A., Marbà, N., Orth, R. J., Duarte, C. M., Kendrick, G. A., Althuizen, I. H. J., Balestri, E., Bernard, G., Cambridge, M. L., Cunha, A., Durance, C., Giesen, W., Han, Q., Hosokawa, S., Kiswara, W., Komatsu, T., Lardicci, C., Lee, K. S., ... Verduin, J. J. (2016). Global analysis of seagrass restoration: The importance of large-scale planting. *Journal of Applied Ecology*, 53(2), 567–578. <https://doi.org/10.1111/1365-2664.12562>
- Ward, L. G., Kemp, W. M., & Boynton, W. R. (1984). The influence of waves and seagrass communities on suspended particulates in an estuarine embayment. *Marine Geology*, 59(1–4), 85–103. [https://doi.org/10.1016/0025-3227\(84\)90089-6](https://doi.org/10.1016/0025-3227(84)90089-6)
- Waycott, M., Duarte, C. M., Carruthers, T. J. B., Orth, R. J., Dennison, W. C., Olyarnik, S., Calladine, A., Fourqurean, J. W., Heck, K. L., Hughes, A. R., Kendrick, G. A., Kenworthy, W. J., Short, F. T., & Williams, S. L. (2009). Accelerating loss of seagrasses across the globe threatens coastal ecosystems. *Proceedings of the National Academy of Sciences of the United States of America*, 106(30), 12377–12381. <https://doi.org/10.1073/pnas.0905620106>
- Xu, S., Zhou, Y., Wang, P., Wang, F., Zhang, X., Yue, S., Zhang, Y., Qiao, Y., & Liu, M. (2021). Temporal-spatial variations in the elemental and stable isotope contents of eelgrass (*Zostera marina* L.) in the Bohai Sea and Yellow Sea, northern China: Sheath as a novel ecological indicator for geochemical research. *Ecological Indicators*, 121, 107181. <https://doi.org/10.1016/j.ecolind.2020.107181>

6.8 Supplementary Information

6.8.1 Sediment grain size distributions

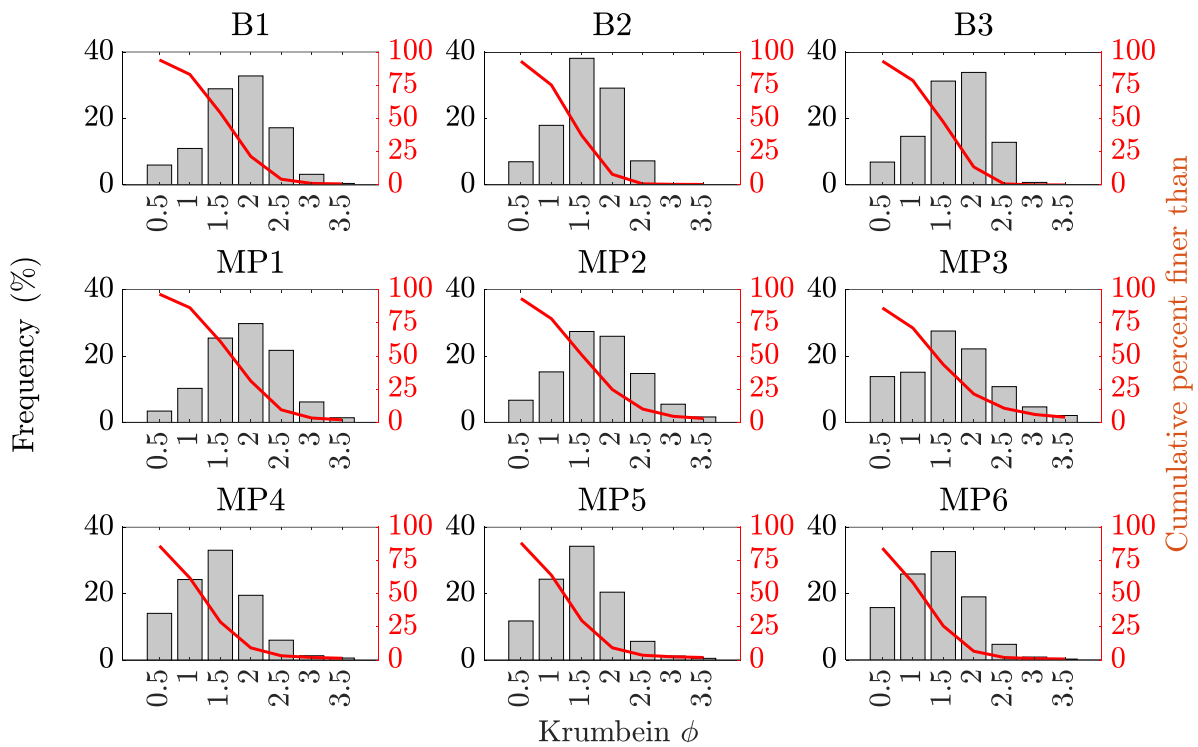


Figure 6.S.1: Near-surface sediment grain size distributions in the Krumbein ϕ scale for the six vegetated stations along the transect and the three sediment surface samples taken in the inlet channel near MP1. Curves denote the proportion of the sample that was finer than a given grain size category.

6.8.2 Carbon and nitrogen content and stable isotope ratio profiles

The asterisks in the subtitles of the MP4 profiles in Figure S2d, S3d, S4d, and S5d are reminders that there was a large quahog lodged in the MP4 core, making determination of cumulative mass difficult.

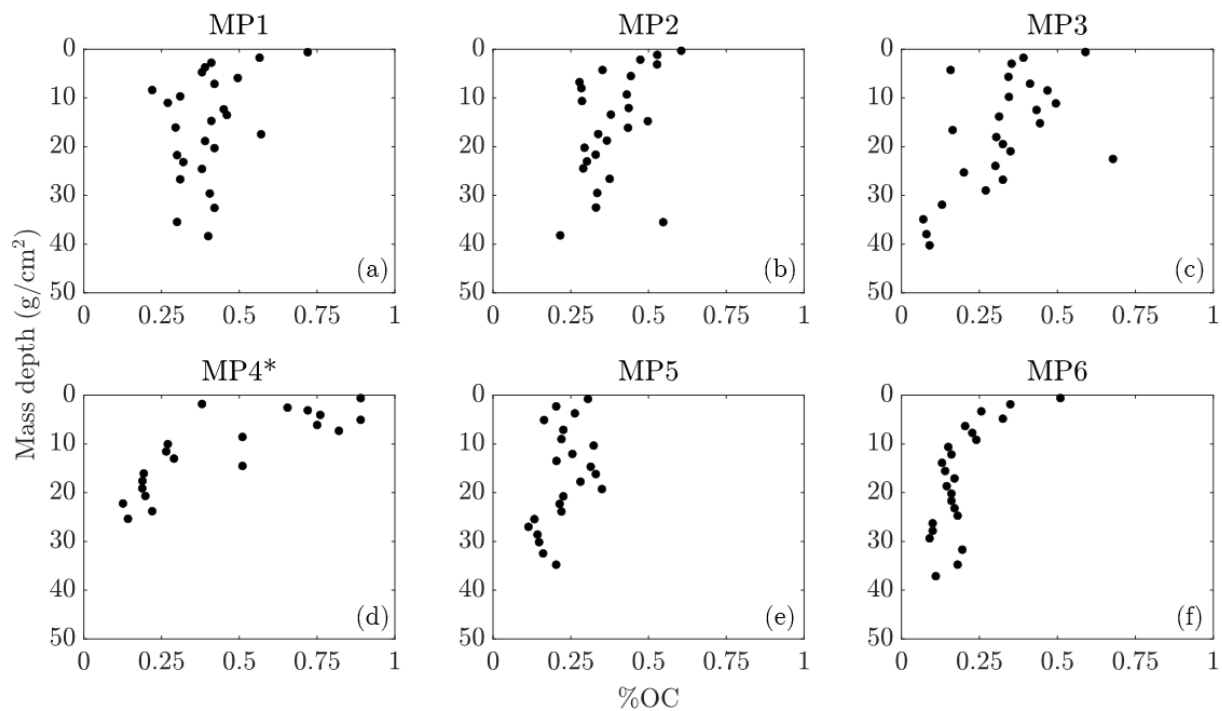


Figure 6.S.2: Profiles of sediment organic carbon content (%OC) versus cumulative mass depth for each sediment core.

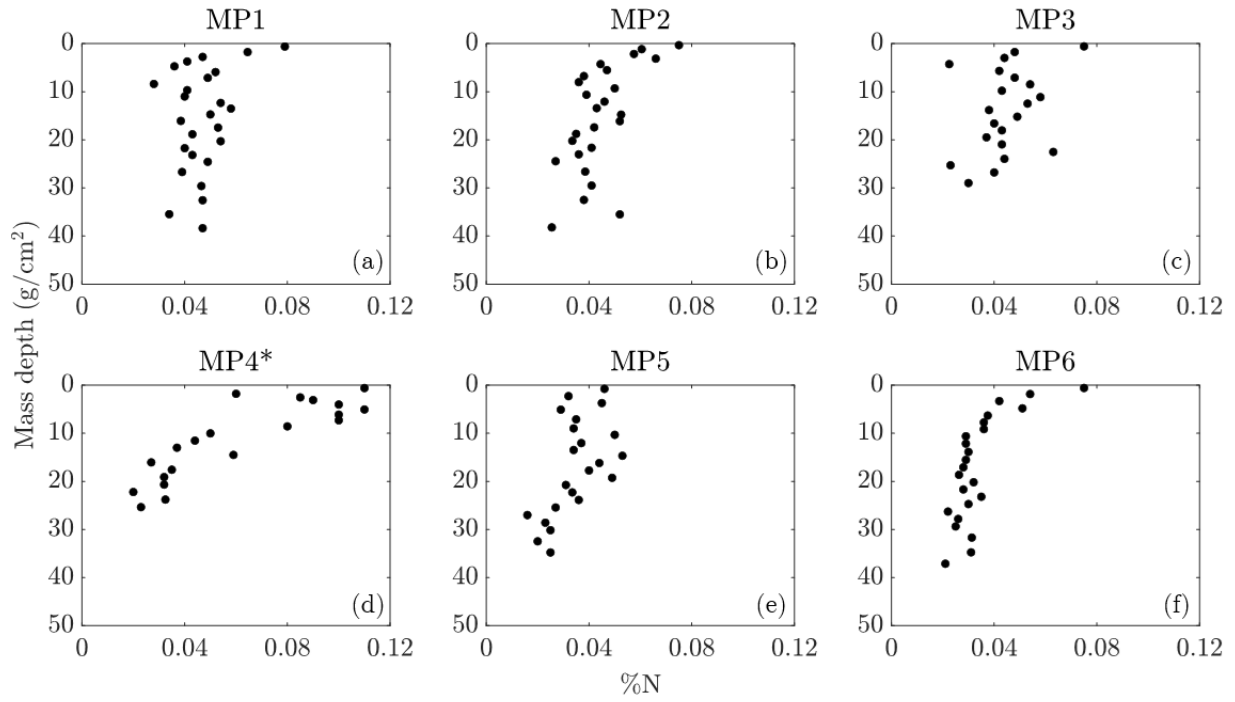


Figure 6.S.3: Profiles of sediment nitrogen content (%N) versus cumulative mass depth for each sediment core.

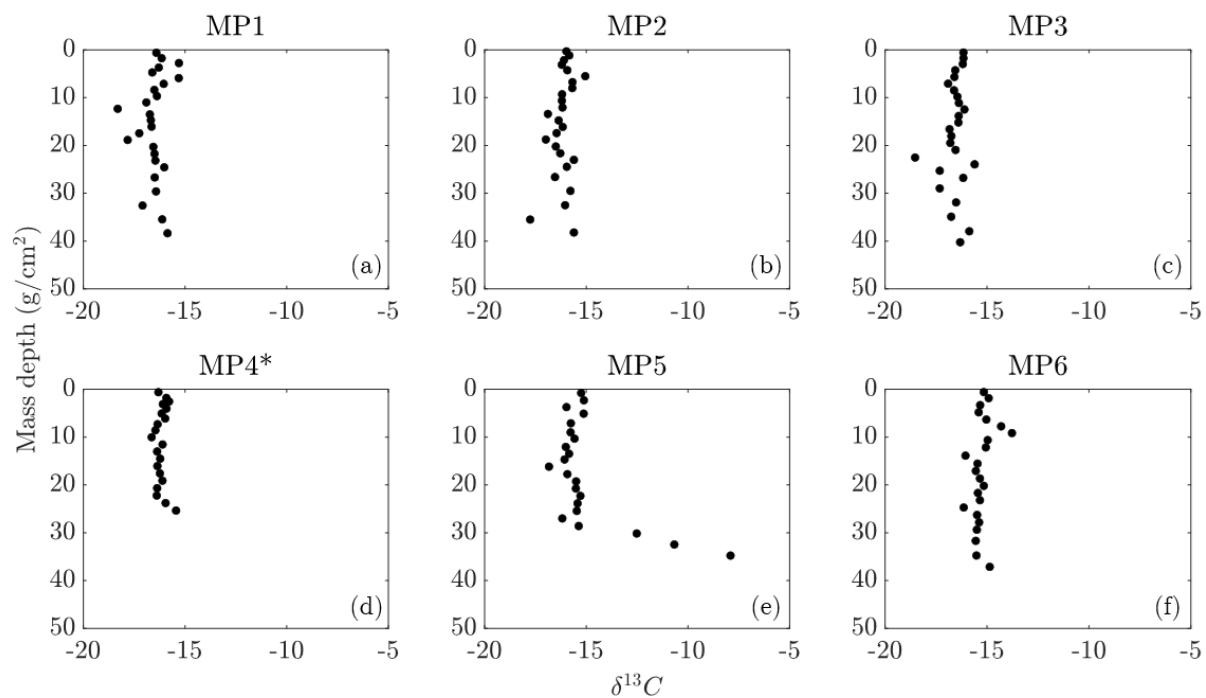


Figure 6.S.4: Profiles of carbon stable isotope ratio $\delta^{13}C$ (in parts per thousand relative to Vienna Pee Dee Belemnite) versus cumulative mass depth for each sediment core.

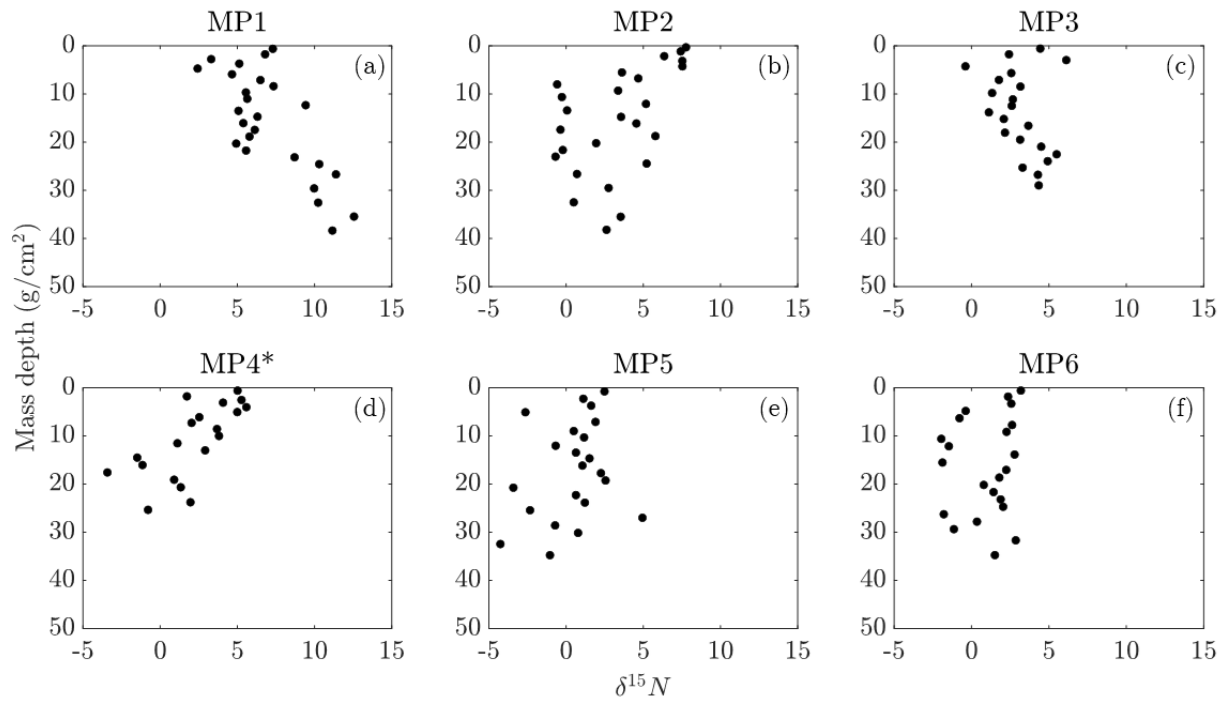


Figure 6.S.5: Profiles of nitrogen stable isotope ratio $\delta^{15}N$ (in parts per thousand relative to atmospheric air) versus cumulative mass depth for each sediment core.

6.8.3 ^{210}Pb sediment core profiles

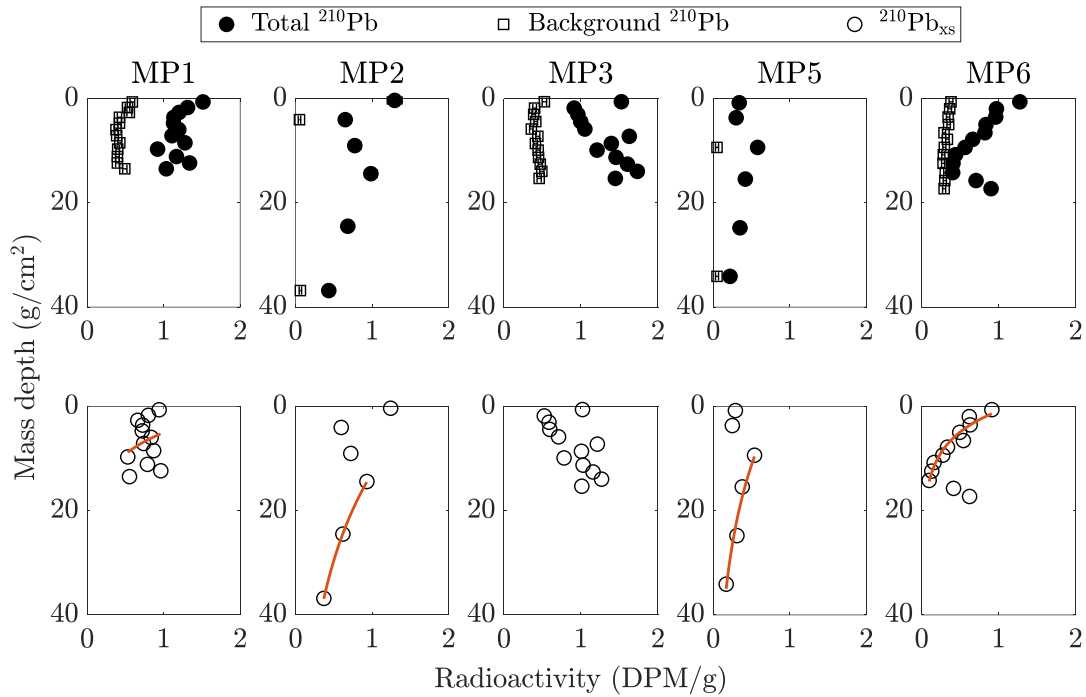


Figure 6.S.6: Profiles of total ^{210}Pb , background ^{210}Pb , and $^{210}\text{Pb}_{\text{xs}}$ versus cumulative mass for each sediment core except MP4. ^{210}Pb measurements were not carried out on the MP4 sediment core due to the fact that there was a large quahog lodged in the MP4 core. Red curves denote the linear regressions of $\ln(^{210}\text{Pb}_{\text{xs}})$ on cumulative mass.

Chapter 7

Stability of a patchy seagrass meadow and implications for carbon retention⁵

Abstract:

Seagrass meadows facilitate the capture and storage of sedimentary organic carbon, but substantial spatial variability in carbon has been observed among different meadows and within a single meadow. This study examined the spatial variation in carbon across a patchy meadow. Tidal velocities were reduced within patches and elevated in surrounding bare regions, which was expected to promote carbon accumulation within the patches. However, sedimentary organic carbon was not correlated with the present-day spatial distributions of seagrass or velocity. Historic aerial images showed that patches have continually shifted, with vegetation persistence

⁵ This chapter has been submitted for publication and is under review.

of less than a decade at every position within the meadow. The highest carbon stock occurred in the largest area of recent vegetation persistence. The long-term carbon accumulation rate was zero, likely due to sediment erosion. Overall, this study provides insight into the vulnerability of seagrass sedimentary organic carbon and a limitation on carbon storage and accretion in patchy meadows.

7.1. Introduction

Seagrasses are marine flowering plants that can form dense meadows along every continent except Antarctica (Unsworth et al., 2019). The ability of seagrass meadows to accumulate and retain sedimentary organic carbon has received growing interest for the potential of meadow restoration projects to compensate for anthropogenic carbon dioxide emissions (Fourqurean et al., 2012; Lafratta et al., 2020). However, significant variability in sediment organic carbon content has been observed both among different seagrass meadows (e.g., Lavery et al., 2013; Mazarrasa et al., 2021) and within the same meadow (e.g., Lei et al., 2023; Ricart et al., 2015), which complicates carbon budget accounting. A wide range of environmental factors influences the spatial differences in carbon content and accretion rates within and among seagrass meadows, including seagrass species (e.g., Serrano et al., 2016), hydrodynamic exposure (e.g., Lei et al., 2023; Samper-Villarreal et al., 2016), sediment grain size, which can be a function of hydrodynamic exposure (Serrano et al., 2016; Kennedy et al., 2022), climatic region (e.g., Mazarrasa et al., 2021), proximity to carbon sources (e.g., Asplund et al., 2021),

biogeochemistry (e.g., Lavery et al., 2013), and landscape configuration, i.e., patchy versus continuous meadows (e.g., Asplund et al., 2021; Ricart et al., 2015, 2017).

When an array of individual shoots forms a meadow (also known as a canopy), meadow-scale drag significantly reduces the current velocity experienced by individual shoots in the meadow (Chen et al., 2013; Raupach et al., 1996), and also reduces wave energy propagating across the meadow (e.g., Infantes et al., 2012; Kobayashi et al., 1993). In this way, seagrasses engineer the local ecosystem to promote their survival (e.g., Jones et al., 1994). Further, by reducing currents and waves, a meadow creates conditions that favor deposition and accretion of sediment. Marine organic matter, derived from both seagrass biomass (known as autochthonous carbon) and non-seagrass sources (known as allochthonous carbon) can be preserved through adsorption on fine sediments (silts and clays; Keil & Hedges, 1993; Hemingway et al., 2019), such that the promotion of deposition within a meadow also promotes carbon accretion. Whether an individual carbon-laden particle will deposit within a meadow depends on the relative time scales of deposition and advection through the meadow, which in turn depends on the size of the meadow. Further, seagrass roots and rhizomes can exude complex oxygen compounds, which may inhibit decomposition, and sugars, such that the roots and rhizomes of some seagrass species may promote organic carbon preservation (Sogin et al., 2022).

Seagrass meadows are disappearing rapidly on a global scale due to human activities and climate change (Orth et al., 2006; Waycott et al., 2009). The loss of seagrass may result in enhanced fragmentation of once continuous meadows into patches of varying scales (see Fahrig, 2003; Lindenmayer & Fischer, 2007; Warry et al., 2009). Patchiness may also result from natural disturbances (e.g., Duarte et al., 2006) and growth through seed dispersal (e.g., Kendrick

et al., 2012). Patchy configurations of seagrass can create complex mosaics of lower velocity regions within patches separated by higher velocity regions within sufficiently large and connected bare regions between patches (Fonseca et al., 1983; Licci et al., 2019). This contrasting hydrodynamic exposure could promote spatial heterogeneity in sediment organic carbon content, with carbon accretion and storage enhanced within the patches but suppressed in bare regions. However, depending on the density of shoots in the meadow and the sediment grain size, it is possible that the presence of seagrass may provide little effective protection for organic carbon particles, and thus would not promote locally enhanced carbon accretion (Dahl et al., 2018).

Only a few studies have examined spatial patterns in sediment organic carbon across patchy seagrass meadows. For large (100 m) patches of *Zostera muelleri* Irmisch ex Asch., Ricart et al. (2015) observed that sediment organic carbon content in the top 10 cm of sediment was lower near the patch edge, which they attributed to higher hydrodynamic exposure and younger shoot ages near patch edges. A similar observation (lower sediment organic carbon at meadow edge) was made by Oreska et al (2017), who proposed that a large continuous meadow should be more effective at accumulating organic carbon than a patchy meadow of the same overall size, due to the lower proportion of area near an edge. Consistent with this, Ricart et al. (2017) observed that carbon stock in the upper 2 cm of sediment was higher in continuous meadows than in nearby patchy meadows of *Posidonia oceanica* (L.) Delile, where patches were typically 2 m × 2 m in size. When considering the influence of landscape configuration on sediment carbon storage, the size of the patches, as well as the species of seagrass, is important (see discussion of landscape fragmentation scales in Bunnell, 1999; Wu, 2004). In particular, a vegetated patch must be of a sufficient size and shoot density to reduce current velocity and

create a region of distinct hydrodynamic exposure (Chen et al., 2013; Fonseca et al., 1982; Licci et al., 2019), which might lead to a region of enhanced sediment deposition. Similarly, a bare patch within a meadow must be of a sufficient size to accelerate the flow and experience enhanced velocities relative to the nearby vegetated patches. However, Asplund et al. (2021) found that patchy landscape metrics, such as mean patch size and patch edge perimeter, did not consistently predict spatial patterns in carbon storage across different patchy meadows in Tsimipaika Bay, Madagascar. Therefore, patch size is not the only factor controlling spatial variability in carbon stocks in patchy meadows.

The present study sought to contribute additional insight into patchy meadow dynamics by combining measurements of hydrodynamic exposure and carbon stock within a patchy seagrass (*Zostera marina* Linnaeus, also known as eelgrass) meadow. The original hypothesis was that, at a current-dominated site, hydrodynamic intensity would be lower within patches, compared to adjoined bare areas, which would result in higher sediment organic carbon content and carbon accretion rates within the patches. However, this hypothesis was proven to be wrong. Although current and resuspension were lower within patches, compared to the bare regions, this did not translate into enhanced organic matter or carbon stock within patches. Instead, the spatial variation in carbon stock seemed to be related to the persistence of individual patches within a meadow of shifting patches. By revealing a dynamically shifting state of individual patches within a meadow, this study provides insight into the vulnerability of seagrass sediment carbon pools in patchy landscapes.

7.2. Methods and Materials

7.2.1 Study site

The field site was a patchy meadow of *Z. marina* L. near the northern mouth of the Annisquam River in Gloucester, Massachusetts, on the East Coast of the United States of America. The Annisquam River is a waterway that cuts through Gloucester. To capture the landscape configuration before field measurements, a drone photographic survey was conducted in July 2022 at 60-m altitude (Figure 7.1). Four seagrass patches and four adjacent unvegetated bare areas were chosen as stations, numbered S1 through S4, with a 'V' suffix denoting a vegetated patch and a 'B' suffix denoting an unvegetated bare area. A boat survey in August 2022 recorded bathymetric contours using side-scan sonar. Mean lower low tide water depth ranged from about 0.5 to 1.5 m (Figure 7.1), such that all stations were always submerged. The mean tidal range at the nearby Lobster Cove, Massachusetts tidal gauge station is 2.7 m.



Figure 7.1: Left-hand image shows the field site in Gloucester, MA, United States of America. Unvegetated bare (white circles) and vegetated (green circles) measurement stations are marked

on a drone orthomosaic image. Bathymetric contours are at mean lower low tide. Purple squares mark the end points of the surface soil transect. Map data outside of drone orthoimage from Google. Bottom right image is a Google composite of images from Scripps Institute of Oceanography, National Oceanic and Atmospheric Administration, United States Navy, National Geospatial-Intelligence Agency, General Bathymetric Chart of the Oceans. The green rectangle in the bottom right image encompasses the left image. Image copyright United States Geological Survey. The top right image of the United States East Coast is copyright Landsat/Copernicus.

7.2.2 Sediment and seagrass sample collection

At each station, suspended sediment was collected in a sediment trap consisting of a horizontal frame holding three cylindrical polyvinyl chloride (PVC) tubes of length 15 cm and inner diameter 5 cm, with the bottoms of the tubes resting on the bed, following common practice discussed in Blomqvist & Kofoed (1981). Sediment traps were placed at least 5 m into the vegetated or bare region, i.e., at least 5 m from the nearest vegetated-unvegetated edge. The sediment trap tubes were fitted with honeycomb baffles (Plascore, Zeeland, Michigan) to reduce sediment resuspension out of the tubes. Sediment traps were deployed for 14 days between July and August, 2022.

During the same time period, one sediment core was taken at each station. To extract a core, a 50-cm long (7.0-cm outer diameter, 6.7-cm inner diameter) polycarbonate tube was manually driven with a T-handled core driver into the sediment by scientific divers to the greatest possible depth, which was limited by rocks. The sediment core lengths ranged from 20 to 30 cm long. The sediment cores were capped underwater and kept vertical during transport out of the water to the beach. Core compression during the coring process was recorded by marking the tube at the level of exterior sediment surface before the core head was extracted. On the shore, the sediment cores were systematically extruded into 1-cm thick cylindrical slices between

0 and 20 cm and 2-cm thick slices for sediment deeper than 20 cm. Each slice was stored in a separate pre-weighed Whirl-Pak bag and placed into a cooler for transport to a laboratory.

Measured compression during the coring and extrusion processes ranged from 11% to 27%, with an average of $19\% \pm 3\%$ (\pm standard error).

At each vegetated station, seagrass shoots were counted within five haphazardly placed 0.0625 m^2 quadrats and used to estimate the density of shoots per bed area. Five to ten shoots were randomly removed from each station to measure the length of the longest leaf above the sheath, sheath length, width, and number of leaves per shoot on the shore. Seagrass samples were stored in plastic bags filled with seawater and kept in a cooler. The second leaf of each shoot was retained for laboratory analysis.

To obtain a higher spatial resolution of sediment organic matter than provided by the eight sediment cores, a transect of surface sediment samples (endpoints shown with purple squares in Figure 1) was collected in 20-mL lined scintillation vials by pushing each vial 2 to 3 cm into the sediment surface and capping it. Twenty samples were taken with 2.5 m increments between them, and each sample was divided into two subsamples. The latitude and longitude at each sampling point were recorded with a handheld GPS. The presence or absence of vegetation at each location was recorded to corroborate with drone imagery. The samples were stored in containers with ice water until being transferred to a laboratory.

7.2.3 Laboratory sample analysis

After collection, sediment core, sediment trap, sediment vial, and seagrass samples were transported in a cooler to a laboratory. In the laboratory, each sediment trap tube was uncapped and left alone to allow sediment to settle before the overlying water in the tubes was decanted. The sediment from each trap tube was stored in a separate pre-weighed Whirl-Pak bag. Shellfish, arthropods, shell fragments, as well as living and dead roots and rhizomes, were removed from each sample so that organic carbon measurements represented the long-term storage component (see Greiner et al., 2013; Novak et al., 2020). Only a small fraction of seagrass detritus, consisting of microaggregates that can attach to finer sediment particles, is immobilized in the sediment (Hassink, 1995) and should be considered to be part of long-term carbon stocks. Sediment samples were dried in a drying oven at 60°C to constant mass and homogenized into powder using a mortar and pestle. In addition, seagrass leaf samples were scraped clean of epiphytes, dried, and ground into powder.

Sediment core slices were also dried at 60°C to constant mass. The dry mass of each sample was divided by the wet volume of a core slice to calculate the dry bulk density. Animals, shell fragments, and plant matter were removed from the samples before they were homogenized with a mortar and pestle. Sediment grain size distributions were measured for each station by combining subsamples from the top 5 cm of homogenized sediment core slices and dry sieving into the Krumbein ϕ size fractions 3.5 to 0.5, in increments of 0.5.

Stable isotope ratios $\delta^{13}\text{C}$ (relative to the Vienna Pee Dee Belemnite [VPDB] international standard) and $\delta^{15}\text{N}$ (relative to atmospheric air), as well as the dry weight percentage of organic carbon content (%OC) and dry weight percentage of nitrogen content

(%N) were measured in tinned subsamples of sediment trap and sediment core samples and tinned seagrass samples using the Isoprime 100 isotope ratio mass spectrometer (IRMS) interfaced with a Micro Vario Elemental Analyzer (Elementar Americas, Mt. Laurel, New Jersey). Internal laboratory standards (peptone and glycine) were run every 10 to 20 samples. Due to the mechanical removal of visible calcified structures and the low inorganic carbon measured in sediments of similar *Z. marina* L. meadows in the northeastern USA (based on Environmental Protection Agency blue carbon surveys), as well as the unpredictable impacts of acid washing on biasing %C, %N, $\delta^{13}\text{C}$, and $\delta^{15}\text{N}$ (e.g., Brodie et al., 2011), sediment samples were not washed with acid. Note that the IRMS did not produce reliable nitrogen measurements with sediment core subsamples due to very low nitrogen content and instrument limitations.

To obtain estimates of sediment mass accumulation rates, one subsample from what remained of each sediment core slice was sent to the Virginia Institute of Marine Science Geochronology Lab for tracer analysis of ^{210}Pb and ^{137}Cs radionuclides using gamma spectrometry (Canberra GL 2020 Low Energy Germanium detector). However, sediment mass accumulation rates could not be determined from the ^{210}Pb and ^{137}Cs activity profiles, potentially due to frequent mixing or coarse median sediment grain sizes. See Section 1 of the Supplementary Information for details of the geochronology methods, with an example set of profiles in Figure 7.S.1.

Finally, the surface sediment vial samples were dried to constant mass, cleaned of shells and plant material, and homogenized into powder. The two subsamples from each vial were burned in crucibles in a furnace at 450°C for 6 hours to maximize the loss of organic carbon while minimizing the loss of inorganic carbon (Dean, Jr., 1974; Froelich, 1980). The difference in mass

before and after burning was used to calculate the percent loss-on-ignition (%organic matter, %OM). Organic matter content values were converted to organic carbon content (%OC) based on a linear regression compiled from measurements in other similar *Z. marina* L. meadows in Massachusetts, USA, $\%OC = (0.338 \pm 0.03)\%OM - (0.138 \pm 0.010)$ (Novak et al., 2020).

7.2.4 Velocity data collection and processing

Tilt current meters (Lowell Instruments, Massachusetts) were tethered to square concrete paving stones at six stations (S1V, S2V, S3V, S1B, S2B, S3B) and measured the magnitude and direction of velocity at 16 Hz for 60 second bursts every five minutes. Velocity data were bisected based on the tilt direction into flood (moving south toward the Annisquam River, denoted as positive) and ebb (moving north away from the Annisquam River, denoted as negative). The index of each tidal flow peak was found using the MATLAB findpeaks function. The velocities of the peaks during the flood phases and ebb phases were separately averaged and denoted as $\overline{U_{c,peak}}$. Both the seagrass shoots and the tilt current meters are deflected by current, and at peak tidal velocity, the heights of the deflected shoots were lower than the deflected tilt current meters. In this condition, the tilt current meter recorded an average of velocity within and above the meadow patch. As the velocities near the bed are most important for sediment transport, we used a two-layer velocity model to infer the velocity within the canopy, U_1 , from measured velocity and meadow characteristics. The in-canopy velocity was used to estimate $\overline{U_{1,peak}}$ for the TCM sites located within meadow patches. Details are provided in Section 7.8.2.

See the Supplementary Information of Lei et al. (2023) for more details and laboratory flume testing of measuring wave velocities with tilt current meters.

7.2.5 Image analysis

We used historical aerial and satellite images of the field site to estimate patch distribution at discrete points in time between 1972 and 2022. The image sources and dates are listed in Table 7.S.1. Images were selected based on minimal cloud cover, optimal water depth and surface conditions, and spatial resolution. In addition, images were only drawn from months corresponding to the typical *Z. marina* L. growing season in Massachusetts, USA. Images, including the drone orthoimage, were geometrically transformed into alignment using the MATLAB Registration Estimator tool, cropped, and resampled to the same area of interest and pixel resolution. Vegetation patches were delineated using the MATLAB Image Segmenter tool. The MATLAB Image Processing Toolbox was used for further analysis of the delineated patches. Figure 7.S.2 shows a chronology of vegetated pixels across the images.

The images were used to estimate the total area of all vegetated patches within the meadow and to delineate the area of the whole meadow. In each image, the first and last pixels that were determined to be vegetated in each column were connected by lines to the first and last vegetated pixels of adjacent columns to create an outline of the entire meadow. The number of pixels contained within this outline defined the total meadow area A . The number of pixels contained within each of the delineated patches was summed to define the area of vegetation, A_v . See Figure 7.S.3 for an example of this method.

To quantify the persistence of vegetation through time, we counted the number of images across the collection of 21 images in which a given pixel was vegetated, denoted as N_{21} , and across the most recent ten images (2013-2022, with one image per year), denoted as N_{last10} . The last 10 images were considered because the gaps in time between successive images increased before 2013 (Table 7.S.1). Finally, we considered the number of consecutive images in which a given pixel was vegetated stepping back from 2022, denoted as $N_{lastcons}$. Each quantity was calculated at each pixel and then an average of pixel values was made within a circle of 3-m diameter around the GPS waypoints, which conservatively accounted for the typical accuracy of the handheld GPS model that was used.

7.2.6 Statistical analyses

Statistical analyses on sediment trap, surface sediment samples, and sediment core data were carried out using R packages (R Core Team, 2024). Given the small sample sizes, we used approximate Bayesian inference with integrated nested Laplace approximations (INLA, www.r-inla.org, Rue et al., 2009), using the default log-gamma priors. We combined the INLA model with a stochastic partial differential equation approach (SPDE, Lindgren et al., 2011, with the default multivariate normal priors to account for spatial dependence among the measurement stations. Point estimates and two-tailed 95% credible intervals were calculated for the predictor variables. Meshes based on longitude and latitude quantified the distances between measurement stations and between points along the surface sediment vial transect.

7.3. Results

7.3.1 Stable isotope measurements

Comparing the carbon stable isotope ratio $\delta^{13}\text{C}$ between seagrass and sediment samples provides insight into similarity of carbon sources. The sediment samples were more depleted in $\delta^{13}\text{C}$ than the seagrass. Specifically, seagrass leaf $\delta^{13}\text{C}$ ranged from -13.12 to -10.43‰, sediment trap $\delta^{13}\text{C}$ ranged from -29.30‰ to -18.14‰, and sediment core $\delta^{13}\text{C}$ ranged from -28.12‰ to -12.35‰ (Figure 7.2). While there was a wide range in individual $\delta^{13}\text{C}$ measurements in the sediment cores, there were no clear trends with sediment depth in the profiles of $\delta^{13}\text{C}$ (see example for S1V in Figure 7.3, and more details in Figure 7.S.4).

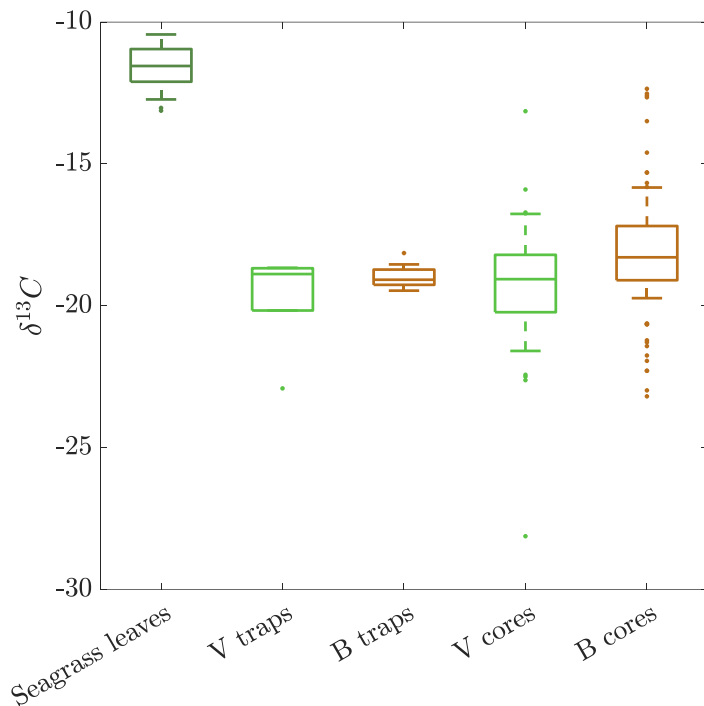


Figure 7.2: Box plots of carbon isotope ratio $\delta^{13}\text{C}$ (‰ relative to Vienna Pee Dee Belemnite) from seagrass leaves, sediment trap, and sediment cores from vegetated (“V”) stations and from unvegetated bare (“B”) stations. The upper and lower boundaries of each box represent the 75th and 25th quartiles, respectively. The horizontal line within each box denotes the median. Whisker lengths denote the 5th and 95th percentiles. Dots denote outliers.

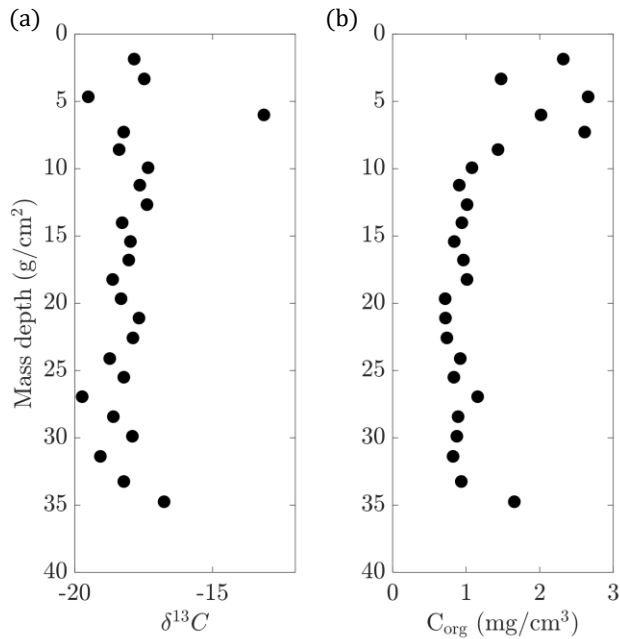


Figure 7.3: Profiles of (a) $\delta^{13}\text{C}$ (‰, relative to VPDB) and (b) organic carbon C_{org} density over cumulative mass depth for station S1V.

7.3.2 Seagrass meadow parameters

Shoot density and morphological measurements for the vegetated stations are given in Table 7.S.2. The shoot density in July 2022 varied between the measurement stations (166 ± 12 shoots m^{-2} at S1V, 291 ± 17 shoots m^{-2} at S2V, 300 ± 30 shoots m^{-2} at S3V, and 210 ± 20 shoots m^{-2} at S4V). However, the number of leaves per shoot, sheath length, longest leaf length, and shoot width were similar across the vegetated stations. The number of leaves per shoot ranged from 3.80 ± 0.13 at S2V to 4.10 ± 0.10 at S4V. The sheath length ranged from 18.6 ± 1.8 cm at S2V to 19.8 ± 0.9 cm at S4V. The length of the longest leaf (beginning at the top of the sheath) ranged from 9.5 ± 0.9 cm at S2V to 12.3 ± 0.8 cm at S1V. Finally, the shoot width ranged from 0.35 ± 0.04 cm at S3V to 0.43 ± 0.02 cm at S1V.

7.3.3 Hydrodynamic conditions

Moving averages with a 60-minute time window of velocities measured by the tilt current meters, denoted as $U_{c,TCM}$, are shown in Figure 7.4a, with positive denoting the flood direction and negative denoting the ebb direction. Hourly-averaged wave velocities are shown in Figure 7.4b. Because the tilt current meter extended above the height of the meadow, especially during peak tidal velocity, the velocity within the patches, U_1 , was only 30-50% of the velocity measured by the TCM, $U_{c,TCM}$, (see Section 7.8.2). In bare regions, the peak current velocities were typically twice as large as peak wave velocities (except on day 11), indicating that on most days of the deployment tidal currents dominated hydrodynamic exposure and therefore sediment transport. This difference was smaller within vegetation patches, where current velocity experience greater reduction relative to adjacent bare areas than did wave velocity. The higher current velocities outside the patches can reinforce the patch edge by reducing the probability of colonization of bare areas (Luhar et al., 2008; Meysick et al., 2019; van Wesenbeeck et al., 2008).

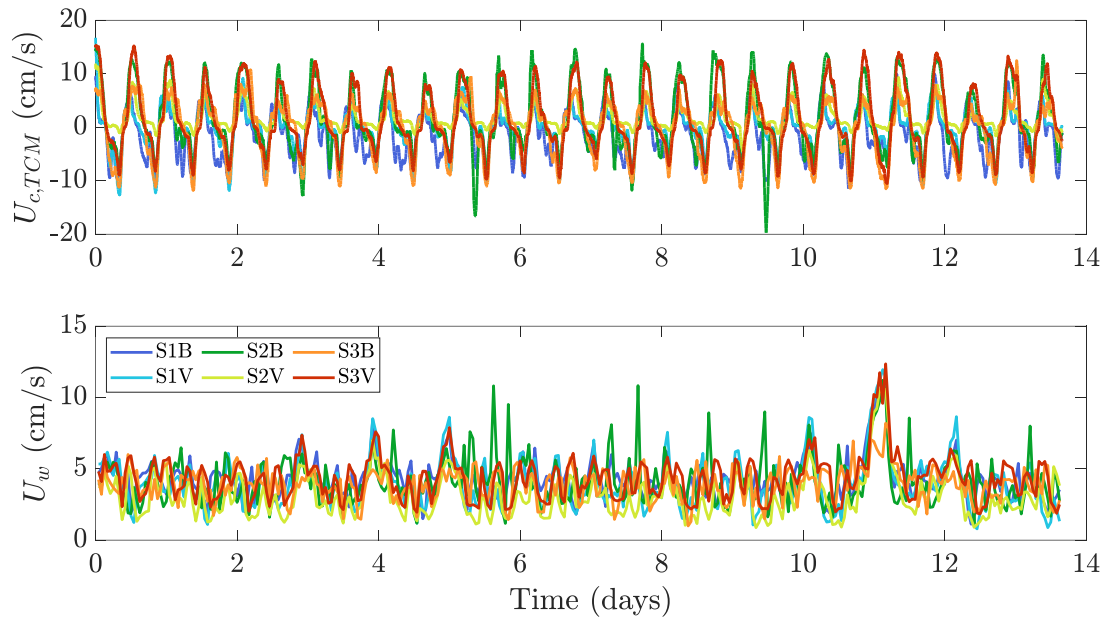


Figure 7.4: (a) Time series of sixty-minute moving average velocity $U_{c,TCM}$. (b) Time series of hourly-averaged wave velocity U_w , defined as $\sqrt{2}$ multiplied by hourly-averaged root-mean-square velocity, $U_{w,RMS}$.

7.3.4 Sediment sample analyses

7.3.4.1 Sediment mass and organic carbon content in sediment traps

The sediment trap masses at bare stations ($n=12$) were greater than at vegetated stations ($n = 12$), with a 95% posterior probability of vegetated stations having lower sediment trap mass than bare stations (Table 7.1; compare left-hand brown and green bars for each site in Figure 7.5a). The sediment %OC in the sediment traps was higher at vegetated stations compared to bare stations, with a 95% posterior probability of vegetated stations having higher %OC than bare stations (Table 7.1; compare right-hand stippled brown and green bars for each site in Figure 7.5a). The average sediment trap mass increased with average peak in-canopy tidal

velocity, $\overline{U_{1,peak}}$ (Figure 7.5b), and the bare stations, which experienced higher velocity, collected higher sediment trap mass, compared to vegetated sites. Finally, note that the organic carbon content of the sediment traps was roughly ten times greater than that of the sediment cores, which could be due to the higher lability of the particulate organic matter present in the traps combined with shorter timescales of exposure to microbial decomposition processes.

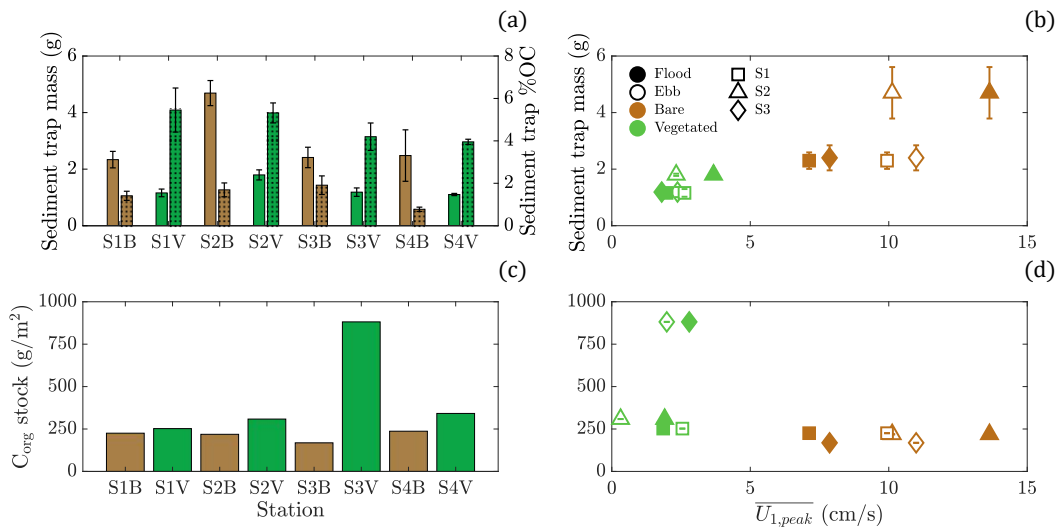


Figure 7.5: (a) Sediment trap mass (left bar in each site pair; left axis) and sediment trap percent organic carbon content (right stippled bar in each site pair; right axis), (b) Sediment trap mass versus average peak tidal velocity $\overline{U_{1,peak}}$. Sediment organic carbon stocks in top 20 cm of sediment cores, C_{org} (c) at each station and (d) versus average peak tidal velocity $\overline{U_{1,peak}}$. Vertical bars represent standard error. Green and brown bars and symbols denote vegetated and bare sites, respectively.

Table 7.1: Integrated nested Laplace approximations (INLA) with stochastic partial differential equation (SPDE) model results, with bare stations as the baseline. Results include the mean, standard deviation (SD), and 95% credible interval for each estimated effect.

Predictor	Response			
	Sediment trap mass	Sediment trap %OC	Vial surface sample %OC	Sediment core carbon stock
Bare → Vegetated status	Mean: -1.85 SD: 0.47 2.5%: -2.86 50%: -1.83 97.5%: -0.96	Mean: 3.29 SD: 0.42 2.5%: 2.47 50%: 3.29 97.5%: 4.13	Mean: -.002 SD: 0.036 2.5%: -0.076 50%: 0.066 97.5%: 0.074	Mean: 12.21 SD: 31.38 2.5%: -49.45 50%: 12.26 97.5%: 73.60

7.3.4.2 Sediment core organic carbon stocks

The sediment organic carbon content at each station was characterized by the total carbon stock in the top 20 cm of each sediment core (as all cores were at least 20 cm long). See Figure 7.S.5 for the full sediment core carbon density profiles (and Figure 7.3b for an example profile). Whether a core location was vegetated or bare at the time of core collection likely had no effect on sediment organic carbon stock (the 95% credible interval for this effect contains zero, see Table 7.1). The vegetated site S3V had higher carbon stock compared to all other sites (Figure 7.5c), even though S3V experienced similar velocity to other vegetated sites (green symbols in Figure 7.5d), an anomaly that is reflected in the large range of values in Table 7.1. The excess ^{210}Pb activity (beyond background levels of ^{210}Pb) in the core samples were too low to extract a mass accumulation rate, which was likely due to a combination of coarse sediments and sediment mixing (see Arias-Ortiz et al., 2018). Further, there were no ^{137}Cs peaks outside of the range of detector uncertainty. Based on the ^{137}Cs and excess ^{210}Pb activity results, we assume the long-term average organic carbon accumulation rate is zero.

7.3.4.3 Surface sediment vial samples

Compared to the cores, the surface sediment samples added more detailed horizontal resolution, but were limited to a shallower vertical resolution. At bare locations the estimated %OC was 0.138 ± 0.018 % (\pm propagated standard error; $n=8$ samples), which was the same within uncertainty to vegetated locations, %OC = 0.151 ± 0.011 % (\pm propagated standard error; $n=12$ samples). The presence of aboveground vegetation at an individual vial location likely had no effect on the surficial organic carbon content (Table 7.1). Further, the surface %OC estimated from the vials, which captured the top 2 to 3 cm of sediment, were comparable to the %OC measured in the top 3 cm of the sediment cores, which ranged from 0.080 ± 0.006 to 0.14 ± 0.03 , excluding S3V (see sediment core profiles of organic carbon content in Figure 7.S.6). At S3V, the average over the top 3 cm was %OC = 0.345 ± 0.018 . Unfortunately, due to swell during field site visits, no vial samples could be collected near S3V, where higher surface organic carbon content may be expected.

7.3.4.4 Sediment grain size distributions

The surface grain size distributions are shown in Figure 7.S.7. S3V and S3B had slightly finer median grain sizes than the other stations, 0.13 mm compared to 0.18 mm, likely due to the closer proximity to the mouth of the Annisquam River. The percentage finer than $\phi=3.5$ on the Krumbein ϕ scale, equivalent to a diameter of 0.09 mm (the finest threshold tested), was less than 0.01% across the stations.

Summarizing the conclusions drawn from the sediment samples, sediment core organic carbon stocks did not vary with exposure to different peak tidal velocities (Figure 7.5d), and was

higher at the vegetated site (S3V), which was not hydrodynamically distinct from the other vegetated sites (Figure 7.5d). Therefore, the two-week snapshot of spatial differences in hydrodynamic exposure measured in the summer of 2022 (Figures 7.4 and 7.5b, 7.5d) cannot explain the observed distribution of sediment organic carbon stocks. Next, we considered how past changes to hydrodynamic spatial variability associated with patch persistence and migration correlated with spatial variability in sediment organic carbon content.

7.3.5 Landscape configuration analysis

Historical aerial and satellite images show that the seagrass patches within the meadow have continuously shifted over time; in other words, the landscape distribution has not been static. Figure 7.6a shows a heat map of N_{21} , the frequency of vegetation presence in each pixel between 1972 to 2022 (21 images). Warmer colors indicate areas that have been vegetated more often. White pixels never vegetated in the images. Importantly, no regions were vegetated for all of the time periods captured by the curated images. The heights of the pink vertical bars represent the cumulative sediment organic carbon stocks in the top 20 cm of the sediment core taken at the position of the bar. While S3V had the highest carbon stock, it did not occur in a particularly distinct hotspot of N_{21} compared to other sites. Therefore, we narrowed the time frame to the most recent 10 years (one image per year from 2013 to 2022) in Figure 7.6b. Within this time frame, the distinctly higher carbon stock at site S3V corresponded with the largest number of years in the last decade with vegetation (N_{last10} , Figure 7.7). Station S3V had the highest N_{last10} and $N_{lastcons}$ among the stations. Further, S3V was located within a larger contiguous region of high N_{last10} compared to the other stations.

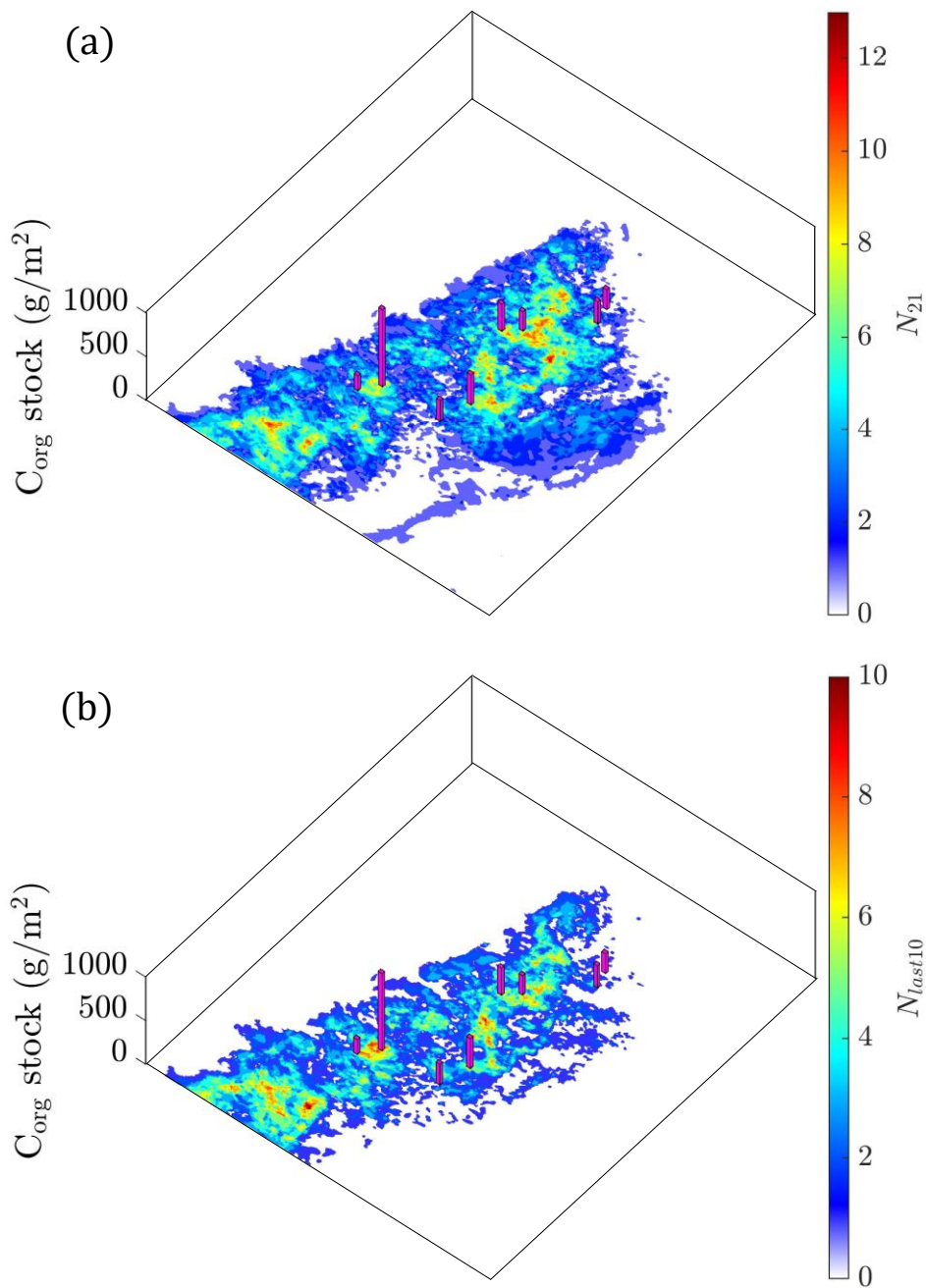


Figure 7.6: Heat maps describing the number of times a pixel was vegetated over (a) all 21 images (1972 to 2022), N_{21} , and (b) over the last 10 images, $N_{\text{last}10}$, with one image per year 2013 to 2022. A white color denotes that N_{21} or $N_{\text{last}10}$ for that pixel is zero. The vertical pink bars indicate the sediment organic carbon stock in the top 20 cm of the sediment cores at the location corresponding to the base of the bar.

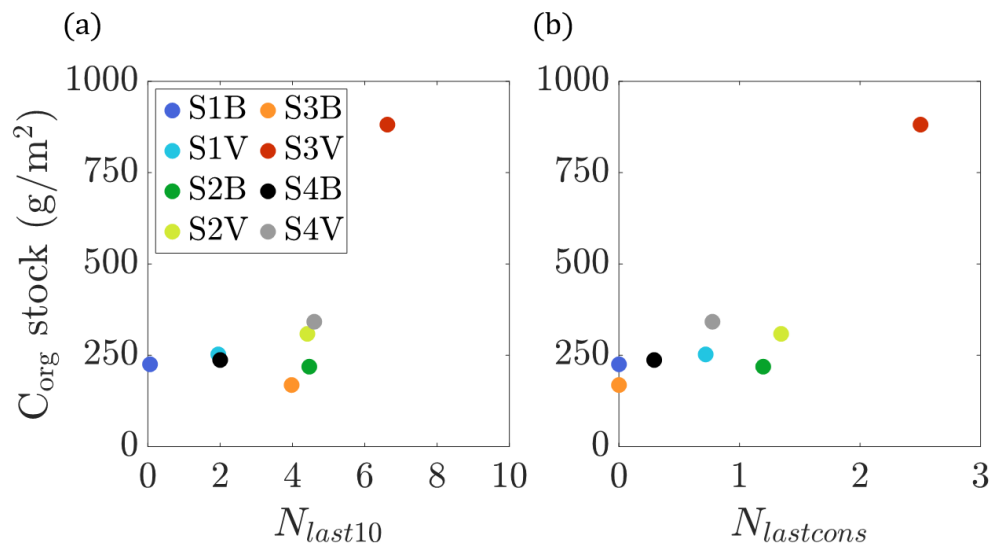


Figure 7.7: Sediment organic carbon stocks in top 20 cm of sediment cores versus (a) N_{last10} , the number of times the corresponding station was vegetated within the past 10 years (images), and (b) $N_{lastcons}$, the number of years the corresponding station was vegetated in consecutive images stepping back from 2022 in year intervals, both calculated as averages over 3-m diameter circles centered at the station GPS locations. Standard errors in N_{last10} and $N_{lastcons}$ are smaller than the symbol sizes.

7.4. Discussion

The original hypothesis motivating this study was that tidal velocities would be attenuated within the patches (of scale 10 to 20 m), which would promote the deposition and retention of organic carbon, producing differences in the carbon stock between vegetated and bare regions within the meadow. A two-week snapshot of hydrodynamic conditions confirmed that patches of this size did attenuate tidal velocity. However, this did not correlate with observed spatial distribution of carbon stocks. For most bare and vegetated regions in the meadow the carbon stock and %OM was the same, and the single patch with high carbon stock experienced similar

hydrodynamic conditions as other patches in the meadow, *i.e.*, the contemporary mosaic of hydrodynamic conditions within the meadow did not explain the observed spatial variation in carbon stock. Factors that might explain the observed spatial distribution in organic carbon stocks are explored next.

7.4.1 Sediment transport and resuspension

The depletion of $\delta^{13}\text{C}$ in sediment samples compared to seagrass samples (Figure 7.2) indicated a dominant contribution to sediment carbon from non-seagrass sources, *i.e.*, allochthonous carbon. The likely sources that are more depleted in $\delta^{13}\text{C}$ than seagrass are salt marshes along the Annisquam River and terrestrial vegetation within the Annisquam River watershed. For example, common salt marsh plants can have $\delta^{13}\text{C}$ values between -27‰ and -14‰ (Bouillon & Boschker, 2006). The median $\delta^{13}\text{C}$ among sediment cores at bare stations was slightly less depleted than that at vegetated stations, which could be related to the exclusion of larger seagrass detrital fragments by the sediment trap baffles as well as localized enhancement of the eelgrass contribution within certain sections of the sediment cores. The presence of predominantly allochthonous carbon suggests the importance of hydrodynamic conditions in determining carbon storage across the meadow. In this seagrass meadow, most organic matter would be expected to originate from the Annisquam River at the southern end of the meadow (Figure 7.1). A comparison of advection and settling time-scale of fine sediments suggested that an even supply of suspended material over the meadow was likely. In saline conditions, clay particles and organic matter form irregularly shaped, porous flocs (Abolfazli & Strom, 2023; Sutherland et al., 2015). The settling velocity of a floc depends on the floc diameter and density, and for an

exposed marine environment, such our site, has been measured to be roughly 0.5 mm/s (Droppo, 2004). Across the meadow, the average water depth was 1 m at low tide (Figure 7.1), indicating a lower limit of the flocculation time-scale of 2000 s. In contrast, the peak tidal velocities were on the order of 0.1 m/s, which indicates a transit time of 1500 s across the roughly 150 m meadow. Because the settling time scale is comparable to or larger than the advection time scale, flocs could be delivered to the entire meadow without supply limitation. If supply is not limiting, differences in net deposition are attributed to differences in resuspension. Based on the near-surface median grain sizes (fine sand), the critical friction velocity u_{*c} for the initiation of sediment motion is 1.2 cm/s (Julien, 2010). Many studies report depth-averaged current velocity to friction velocity ratios $U_c/u_* = 10$ (e.g., Amos et al., 1992; McPhee, 2002), from which we infer a critical depth-averaged current velocity of 10 cm/s. The tidal velocities at bare sites exceeded this during ebb tide (Figure 7.4d), suggesting the bed material was regularly resuspended at bare sites. In contrast, tidal velocity within the patches (Figure 7.4d) was likely too low to regularly remobilize the bed. Higher resuspension rates near bare sites, which would locally enhance suspended sediment concentration, could explain the higher sediment trap mass at bare sites (Figure 7.5a). We did not have suspended sediment concentration to support this conjecture. Similarly, lower resuspension within vegetated patches could explain the higher organic carbon content (percentage by weight) in the sediment traps at vegetated sites (Figure 7.5a). Organic carbon particles passing through bare patches could mix with higher levels of sediment resuspended from the bed. Note that the small percentages of silt and clay particles at the site suggests that a substantial portion of organic carbon storage could be related to sorption to sand surfaces or deposition as unattached particles. Nevertheless, it is difficult to determine the relative contributions of the different size fractions to organic carbon preservation.

Sediment can also be remobilized from the bed during high-energy storm events or by ship wakes, but the relative contributions of the tidal currents, storms, and ship wakes to sediment resuspension could not be identified from this two-week study. Specifically, higher winds during the winter months (14 to 16 km hr⁻¹ in January through April versus 10 to 11 km hr⁻¹ in July and August, as reported by a local Windfinder weather station) could shift the hydrodynamic conditions from tidal-current dominate to wave-domination, which can be more efficient in resuspending material within vegetation, because wave-velocity more readily penetrates through the vegetation layer (see Lowe et al., 2005). In addition, a lower leaf density during winter months could expose the bed to higher currents and thus greater sediment mobilization.

Frequent remobilization of sediment could explain the absence of long-term sediment carbon storage. In particular, the organic carbon density in this patchy meadow (1.25 ± 0.05 mg cm⁻³ C_{org} over the top 20 cm averaged across stations, but excluding S3V; see Figure 7.S.5) was lower than values measured in continuous *Z. marina* L. meadows in similar substrates (fine to medium sands) in New England reported in Novak et al. (2020), 5.3 to 15.6 mg cm⁻³ C_{org}, and in Lei et al. (2023), 2.7 to 8.0 mg cm⁻³ C_{org}, and comparable to values measured at bare sites adjacent to those meadows (1.0 to 10.4 mg cm⁻³ C_{org} in Novak et al., 2020 and 2.8 to 4.0 mg cm⁻³ C_{org} in Lei et al., 2023). That is, over most of its area, the patchy meadow had not enhanced the sediment carbon density. In contrast, the carbon density at S3V (with an average of 4.41 ± 0.6 mg cm⁻³ C_{org} over the top 20 cm) fell within the range of other continuous New England meadows. Recall that S3V was within a region of the meadow that maintained vegetation for most of the last 10 years (Figure 7.6). It is likely that the other patches have not persisted over sufficient time to accumulate organic carbon. The higher levels of resuspension at the bare sites

suggested that once a site becomes bare, the previously stored carbon is remobilized and removed, so that a meadow of shifting patches will remain carbon-poor.

7.4.2 Mechanisms sustaining a patchy landscape configurations

Let's consider how this patchy meadow persists. Patches of *Z. marina* L. can maintain and expand their populations through clonal (horizontal rhizome extension) or sexual (seedling dispersal) reproduction (Duarte et al., 2006). Overall, *Z. marina* L. meadows in shallow water depths are typically more successful at clonal than sexual reproduction (Olesen et al., 2017; Cunha et al., 2004; Greve et al., 2005; Plus et al., 2003), such that the survival of a meadow requires the clonal growth rate to outpace the rate of mortality. Seed dispersal through sexual reproduction may be more important for large-scale recolonization of previously vegetated areas (e.g., Olesen et al., 2017; Orth et al., 2020). Furthermore, seedling burial in one year and growth in a future year could contribute to the substantial spatiotemporal shifts in patch configuration within a particularly dynamic meadow (e.g., Johnson et al., 2021). Setting aside the effects of seedling growth for simplicity as well as due to the high tidal velocities at the field site that may reduce the survival of seeds (e.g., Orth et al., 1994), the effect of clonal growth on patch dynamics has been modeled as a stochastic contact process (Oborny et al., 2007), in which at each time step empty parts of a patchy meadow can be colonized with a certain growth probability only if there is a shoot within the range of annual horizontal rhizome extension, and existing seagrass shoots each have a certain probability of mortality. The ratio of growth rate to decay rate has a critical threshold of 1.65, below which patches completely disappear over long periods of time (Marro & Dickman, 1999).

Marro & Dickman (1999) only considered biological processes, but the seagrass landscape is also sensitive to hydrodynamic drivers that produce feedback mechanisms that stabilize a patchy distribution. Within vegetated patches of sufficient size, velocity is reduced within the patch (e.g., Figure 5b), which enhances sediment retention and shoot survival, providing a positive feedback to patch stability (e.g., Licci et al., 2019; van Wesenbeeck et al., 2008). Complementary to this, where flow is directed into bare areas between vegetated patches, the local velocity increases, which can reinforce the bare region (another positive feedback) by eroding the edges of patches and reducing the chances of successful seagrass colonization in bare areas (e.g., Fonseca & Fisher, 1986). It is important to note that the positive feedbacks that maintain a patchy meadow structure only exist if flow can be redirected from vegetated to bare regions, which requires that the bare regions be sufficiently connected to facilitate a continuum of flow (Luhar et al., 2008). In other words, an isolated bare patch within a broader meadow will not experience elevated current, because continuity requires that the elevated current have a contiguous channel through which to travel.

Luhar et al. (2008) used percolation theory to identify the threshold of vegetation coverage at which bare regions of low flow resistance connect into contiguous channels. Consider a two-dimensional grid of squares, where each square has a certain probability (p) of being bare and probability ($1-p$) of being vegetated. According to percolation theory, at the critical probability $p = 0.593$, bare regions can connect and form percolation channels (Table 1 in Stauffer & Aharony, 1985). Below this threshold, individual bare points tend to remain isolated (Luhar et al., 2008; Stauffer & Aharony, 1985). Luhar et al. (2008) hypothesized that if vegetated area fraction fell below ($1-p = 0.407$), channels would emerge, and once channels existed, they would persist because of the positive feedbacks described above. Consistent with this, Luhar et

al. (2008) used observations of Fonseca & Bell (1998) to show that individual seagrass meadows clustered around two landscape conditions, a continuous meadow (100% area coverage) and a fragmented meadow (40% area coverage). That is, a fragmented meadow near the percolation threshold of 40% vegetated area coverage is a stable configuration.

A similar threshold was observed at the field site. The percentage of vegetated area within the meadow area, A_v/A , estimated from the historical images is shown in Figure 7.8a. The average $A_v/A = 40 \pm 3\%$ (mean \pm standard error), which is consistent with percolation theory and hydrodynamic feedback described above. Note that between individual consecutive years the vegetation coverage showed variability, sometimes higher or lower than 40%, which could be related to the uncertainty in determining the irregularly-shaped A and lack of pure randomness in seagrass growth. The persistence of vegetation coverage near 40% suggested that the meadow was stable in a patchy landscape configuration. The meadow has apparently not exceeded the critical threshold that might lead to a continuous meadow. Or, if it has exceeded the threshold, sporadic disturbances reduced percentage cover to below the threshold (see Duarte, 1991). The meadow was not detected in the 1978 image (open symbol in Figure 7.8a), which was likely due to the cyclone and/or notable winter storms between the 1975 and 1978. Note that it is possible that there were small patches of surviving seagrass not distinguished by the aerial camera sensor technology used in the 1978 image. It is possible that seeds and rhizome fragments buried within the sediment survived and drove the recolonization of the area.

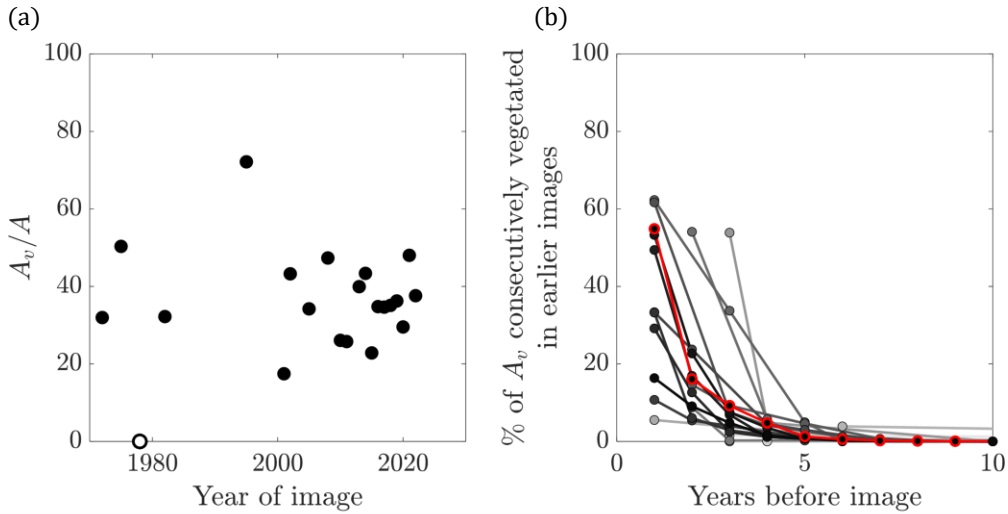


Figure 7.8: (a) Area of vegetation cover A_v within the meadow area A , versus year of the image. In 1978 (open symbol) there was no vegetation, so the ratio A_v/A was not determinable. (b) Percentage of vegetation cover in an image of interest that was consecutively vegetated in chronologically earlier images versus the time interval between the images. The red symbols and line denote comparisons with the July 2022 drone image. More recent images are denoted by increasingly darker shades of gray.

Figure 7.8b shows the history of vegetation persistence marching back in time from different initial time points (different initial images). These data suggest that at each point within the meadow, vegetation persists for less than five years. When jointly considering Figure 7.8a and 7.8b, the changes in patch patterns over time resemble the shifting mosaic, steady-state ecological model proposed in Bormann & Likens (1979) for terrestrial forests. In their model, biomass patterns shift over time as trees propagate or fall, but on the scale of the entire forest, there is no long-term change in total biomass. At the seagrass meadow of interest, while individual patches have actively moved across the landscape, the total seagrass area fraction has remained near at mean value of $40 \pm 3\%$ (mean \pm standard error).

7.4.3 Persistence of sediment organic carbon pools

Even though S3V had significantly higher organic carbon compared to other sites in the summer of 2022 (Figure 7.5), if it became bare in the future, it would likely lose its elevated sediment organic carbon stocks, returning to the average state represented throughout the rest of the meadow. Rapid changes in organic carbon over the top 20 cm of sediment following a shift from vegetated to bare status could result from a combination of enhanced sediment erosion (Marbà et al., 2015) and enhanced rates of aerobic decomposition due to higher oxygen exposure at the unvegetated sediment-water surface (e.g., Scheef & Marcus, 2011). Higher near-bed current velocities in bare sediment regions not only promote erosion and mixing, but also enhance oxygen fluxes across the sediment-water interface (Berg et al., 2013). Furthermore, the burrowing and pumping of bivalves and other bio-irrigating organisms through the sediment column facilitate the diffusion of oxygen into the sediment and enhance sediment mixing (Norkko & Shumway, 2011; Volkenborn et al., 2012). Large hard-bodied burrowing organisms cannot penetrate as easily beyond the dense near-surface network of living seagrass roots and rhizomes as in bare sediments (Brenchley, 1982; González-Ortiz et al., 2016; Goshima & Peterson, 2012).

The top meter of sediment is particularly vulnerable to remineralization and erosion when seagrass is lost (Fourqurean et al., 2012; Pendleton et al., 2012). For example, Moksnes et al. (2021) found that the loss of *Z. marina* L. at various sites and over 10 to 40 years before their study reduced organic carbon over at least 35 cm of sediment depth. Macreadie et al. (2015) found that a disturbance-induced seagrass loss reduced organic carbon in the top meter of sediment in Australian *P. oceanica* seagrass meadows, but once aboveground biomass returned,

half of the carbon lost was recovered within five to 10 years. Finally, Serrano et al. (2021) compared seagrass meadows (*Amphibolis antarctica* [Labill.] and *Posidonia australis* Hook.f., Shark Bay, Australia) with nearby bare areas that lost seagrass to a heat wave six years prior. They found significantly lower sediment organic carbon stocks in the previously vegetated bare areas compared to the vegetated areas, indicating a significant loss in carbon over six years. Considering the studies described above alongside the present study, the loss and subsequent recovery of buried sediment organic carbon in seagrass meadows occurs on time scales of five to ten years. Even though site S3V was occasionally bare within the 10 years prior to 2022, it did not remain bare long enough for the accumulated sediment organic carbon to be lost.

Understanding the effectiveness of seagrass in accumulating and retaining carbon is important for monitoring, reporting and verifying carbon credits (Lafratta et al., 2020; Howard et al., 2023). The present study demonstrated conditions in which a patchy meadow can persist for decades, but not accumulate any permanent carbon stock, which was attributed to the shifting mosaic of patches that comprise the meadow. An aggressive restoration project might try to lift the A_v/A ratio above the critical percolation threshold to facilitate the coalescence of patches and thereby the stabilization of carbon stores. However, it is possible that the hydrodynamic conditions at this site might drive the system back toward the current dynamic stability of migrating patches. When assessing potential locations for blue carbon and/or restoration, managers should consider not only the historical persistence of a meadow, but also the shifting distribution of vegetation within the meadow. Aerial imagery may aid managers in narrowing down the primary causes of seagrass loss, which should be addressed before beginning a restoration. Furthermore, when choosing sites to measure sediment organic carbon within a

seagrass meadow, scientists should use aerial imagery to evaluate the potential influence of landscape configuration on spatial heterogeneity in carbon stores.

7.5. Conclusions

The spatial variability in hydrodynamic intensity across a patchy seagrass meadow correlated with the spatial variability in sediment resuspension but did not correlate with the spatial variability in sediment organic carbon stocks. Our hypothesis that organic carbon stocks would be higher within vegetated patches, compared to bare patches, was based on the assumption of a static landscape configuration. However, analysis of historical aerial images revealed that the meadow was in a dynamic stable state, with individual patches shifting positions in time, while maintaining an overall coverage fraction close to the percolation limit. The constant shifting of patch location limited sediment carbon to levels comparable to other bare sites in the region. This sort of historical analysis could provide insight into the suitability of a seagrass meadow for restoration to a contiguous meadow and its potential for carbon storage. If a meadow is patchy but the patches have not shown substantial movement over time, it is likely that the patches would be able to enhance the long-term accumulation and retention of organic carbon.

7.6 Acknowledgments

This study was supported by Shell International Exploration and Production through the MIT Energy Initiative. R. Schaefer was supported by the National Science Foundation Graduate Research Fellowship under Grant No. 2141064 and the Massachusetts Institute of Technology

Department of Civil and Environmental Engineering. We thank the U.S. Environmental Protection Agency dive team for their assistance in the field: Eric Nelson, Jean Brochi, Danielle Gaito, Chuck Protzmann, Brent England. The bathymetry and meadow mapping were collected by Mike Sacarny under award NA18OAR4170105 from the National Sea Grant College Program of the U.S. Department of Commerce's National Oceanic and Atmospheric Administration. Mike Sacarny also provided boat support for divers. Gary Lei, Ian Koe, and Ernie Lee assisted with field data collection. Kimberly Candelario assisted with field data collection and laboratory sample processing. Advice on spatial statistics was provided by data science specialist Steven Worthington, at the Institute for Quantitative Social Science, Harvard University.

7.7 References

- Abolfazli, E., & Strom, K. (2023). Salinity impacts on floc size and growth rate with and without natural organic matter. *Journal of Geophysical Research: Oceans*, 128(7), 1–16. <https://doi.org/10.1029/2022JC019255>
- Amos, C. L., Grant, J., Daborn, G. R., & Black, K. (1992). Sea Carousel-A benthic, annular flume. *Estuarine, Coastal and Shelf Science*, 34(6), 557–577. [https://doi.org/10.1016/S0272-7714\(05\)80062-9](https://doi.org/10.1016/S0272-7714(05)80062-9)
- Arias-Ortiz, A., Masqué, P., Garcia-Orellana, J., Serrano, O., Mazarrasa, I., Marbá, N., Lovelock, C. E., Lavery, P. S., & Duarte, C. M. (2018). Reviews and syntheses: 210Pb-derived sediment and carbon accumulation rates in vegetated coastal ecosystems - Setting the record straight. *Biogeosciences*, 15(22), 6791–6818. <https://doi.org/10.5194/bg-15-6791-2018>
- Asplund, M. E., Dahl, M., Ismail, R. O., Arias-Ortiz, A., Deyanova, D., Franco, J. N., Hammar, L., Hoamby, A. I., Linderholm, H. W., Lyimo, L. D., Perry, D., Rasmusson, L. M., Ridgway, S. N., Salgado Gispert, G., D'Agata, S., Glass, L., Mahafina, J. A., Ramahery, V., Masque, P., ... Gullström, M. (2021). Dynamics and fate of blue carbon in a mangrove–seagrass seascape: influence of landscape configuration and land-use change. *Landscape Ecology*, 36(5), 1489–1509. <https://doi.org/10.1007/s10980-021-01216-8>

- Berg, P., Long, M. H., Huettel, M., Rheuban, J. E., McGlathery, K. J., Howarth, R. W., Foreman, K. H., Giblin, A. E., & Marino, R. (2013). Eddy correlation measurements of oxygen fluxes in permeable sediments exposed to varying current flow and light. *Limnology and Oceanography*, 58(4), 1329–1343. <https://doi.org/10.4319/lo.2013.58.4.1329>
- Blomqvist, S., & Kofoed, C. (1981). Sediment trapping—A subaquatic in situ experiment. *Limnology and Oceanography*, 26(3), 585–590. <https://doi.org/10.4319/lo.1981.26.3.0585>
- Bormann, F. H., & Likens, G. E. (1979). Catastrophic disturbance steady state in northern hardwood forests: a new look at the role of disturbance in the northern hardwood forests. *American Scientist*, 67(6), 660–669.
- Bouillon, S., & Boschker, H. T. S. (2006). Bacterial carbon sources in coastal sediments: a review based on stable isotope data of biomarkers. *Biogeosciences*, 3, 175–185.
- Brenchley, G. A. (1982). Mechanisms of spatial competition in marine soft-bottom communities. *Journal of Experimental Marine Biology and Ecology*, 60(1), 17–33. [https://doi.org/10.1016/0022-0981\(81\)90177-5](https://doi.org/10.1016/0022-0981(81)90177-5)
- Brodie, C. R., Leng, M. J., Casford, J. S. L., Kendrick, C. P., Lloyd, J. M., Yongqiang, Z., & Bird, M. I. (2011). Evidence for bias in C and N concentrations and $\delta^{13}\text{C}$ composition of terrestrial and aquatic organic materials due to pre-analysis acid preparation methods. *Chemical Geology*, 282(3–4), 67–83. <https://doi.org/10.1016/j.chemgeo.2011.01.007>
- Bunnell, F. L. (1999). Let's kill a panchreston – giving fragmentation meaning. In J. A. Rochelle, L. Lehmann, & J. Wisniewski (Eds.), *Forest fragmentation: Wildlife and management implications* (pp. 1–7). Brill Publishers.
- Chen, Z., Jiang, C., & Nepf, H. (2013). Flow adjustment at the leading edge of a submerged aquatic canopy. *Water Resources Research*, 49(9), 5537–5551. <https://doi.org/10.1002/wrcr.20403>
- Cunha, B. A. H., Duarte, C. M., & Krause-Jensen, D. (2004). How long time does it take to recolonize seagrass beds? In J. Borum, C. M. Duarte, D. Krause-Jensen, & T. M. Greve (Eds.), *European seagrasses: An introduction to monitoring and management* (pp. 72–76).
- Dahl, M., Infantes, E., Clevesjö, R., Linderholm, H. W., Björk, M., & Gullström, M. (2018). Increased current flow enhances the risk of organic carbon loss from *Zostera marina* sediments: Insights from a flume experiment. *Limnology and Oceanography*, 63(6), 2793–2805. <https://doi.org/10.1002/lno.11009>
- Dean, Jr., W. E. (1974). Determination of carbonate and organic matter in calcareous sediments and sedimentary rocks by loss on ignition: comparison with other methods. *Journal of Sedimentary Petrology*, 44(I), 242–248.
- Droppo, I. G. (2004). Structural controls on floc strength and transport. *Canadian Journal of Civil Engineering*, 31(4), 569–578. <https://doi.org/10.1139/L04-015>
- Duarte, C. M. (1991). Variance and the description of nature. In J. Cole, G. Lovett, & S. Findlay (Eds.), *Comparative ecology of ecosystems: Patterns, mechanisms and theories*. (pp. 301–318). Springer-Verlag.

- Duarte, C. M., Fourqurean, J. W., Krause-Jensen, D., & Olesen, B. (2006). Dynamics of seagrass stability and change. In A. W. D. Larkum, R. J. Orth, & C. M. Duarte (Eds.), *Seagrasses: Biology, ecology and conservation* (pp. 271–294). Springer.
- Fahrig, L. (2003). Effects of habitat fragmentation on biodiversity. *Annual Review of Ecology, Evolution, and Systematics*, 34, 487–515. <https://doi.org/10.1146/132419>
- Fonseca, M. S., & Bell, S. S. (1998). Influence of physical setting on seagrass landscapes. *Marine Ecology Progress Series*, 171, 109–121. <https://doi.org/10.3354/meps171109>
- Fonseca, M. S., & Fisher, J. S. (1986). A comparison of canopy friction and sediment movement between four species of seagrass with reference to their ecology and restoration. *Marine Ecology Progress Series*, 29(15–22), 15–22. <https://doi.org/10.3354/meps029015>
- Fonseca, M. S., Fisher, J. S., Zieman, J. C., & Thayer, G. W. (1982). Influence of the seagrass, *Zostera marina* L., on current flow. *Estuarine, Coastal and Shelf Science*, 15(4), 351–364. [https://doi.org/10.1016/0272-7714\(82\)90046-4](https://doi.org/10.1016/0272-7714(82)90046-4)
- Fonseca, M. S., Zieman, J. C., Thayer, G. W., & Fisher, J. S. (1983). The role of current velocity in structuring eelgrass (*Zostera marina* L.) meadows. *Estuarine, Coastal and Shelf Science*, 17(4), 367–380. [https://doi.org/10.1016/0272-7714\(83\)90123-3](https://doi.org/10.1016/0272-7714(83)90123-3)
- Fourqurean, J. W., Duarte, C. M., Kennedy, H., Marbà, N., Holmer, M., Mateo, M. A., Apostolaki, E. T., Kendrick, G. A., Krause-Jensen, D., & Serrano, O. (2012). Seagrass ecosystems as a globally significant carbon stock. *Nature Geoscience*, 5, 505–509. <https://doi.org/10.1038/ngeo1477>
- Froelich, P. N. (1980). Analysis of organic carbon in marine sediments. *Limnology and Oceanography*, 25(3), 564–572. <https://doi.org/10.4319/lo.1980.25.3.0564>
- González-Ortiz, V., Egea, L. G., Jiménez-Ramos, R., Moreno-Marín, F., Pérez-Lloréns, J. L., Bouma, T., & Brun, F. (2016). Submerged vegetation complexity modifies benthic infauna communities: the hidden role of the belowground system. *Marine Ecology*, 37(3), 543–552. <https://doi.org/10.1111/maec.12292>
- Goshima, S., & Peterson, C. H. (2012). Both below- and aboveground shoalgrass structure influence whelk predation on hard clams. *Marine Ecology Progress Series*, 451, 75–92. <https://doi.org/10.3354/meps09587>
- Greiner, J. T., McGlathery, K. J., Gunnell, J., & McKee, B. A. (2013). Seagrass restoration enhances “Blue Carbon” sequestration in coastal waters. *PLoS ONE*, 8(8), 1–8. <https://doi.org/10.1371/journal.pone.0072469>
- Greve, T. M., Krause-Jensen, D., Rasmussen, M. B., & Christensen, P. B. (2005). Means of rapid eelgrass (*Zostera marina* L.) recolonisation in former dieback areas. *Aquatic Botany*, 82, 143–156. <https://doi.org/10.1016/j.aquabot.2005.03.004>
- Hassink, J. (1995). Decomposition rate constants of size and density fractions of Soil organic matter. *Soil Science Society of America Journal*, 59(6), 1631–1635. <https://doi.org/10.2136/sssaj1995.03615995005900060018x>

- Hemingway, J. D., Rothman, D. H., Grant, K. E., Rosengard, S. Z., Eglinton, T. I., Derry, L. A., & Galy, V. V. (2019). Mineral protection regulates long-term global preservation of natural organic carbon. *Nature*, 570(7760), 228–231. <https://doi.org/10.1038/s41586-019-1280-6>
- Howard, J., Sutton-Grier, A. E., Smart, L. S., Lopes, C.C., Hamilton, J., Kleypas, J., Simpson, S., McGowan, J., Pessarrodona, A., Alleway, H. K., & Landis, E. (2023). Blue carbon pathways for climate mitigation: Known, emerging, and unlikely. *Marine Policy*, 156. <https://doi.org/10.1016/j.marpol.2023.105788>.
- Infantes, E., Orfila, A., Simarro, G., Terrados, J., Luhar, M., & Nepf, H. (2012). Effect of a seagrass (*Posidonia oceanica*) meadow on wave propagation. *Marine Ecology Progress Series*, 456, 63–72. <https://doi.org/10.3354/meps09754>
- Johnson, A. J., Shields, E. C., Kendrick, G. A., & Orth, R. J. (2021). Recovery dynamics of the seagrass *Zostera marina* following mass mortalities from two extreme climatic events. *Estuaries and Coasts*, 44(2), 535–544. <https://doi.org/10.1007/s12237-020-00816-y>
- Jones, C. G., Lawton, J. H., Shachak, M., & Organisms, M. (1994). Organisms as ecosystem engineers. *Oikos*, 69(3), 373–386. <https://doi.org/10.2307/3545850>
- Keil, R. G., & Hedges, J. I. (1993). Sorption of organic matter to mineral surfaces and the preservation of organic matter in coastal marine sediments. *Chemical Geology*, 107(3–4), 385–388. [https://doi.org/10.1016/0009-2541\(93\)90215-5](https://doi.org/10.1016/0009-2541(93)90215-5)
- Kendrick, G. A., Waycott, M., Carruthers, T. J., Cambridge, M. L., Hovey, R., Krauss, S. L., ... & Verduin, J. J. (2012). The central role of dispersal in the maintenance and persistence of seagrass populations. *Bioscience*, 62(1), 56–65. <https://doi.org/10.1525/bio.2012.62.1.10>
- Kennedy, H., Pagès, J. F., Lagomasino, D., Arias-Ortiz, A., Colarusso, P., Fourqurean, J. W., Githaiga, M. N., Howard, J. L., Krause-Jensen, D., Kuwae, T., Lavery, P. S., Macreadie, P. I., Marbà, N., Masqué, P., Mazarrasa, I., Miyajima, T., Serrano, O., & Duarte, C. M. (2022). Species traits and geomorphic setting as rivers of global soil carbon stocks in seagrass meadows. *Global Biogeochemical Cycles*, 1–18. <https://doi.org/10.1029/2022gb007481>
- Kobayashi, N., Raichle, A. W., & Asano, T. (1993). Wave attenuation by vegetation. *Journal of Waterway, Port, Coastal, and Ocean Engineering*, 119(1), 30–48. [https://doi.org/10.1061/\(ASCE\)0733-950X\(1993\)119:1\(30\)](https://doi.org/10.1061/(ASCE)0733-950X(1993)119:1(30))
- Lafratta, A., Serrano, O., Masqué, P., Mateo, M. A., Fernandes, M., Gaylard, S., & Lavery, P. S. (2020). Challenges to select suitable habitats and demonstrate ‘additionality’ in Blue Carbon projects: A seagrass case study. *Ocean and Coastal Management*, 197. <https://doi.org/10.1016/j.ocecoaman.2020.105295>
- Lavery, P. S., Mateo, M. A., Serrano, O., & Rozaimi, M. (2013). Variability in the carbon storage of seagrass habitats and its implications for global estimates of blue carbon ecosystem service. *PLoS ONE*, 8(9). <https://doi.org/10.1371/journal.pone.0073748>
- Lei, J., Schaefer, R., Colarusso, P., Novak, A., Simpson, J. C., Masqué, P., & Nepf, H. (2023). Spatial heterogeneity in sediment and carbon accretion rates within a seagrass meadow

- correlated with the hydrodynamic intensity. *Science of the Total Environment*, 854(April 2022). <https://doi.org/10.1016/j.scitotenv.2022.158685>
- Licci, S., Nepf, H., Delolme, C., Marmonier, P., Bouma, T. J., & Puijalon, S. (2019). The role of patch size in ecosystem engineering capacity: a case study of aquatic vegetation. *Aquatic Sciences*, 81(3), 1–11. <https://doi.org/10.1007/s00027-019-0635-2>
- Lindenmayer, D. B., & Fischer, J. (2007). Tackling the habitat fragmentation panchreston. *Trends in Ecology and Evolution*, 22(3), 127–132. <https://doi.org/10.1016/j.tree.2006.11.006>
- Lindgren, F., Rue, H., & Lindström, J. (2011). An explicit link between Gaussian fields and Gaussian Markov random fields: The stochastic partial differential equation approach. *Journal of the Royal Statistical Society. Series B: Statistical Methodology*, 73(4), 423–498. <https://doi.org/10.1111/j.1467-9868.2011.00777.x>
- Lowe, R. J., Koseff, J. R., & Monismith, S. G. (2005). Oscillatory flow through submerged canopies: 1. Velocity structure. *J. Geophys. Res.: Oceans*, 110(C10). <https://doi.org/10.1029/2004JC002788>
- Luhar, M., Rominger, J., & Nepf, H. (2008). Interaction between flow, transport and vegetation spatial structure. *Environmental Fluid Mechanics*, 8, 423–439. <https://doi.org/10.1007/s10652-008-9080-9>
- Macreadie, P. I., Trevathan-Tackett, S. M., Skilbeck, C. G., Sanderman, J., Curlevski, N., Jacobsen, G., & Seymour, J. R. (2015). Losses and recovery of organic carbon from a seagrass ecosystem following disturbance. *Proceedings of the Royal Society B: Biological Sciences*, 282(1817). <https://doi.org/10.1098/rspb.2015.1537>
- Marbà, N., Arias-Ortiz, A., Masqué, P., Kendrick, G. A., Mazarrasa, I., Bastyan, G. R., Garcia-Orellana, J., & Duarte, C. M. (2015). Impact of seagrass loss and subsequent revegetation on carbon sequestration and stocks. *Journal of Ecology*, 103(2), 296–302. <https://doi.org/10.1111/1365-2745.12370>
- Marro, J., & Dickman, R. (1999). The contact process. In *Nonequilibrium phase transitions in lattice models* (pp. 161–188). Cambridge University Press. <https://doi.org/10.1017/cbo9780511524288.007>
- Mazarrasa, I., Lavery, P., Duarte, C. M., Lafratta, A., Lovelock, C. E., Macreadie, P. I., Samper-Villarreal, J., Salinas, C., Sanders, C. J., Trevathan-Tackett, S., Young, M., Steven, A., & Serrano, O. (2021). Factors determining seagrass blue carbon across bioregions and geomorphologies. *Global Biogeochemical Cycles*, 35(6), 1–17. <https://doi.org/10.1029/2021GB006935>
- McPhee, M. G. (2002). Turbulent stress at the ice/ocean interface and bottom surface hydraulic roughness during the SHEBA drift. *Journal of Geophysical Research: Oceans*, 107(10), 1–15. <https://doi.org/10.1029/2000jc000633>
- Meysick, L., Infantes, E., & Boström, C. (2019). The influence of hydrodynamics and ecosystem engineers on eelgrass seed trapping. *PLoS ONE*, 14(9), 1–17. <https://doi.org/10.1371/journal.pone.0222020>

- Moksnes, P. O., Röhr, M. E., Holmer, M., Eklöf, J. S., Eriander, L., Infantes, E., & Boström, C. (2021). Major impacts and societal costs of seagrass loss on sediment carbon and nitrogen stocks. *Ecosphere*, 12(7). <https://doi.org/10.1002/ecs2.3658>
- Norkko, J., & Shumway, S. E. (2011). Biovalves as bioturbators and bioirrigators. In S. E. Shumway (Ed.), *Shellfish aquaculture and the environment* (pp. 297–317). John Wiley & Sons, Inc. <https://doi.org/10.1002/9780470960967.ch10>
- Novak, A. B., Pelletier, M. C., Colarusso, P., Simpson, J., Gutierrez, M. N., Arias-Ortiz, A., Charpentier, M., Masque, P., & Vella, P. (2020). Factors influencing carbon stocks and accumulation rates in eelgrass meadows across New England, USA. *Estuaries and Coasts*, 43(8), 2183–2184. <https://doi.org/10.1007/s12237-020-00815-z>
- Oborny, B., Szabó, G., & Meszéna, G. (2007). Survival of species in patchy landscapes: percolation in space and time. In D. Storch, P. Marquet, & J. Brown (Eds.), *Scaling biodiversity* (pp. 409–440). Cambridge University Press. <https://doi.org/10.1017/cbo9780511814938.022>
- Olesen, B., Krause-Jensen, D., & Christensen, P. B. (2017). Depth-Related Changes in Reproductive Strategy of a Cold-Temperate *Zostera marina* Meadow. *Estuaries and Coasts*, 40(2), 553–563. <https://doi.org/10.1007/s12237-016-0155-4>
- Oreska, M. P. J., McGlathery, K. J., & Porter, J. H. (2017). Seagrass blue carbon spatial patterns at the meadow-scale. *PLoS ONE*, 12(4), 1–18. <https://doi.org/10.1371/journal.pone.0176630>
- Orth, R. J., Carruthers, T. J. B., Dennison, W. C., Duarte, C. M., Fourqurean, J. W., Heck, K. L., Hughes, A. R., Kendrick, G. A., Kenworthy, W. J., Olyarnik, S., Short, F. T., Waycott, M., & Williams, S. L. (2006). A global crisis for seagrass ecosystems. *BioScience*, 56(12), 987–996. [https://doi.org/10.1641/0006-3568\(2006\)56\[987:agcfse\]2.0.co;2](https://doi.org/10.1641/0006-3568(2006)56[987:agcfse]2.0.co;2)
- Orth, R., Luckenbach, M., & Moore, K. A. (1994). Seed dispersal in a marine macrophyte: Implications for colonization and restoration. *Ecology*, 75(7), 1927–1939. <https://doi.org/10.2307/1941597>
- Orth, R. J., Lefcheck, J. S., McGlathery, K. S., Aoki, L., Luckenbach, M. W., Moore, K. A., Oreska, M. P. J., Snyder, R., Wilcox, D. J., & Lusk, B. (2020). Restoration of seagrass habitat leads to rapid recovery of coastal ecosystem services. *Science Advances*, 6(41), 1–9. <https://doi.org/10.1126/sciadv.abc6434>
- Pendleton, L., Donato, D. C., Murray, B. C., Crooks, S., Jenkins, W. A., Sifleet, S., Craft, C., Fourqurean, J. W., Kauffman, J. B., Marbà, N., Megonigal, P., Pidgeon, E., Herr, D., Gordon, D., & Baldera, A. (2012). Estimating global “blue carbon” emissions from conversion and degradation of vegetated coastal ecosystems. *PLoS ONE*, 7(9). <https://doi.org/10.1371/journal.pone.0043542>
- Plus, M., Deslous-Paoli, J. M., & Dagault, F. (2003). Seagrass (*Zostera marina* L.) bed recolonisation after anoxia-induced full mortality. *Aquatic Botany*, 77(2), 121–134. [https://doi.org/10.1016/S0304-3770\(03\)00089-5](https://doi.org/10.1016/S0304-3770(03)00089-5)

- Pribyl, D. W. (2010). A critical review of the conventional SOC to SOM conversion factor. *Geoderma*, 156, 75–83. <https://doi.org/10.1016/j.geoderma.2010.02.003>
- R Core Team (2024). R: A language and environment for statistical computing. R Foundation for Statistical Computing, Vienna, Austria. URL <https://www.R-project.org/>.
- Raupach, M. R., Finnigan, J. J., & Brunet, Y. (1996). Coherent eddies and turbulence in vegetation canopies: the mixing-layer analogy. *Boundary-Layer Meteorology*, 78(3–4), 351–382. <https://doi.org/10.1007/BF00120941>
- Ricart, A. M., Pérez, M., & Romero, J. (2017). Landscape configuration modulates carbon storage in seagrass sediments. *Estuarine, Coastal and Shelf Science*, 185, 69–76. <https://doi.org/10.1016/j.ecss.2016.12.011>
- Ricart, A. M., York, P. H., Rasheed, M. A., Pérez, M., Romero, J., Bryant, C. V., & Macreadie, P. I. (2015). Variability of sedimentary organic carbon in patchy seagrass landscapes. *Marine Pollution Bulletin*, 100(1), 476–482. <https://doi.org/10.1016/j.marpolbul.2015.09.032>
- Rue, H., Martino, S., & Chopin, N. (2009). Approximate Bayesian inference for latent Gaussian models by using integrated nested Laplace approximations. *Journal of the Royal Statistical Society. Series B: Statistical Methodology*, 71(2), 319–392. <https://doi.org/10.1111/j.1467-9868.2008.00700.x>
- Samper-Villarreal, J., Lovelock, C. E., Saunders, M. I., Roelfsema, C., & Mumby, P. J. (2016). Organic carbon in seagrass sediments is influenced by seagrass canopy complexity, turbidity, wave height, and water depth. *Limnology and Oceanography*, 61(3), 938–952. <https://doi.org/10.1002/lno.10262>
- Scheef, L. P., & Marcus, N. H. (2011). Mechanisms for copepod resting egg accumulation in seagrass sediments. *Limnology and Oceanography*, 56(1), 363–370. <https://doi.org/10.4319/lo.2011.56.1.0363>
- Serrano, O., Arias-Ortiz, A., Duarte, C. M., Kendrick, G. A., & Lavery, P. S. (2021). Impact of marine heatwaves on seagrass ecosystems. In J. G. Canadell & R. B. Jackson (Eds.), *Ecosystem collapse and climate change* (pp. 345–364). Springer Nature Switzerland. https://doi.org/10.1007/978-3-030-71330-0_13
- Serrano, O., Lavery, P. S., Duarte, C. M., Kendrick, G. A., Calafat, A., York, P. H., Steven, A., & Macreadie, P. I. (2016). Can mud (silt and clay) concentration be used to predict soil organic carbon content within seagrass ecosystems? *Biogeosciences*, 13, 4915–4926. <https://doi.org/10.5194/bg-13-4915-2016>
- Sogin, E. M., Michellod, D., Gruber-Vodicka, H. R., Bourceau, P., Geier, B., Meier, D. V., Seidel, M., Ahmerkamp, S., Schorn, S., D’Angelo, G., Procaccini, G., Dubilier, N., & Liebeke, M. (2022). Sugars dominate the seagrass rhizosphere. *Nature Ecology and Evolution*, 6(7), 866–877. <https://doi.org/10.1038/s41559-022-01740-z>
- Stauffer, D., & Aharony, A. (1985). *Introduction to percolation theory* (Rev 2nd ed). Taylor & Francis Inc.

- Sutherland, B. R., Barrett, K. J., & Gingras, M. K. (2015). Clay settling in fresh and salt water. *Environmental Fluid Mechanics*, 15(1), 147–160. <https://doi.org/10.1007/s10652-014-9365-0>
- Unsworth, R. K. F., McKenzie, L. J., Collier, C. J., Cullen-Unsworth, L. C., Duarte, C. M., Eklöf, J. S., Jarvis, J. C., Jones, B. L., & Nordlund, L. M. (2019). Global challenges for seagrass conservation. *Ambio*, 48(8), 801–815. <https://doi.org/10.1007/s13280-018-1115-y>
- van Wesenbeeck, B. K., van De Koppel, J., Herman, P. M. J., & Bouma, T. J. (2008). Does scale-dependent feedback explain spatial complexity in salt-marsh ecosystems? *Oikos*, 117(1), 152–159. <https://doi.org/10.1111/j.2007.0030-1299.16245.x>
- Volkenborn, N., Meile, C., Polerecky, L., Pilditch, C. A., Norkko, A., Norkko, J., Hewitt, J. E., Thrush, S. F., Wethey, D. S., & Woodin, S. A. (2012). Intermittent bioirrigation and oxygen dynamics in permeable sediments: An experimental and modeling study of three tellinid bivalves. *Journal of Marine Research*, 70(6), 794–823. <https://doi.org/10.1357/002224012806770955>
- Warry, F. Y., Hindell, J. S., Macreadie, P. I., Jenkins, G. P., & Connolly, R. M. (2009). Integrating edge effects into studies of habitat fragmentation: A test using meiofauna in seagrass. *Oecologia*, 159(4), 883–892. <https://doi.org/10.1007/s00442-008-1258-9>
- Waycott, M., Duarte, C. M., Carruthers, T. J. B., Orth, R. J., Dennison, W. C., Olyarnik, S., Calladine, A., Fourqurean, J. W., Heck, K. L., Hughes, A. R., Kendrick, G. A., Kenworthy, W. J., Short, F. T., & Williams, S. L. (2009). Accelerating loss of seagrasses across the globe threatens coastal ecosystems. *Proceedings of the National Academy of Sciences of the United States of America*, 106(30), 12377–12381. <https://doi.org/10.1073/pnas.0905620106>
- Wu, J. (2004). Effects of changing scale on landscape pattern analysis: Scaling relations. *Landscape Ecology*, 19(2), 125–138. <https://doi.org/10.1023/B:LAND.0000021711.40074.ae>

7.8 Supplementary Information

7.8.1 Details of ^{210}Pb and ^{137}Cs methodology

To obtain estimates of sediment mass accumulation rates, a subsample from each sediment core slice was sent to the Virginia Institute of Marine Science Geochronology Lab for tracer analysis of ^{210}Pb and ^{137}Cs radionuclides using gamma spectrometry (Canberra GL 2020 Low Energy

Germanium detector). The samples were packed into Petri dishes and sealed with electrical tape and paraffin wax 30 days prior to analysis to allow for equilibration between ^{226}Ra and its daughter isotopes, ^{214}Pb and ^{214}Bi (Martz & Langner, Jr, 1991). The activities of ^{214}Pb and ^{214}Bi were used to determine the background levels of ^{210}Pb . Total ^{210}Pb activities (the sum of background and excess ^{210}Pb) were corrected for detector efficiency and self-attenuation using the point-source method (Cutshall et al., 1983). Concentrations of excess ^{210}Pb used to obtain age models were determined as the difference between total ^{210}Pb and background ^{210}Pb . Constant flux-constant sedimentation (CFCS; Corbett & Walsh, 2015) and constant rate of supply (CRS; Appleby & Oldfield, 1978) models were used to calculate sedimentation rates.

The ^{210}Pb laboratory analysis of sediment core samples was complemented by ^{137}Cs activity measurements. ^{137}Cs is a bomb-produced radionuclide commonly used to verify sediment accumulation rates determined by ^{210}Pb geochronology (Nittrouer et al., 1984; Ritchie & McHenry, 1990). Peak ^{137}Cs activity was assumed to have occurred in 1963 (Pennington et al., 1973), as has been measured elsewhere in the northern hemisphere (Ritchie & McHenry, 1990), but no strong peaks were detected in the sediment core ^{137}Cs activity profiles.

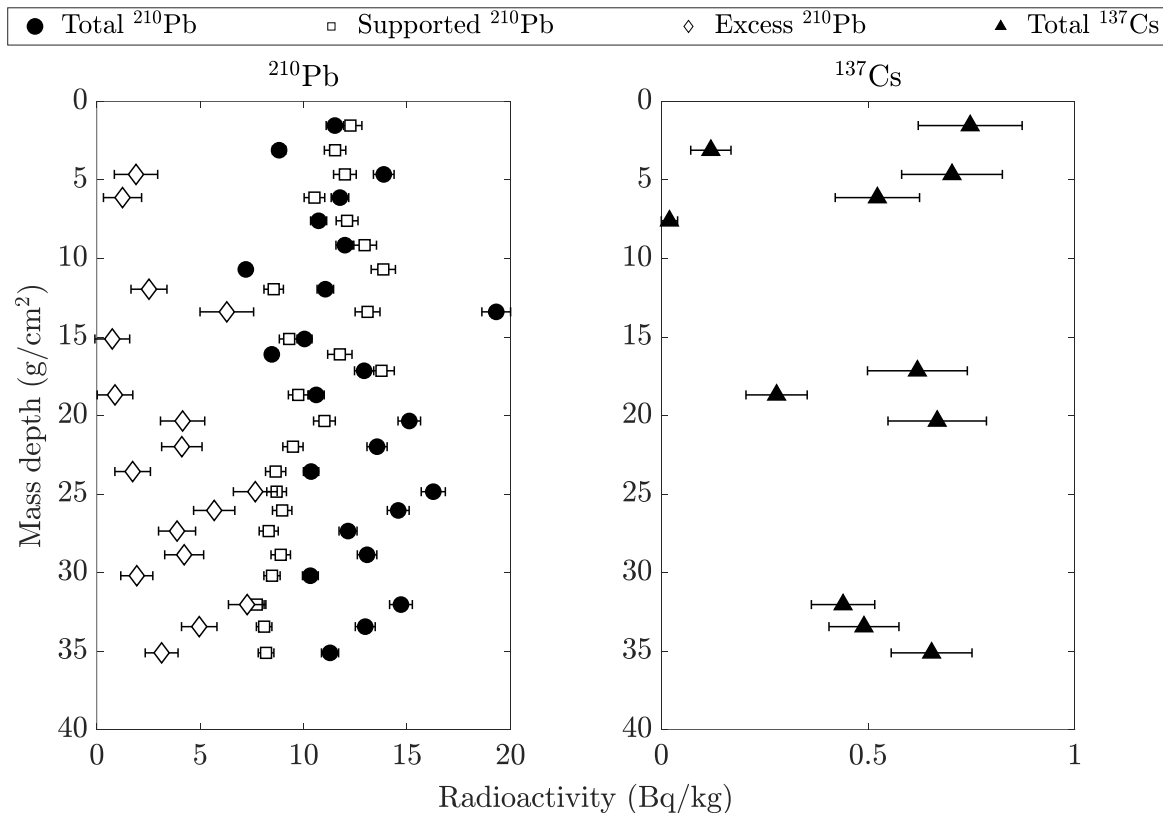


Figure 7.S.1: Profiles of total, supported, and excess ^{210}Pb as well as total ^{137}Cs over cumulative mass depth for station S4B.

References

- Appleby, P. G., & Oldfield, F. (1978). The calculation of lead-210 dates assuming a constant rate of supply of unsupported ^{210}Pb to the sediment. *Catena*, 5, 1–8. [https://doi.org/10.1016/S0341-8162\(78\)80002-2](https://doi.org/10.1016/S0341-8162(78)80002-2)
- Cutshall, N. H., Larsen, I. L., & Olsen, C. R. (1983). Direct analysis of ^{210}Pb in sediment samples: Self-absorption corrections. *Nuclear Instruments and Methods In Physics Research*, 206, 309–312. [https://doi.org/10.1016/0167-5087\(83\)91273-5](https://doi.org/10.1016/0167-5087(83)91273-5)
- Martz, D. E., & Langner, Jr, G. H. (1991). Half-lives of ^{214}Pb and ^{214}Bi . *Health Physics*, 61(4), 511–518. <https://doi.org/10.1097/00004032-199110000-00006>
- Nittrouer, C. A., DeMaster, D. J., McKee, B. A., Cutshall, N. H., & Larsen, I. L. (1984). The effect of sediment mixing on Pb-210 accumulation rates for the Washington continental shelf. *Marine Geology*, 54(3–4), 201–221. [https://doi.org/10.1016/0025-3227\(84\)90038-0](https://doi.org/10.1016/0025-3227(84)90038-0)
- Pennington, W., Cambray, R. S., & Fisher, E. M. (1973). Observations on lake sediments using fallout ^{137}Cs as a tracer. *Nature*, 242(5396), 324–326. <https://doi.org/10.1038/242324a0>

Reide Corbett, D., & Walsh, J. P. (2015). 210Lead and 137Cesium: Establishing a chronology for the last century. *Handbook of Sea-Level Research*, 361–372. <https://doi.org/10.1002/9781118452547.ch24>

Ritchie, J. C., & McHenry, J. R. (1990). Application of radioactive fallout Cesium-137 for measuring soil erosion and sediment accumulation rates and patterns: A review. *Journal of Environmental Quality*, 19(2), 215–233. <https://doi.org/10.2134/jeq1990.00472425001900020006x>

7.8.2 Velocity measurement processing details

The velocities within and above a meadow of vegetation can be described using a two-layer model (e.g., Huthoff et al., 2007). Combining layer-averaged continuity and momentum conservation, the time-mean velocity in the meadow is (Chen et al., 2013; Lei & Nepf, 2021)

$$U_1 = \frac{U_\infty}{1 - \frac{h_d}{D} \phi + \sqrt{\frac{C_{D,b} a_{v,b} (l_{s,eq} + l_e)}{2C(1 - \phi)} \left(\frac{D - h_d}{D}\right)^3}}. \quad (7.8.2.1)$$

with depth-averaged velocity U_∞ , total water depth D , deflected canopy height h_d , and drag coefficient C_D . The frontal area per canopy volume, a_v , was estimated by assuming each shoot consisted of n_b flexible blades, each of length l_b , extending from a rigid sheath of length l_s , with both blades and sheath having the same width w_b . For m_p shoots per unit bed area, in the blade region of the shoot $a_{v,b} = n_b m_p w_b$, while in the sheath region of the shoot $a_{v,s} = m_p w_b$. Shoot densities m_p were based on five 0.0625 m² quadrats randomly placed near each sediment core location, and shoot dimensions were based on measurements of five shoots randomly removed from around each sediment core location. See Table 7.S.1 for the measurements.

We calculated an adjusted sheath length $l_{s,eq}$ that had an equivalent $C_D a_v$ to that of the blades (Lei & Nepf, 2019b). As the width w_b was the same for both sheath and blade, $C_{D,b} n_b l_{s,eq} = C_{D,s} l_s$, in which $C_{D,b}$ is the blade drag coefficient and $C_{D,s}$ is the sheath drag coefficient. We assumed $C_{D,s} = 1$ for the cylindrical sheath and $C_{D,b} = 2$ for the rectangular blades (Vogel, 1994). ϕ is the shoot solid volume fraction. For seagrasses, the value is small enough, $\phi = 0.004$ to 0.04 (as summarized in Zhang et al., 2020), that we assume $\phi = 0$ for simplicity. $C = K_c (\delta_e/D)^{1/3}$ is a friction coefficient which characterizes the turbulent stress at the top of the canopy (Huthoff et al., 2007; Konings et al., 2012). The length scale δ_e is the vertical distance into the canopy over which canopy-scale turbulent eddies penetrate. In shallow water, $D/h_d < 2$, $\delta_e = 0.23 \left(\frac{D}{h_d} - 1 \right) (C_D a_v)^{-1}$, and otherwise $\delta_e = 0.23 (C_D a_v)^{-1}$ (Chen et al., 2013; Nepf et al., 2007). The empirical factor $K_c = 0.07 \pm 0.02$ (Chen et al., 2013). To apply Eqn. 7.8.2.1, we defined U_∞ as the average peak tidal velocity $\overline{U_{c,peak}}$.

The deflection of the blades in response to flow both reduces the cross-sectional area of the shoot exposed to the direction of flow and streamlines the shoot, both of which reduce the drag on the shoot relative to a rigid shoot of the same length (de Langre, 2008). The deflected canopy height, h_d , captures the first but not the second of these responses to the flow (Luhar & Nepf, 2013). To capture both responses, the concept of an effective length l_e has been defined as the length of a rigid blade that experiences the same magnitude of drag experienced by a flexible blade of a certain length l_b (see Luhar & Nepf, 2011, 2016). Effective lengths can be predicted using the Cauchy number, which is the dimensionless ratio of hydrodynamic forces on a shoot to restoring forces due to shoot stiffness. The Cauchy number is defined as $Ca = C_D w_b l_b^3 U^2 /$

$(2EI)$, in which U is a characteristic velocity, E is the Young's modulus of elasticity, and $I = w_b t_b^3/12$ is the bending moment of inertia for the blade, in which t_b is the blade thickness.

When considering combined wave-current conditions, such as occurs at Norwood Heights Beach, a wave-current Cauchy number, Ca_{wc} , is defined using a characteristic velocity that is based on the time-averaged drag force over a wave period, $U^2 = U_1^2 + \frac{1}{2}U_w^2$, in which U_w is the wave velocity amplitude (Lei & Nepf, 2019a). Based on scaling arguments supported by measurements (Lei and Nepf 2019a), the effective length is predicted as $l_e = 0.9l_b(Ca_{wc})^{-1/3}$. U_w was defined as $U_w = \sqrt{2}U_{w,RMS}$, in which $U_{w,RMS}$ was the average of peak hourly root-mean-squared velocities during each tidal cycle over the 2-week measurement period. E for the flexible leaves was assumed to be 0.3 GPa based on reported measurements of *Zostera marina* shoots (Fonseca et al., 2007; Ghisalberti, 2002). The mean meadow deflected heights at the meadow stations (h_d in Eqn. 7.8.2.1) were estimated using an empirical fit of h_d versus Cauchy number given in Eqn. 4 in Luhar & Nepf, 2013, and then adding in the lengths of the assumed rigid sheaths. As the Cauchy number depends on U_1 , Eqn. 7.8.2.1 was numerically iterated until convergence (until U_1 and h_d reached approximately constant values) starting from an initial guess of $U_1 = \overline{U_{c,peak}}$ and $h_d = l_b + l_s$. While based on several assumptions, these calculations provide a reasonable approximation of the peak tidal velocities within the meadow patches.

References:

- Alben, S., Shelley, M., & Zhang, J. (2002). Drag reduction through self-similar bending of a flexible body. *Nature*, 420, 479–481. <https://doi.org/10.1038/nature01232>
- Chen, Z., Jiang, C., & Nepf, H. (2013). Flow adjustment at the leading edge of a submerged aquatic canopy. *Water Resources Research*, 49(9), 5537–5551. <https://doi.org/10.1002/wrcr.20403>

- de Langre, E. (2008). Effects of wind on plants. *Annual Review of Fluid Mechanics*, 40, 141–168. <https://doi.org/10.1146/annurev.fluid.40.111406.102135>
- Fonseca, M. S., Koehl, M. A. R., & Kopp, B. S. (2007). Biomechanical factors contributing to self-organization in seagrass landscapes. *Journal of Experimental Marine Biology and Ecology*, 340(2), 227–246. <https://doi.org/10.1016/j.jembe.2006.09.015>
- Ghisalberti, M. (2002). Mixing layers and coherent structures in vegetated aquatic flows. *Journal of Geophysical Research*, 107(C2). <https://doi.org/10.1029/2001jc000871>
- Huthoff, F., Augustijn, D. C. M., & Hulscher, S. J. M. H. (2007). Analytical solution of the depth-averaged flow velocity in case of submerged rigid cylindrical vegetation. *Water Resources Research*, 43(6), 1–10. <https://doi.org/10.1029/2006WR005625>
- Konings, A. G., Katul, G. G., & Thompson, S. E. (2012). A phenomenological model for the flow resistance over submerged vegetation. *Water Resources Research*, 48(2), 1–9. <https://doi.org/10.1029/2011WR011000>
- Lei, J., & Nepf, H. (2021). Evolution of flow velocity from the leading edge of 2-D and 3-D submerged canopies. *Journal of Fluid Mechanics*, 916, 1–27. <https://doi.org/10.1017/jfm.2021.197>
- Lei, J., & Nepf, H. M. (2019a). Blade dynamics in combined waves and current. *Journal of Fluids and Structures*, 87, 137–149. <https://doi.org/10.1016/j.jfluidstructs.2019.03.020>
- Lei, J., & Nepf, H. M. (2019b). Wave damping by flexible vegetation: Connecting individual blade dynamics to the meadow scale. *Coastal Engineering*, 147(October 2018), 138–148. <https://doi.org/10.1016/j.coastaleng.2019.01.008>
- Luhar, M., & Nepf, H. M. (2011). Flow-induced reconfiguration of buoyant and flexible aquatic vegetation. *Limnology and Oceanography*, 56(6), 2003–2017. <https://doi.org/10.4319/lo.2011.56.6.2003>
- Luhar, M., & Nepf, H. M. (2013). From the blade scale to the reach scale: A characterization of aquatic vegetative drag. *Advances in Water Resources*, 51, 305–316. <https://doi.org/10.1016/j.advwatres.2012.02.002>
- Luhar, M., & Nepf, H. M. (2016). Wave-induced dynamics of flexible blades. *Journal of Fluids and Structures*, 61, 20–41. <https://doi.org/10.1016/j.jfluidstructs.2015.11.007>
- Nepf, H., Ghisalberti, M., White, B., & Murphy, E. (2007). Retention time and dispersion associated with submerged aquatic canopies. *Water Resources Research*, 43(4), 1–10. <https://doi.org/10.1029/2006WR005362>
- Vogel, S. (1994). *The Drag of Simple Shapes and Sessile Systems. In Life in Moving Fluids.* Princeton University Press. <https://doi.org/10.2307/j.ctvzsmfc6.10>
- Zhang, J., Lei, J., Huai, W., & Nepf, H. (2020). Turbulence and particle deposition under steady flow along a submerged seagrass meadow. *Journal of Geophysical Research: Oceans*, 125, 1–19. <https://doi.org/10.1029/2019JC015985>

7.8.3 Historical imagery sources

Table 7.S.1: List of year, time of year, and source of curated historical imagery used in the study.

Year	Month	Source
1972	May	USGS Aerial Photo Single Frame Records collection
1975	October	USGS Aerial Photo Single Frame Records collection
1978	April	USGS Aerial Photo Single Frame Records collection
1982	March	USGS Aerial Photo Single Frame Records collection
1995	March	NAPP
2001	Spring	MassGIS
2002	August	Maxar Technologies
2005	March	MassGIS
2008	July	NAIP
2010	June	Google
2011	Spring	MassGIS
2013	August	Google
2014	July	NAIP
2015	June	Google
2016	May	Google
2017	April	Planet
2018	April	NAIP
2019	Spring	MassGIS
2020	May	Planet
2021	October	Google
2022	July	Drone flight orthomosaic

7.8.4 Differences in delineated vegetated pixels over time

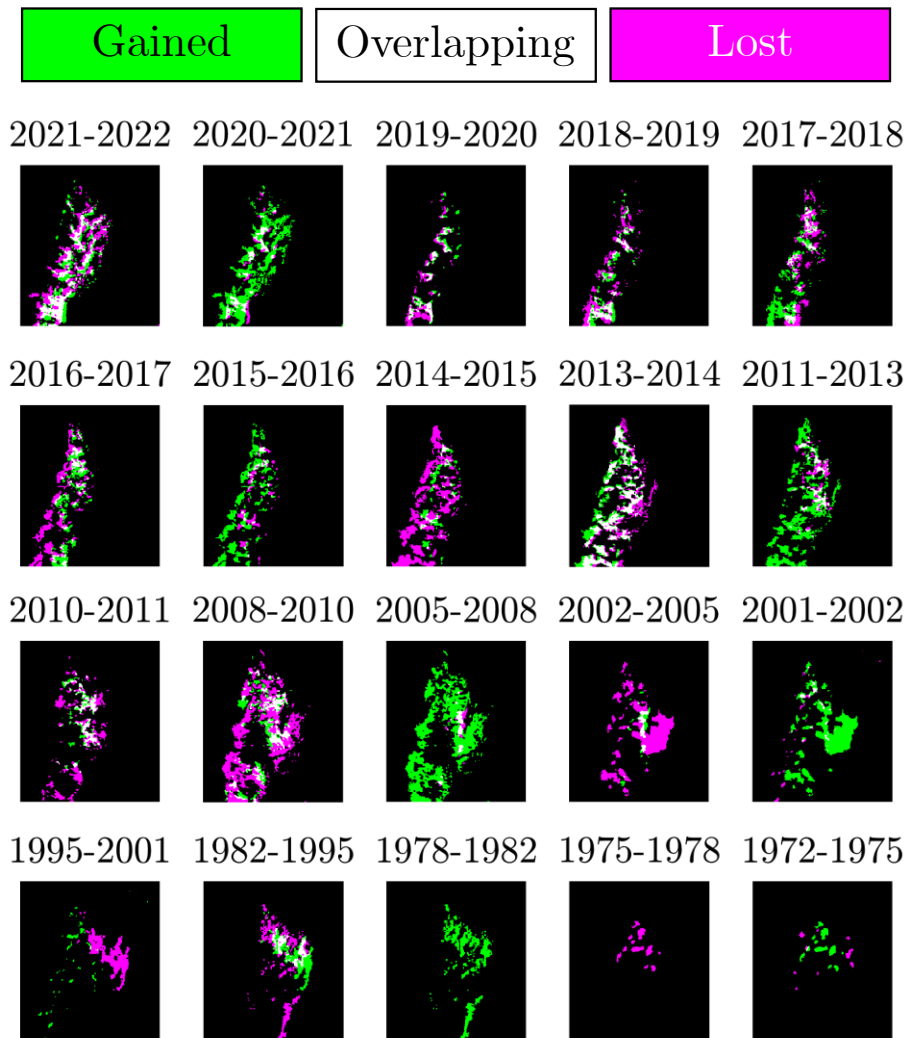


Figure 7.S.2: Differences in delineated vegetated pixels between chronologically successive images within the collection of historical images. Pink areas denote areas present in the earlier image but not in the later image. Green areas denote areas present in the later image but not in the earlier image. White regions denote regions of overlap between the two images.

7.8.5 Total meadow area delineation example

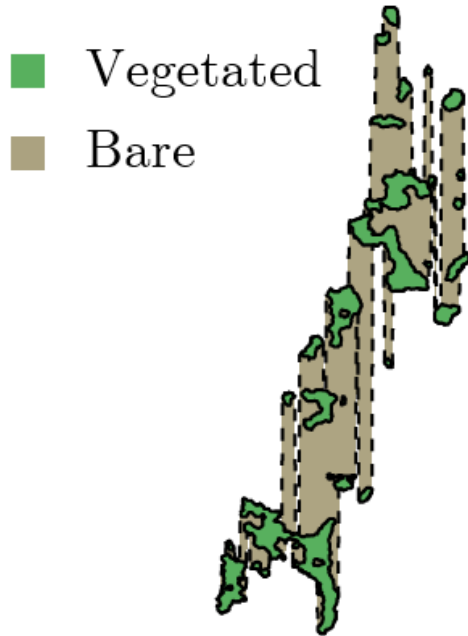


Figure 7.S.3: Example delineation of the total area of a meadow *A*. Green pixels are pixels delineated as vegetated. The dashed black lines connect the vegetated patches to create a boundary around the meadow. The brown pixels denote bare pixels contained within the boundaries.

7.8.6 Seagrass meadow density and morphology measurements

Table 7.S.2: Seagrass meadow density and morphological characteristics measured in July, 2022 at the vegetated stations. m_p is the average shoot density per unit area, n_b is the average number of blades per shoot, l_l is the average length of the longest leaf, l_s is the average sheath length, and w_b is the average shoot width. Averages are reported with standard errors.

Station	m_p (m ⁻²)	n_b	l_b (cm)	l_l (cm)	w_b (cm)
S1V	166 ± 12	3.90 ± 0.10	19.6 ± 1.0	12.3 ± 0.8	0.43 ± 0.02
S2V	291 ± 17	3.80 ± 0.13	18.6 ± 1.8	9.5 ± 0.9	0.40 ± 0.03
S3V	300 ± 30	3.83 ± 0.17	19 ± 3	10 ± 2	0.35 ± 0.04
S4V	210 ± 20	4.10 ± 0.10	19.8 ± 0.9	10.9 ± 0.7	0.380 ± 0.013

7.8.7 Sediment core profiles of carbon isotope ratios and organic carbon stocks

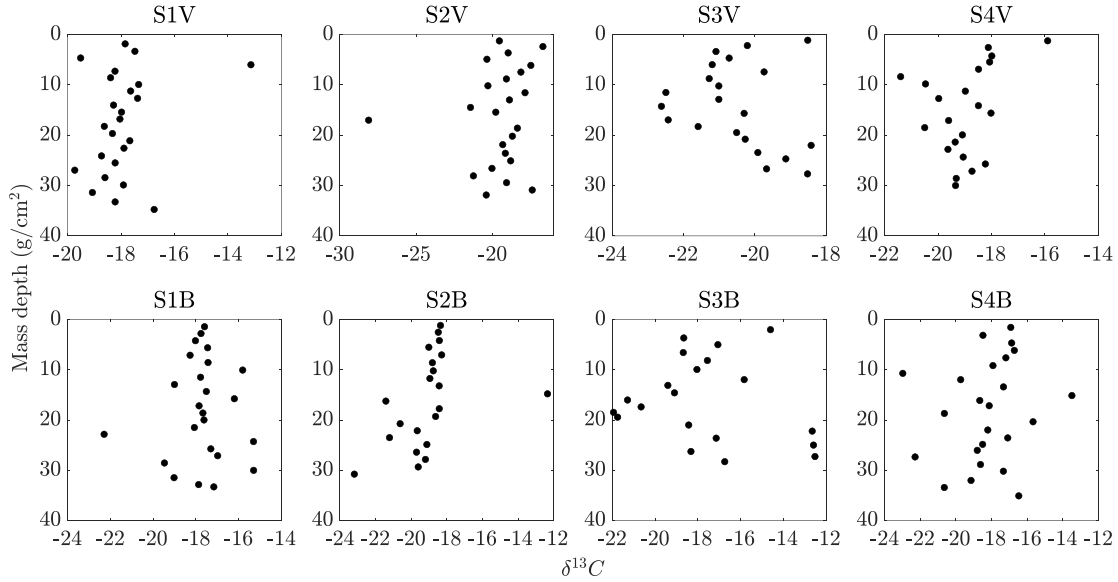


Figure 7.S.4: Profiles of carbon isotope signature $\delta^{13}C$ (parts per thousand relative to Vienna Pee Dee Belemnite) versus cumulative mass depth (showing top 20 cm of core), with different horizontal axes to show details in changes over depth.

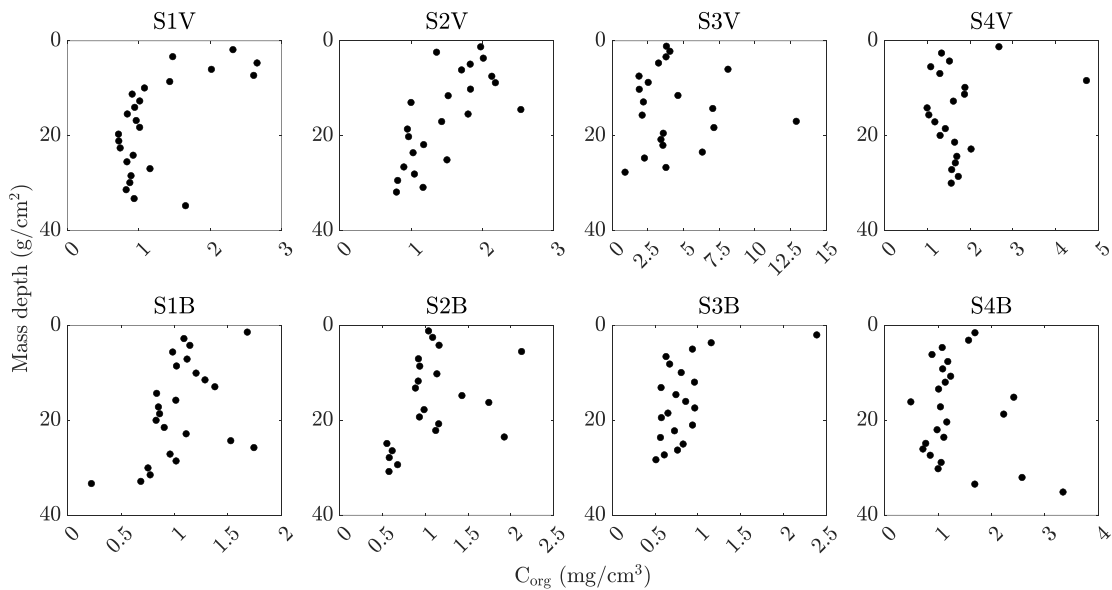


Figure 7.S.5: Profiles of organic carbon density C_{org} versus cumulative mass depth, with different horizontal axes to show details in changes over depth.

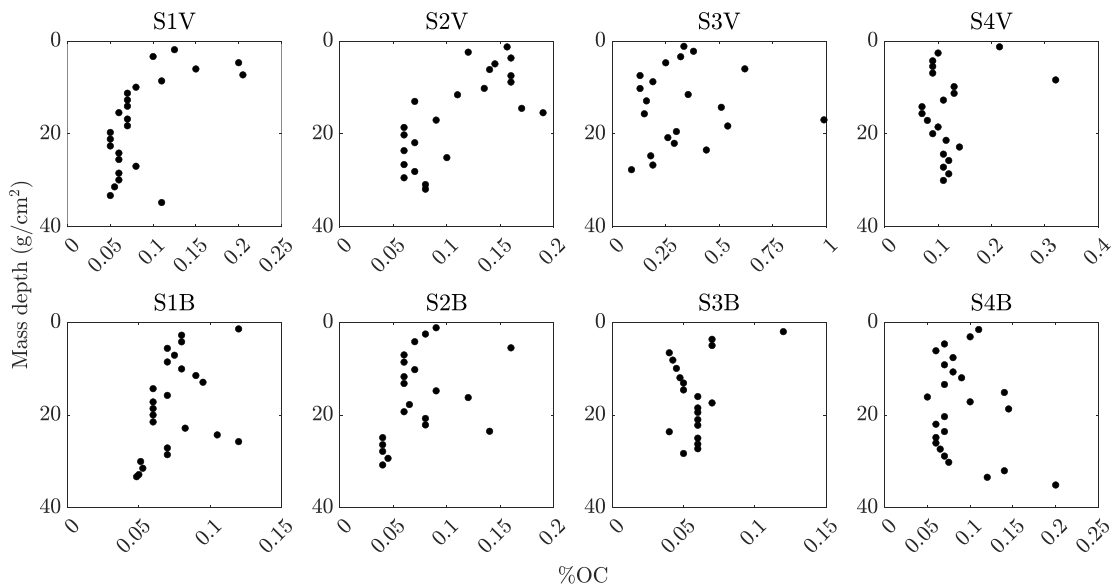


Figure 7.S.6: Profiles of organic carbon content %OC versus cumulative mass depth, with different horizontal axes to show details in changes over depth.

7.8.8 Near-surface grain size distributions

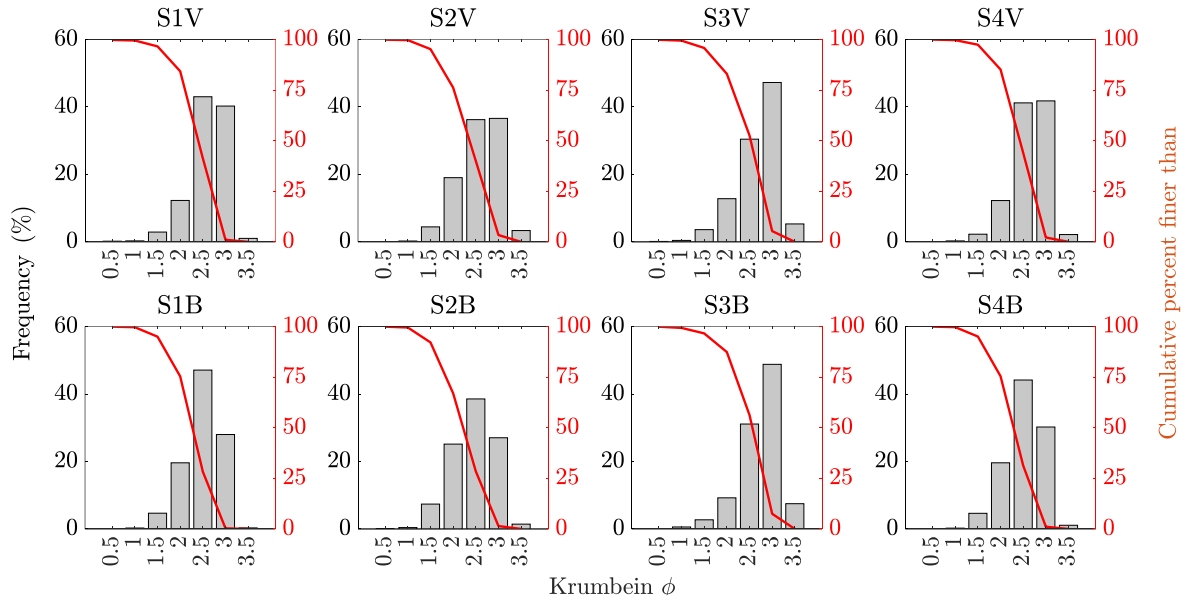


Figure 7.S.7: Grain size distributions measured using sieves from the top 5 cm of each sediment core, using the Krumbein ϕ grain size scale. The bars denote the proportional percentage of the grain size category within the sample. The curves denote the cumulative percentages of the samples that were finer.

Chapter 8

Preliminary results for comparing different methods of estimating the net ecosystem carbon exchange in a seagrass meadow

8.1. Introduction

This chapter consists of a summary of preliminary data and analyses for an ongoing study in a seagrass meadow in Hadley Harbor off of Uncatena Island in Gosnold, Massachusetts, United States of America. Collaborators on the project include Dr. Phil Colarusso, Dr. Julie Simpson, Dr. Alyssa Novak, Dr. Heidi Nepf, and Dr. Matthew Long.

Meadows of seagrass (which are aquatic photosynthesizing plants) are known to be hotspots for sediment organic carbon sequestration; for example, it has been estimated that seagrass meadow sediments have about twice as much carbon per unit area as terrestrial ecosystem sediments (e.g., Fourqurean et al., 2012). Globally, about 50% of the organic carbon stored in seagrass meadow sediments consists of seagrass biomass (known as autochthonous

carbon), with the rest coming from non-seagrass sources originating within or outside of the meadow (known as allochthonous carbon; Kennedy et al., 2010). The production of autochthonous carbon is related to seagrass metabolic processes, which include photosynthesis and respiration. Gaining a better understanding of seagrass metabolism can therefore enhance insight into the contributions of seagrass sources to sediment organic carbon storage.

One of the possible methods to assess seagrass metabolism is to measure the benthic fluxes of oxygen and carbon into and out of a meadow, which are critical to photosynthetic and respiratory processes in the ecosystem. These fluxes can be measured using a technique known as aquatic eddy covariance. Aquatic eddy covariance is based on the concept of hydrodynamic turbulence being the dominant factor in driving the vertical mixing of gases through the water column above a submerged ecosystem. For example, at a particular position in the water column, when the instantaneous vertical velocity is directed downward at the sediment bed, the oxygen concentration is typically slightly higher than average, and when the vertical velocity is pointed upward toward the water surface, the oxygen concentration is typically slightly lower than average (Berg et al., 2003). The resulting nonzero correlation between vertical velocity fluctuations and oxygen concentration fluctuations drives a net flux of oxygen toward the sediment. The time-averaged oxygen flux can be expressed as $\overline{\text{flux}} = \overline{u_z' C_o'}$, where u_z is the vertical velocity, C_o is the oxygen concentration, and $'$ denotes fluctuations about an average (as in a Reynolds decomposition). Thus, a system which can simultaneously measure instantaneous velocities and concentrations can produce time-averaged oxygen fluxes. Dr. Long is continuing to improve his design of the Eddy Covariance Hydrogen ion and Oxygen Exchange System (ECHOES), a suite of co-located instruments that can accurately capture correlations between

fluctuations in vertical velocities and oxygen concentrations (Coogan & Long, 2023; Long et al., 2015).

Using a first-order assumption of a 1:-1 molar ratio of oxygen and carbon in seagrass metabolism (see Duarte et al., 2010; Ziegler & Benner, 1998), net daily oxygen fluxes (calculated from eddy covariance measurements) can be compared with net primary production (calculated from seagrass growth measurements) to gain new insights into how seagrass meadows fix organic carbon, as in Long et al. (2015). In this study, we aimed to compare daily oxygen fluxes, net primary production, as well as carbon accumulation rates from sediment cores taken from the seagrass meadow of interest.

This type of study is novel for a subtidal environment, where a significant challenge includes removing biases from wave-induced motions on turbulence measurements (Long, 2021), as well as considering the wide range of biogeochemical processes occurring on varying time scales. A similar comparison was done for wetlands in Arias-Ortiz et al. (2021), in which net atmospheric carbon uptake rates calculated from carbon dioxide and methane flux measurements from eddy covariance towers were compared against carbon accumulation rates obtained from sediment cores. More specifically, the authors modeled the net ecosystem carbon balance as $NECB = -NEE + F_{CH_4} + F_{hydrologic}$, in which the net ecosystem exchange NEE represents the wetland-atmosphere carbon dioxide exchange, F_{CH_4} is the wetland-atmosphere methane exchange, and $F_{hydrologic}$ is the tidally-driven flux of carbon. They found that $-NEE + F_{CH_4}$ was equal to the carbon accumulation rate within uncertainty in two nontidal wetlands, but was greater than the carbon accumulation rate in a tidal wetland. The difference in agreement between tidal and nontidal wetlands implies that the tidal flows physically transport some

amount of carbon that is not accounted for in the eddy covariance flux measurements, represented by the $F_{hydrologic}$ term.

Our study will build on Arias-Ortiz et al. (2021) and Long et al., (2015) in relating seagrass productivity and sediment carbon accumulation while considering additional hydrodynamic measurements to aim to account for the hydrodynamic import or export of carbon.

8.2 Methods

8.2.1 Field site stations

The field site of interest is a *Zostera marina* Linnaeus (also known as eelgrass) meadow off of Uncatena Island in Hadley Harbor, Massachusetts, United States of America (Figure 8.1). Originally, for the first field data collection and deployment in April-May, 2023 (April 19 to May 5, hereafter referred to as the May deployment) associated with this study, five station locations were chosen, named HH1, HH2, HH3, HH4, and HH5 (denoted by squares in Figure 1). For the subsequent data collections and deployments in July (July 13 to July 28), August (August 17 to August 30), and October (October 4 to October 19) of 2023, the station locations were shifted, and one fewer station was used; the new station labels were HH1N, HH2N, HH3N, and HH4N. The position of the ECHOES system shifted from the May deployment (blue square in Figure 8.1) to the following deployments (blue circle in Figure 8.1). HH2 and HH2N were both placed as close as possible to the ECHOES system while avoiding disturbing ECHOES flow measurements. The tidal range at the field site is 1 m. Water depths across the northeast-to-

southwest transect (HH1 to HH3N) and near HH5 were 2 to 3 m, and decreased toward the shore.

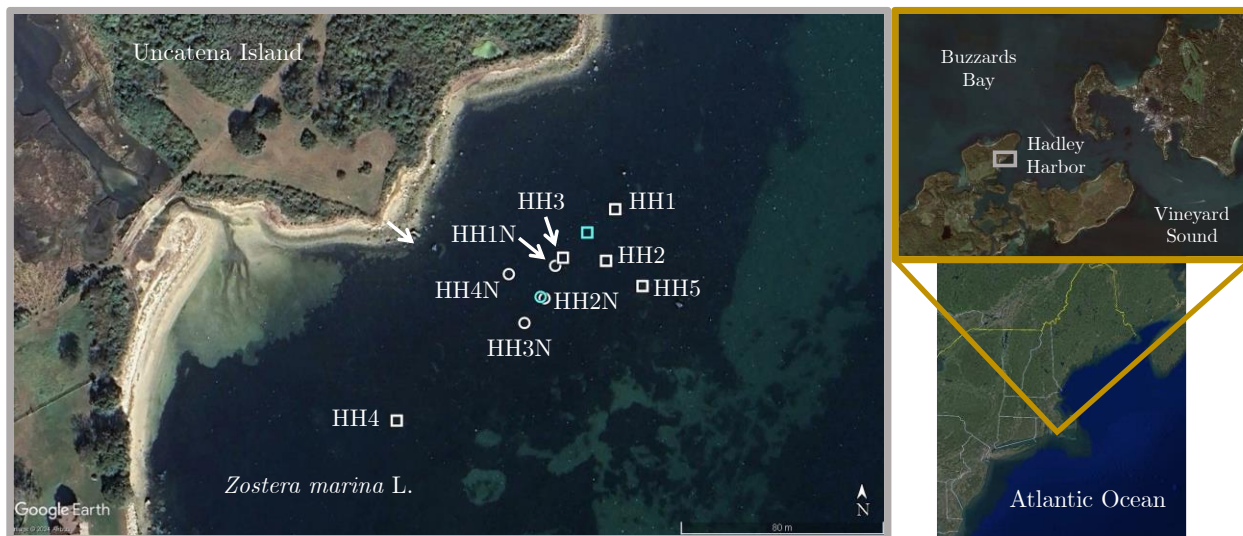


Figure 8.1: Map of field site in Hadley Harbor, Massachusetts, United States of America. The grey rectangle in the top right image corresponds to the grey-bordered left image. The bottom right image shows the position of the field site on the United States East Coast. Squares denote original station locations in the May deployment. Circles denote new locations of stations. Blue symbols denote positions of the ECHOES system. Left image copyright Airbus 2024. Top right image copyright Google 2021. Bottom right image copyright Landsat/Copernicus.

8.2.2 Sediment sample collection and laboratory processing

One sediment core was collected at each station during the August deployment. To extract a core, scientific divers used a manual T-handled driver to push a 50-cm long polycarbonate tube (6.7 cm inner diameter, 7.0 cm outer diameter) to the point beyond which the core could not go deeper. Core lengths ranged from 7.4 to 13 cm, as there appeared to be a rocky sediment layer not far below the sediment surface. Sediment cores were systematically extruded and divided into 1-cm slices. Each slice was placed into a separate pre-weighed Whirl-Pak bag. Furthermore,

during the May deployment, 50-mL centrifuge tubes were pushed into the sediment at every station to collect a sample of near-surface sediment (top 2 to 3 cm) for grain size analysis.

During each deployment, a frame consisting of three sediment traps was placed at each station. Each trap was a cylindrical polyvinyl chloride tube of length 15 cm and inner diameter 5 cm that rested on the bed, the dimensions of which follow common practice described in Blomqvist & Kofoed (1981). A honeycomb baffle was inserted into each tube to reduce material resuspension out of the tube. The heights of the sediment traps exceeded the heights of most of the shoots during the May deployment.

After each deployment, the contents of the collected sediment traps were allowed to settle before each sediment trap was decanted. Each individual sediment trap sample was placed into a separate pre-weighed Whirl-Pak bag. Shellfish, arthropods, shell fragments, and visible plant matter were mechanically removed from all sediment core, sediment trap, and centrifuge tube samples with forceps in order to capture the long-term storage component of the sediment carbon pool (e.g., Greiner et al., 2013). Prior to further laboratory analyses, sediment samples were dried to constant mass at 60°C in a drying oven and weighed. Samples were then homogenized using a mortar and pestle and washed with acid to remove inorganic carbon. The centrifuge tube sediment samples were dry-sieved over size fractions of 0.075 mm to 1.4 mm.

8.2.3 Seagrass sample collection

During each deployment, scientific divers haphazardly tossed three 25 cm × 25 cm quadrats at each station and then counted the number of shoots within each quadrat to estimate the shoot density. Shoot densities were not measured during the May deployment because shoots were too

short to effectively count them. Five to twelve vegetative shoots were randomly removed from each station to measure the number of leaves per shoot, shoot width, sheath length, and length of the longest leaf (note that only shoots near the ECHOES location were collected during the August deployment). Collected shoots were scraped clean of epiphytes using a razor blade and ground into powder for further analyses.

Seagrass growth rates were determined using an adaptation of the Zieman marking method (Zieman, 1974). During the first visit of each deployment, punch holes were inserted through the sheath into each leaf of 12 to 14 randomly chosen plants near the ECHOES location. Seagrass growth was not measured during the May deployment visits due to the difficulty of marking small shoots. During the second visit of each deployment, the distances between the original locations of the punch marks and their new locations on each leaf were measured as the amount of leaf growth. The lengths of new, unmarked leaves that appeared in between the first and second visits were also recorded. The growth in length was multiplied by the shoot width for each leaf and then summed over all of the leaves for each shoot to estimate the total increase in leaf area per shoot during the growth measurement period, and therefore the growth rate. The leaf area values were converted to biomass values using a linear relationship obtained through measurements of seagrass meadows in the northeastern United States, where the biomass (g dry weight) = $(0.00581 \pm 9 \times 10^{-5})(\text{leaf area (cm}^2)) + 0.016 \pm 0.009$ ($R^2=0.86$, shared by Dr. Phil Colarusso of the US Environmental Protection Agency).

8.2.4 Hydrodynamic intensity measurements

To capture potential spatial variability in hydrodynamic intensity, a tilt current meter (Lowell Instruments, Massachusetts, USA) tethered to a paving stone anchor was set out at each station during each deployment. During the May, August, and October deployments, tilt current meters measured in burst mode at 16 Hz for 60 seconds every five minutes. During the July deployment, tilt current meters measured continuously at 16 Hz. Flow speeds were denoted as positive when the tilt current meter was tilting toward the southwest end of the northeast-to-southwest transect in Figure 1 (HH1 to HH4) and denoted as negative when they were tilting toward the northeast end of the transect. Wave velocities U_w were estimated for each hour by multiplying the root-mean-square of each hour of velocity data by $\sqrt{2}$. Each tilt current meter contained an internal thermistor that measured water temperatures once every five minutes. Finally, a pressure sensor located near HH2N recorded water pressures at 16 Hz during part of the July deployment.

Note that a submerged meadow can attenuate tidal velocities below the height of the shoots through the hydrodynamic drag force (Brunet et al., 1994; Raupach et al., 1996), the effectiveness of which depends on environmental factors that include leaf density, shoot width, flow speeds, meadow height, and water depth (e.g., Chen et al., 2013). A tilt current meter fully covered by a meadow (such that during typical flow conditions, the height of the deflected meadow exceeds the height of the instrument) can capture the reduced velocities within the meadow. However, the total height of the tilt current meter setup is 33 cm, which exceeded the heights of most shoots during the May deployment and likely the deflected heights of a large fraction of shoots during the July deployment. This preliminary report will not include further discussion of this topic for simplicity, but this idea should be kept in mind.

8.2.5 Elemental analyses and stable isotope ratios

To obtain organic carbon content, organic nitrogen content, and stable isotope ratio values, homogenized sediment trap, sediment core, and eelgrass samples were combusted in a Costech Analytical Elemental Combustion System (ECS) 4010 (Valencia, CA, USA) interfaced with a Thermofinnigan DeltaXP continuous flow isotope ratio mass spectrometer (Bremen, Germany). Carbon stable isotope ratios $\delta^{13}C$ were measured relative to the international Vienna Pee Dee Belemnite (VPDB) standard, while nitrogen stable isotope ratios $\delta^{15}N$ were measured relative to the international atmospheric air standard. Internal laboratory running standards calibrated against reference materials were used for quality control.

8.2.6 Sediment accumulation rates

To measure sediment accumulation rates *SAR*, one subsample from what remained of each sediment core slice was analyzed for ^{210}Pb radioisotope activity with alpha spectrometry (using an EG&G Ortec Octet spectrometer). Total ^{210}Pb activities were measured using ^{210}Po as a proxy (based on Eakins & Morrison, 1978), and background ^{210}Pb activities were measured using ^{226}Ra as a proxy, which was inferred from measurements of ^{222}Rn using a SPECTECH UCS-30 alpha spectrometer (based on Mathieu et al., 1988).

Excess ^{210}Pb activity for each core was determined as the difference between total ^{210}Pb and the nearest neighboring ^{226}Ra measurement. A constant flux-constant sedimentation model (CFCS; Corbett & Walsh, 2015) was used to calculate a mass accumulation rate *MAR* for each core with a clear decreasing trend in excess ^{210}Pb activity with increasing sediment depth; only the HH4N core showed such a trend. The *MAR* value was multiplied by the respective average

sediment organic carbon content in the sediment core to yield a carbon accretion rate *CAR*. Finally, even though ^{137}Cs activity profiles are commonly used to validate ^{210}Pb results, the HH4N sediment core section ages estimated from the ^{210}Pb modelling indicated that the bottom of the core was not old enough to include the assumed 1963 peak in ^{137}Cs associated with bomb-produced radionuclides (Nittrouer et al., 1984; Pennington et al., 1973; Ritchie & McHenry, 1990). Therefore, ^{137}Cs activity was not measured.

8.3 Preliminary Results and Discussion

8.3.1 Seagrass characteristics and growth

Average seagrass shoot densities showed an overall decreasing trend across the July, August, and October deployments, while average plant lengths (using the lengths of the longest leaves) increased between the May and August deployments and then remained about the same within uncertainty between the August and October deployments (Figure 8.2). At the same time, the average seagrass growth rate per shoot decreased between the July and October deployments (Figure 8.3). The number of daylight hours in Boston, Massachusetts, USA on July 15th, August 15th, and October 15th decreased from 15 to 14 to 11, which progressively limited seagrass photosynthetic activity and contributed to decreasing growth rates over that period of time. Seagrass productivity also depends on water temperature, which itself depends on irradiance (Lee et al., 2007). Water temperatures increased from 10°C during the May deployment to 25°C during the July deployment, and then decreased to 15°C during the October deployment (Figure 8.4).

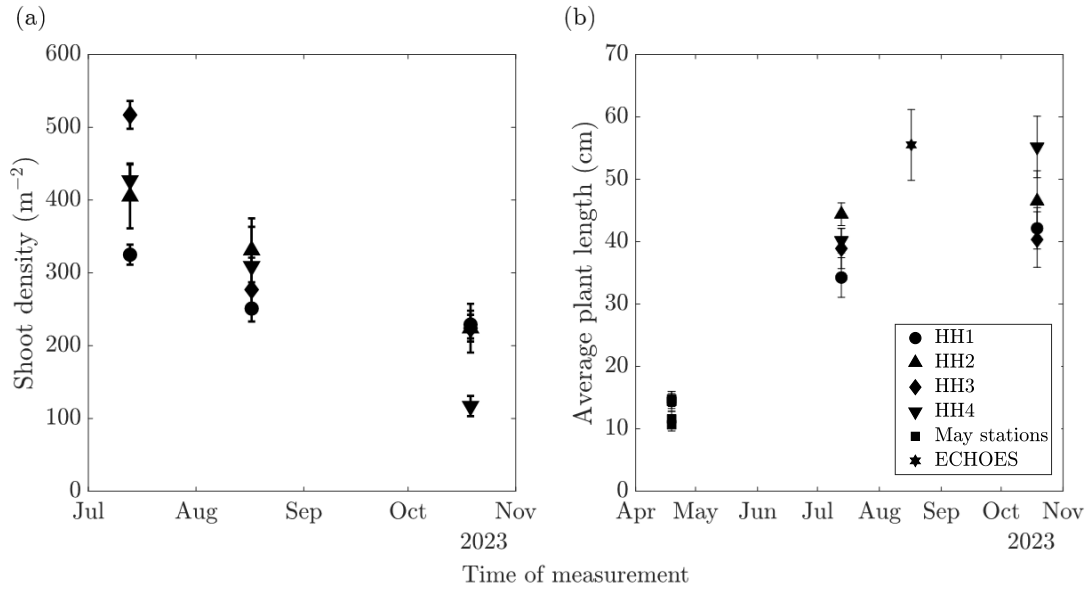


Figure 8.2: Average seagrass shoot (a) density and (b) length (using the length of the longest leaf) measured during the deployments. Shoot densities were not measured during the May deployment due to the difficulty of counting the shoots. During the August deployment, shoots were collected near the ECHOES location.

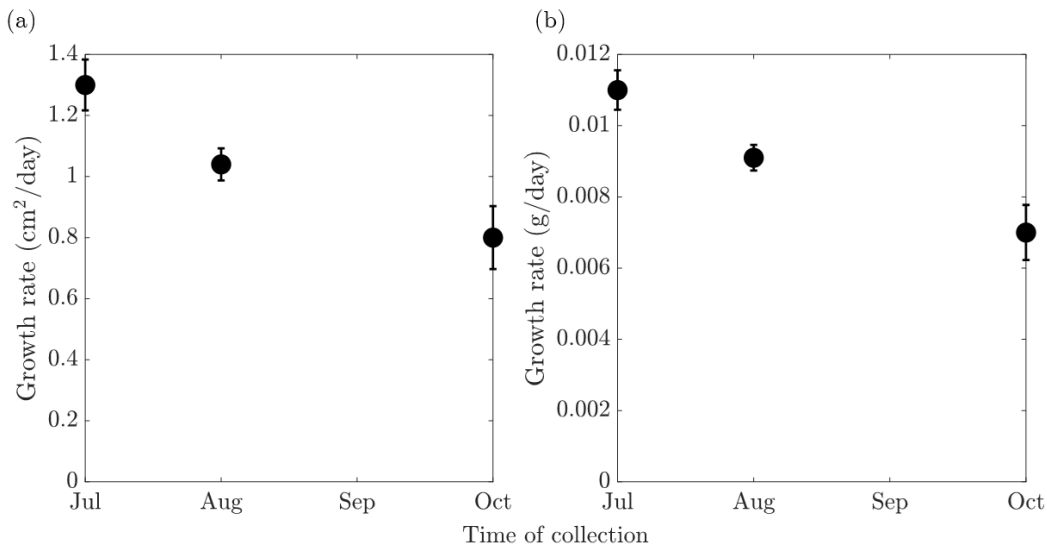


Figure 8.3: Average seagrass growth rates per shoot over time expressed in terms of (a) leaf area and (b) biomass, based on an experimentally measured linear correlation between seagrass leaf area and biomass in the northeastern USA.

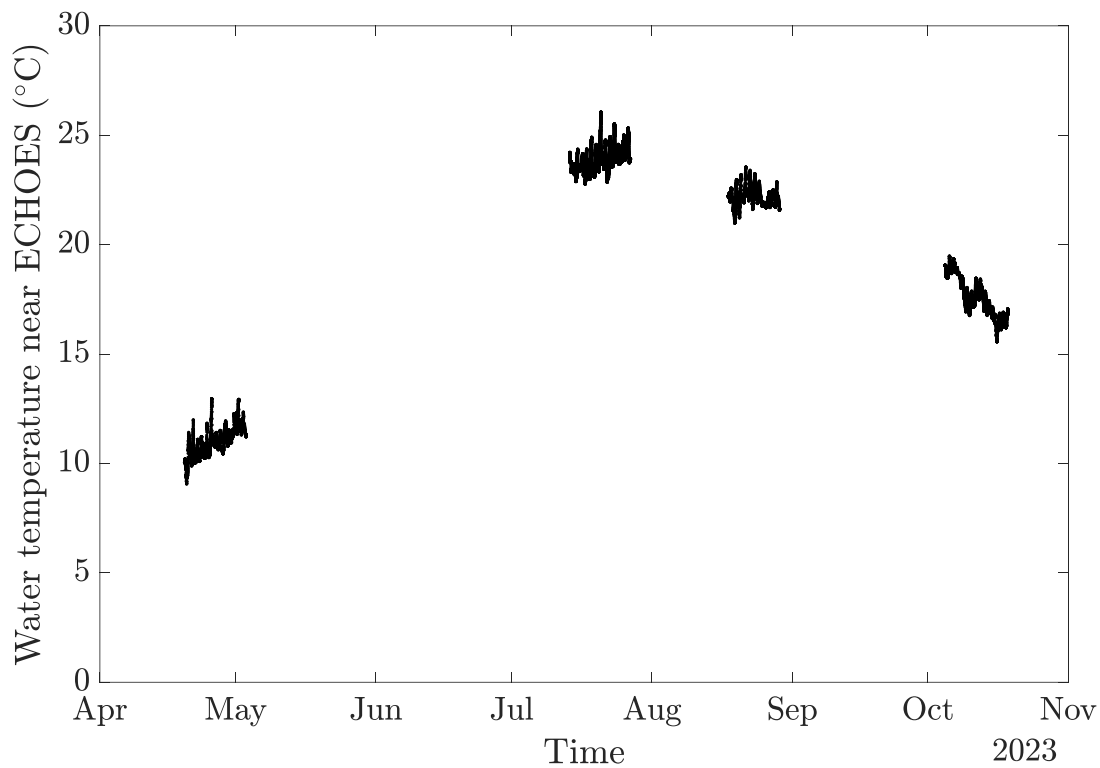


Figure 8.4: Water temperature near the ECHOES location during tilt current meter deployments.

Seagrass tissue carbon stable isotope ratios as well as organic carbon and nitrogen content did not show overall increasing or decreasing trends within uncertainty across the deployments. The nitrogen stable isotope ratios increased between the May and August deployments and then slightly decreased between the August and October deployments, likely reflecting changes in seagrass productivity and available nitrogen sources (e.g., Anderson & Fourqurean, 2003).

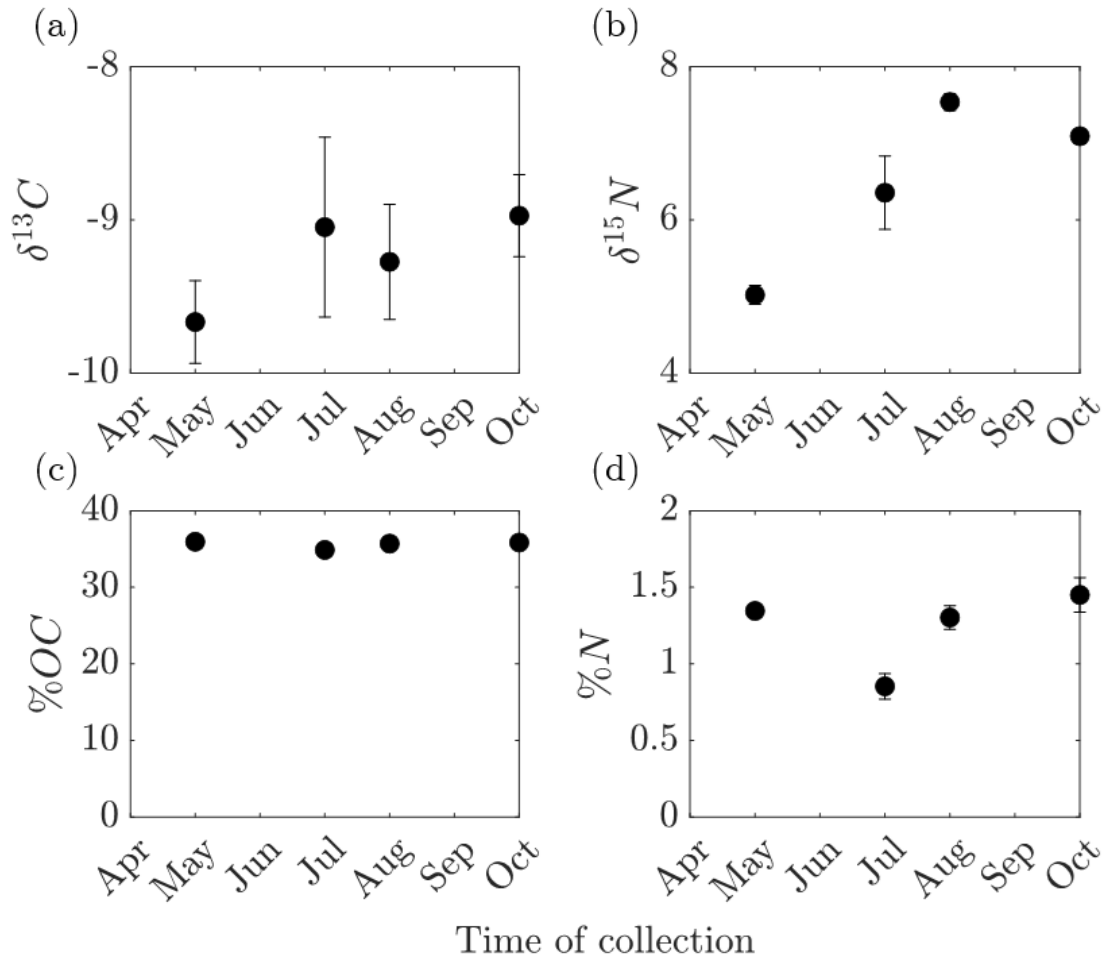


Figure 8.5: Average seagrass sample elemental analysis and mass spectrometry results from samples collected during the deployments. (a) Stable carbon isotope ratios $\delta^{13}C$, (b) stable nitrogen isotope ratios $\delta^{15}N$, (c) organic carbon content, and (d) nitrogen content.

8.3.2 Sediment sample properties

The changes in seagrass shoot density, morphology, %OC, %N, and carbon and nitrogen stable isotope ratios can be considered alongside changes in sediment trap deposition rates, sediment %OC, %N, and carbon and nitrogen stable isotope ratios. The average sediment trap deposition rates increased between the July and August deployments (Figure 8.6), which could be related to some extent to the reduction in average shoot densities over that period of time. Sparser

meadows are generally less effective at attenuating current velocities within the meadow than denser meadows (e.g., Bentham & Britter, 2003; Lowe et al., 2005), such that higher levels of sediment resuspension, and therefore greater sediment mass in the sediment traps, may be expected.

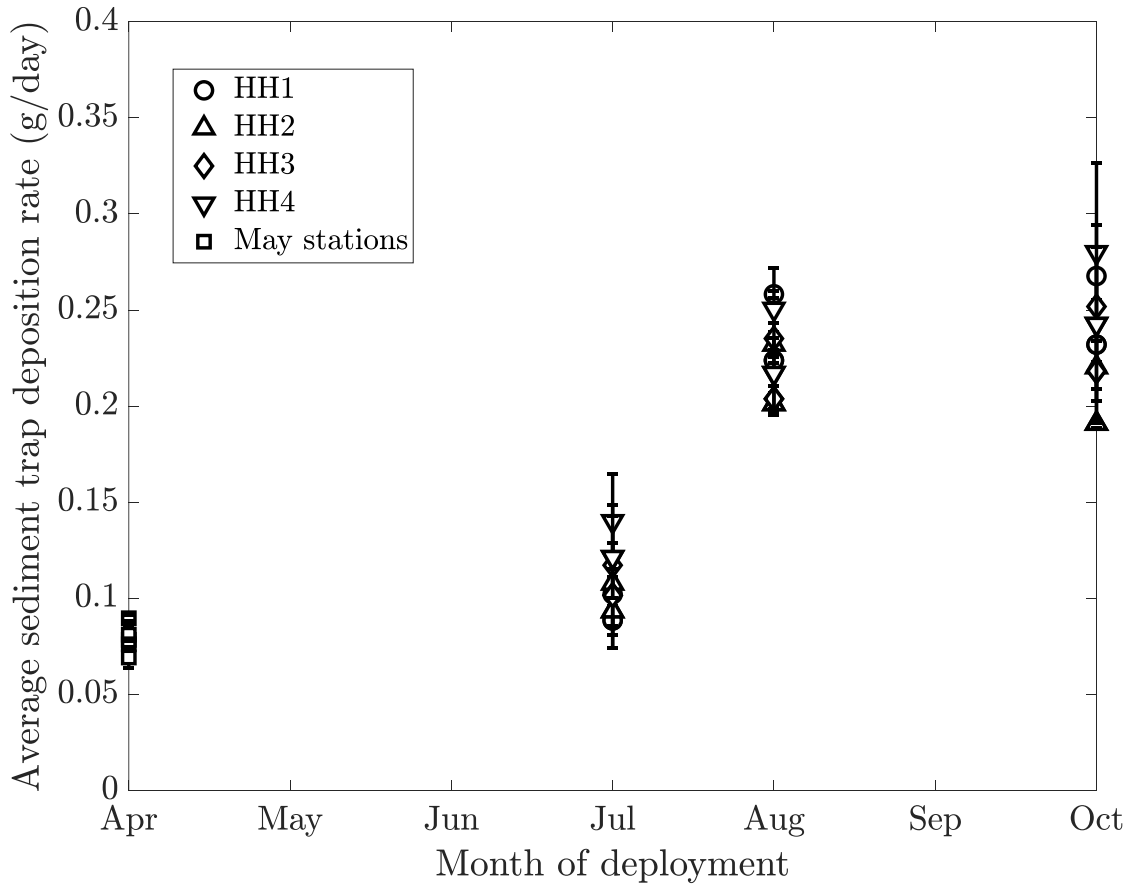


Figure 8.6: Sediment trap deposition rates (average sediment trap mass divided by number of days trap was deployed) during each deployment.

The sediment deposited in the sediment traps became less depleted in carbon between the May and October deployments (Figure 8.7a), which could indicate shifting contributions of carbon sources to organic matter adsorbed to the sediments (as all visible organic matter was

mechanically removed from the samples). Meanwhile, the sediment became more depleted in nitrogen between the May and July deployments (Figure 8.7b). Changes in %OC (Figure 8.7c) were mirrored in changes in %N (Figure 8.7d), such that the carbon-to-nitrogen (C:N) ratio was consistent among the sediment samples.

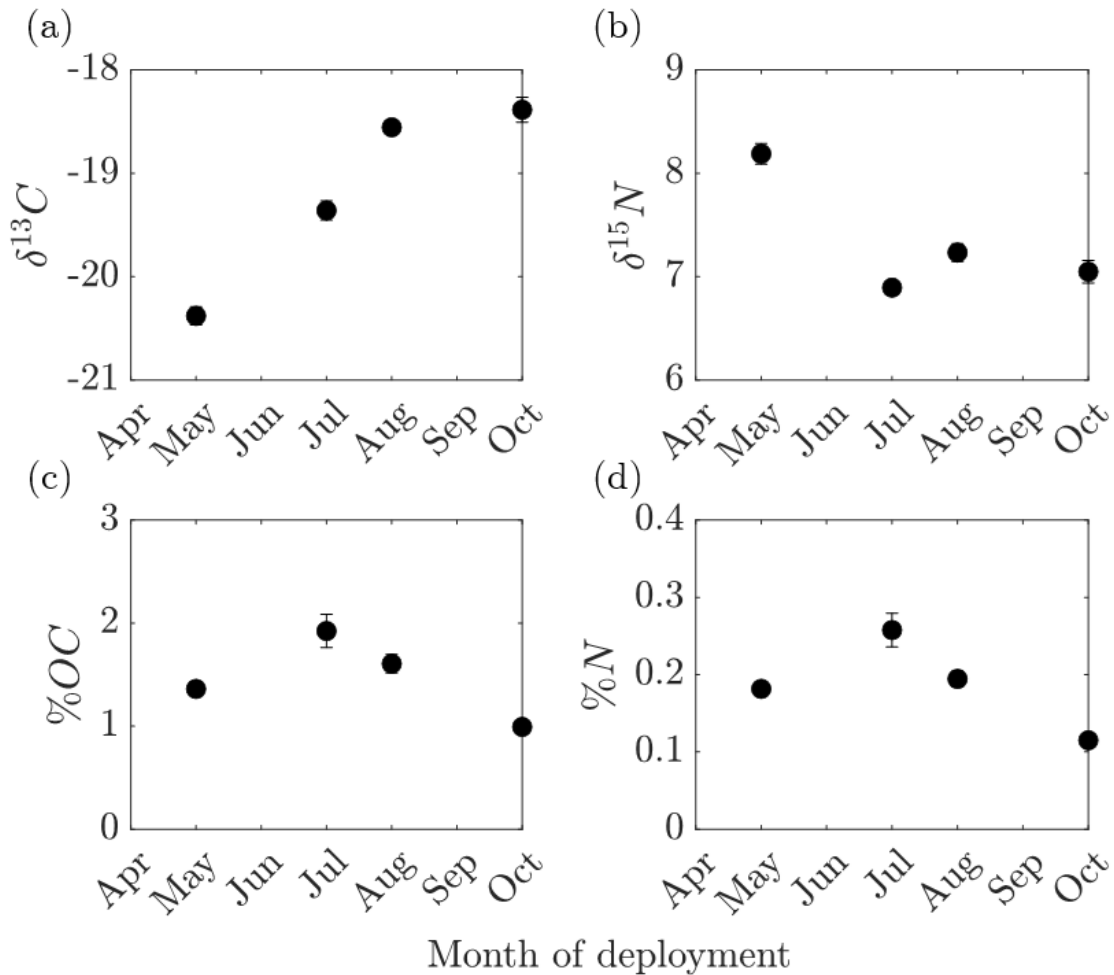


Figure 8.7: Average sediment trap sample elemental analysis results over time. (a) Stable carbon isotope ratios $\delta^{13}C$ (‰, relative to VPDB), (b) stable nitrogen isotope ratios $\delta^{15}N$ (‰, relative to atmospheric air), (c) organic carbon content, and (d) nitrogen content.

Spatial changes in %OC with sediment depth also mirrored spatial changes in %N in the sediment cores (Figure 8.S.1). The HH4N core had a somewhat elevated region of %OC and %N several cm below the sediment surface. The decline of %OC and %N toward the bottom of the HH4N cores corresponded to increasing $\delta^{13}C$ and decreasing $\delta^{15}N$ (Figure 8.S.2). Overall, relationships between carbon and nitrogen stable isotope ratios among the sediment trap, sediment core, and eelgrass samples are shown in Figure 8.8. The eelgrass carbon stable isotope ratios are distinct from those of the sediment samples, implying substantial contributions from non-seagrass sources more depleted in ^{13}C than seagrass to organic carbon at the field site.

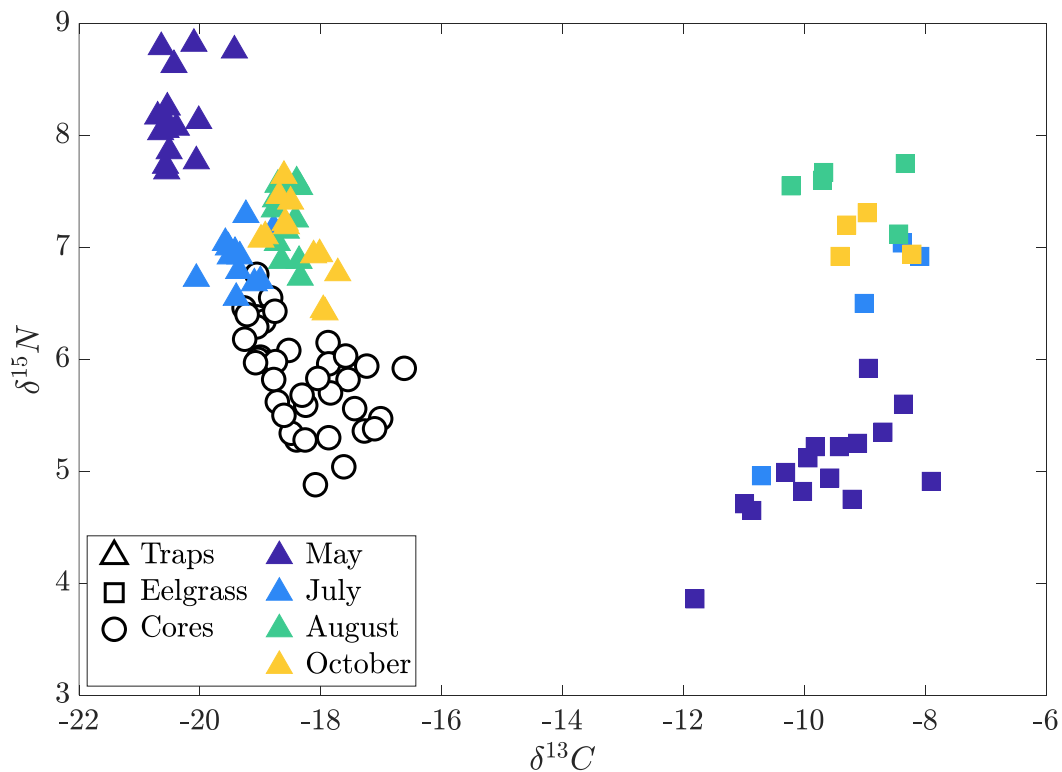


Figure 8.8: Carbon stable isotope ratios $\delta^{13}C$ (‰, relative to VPDB) versus nitrogen stable isotope ratios $\delta^{15}N$ (‰, relative to atmospheric air) for sediment trap, sediment core, and eelgrass samples.

The ^{210}Pb geochronology analyses to estimate sediment accumulation rates were not successful for the HH1N, HH2N, and HH3N cores, likely due to a combination of sediment mixing, short core lengths, and coarse sediments at the field site (the median sediment grain sizes from the centrifuge tube samples were 0.3 mm at HH1 and HH3 and 0.4 mm at HH2, HH4, and HH5). Outside of the surface mixing layer in the HH4N core, the sediment accumulation rate was estimated to be $0.33 \pm 0.07 \text{ g cm}^{-2} \text{ yr}^{-1}$ (with uncertainty based on the regression standard error; see Figure 8.S.3 for the radioactivity profiles and model fit for HH4N). Using the average %OC in the HH4N core, the *CAR* is approximately $0.0013 \pm 0.0003 \text{ g C cm}^{-2} \text{ yr}^{-1}$.

8.3.3 Hydrodynamics across the meadow

Considering the tilt current meter measurements can provide more context for the sediment measurements (as the transport of sediment is a function of hydrodynamic exposure). First focusing on the station closest to the ECHOES location during the continuous measurements for the July deployment (HH2N) as a representative example, the tilt current meter was biased in tilting toward the northeast end of the transect, resulting in negative 60-minute moving averages of the flow velocities (which represent tidal velocities; gray curve in Figure 8.9). Sixty-minute moving averages of the velocity magnitudes (no positive or negative signs associated with tilt direction; black curve in Figure 8.9) showed a periodic pattern with twice the period (roughly 24 hours) of the diurnal tides measured by the co-located pressure sensor (slightly longer than 12 hours; red curve in Figure 8.9). A large fraction of tidal speeds was likely too low for the tilt current meter to accurately capture. The configuration of surrounding islands to the south and southwest as well as the semi-enclosed nature of Buzzards Bay to the north (Figure 8.1) likely

contribute to the skewness in tidal flow. Finally, the long-term periodic variation in the hourly wave velocities U_w (blue curve connecting open circles in Figure 8.9) followed the periodic variation in tidal velocities. The hourly wave velocities were typically greater than the corresponding tidal velocities.

Throughout the four deployments of tilt current meters at the field site, several spikes in tidal velocities occurred, likely associated with storm events (Figure 8.10). The frequent small spikes in velocity during the May deployment could perhaps be related to shear turbulence generated at the tops of the growing seagrass shoots. Finally, there was little spatial variation in tilt current meter tidal flow speeds among the measurement stations during each deployment (Figure 8.10).

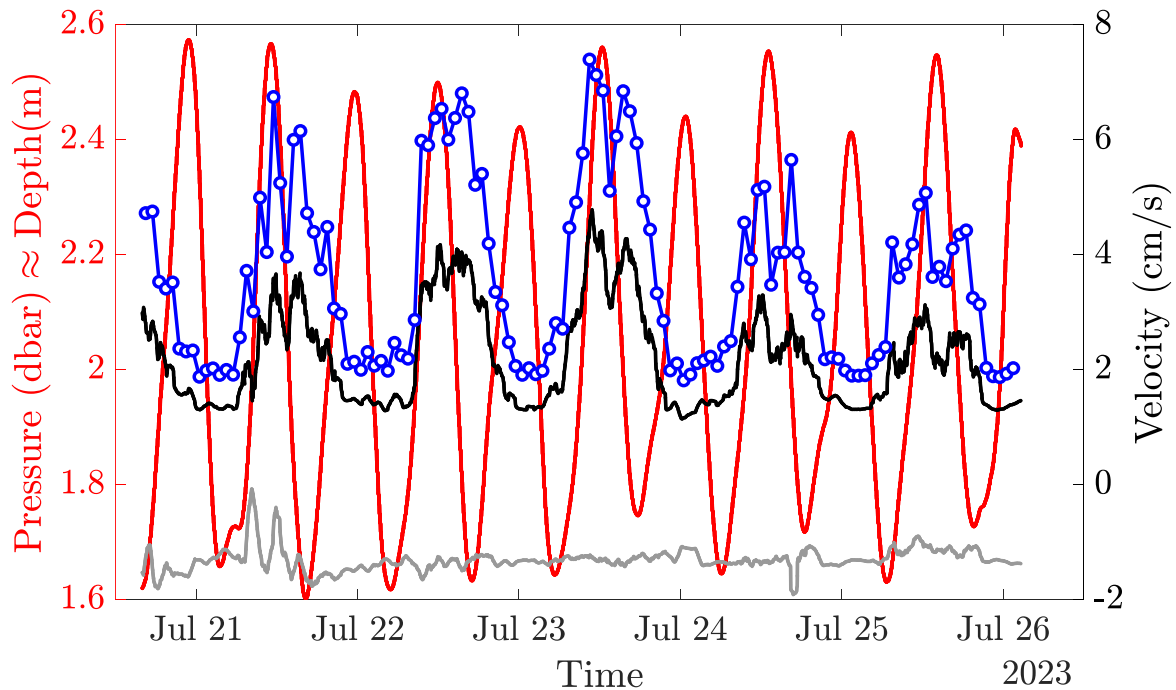


Figure 8.9: Pressure (left axis, red curve, in dbar, approximately equivalent to depth in m), 60-minute moving averages of flow speeds (right axis, black curve), 60-minute moving averages of flow velocities (positive velocities correspond to times when the tilt current meter was tilting toward the southwest end of the new transect in Figure 8.1, and vice versa), and hourly wave

velocities U_w (blue curve connecting open circles) at HH2N over time during part of the July deployment.

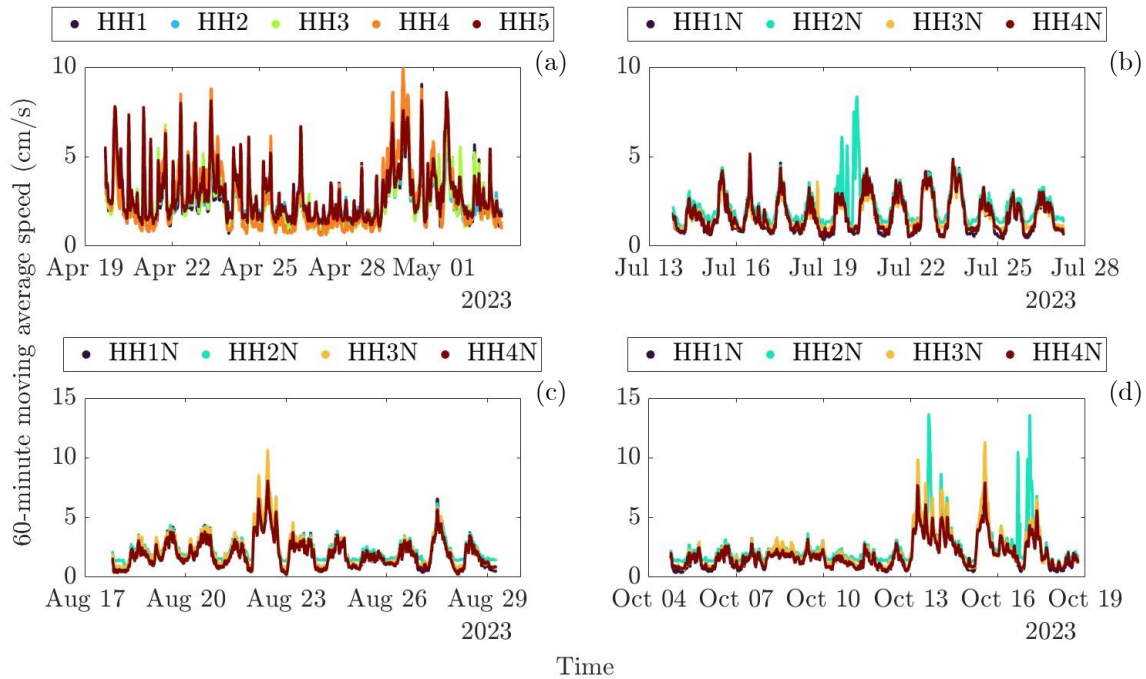


Figure 8.10: 60-minute moving average velocity magnitudes (which represent tidal speeds) during the (a) May, (b) July, (c) August, and (d) October deployments.

8.3.4 Net ecosystem carbon budget

Next, we will use the experimental results to quantify and discuss the net ecosystem carbon budget at the field site, which will involve comparing carbon uptake estimated through seagrass growth rates, the sediment core carbon accumulation rate at HH4N, and ECHOES oxygen flux measurements. Directly connecting seagrass growth with sediment carbon accumulation rates makes several important assumptions. First, doing so assumes negligible contributions of

allochthonous carbon (non-seagrass carbon sources outside of or within the meadow) to long-term sediment carbon storage, which may not be a valid assumption due on the distinct carbon stable isotope ratio values in the sediment samples compared to the eelgrass samples (Figure 8.8). Second, we must assume that there is no lateral transport of seagrass biomass into or out of the system.

Seagrass biomass growth rates per plant were converted to net primary productivity using the average seagrass tissue %OC and shoot density measurements. Net primary productivity values decreased from $138 \pm 11 \text{ mmol C m}^{-2} \text{ d}^{-1}$ in the July deployment to $79 \pm 6 \text{ mmol C m}^{-2} \text{ d}^{-1}$ in the August deployment and then to $44 \pm 6 \text{ mmol C m}^{-2} \text{ d}^{-1}$ in the October deployment. These values were measured during the eelgrass growing season and therefore overestimate the year-round integrated seagrass productivity. The ECHOES data collected during the July, August, and October deployments have not yet been fully processed and analyzed. After data processing and analyses are complete, net daily carbon fluxes could be inferred from net daily oxygen fluxes during the deployment time periods and then compared against the corresponding net primary productivity values.

The *CAR* from the HH4N core, $0.0013 \pm 0.0003 \text{ g C cm}^{-2} \text{ yr}^{-1}$, is equivalent to $3.0 \pm 0.7 \text{ mmol C m}^{-2} \text{ d}^{-1}$. Based on eddy covariance measurements from a prior deployment of the ECHOES system from May through November in the seagrass meadow of interest, Coogan & Long (2023) estimated a net ecosystem metabolism of 1.7 to 2.4 $\text{mmol O}_2 \text{ m}^{-2} \text{ d}^{-1}$. Using a 1:-1 molar ratio of oxygen to carbon during seagrass metabolism yields a net ecosystem metabolism of 1.7 to 2.4 $\text{mmol C m}^{-2} \text{ d}^{-1}$, which is comparable to the converted HH4N sediment core *CAR*. Note that the May-November ECHOES net ecosystem metabolism value may be higher than

what the year-round value would be due to lower ecosystem productivity during the winter months. The ECHOES has been collecting data throughout the winter of 2023-2024 and spring of 2024 with the goal of producing a year-round estimate. The *CAR* and the upper range of the likely overestimated net ecosystem metabolism values are the same within uncertainty.

Meanwhile, the net primary productivity values estimated from the seagrass growth rates are substantially higher than the *CAR*. This is because the growth rates represent narrow windows of time during the seagrass growing season, while the *CAR* represents the integrated year-round ecosystem carbon exchange on a decadal time-scale.

While it is exciting that the *CAR* and May-November ECHOES net ecosystem carbon uptake values are similar, we strongly caution that this field site represents one data point, and both values are composites of many biogeochemical and physical processes. Even though tidal velocities at the field site are small, they may still transport seagrass detritus or other organic matter into or away from the field site, a factor that is represented in the *CAR* but not captured by the ECHOES measurements.

8.4 Conclusions and Next Steps

The results described in this chapter are preliminary and demonstrate a promising start for the project. This study will be continued after ECHOES data are collected during the spring season, which would give a full year of measurements. Ideally, the field experiment described here would be repeated in several other seagrass meadows to provide more data points. However, aquatic eddy covariance systems are more difficult to set up and maintain than traditional terrestrial eddy covariance towers. In addition, the methodology for calculating oxygen and

hydrogen fluxes (through pH) based on ECHOES measurements is continuing to evolve. Net daily oxygen fluxes calculated from ECHOES measurements during the July, August, and October, 2023 deployments once the data are processed could be compared against the net primary productivity values estimated from seagrass growth rate measurements. Combined together, the comparisons will contribute to improved knowledge about as well as a potentially improved ability to predict seagrass ecosystem carbon uptake.

8.5 References

- Anderson, W. T., & Fourqurean, J. W. (2003). Intra- and interannual variability in seagrass carbon and nitrogen stable isotopes from south Florida, a preliminary study. *Organic Geochemistry*, *34*(2), 185–194. [https://doi.org/10.1016/S0146-6380\(02\)00161-4](https://doi.org/10.1016/S0146-6380(02)00161-4)
- Arias-Ortiz, A., Oikawa, P. Y., Carlin, J., Masqué, P., Shahan, J., Kanneg, S., Paytan, A., & Baldocchi, D. D. (2021). Tidal and nontidal marsh restoration: A trade-off between carbon sequestration, methane emissions, and soil accretion. *Journal of Geophysical Research: Biogeosciences*, *126*(12), 1–22. <https://doi.org/10.1029/2021JG006573>
- Bentham, T., & Britter, R. (2003). Spatially averaged flow within obstacle arrays. *Atmospheric Environment*, *37*(15), 2037–2043. [https://doi.org/10.1016/S1352-2310\(03\)00123-7](https://doi.org/10.1016/S1352-2310(03)00123-7)
- Berg, P., Røy, H., Janssen, F., Meyer, V., Jørgensen, B. B., Huettel, M., & De Beer, D. (2003). Oxygen uptake by aquatic sediments measured with a novel non-invasive eddy-correlation technique. *Marine Ecology Progress Series*, *261*, 75–83. <https://doi.org/10.3354/meps261075>
- Blomqvist, S., & Kofoed, C. (1981). Sediment trapping—A subaquatic in situ experiment. *Limnology and Oceanography*, *26*(3), 585–590. <https://doi.org/10.4319/lo.1981.26.3.0585>
- Brunet, Y., Finnigan, J. J., & Raupach, M. R. (1994). A wind tunnel study of air flow in waving wheat: Single-point velocity statistics. *Boundary-Layer Meteorology*, *70*(1–2), 95–132. <https://doi.org/10.1007/BF00712525>
- Chen, Z., Jiang, C., & Nepf, H. (2013). Flow adjustment at the leading edge of a submerged aquatic canopy. *Water Resources Research*, *49*(9), 5537–5551. <https://doi.org/10.1002/wrcr.20403>

- Coogan, J., & Long, M. H. (2023). Development and deployment of a long-term aquatic eddy covariance system. *Limnology and Oceanography: Methods*, 21(9), 552–562. <https://doi.org/10.1002/lom3.10564>
- Duarte, C. M., Marbà, N., Gacia, E., Fourqurean, J. W., Beggins, J., Barrón, C., & Apostolaki, E. T. (2010). Seagrass community metabolism: Assessing the carbon sink capacity of seagrass meadows. *Global Biogeochemical Cycles*, 24(4), 1–8. <https://doi.org/10.1029/2010GB003793>
- Eakins, J. D., & Morrison, R. T. (1978). A new procedure for the determination of lead-210 in lake and marine sediments. *The International Journal Of Applied Radiation And Isotopes*, 29(9–10), 531–536. [https://doi.org/10.1016/0020-708X\(78\)90161-8](https://doi.org/10.1016/0020-708X(78)90161-8)
- Fourqurean, J. W., Duarte, C. M., Kennedy, H., Marbà, N., Holmer, M., Mateo, M. A., Apostolaki, E. T., Kendrick, G. A., Krause-Jensen, D., & Serrano, O. (2012). Seagrass ecosystems as a globally significant carbon stock. *Nature Geoscience*, 5, 505–509. <https://doi.org/10.1038/ngeo1477>
- Greiner, J. T., McGlathery, K. J., Gunnell, J., & McKee, B. A. (2013). Seagrass restoration enhances “blue carbon” sequestration in coastal waters. *PLoS ONE*, 8(8), 1–8. <https://doi.org/10.1371/journal.pone.0072469>
- Kennedy, H., Beggins, J., Duarte, C. M., Fourqurean, J. W., Holmer, M., Marbà, N., & Middelburg, J. J. (2010). Seagrass sediments as a global carbon sink: Isotopic constraints. *Global Biogeochemical Cycles*, 24, 1–8. <https://doi.org/10.1029/2010GB003848>
- Lee, K. S., Park, S. R., & Kim, Y. K. (2007). Effects of irradiance, temperature, and nutrients on growth dynamics of seagrasses: A review. *Journal of Experimental Marine Biology and Ecology*, 350(1–2), 144–175. <https://doi.org/10.1016/j.jembe.2007.06.016>
- Long, M. H. (2021). Aquatic Biogeochemical Eddy Covariance Fluxes in the Presence of Waves. *Journal of Geophysical Research: Oceans*, 126(2), 1–23. <https://doi.org/10.1029/2020JC016637>
- Long, M. H., Berg, P., McGlathery, K. J., & Zieman, J. C. (2015). Sub-tropical seagrass ecosystem metabolism measured by eddy covariance. *Marine Ecology Progress Series*, 529, 75–90. <https://doi.org/10.3354/meps11314>
- Long, M. H., Charette, M. A., Martin, W. R., & Mccorkle, D. C. (2015). Oxygen metabolism and pH in coastal ecosystems: Eddy Covariance Hydrogen ion and Oxygen Exchange System (ECHOES). *Limnology and Oceanography: Methods*, 13(8), 438–450. <https://doi.org/10.1002/lom3.10038>
- Lowe, R. J., Koseff, J. R., & Monismith, S. G. (2005). Oscillatory flow through submerged canopies: 1. Velocity structure. *J. Geophys. Res.: Oceans*, 110(C10). <https://doi.org/10.1029/2004JC002788>

- Mathieu, G. G., Biscaye, P. E., & Lupton, R. A. (1988). System for measurement of ^{222}Rn at low levels in natural waters. *Health Physics*, 55(6), 989–992. <https://doi.org/10.1097/00004032-198812000-00015>
- Nittrouer, C. A., DeMaster, D. J., McKee, B. A., Cutshall, N. H., & Larsen, I. L. (1984). The effect of sediment mixing on Pb-210 accumulation rates for the Washington continental shelf. *Marine Geology*, 54(3–4), 201–221. [https://doi.org/10.1016/0025-3227\(84\)90038-0](https://doi.org/10.1016/0025-3227(84)90038-0)
- Pennington, W., Cambray, R. S., & Fisher, E. M. (1973). Observations on lake sediments using fallout ^{137}Cs as a tracer. *Nature*, 242(5396), 324–326. <https://doi.org/10.1038/242324a0>
- Raupach, M. R., Finnigan, J. J., & Brunet, Y. (1996). Coherent eddies and turbulence in vegetation canopies: the mixing-layer analogy. *Boundary-Layer Meteorology*, 78(3–4), 351–382. <https://doi.org/10.1007/BF00120941>
- Reide Corbett, D., & Walsh, J. P. (2015). ^{210}Pb and ^{137}Cs : Establishing a chronology for the last century. *Handbook of Sea-Level Research*, 361–372. <https://doi.org/10.1002/9781118452547.ch24>
- Ritchie, J. C., & McHenry, J. R. (1990). Application of radioactive fallout Cesium-137 for measuring soil erosion and sediment accumulation rates and patterns: A review. *Journal of Environmental Quality*, 19(2), 215–233. <https://doi.org/10.2134/jeq1990.00472425001900020006x>
- Ziegler, S., & Benner, R. (1998). Ecosystem metabolism in a subtropical, seagrass-dominated lagoon. *Marine Ecology Progress Series*, 173, 1–12. <https://doi.org/10.3354/meps173001>
- Zieman, J. C. (1974). Methods for the study of the growth and production of turtle grass, *Thalassia testudinum* König. *Aquaculture*, 4, 139–143. [https://doi.org/10.1016/0044-8486\(74\)90029-5](https://doi.org/10.1016/0044-8486(74)90029-5)

8.6. Supplementary Figures

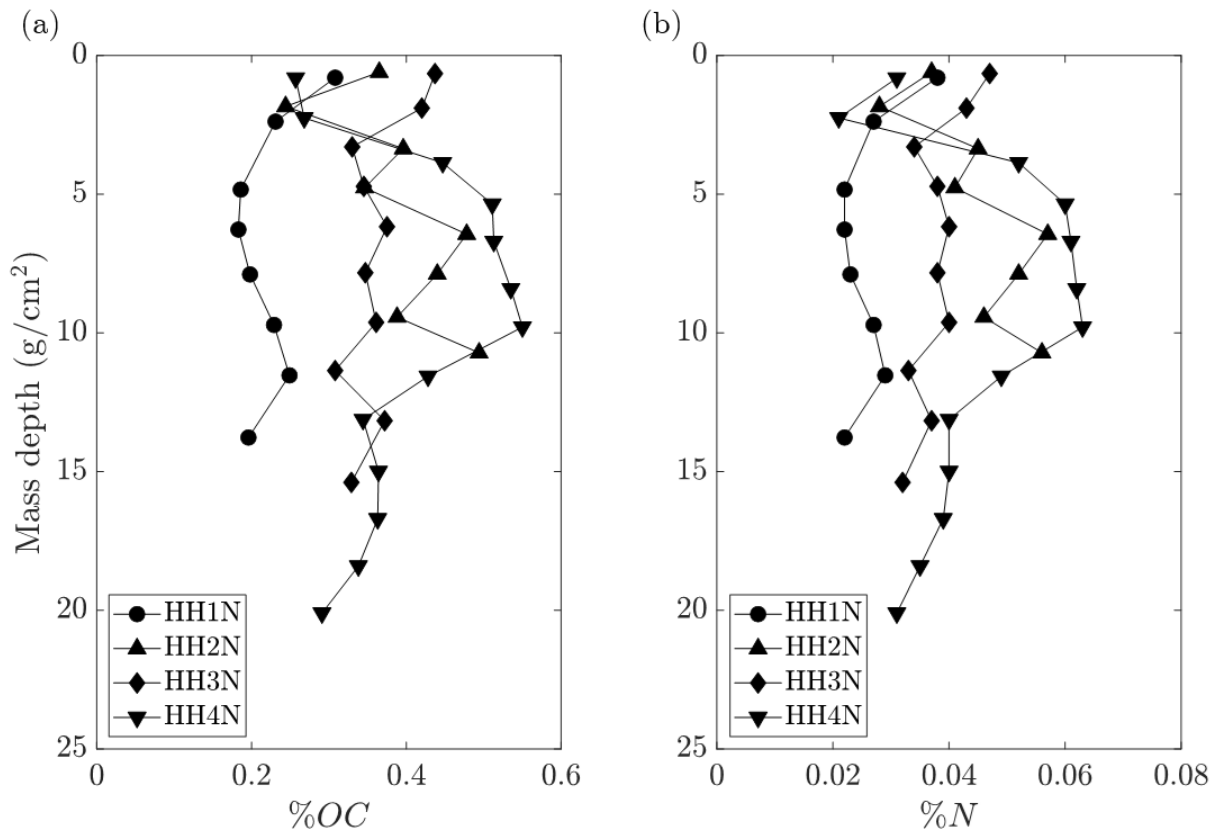


Figure 8.S.1: Profiles of organic carbon content %OC and nitrogen content %N versus cumulative mass depth in the sediment cores.

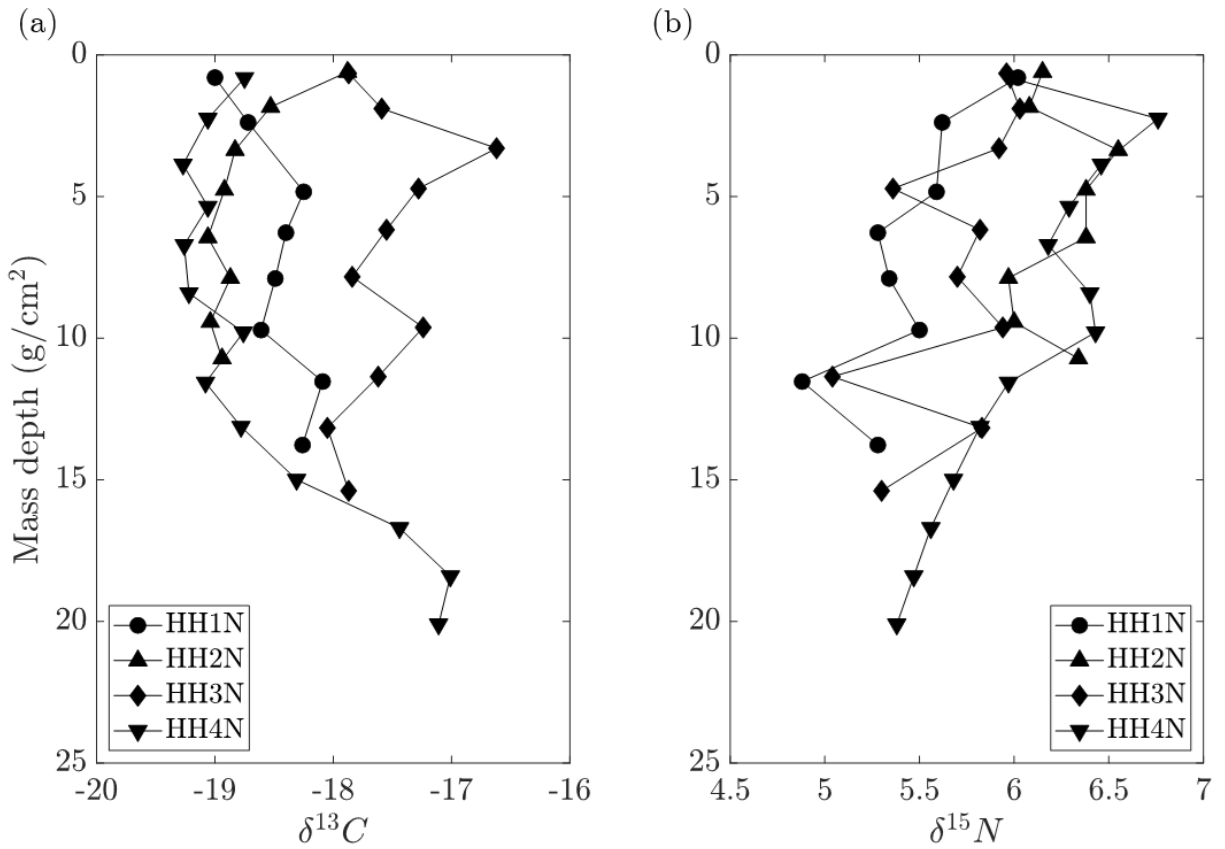


Figure 8.S.2: Profiles of carbon stable isotope ratio $\delta^{13}C$ (‰, relative to Vienna Pee Dee Belemnite) and nitrogen stable isotope ratio $\delta^{15}N$ (‰, relative to atmospheric air) versus cumulative mass depth in the sediment cores.

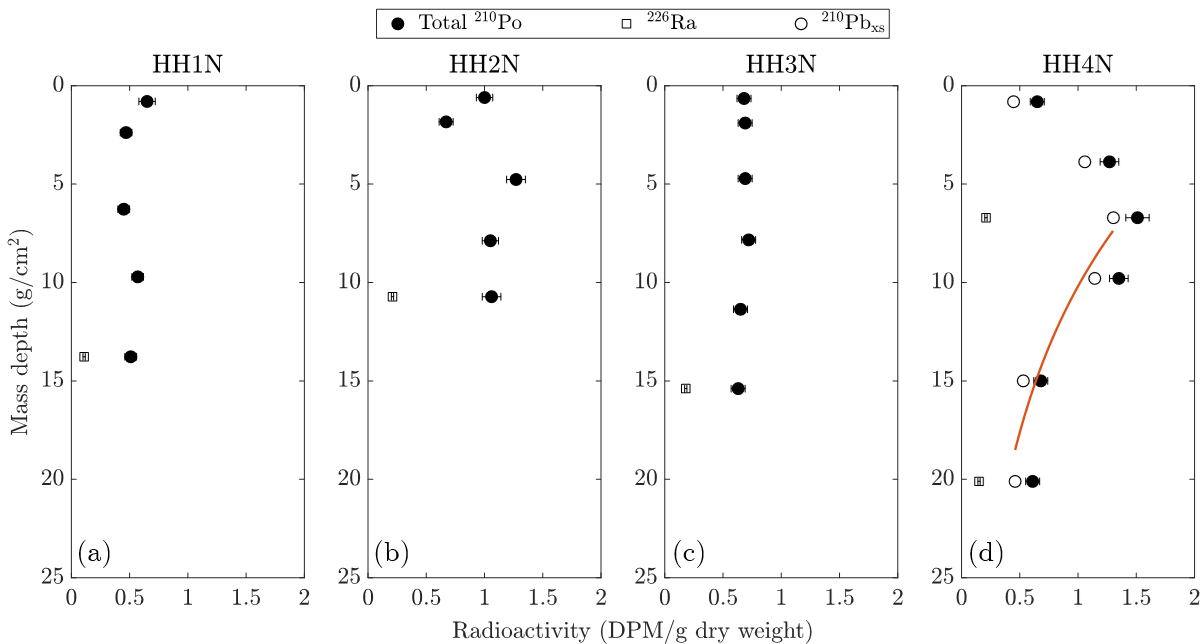


Figure 8.S.3: Profiles of total ²¹⁰Po (a proxy for ²¹⁰Pb) activity, ²²⁶Ra (a proxy for background ²¹⁰Pb activity) for all sediment cores, and excess ²¹⁰Pb activity for the HH4N core, versus cumulative mass depth in the sediment cores. The red curve in (d) represents the constant flux-constant sedimentation (CFCS) fit used to extract a sediment accumulation rate (below the surface mixing layer).

Chapter 9

Summary and ideas for future work

This thesis aimed to advance our understanding of the hydrodynamics of submerged aquatic vegetation such as seagrass and to connect that knowledge to the ecosystem services provided by such meadows of vegetation. In particular, the thesis focused on coastal protection through wave damping and carbon sequestration. In this chapter, I will synthesize main findings from the thesis and suggest avenues for future work.

Chapters 2 and 3 connected the physical interactions between seagrass meadows, waves, and currents to assess the ability of seagrass meadows to protect coasts by damping wave energy. Chapter 2 showed that a current following the direction of wave propagation could reduce wave damping relative to the corresponding pure wave condition due to additional streamlining and frontal area reduction. However, Chapter 3 showed that the addition of a current may reduce or enhance wave damping, depending on the relative strengths of current and wave velocities, the leaf stiffness, and whether the current is following or opposing the direction of wave energy

propagation. With increasing current velocity, the enhancement in flow velocity will begin to outpace the diminishing returns of the reduction in frontal area (due to deflection) and coincided with a reduction in leaf excursion during a wave period. If the Cauchy number is smaller than about 100, or in other words the plant is stiff enough, the addition of current may only lead to an enhancement in wave damping.

Chapter 4 explored the relative influences of waves and currents on vegetation-generated turbulence. When the ratio of wave velocity amplitude to current velocity was greater than or equal to one, the presence of waves reduced the magnitude of peak Reynolds stress compared to pure current conditions. I proposed a hybrid predictive model for stem-generated turbulent kinetic energy which accounted for the greater efficiency of currents in generating turbulence compared to waves. As an alternative to using the hybrid model, including only contributions from currents or only contributions from waves could lead to good predictions of turbulent kinetic energy when the ratio of wave velocity amplitude to current velocity was less than or greater than one, respectively. Overall, the new insights on stem-generated turbulence in flexible canopies provided by this study can contribute to a better understanding of how seagrass meadows can effectively sequester carbon in different flow conditions.

Chapter 5 investigated the idea of spatial gradients in hydrodynamic turbulence resulting in part from vegetation-induced wave damping correlating with spatial heterogeneity in sediment organic carbon content and accumulation rates. However, in Chapter 6 hydrodynamic intensity was positively correlated with sediment organic carbon content within a current-dominated lagoonal environment. The important factor in controlling sediment organic carbon, which also controlled hydrodynamic intensity, was the distance from the measurement station to the inlet channel to the lagoon. Even though tidal velocities decreased with distance from the inlet, which

created favorable conditions for sediment deposition in the interior of the meadow, most of the carbon-laden sediment had deposited closer to the edge of the meadow near the inlet.

Finally, in Chapter 7 sediment organic carbon stocks was similar across a patchy meadow, with the exception of one location. The present spatial variance of hydrodynamic intensity, in which flow velocities were lower within vegetated patches, did not correlate with the spatial variance in sediment organic carbon content. We concluded that recent persistency in aboveground vegetation coverage at that anomalous measurement station, as compared to the other measurement stations, could substantially contribute to the ability of that localized area of the meadow to accumulate and retain carbon. The study suggested that patchy meadows in which patches continually shift over time but are not able to coalesce into a continuous meadow, may not be effective long-term sediment organic carbon reservoirs.

Chapter 8 is similar to Chapters 5, 6, and 7 in its focus on sediment organic carbon storage in seagrass meadows, but is different in its aim to improve the characterization and analysis of the contribution of seagrass biomass to the organic carbon pool. While the field study described in Chapter 8 is ongoing and the results shown are preliminary, they indicate the promising potential of using aquatic eddy covariance, seagrass growth rates, and sediment core carbon accumulation rates for this purpose.

The results discussed in this thesis invite several additional research questions for further exploration. For example, future work could involve investigating how to integrate the new insights about meadow hydrodynamics and meadow patch persistence into seagrass restoration project plans. Existing frameworks and habitat suitability models for choosing donor locations from which to gather seagrass, target locations to restore, and the specific restoration technique

could be modified to include considerations of the range of peak tidal velocity to wave velocity amplitude ratios as well as predicted spatial gradients in carbon storage resulting from spatial hydrodynamic variability or proximity to carbon sources. When tidal velocities are converted to in-canopy velocities (as discussed throughout the thesis), current-to-wave velocity ratios could be used to improve predictions of wave damping, reducing the chances of overestimating or underestimating the ecosystem service. Current-to-wave velocity ratios could also be used to predict how sediment carbon may vary across a meadow. Furthermore, taking advantage of the increasing temporal and spatial resolution of aerial and satellite images, the frameworks could include algorithms to automatically select and sift through historical imagery of a site of interest to assess the persistence of the patches (including whether the patch configurations are static or dynamic)

Such modifications to restoration project planning demand large amounts of data. Based on detailed morphological, hydrodynamic, and carbon data currently available for seagrass meadows, a map of similarity scores could be generated to predict the provision of ecosystem services for other meadows for which little data are available. These predictions, following validation procedures (such as measuring wave damping or sediment carbon across a meadow), could be used to both apply for carbon credits and predict the economic value of ecosystem services restored through a potential restoration project, which could help reduce the uncertainty in efforts to provide global economic valuations of seagrass ecosystem services.

Additional laboratory flume experiments could complement the gaps in and difficulty in obtaining large quantities of field data for the efforts described above. For example, laboratory experiments in a wave basin could be done to tease out details about the influence of sediment grain size on seagrass carbon sequestration. Spatial variability in sediment grain size, which is a

function of hydrodynamics, can be related to spatial variability in sediment carbon storage through several important mechanisms. First, coarser, heavier particles require higher near-bed turbulence to initiate motion than finer particles, which more effectively adsorb organic matter due to their larger specific surface areas. Second, differences in the relative time scales for a particle to travel from one edge of a meadow to the opposite edge and for the particle to settle to the bed can contribute to spatial gradients in sediment supply and carbon. In a laboratory setting, one has direct control over the particle size distribution of sediment, quantity of sediment, organic carbon properties, meadow parameters, the water depth, and flow conditions. Different sizes of sediments could be dyed with different colors to facilitate the use of imaging in capturing sediment transport, flocculation, and deposition. A team of researchers could set out an array of sensitive instruments to measure suspended sediment concentrations throughout the water column, sediment deposition throughout the meadow, and hydrodynamic turbulence, which would be difficult to calibrate for or unlikely to survive in a field setting. Water and sediment samples could be taken to quantify the concentrations and spatial distributions of organic carbon. Trials should be designed to aim for scenarios where the supply of sediment would limit the reach of organic carbon across a meadow and where supply would not be a limiting factor. The laboratory measurements described above could provide more detailed, mechanistic insights into the influence of particle sizes on seagrass sediment carbon sequestration.

